

QUANTITATIVE ELECTRON PARAMAGNETIC RESONANCE  
SPECTROSCOPY IN HARSH AQUEOUS ENVIRONMENTS

**Dissertation**

zur Erlangung des akademischen Grades  
eines Doktors der Naturwissenschaften (Dr. rer. nat.)  
am Fachbereich Physik der Freien Universität Berlin

vorgelegt von

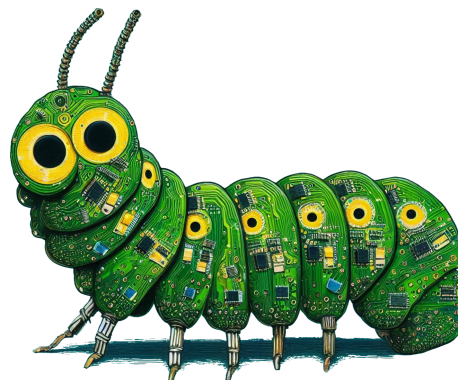
SILVIO DOMINIK LORENZO KÜNSTNER

Berlin, 2024

ERSTGUTACHTER: Prof. Dr. Klaus Lips  
Freie Universität Berlin

ZWEITGUTACHTER: Prof. Dr. Jens Anders  
Universität Stuttgart

TAG DER DISPUTATION: 02.10.2024



Silvio Dominik Lorenzo Künstner: *Quantitative electron paramagnetic resonance spectroscopy in harsh aqueous environments*, © 2024

## ABSTRACT

---

This thesis presents the advancement of electron paramagnetic resonance (EPR) spectroscopy for quantitative analysis of paramagnetic species in harsh aqueous environments.

EPR is the method of choice for investigating and quantifying paramagnetic species in many applications in materials science, biology, and chemistry. Of particular interest is the *in situ* monitoring of paramagnetic states in solution generated by chemical reactions. However, their investigation is limited by the concept of commercial EPR spectrometers, being based on the use of microwave (MW) resonators. To perform such *in situ* experiments, either the entire process must be confined to the resonator, or the sample solution must flow through the resonator by means of tubing, limiting the use of EPR to dedicated laboratories. Consequently, a redesign of EPR spectrometers is required for the more widespread use of this method.

The EPR-on-a-Chip (EPRoC) device circumvents these limitations by integrating the entire spectrometer, except for the magnet, onto a single microchip. Instead of an MW resonator, the planar coil of a voltage-controlled oscillator (VCO) with a diameter of a few hundred micrometers is used simultaneously as the MW source and detector. Frequency-swept EPR spectra can thus be recorded owing to the use of the VCO, which enables the use of permanent magnets. Covering the EPRoC with a protective coating enables it to be submerged directly in the sample solution, leading to a dipstick-type EPR spectrometer, thereby expanding accessible environments.

To acquire quantitative information of the sample, the effect of the inherently inhomogeneous MW magnetic field of the planar coil on the recorded signal amplitude is investigated. It is shown that the simulations are in good agreement with the experimental results.

The sensitivity of EPR, especially for samples with long relaxation times, may be improved by means of rapid-scan EPR. This method is implemented for EPRoC, improving the sensitivity per unit time by almost two orders of magnitude compared to the standard continuous wave operation.

An example of application for the EPRoC dipstick is the state of charge monitoring of a vanadium redox flow battery. Quantitative EPR measurements show that the EPRoC can be used as a monitoring device. In addition, these experiments serve as proof of principle for a quantitative EPRoC dipstick operating in a harsh environment.

In combination with a small permanent magnet, the EPRoC dipstick may find its way beyond the laboratory as a quantification tool for paramagnetic species in solution.





## ZUSAMMENFASSUNG

---

In dieser Arbeit wird der Einsatz der Elektronenspinresonanz-Spektroskopie (ESR, EPR) für die quantitative Analyse paramagnetischer Spezies in chemisch aggressiven Lösungen beschrieben.

EPR eignet sich hervorragend zur Untersuchung und Quantifizierung paramagnetischer Spezies in vielen Anwendungen der Materialwissenschaften, Biologie und Chemie. Von besonderem Interesse ist die *in situ*-Messung paramagnetischer Zustände in Lösungen, die durch chemische Reaktionen erzeugt werden. Solche Untersuchungen werden jedoch durch die Konstruktion üblicher EPR-Spektrometer eingeschränkt, die auf Mikrowellen-Resonatoren (MW) basieren. Um solche Experimente durchzuführen, muss entweder der gesamte Prozess auf den Resonator beschränkt werden oder die Lösung muss durch diesen durchgeleitet werden. Zur Vereinfachung dieser Experimente ist folglich eine Neugestaltung der Spektrometer erforderlich.

EPR-on-a-Chip (EPRoC) umgeht diese Einschränkungen, indem das gesamte Spektrometer, außer des Magneten, auf einen Mikrochip integriert wird. Anstelle eines Resonators wird die planare Spule eines spannungsgesteuerten Oszillators mit einem Durchmesser von einigen hundert Mikrometern verwendet, die gleichzeitig als Mikrowellenquelle und -detektor dient. Dies erlaubt, frequenzvariable Spektren aufzuzeichnen, was wiederum den Einsatz von Permanentmagneten ermöglicht. Durch eine Schutzbeschichtung kann der EPRoC-Dipstick direkt in die Probenlösung eingetaucht werden, wodurch die zugänglichen Probenumgebungen erweitert werden.

Um quantitative Informationen über die Probe zu erhalten, wird der Einfluss des inhärent inhomogenen MW-Feldes der planaren Spule auf das Messsignal untersucht, was mit Simulationen gut übereinstimmt.

Die Rapid-Scan-Methode ist eine hervorragende Möglichkeit um die Empfindlichkeit der EPR zu verbessern. Diese wird in den EPRoC implementiert und getestet, wobei die Empfindlichkeit um fast zwei Größenordnungen gegenüber dem Dauerstrichbetrieb verbessert wird.

Als Beispiel einer Anwendungsmöglichkeit wird der Ladezustand eines Vanadium-Redox-Flussakkumulators untersucht. Quantitative Messungen zeigen, dass EPRoC als Überwachungsmethode verwendet werden kann. Darüber hinaus zeigen die in dieser Arbeit vorgestellten Experimente, dass mit dem EPRoC-Dipstick quantitative Messungen in chemisch aggressiven Lösungen durchgeführt werden können.

Der EPRoC-Dipstick verfügt als innovative Methode über die besten Voraussetzungen, um in Zukunft über das Labor hinaus als Quantifizierungswerkzeug für paramagnetische Spezies in Lösung eingesetzt zu werden.



## PUBLICATIONS

---

Some ideas and figures have appeared previously in the following publications:

- 1 Silvio Künstner, Anh Chu, Klaus-Peter Dinse, Alexander Schnegg, Joseph E. McPeak, Boris Naydenov, Jens Anders and Klaus Lips. 'Rapid-Scan Electron Paramagnetic Resonance Using an EPR-on-a-Chip Sensor'. In: *Magnetic Resonance* 2.2 (25th Aug. 2021), pp. 673–687. DOI: [10.5194/mr-2-673-2021](https://doi.org/10.5194/mr-2-673-2021).
- 2 Silvio Künstner, Joseph E. McPeak, Anh Chu, Michal Kern, Klaus-Peter Dinse, Boris Naydenov, Peter Fischer, Jens Anders and Klaus Lips. 'Monitoring the state of charge of Vanadium redox flow batteries with an EPR-on-a-Chip dipstick sensor'. In: *Physical Chemistry Chemical Physics* 26.25 (2024), pp. 17785–17795. DOI: [10.1039/D4CP00373J](https://doi.org/10.1039/D4CP00373J).
- 3 Silvio Künstner, Joseph E. McPeak, Anh Chu, Michal Kern, Markus Wick, Klaus-Peter Dinse, Jens Anders, Boris Naydenov and Klaus Lips. 'Microwave field mapping for EPR on a Chip experiments'. In: *Science Advances* 10.33 (2024), ead05467. DOI: [10.1126/sciadv.ad05467](https://doi.org/10.1126/sciadv.ad05467).



## CONTENTS

---

1	Introduction	1
2	Basic principles of electron paramagnetic resonance	5
2.1	The resonance phenomenon	5
2.2	Spin Hamiltonian	7
2.2.1	Electron Zeeman interaction	7
2.2.2	Hyperfine Interaction	9
2.3	Vector picture	10
2.3.1	Motion of the magnetisation in a B-field	10
2.3.2	Relaxation and Bloch equations	12
2.3.3	Line broadenings	15
2.4	Resonator-based continuous-wave EPR	15
2.4.1	Quantitative EPR	17
2.4.2	Microwave power	18
2.4.3	Spin sensitivity	19
2.5	Rapid-scan EPR	21
2.5.1	Rapid passage signal	21
2.5.2	Non-adiabatic rapid passage	24
2.5.3	Sinusoidal frequency scans	25
2.5.4	Fourier deconvolution	26
3	Electron paramagnetic resonance on a chip	29
3.1	Working principle	29
3.2	Modelling of the EPRoC	32
3.2.1	Coil filled with paramagnetic material	32
3.2.2	Non-linear oscillator modelling	34
3.2.3	CW frequency-sensitive detection	36
3.2.4	CW amplitude-sensitive detection	37
3.2.5	Transient detection	38
3.2.6	Signal dependence on the bias current	39
3.3	Theoretical spin sensitivity / Limit of detection	41
3.4	Arrays of injection-locked VCOs	42
3.5	Frequency modulation	43
4	Materials and methods	45
4.1	Resonator-based EPR instrumentation	45
4.2	EPR-on-a-Chip instrumentation	46
4.2.1	Experimental configuration	46
4.2.2	FM detection via phase-locked loops	48
4.2.3	AM detection	50
4.2.4	Iterations of the EPR-on-a-Chip	50
4.3	Sample preparation and characterisation	52
4.3.1	Solid state samples	52
4.3.2	Solution samples	57
5	Practical considerations for EPR spectroscopists	61

5.1	Introduction	61
5.2	Materials and Methods	63
5.2.1	Experiment	63
5.2.2	Samples	63
5.2.3	Acquisition settings and post-processing	63
5.2.4	Spectral simulations	66
5.2.5	Extraction of EPR data from literature	67
5.3	Results and discussion	67
5.3.1	Investigation of solid state samples	67
5.3.2	Field and frequency sweeps	76
5.3.3	Paramagnetic species in solution	78
5.3.4	Influence of sample and experimental parameters	88
5.4	Conclusions	102
6	Considerations on the microwave field distribution	105
6.1	Introduction	105
6.2	Materials and methods	108
6.2.1	Samples	108
6.2.2	Experimental configuration	109
6.2.3	Acquisition settings and post-processing	111
6.2.4	Simulations	112
6.2.5	$E_1$ of a TE-102 cavity resonator	114
6.3	Results and discussion	115
6.3.1	Sensitive volume	115
6.3.2	Sensitive height	128
6.3.3	Partial utilisation of the EPRoC array	129
6.4	Conclusions	132
7	Rapid-scan EPR-on-a-Chip	133
7.1	Introduction	133
7.2	Materials and methods	136
7.2.1	Experiment	136
7.2.2	Bandwidth of the RS-EPR signal	138
7.2.3	Deconvolution of RS-EPRoC transients	139
7.2.4	Post-processing and SNR	143
7.2.5	Sample	144
7.3	Results and discussion	144
7.3.1	Comparison of CW- and RS-EPRoC	145
7.3.2	Saturation of RS-EPRoC transients	147
7.3.3	Theoretical limits of rapid-scan EPR	149
7.4	Conclusions	154
8	State of charge monitoring of a vanadium redox flow battery with EPR-on-a-Chip	157
8.1	Introduction	157
8.2	Materials and methods	164
8.2.1	Sample preparation	164
8.2.2	EPRoC configuration	165

8.2.3	Resonator-based EPR	166
8.2.4	Spectral simulations	167
8.2.5	Quantitation procedure	167
8.3	Results and discussion	170
8.3.1	EPRoC spectra of the catholyte	170
8.3.2	Comparison to resonator-based EPR	172
8.3.3	SOC estimation using the entire spectrum	175
8.3.4	SOC estimation using a 2-point truncation	179
8.4	Conclusions	181
9	Summary and conclusions	183
	Bibliography	187

## ACRONYMS

---

AM	amplitude modulated
a-Si	amorphous silicon
a-Si:H	hydrogenated amorphous silicon
BDPA	$\alpha,\gamma$ -bisdiphenylene- $\beta$ -phenylallyl
BM	field modulated
CAES	compressed air energy storage
CMOS	complementary metal-oxide-semiconductor
CW	continuous wave
DB	dangling bond
DC	direct current
DI	double integral
DPPH	2,2-diphenyl-1-picrylhydrazyl
DSLMM	digital single lens mirrorless
EES	electrical energy storage
ENBW	equivalent noise bandwidth
EPR	electron paramagnetic resonance
EPRoC	EPR-on-a-Chip
EPR-MOUSE	EPR mobile-universal-surface-explorer
ESR	electron spin resonance
FDMR	frequency-domain magnetic resonance
FID	free induction decay
FM	frequency modulated
FS	frequency swept
FSDD	field-stepped direct detection
FWHM	full width at half maximum
HEMT	high electron mobility transistor
HFI	hyperfine interaction
HZB	Helmholtz-Zentrum Berlin
ID	inner diameter
IR	infrared
LGR	loop-gap resonator
LIA	lock-in amplifier



LOD	limit of detection
MW	microwave
NARS	non-adiabatic rapid sweep
NMR	nuclear magnetic resonance
N@C <sub>60</sub>	nitrogen-atom-endohedral C <sub>60</sub>
OD	outer diameter
PCB	printed circuit board
PHES	pumped hydroelectric storage
PLL	phase-locked loop
pO <sub>2</sub>	partial oxygen pressure
PSD	phase-sensitive detection
P-EPR	pulsed EPR
Q	quality factor
RF	radio frequency
RFB	redox flow battery
RMS	root mean square
ROS	reactive oxygen species
RS	rapid scan
RT	room temperature
SI	single integral
SNR	signal-to-noise ratio
SOC	state of charge
STD	standard deviation
TE	transverse electric
TMI	transition metal ion
USTUTT	Universität Stuttgart
UV-VIS	ultraviolet–visible
VCO	voltage-controlled oscillator
VRFB	vanadium redox flow battery



## INTRODUCTION

---

Electron paramagnetic resonance (EPR, ESR) spectroscopy is a widely used, powerful and non-invasive spectroscopic technique sensitive to and selective for paramagnetic species employed in a variety of fields such as physics, chemistry, biology, materials science, life science, and medicine. It is commonly applied for quality control and chemical analyses, the identification and characterisation of radicals [1, 2], paramagnetic defects [3–5] and spin dependent processes in semiconductors and devices [6–8], transition metal ion states in biological samples [9], and for assignment of the electronic and atomic structure of paramagnetic states during chemical reactions [10, 11].

Commercial EPR spectrometers are routinely used for sensor-like applications by means of *quantitative* EPR, where the paramagnetic centres in the specimen are quantified [12]. This property is used in numerous applications such as radiation dosimetry [13–16], ESR dating for archaeological objects [17–19], food control [20, 21], environmental science [22–24] and materials science [3, 5, 25–30]. Of particular interest is the *in situ* monitoring of paramagnetic species in solution generated by chemical reactions. Examples of such applications are food analysis, where the degradation of beer [31] and of edible oil [32] is monitored, clinical EPR for the quantitation of reactive oxygen species with spin traps [33, 34] or *in situ* monitoring of the radical concentration in electrolytes of redox flow batteries (RFBs) [35–37].

However, the current design of commercial spectrometers is far from optimal for such experiments. These devices usually employ an microwave (MW) cavity resonator, with a large quality factor ( $Q$ ) to couple the magnetic part of the microwave,  $B_1$ , to the sample. To obtain the resonance condition, an electromagnet is used to sweep the external magnetic field aligned perpendicular to the magnetic field of the MW, while the MW frequency is kept constant. Due to the low bandwidth of the cavity, MW frequency sweeps are not feasible without distorting the EPR spectra. Typically, the sample resides in capillary tubes with diameters of a few millimetres, which is inserted in the centre of the cavity. Consequently, this strongly limits available sample space and with that the applicability of the technique.

Therefore, complicated experimental configurations are required for *in situ* investigations. Relatively simple experiments include flowing the reactants inside tubings through the cavity for the investigation of the electrolyte of redox flow batteries [37, 38] or homogeneous catalytic gas-phase reactions [39]. More complicated experiments include spectro-electrochemical EPR for catalysis research, in which an entire

electrochemical cell or at least its working electrode is placed in the sample tube [40, 41], the observation of film growth of hydrogenated amorphous silicon inside the cavity [42–45], or the investigation of radical formation through heterogeneous reaction of ozone and polycyclic aromatic compounds [46].

For more widespread use, certain application-specific EPR spectrometers have been developed, such as a miniaturised EPR “dipstick” [47] for investigation of paramagnetic species in solution, the EPR mobile-universal-surface-explorer (EPR-MOUSE) to examine surfaces of e.g. ancient pottery/stoneware or paint pigments on canvas [48], a near-field EPR spectrometric probe for biomedical studies [49], and a hand-held EPR probe for transcutaneous oximetry [50]. Most of these spectrometers are built such that the EPR probe is inserted in or placed onto the sample. This paradigm shift allows the investigation of samples that could not be investigated previously. However, most of the aforementioned spectrometers still require external MW circuitry, commonly referred to as MW bridge, for generation and detection of the MW. This limits their application again to dedicated laboratories.

Consequently, a complete redesign of EPR spectrometers, including the MW bridge, is necessary. Advancements in semiconductor fabrication technology have driven the development of new types of EPR spectrometers known as EPR-on-a-Chip (EPRoC) devices [51–54]. In these devices, either a traditional MW bridge [53, 54] or variations thereof are miniaturised into a single integrated circuit. The latter utilises either a fixed-frequency oscillator [51, 52] or a voltage-controlled oscillator (VCO) [55] to detect the EPR signal. In the latter method, a planar microcoil with a diameter of a few hundred micrometres, which is part of the VCO circuit, functions as both an MW source and EPR detector. The concept of employing a VCO instead of an MW bridge to excite and detect nuclear magnetic resonance signals was initially proposed in 1950 [56]. This approach is significant because it overcomes the conventional trade-off between the resonator  $Q$  and detection sensitivity, enabling frequency-swept EPR across wide MW frequency ranges with nearly constant sensitivity [57]. Consequently, it allows the use of permanent magnets, resulting in smaller, cost-effective, battery-operated spectrometers, as recently demonstrated [55, 58–60]. To arrive at a hand-held, battery-operated, frequency-swept, and quantitative in situ EPRoC device with a small permanent magnet utilisable for environmental or medical applications, a plethora of requirements need to be met.

Based on the previous studies, the development of the EPRoC towards a submersible dipstick-type spectrometer for harsh aqueous environments capable of delivering quantitative in situ data will be discussed in this thesis from a spectroscopist’s perspective. The EPRoC dipstick will then be applied to a real-world problem, that is the state of charge (SOC) monitoring for a vanadium redox flow battery (VRFB).

While this thesis focusses on understanding of the EPRoC from the application side, the development of further designs of the EPRoC, suitable permanent magnets as well as additional required electronics is discussed elsewhere. Each of the following paragraphs shortly introduces one of the main chapters in this thesis describing one of the requirements for developing a quantitative EPRoC spectrometer that may be utilised in harsh aqueous environments.

First, the general properties of the spectra recorded with the EPRoC as well as the influence of experimental parameters need to be understood in detail. Possible means to investigate powder, thin film and solution samples are presented.

Second, for quantitative EPR, ideally the exciting  $B_1$  should uniformly cover the entire sample; however, the  $B_1$  inhomogeneity of planar microcoils especially perpendicular to the plane is generally large. In addition, commonly, the sample can extend beyond the effective  $B_1$  or only occupy a small portion, which significantly complicates quantitative analysis. To accurately quantify an extended sample, a calibration sample with a known number of spins of exactly the same geometry and properties is necessary to minimise the impact of inhomogeneous  $B_1$ . Alternatively, the spatial distribution of  $B_1$  must be experimentally determined to correct for varying signal amplitudes resulting from inhomogeneities in the  $B_1$  distribution across the sample volume. The latter approach allows to calibrate the spectrometer such that only the sample geometry needs to be determined. In resonator-based EPR, the spatial distribution is typically established by comparing the EPR signal of a point sample relative to its position within the cavity. Similar experiments are performed to map the microwave magnetic field for the EPRoC, which are complemented by finite-element simulations of the  $B_1$  distribution.

Third, the sensitivity of any spectroscopy is one of its most important characteristics. Generally, there are multiple routes to improve the sensitivity of the EPRoC. For instance, by injection locking of multiple VCOs to a so-called EPRoC array [61], spatial averaging may be achieved improving the sensitivity with the square root of the number of VCOs. The sensitivity may also be improved by utilising the rapid-scan EPR (RS-EPR) technique introduced by the Eaton group [62]. It is particularly useful for samples with long relaxation times. This technique offers an advantage over continuous wave EPR (CW-EPR) because it permits the application of much higher microwave excitation fields ( $B_1$ ) to the sample before saturation effects become apparent. By spending less time on resonance, the RS technique overcomes the MW saturation limitations of the spin system and enhances the signal-to-noise ratio (SNR) compared to traditional CW-EPR [62]. This is achieved by rapidly scanning the magnetic field or MW frequency such that the resonance is passed in a time shorter than the relaxation times. While usually the magnetic field is rapidly scanned, the frequency sweep capability

of the EPRoC offers a simple means to accomplish RS-EPRoC, without the need for complicated instrumentation such as dedicated RS coils and amplifiers. Within this thesis, the RS technique with successful deconvolution is established.

Finally, the EPRoC dipstick is applied to a real-world application. Ex situ quantitative EPRoC experiments of the positive electrolyte solution of a VRFB battery for monitoring the state of charge serve as proof-of-concept experiments for quantitative dipstick type EPRoC experiments in a strongly acidic solution.

The thesis is structured as follows. [Chapter 2](#) provides the basic theoretical principles of EPR including the resonance phenomenon, the spin Hamiltonian formalism, the famous *Bloch* equations and their steady-state solution for CW-EPR. A short introduction to RS-EPR is given. [Chapter 3](#) lays the foundations for the EPRoC work discussed in the remainder of the thesis. This includes a review of “micro”-EPR (microresonator, oscillator), different detection schemes with the EPRoC, the EPRoC array and the saturation behaviour. In [Chapter 4](#), the experimental configuration in the Berlin Joint EPR Laboratory at Helmholtz-Zentrum Berlin for CW- and RS-EPRoC, preparation of the standard samples and the resonator-based EPR experimental configurations are discussed. In this chapter, the materials and methods relevant for all main chapters may be found. Each of the main chapters described below contains its own introduction as well as materials and methods sections specific for the chapter, so that each main chapter stands on its own. [Chapter 5](#) is hands-on and focuses on understanding of the EPRoC signals in detail. Several means to investigate samples with different phases are described, including the introduction of the EPRoC dipstick. Additionally, the influence of experimental and sample parameters on the EPRoC signals is discussed. The MW magnetic field distribution and its effect on the measured EPRoC signal is discussed in [Chapter 6](#). Furthermore, the injection-locked EPRoC array will be explored. While chapters [5](#) and [6](#) were mainly concerned with a basic understanding of CW-EPRoC, [Chapter 7](#) deals with the application of a recently developed measurement technique, RS-EPR, on the EPRoC. Here, proof-of-principle RS-EPRoC experiments exhibit an improved sensitivity compared to CW-EPRoC. In addition, a perspective for future improvements is given. [Chapter 8](#) shows a possible real-world application of the EPRoC. This is the monitoring of the SOC of a VRFB with a submersible quantitative EPRoC sensor. With regard to the EPRoC technology, these experiments serve as proof-of-principle experiments for further applications of the EPRoC in harsh solution environments. The [last chapter](#) summarises the findings of this thesis and puts them in a broader perspective for future applications.

## BASIC PRINCIPLES OF ELECTRON PARAMAGNETIC RESONANCE

---

The theoretical part is divided into two chapters. While this chapter covers the basic principles to understand conventional electron paramagnetic resonance (EPR) spectroscopy, the [second theory chapter](#) deals with the EPR-on-a-Chip (EPRoC) technology. This chapter is structured as follows. The physical principles of EPR are explained based on the spin Hamiltonian formalism and the vector picture including *Bloch's* equations. The latter are used to describe continuous wave EPR (CW-EPR) spectra. Certain lineshape broadening mechanisms are discussed. Resonator-based CW-EPR spectrometers are introduced in a nutshell. Furthermore, quantitative EPR, saturation and one of the most important parameters, the spin sensitivity, is introduced. At last, the rapid-scan EPR (RS-EPR) technique is introduced with theoretical considerations based on *Bloch's* equations.

### 2.1 THE RESONANCE PHENOMENON

Electrons possess an intrinsic spin angular momentum associated with the operator  $S$  inducing a magnetic moment  $\mu_e$ . The classical analogon for a free electron spin is a spinning charged sphere of which the magnetic moment may be calculated by

$$\mu_e = \gamma S = -g_e \frac{e}{2m_e} S = -\frac{g_e \mu_B}{\hbar} S, \quad (2.1)$$

where  $\gamma = -g_e \mu_B / \hbar$  is the gyromagnetic ratio of the electron,  $g_e \approx 2.0023$  is the  $g$ -factor of the free electron,  $\mu_B$  is the *Bohr* magneton,  $e$  is the elementary charge,  $m_e$  is the mass of the electron, and  $\hbar$  is the reduced Planck's constant. In the classical picture, the  $g$ -factor is required to account for the deviations of the behaviour of the electron as a quantum object. The negative sign indicates that the magnetic moment for an electron is anti-parallel to its spin. The *Bohr* magneton

$$\mu_B = \frac{e\hbar}{2m_e} \quad (2.2)$$

introduced in [Equation 2.1](#) is the magnetic moment for one unit of quantum mechanical angular momentum. Classically, the energy,  $E$  of a magnetic moment,  $\mu$  in a magnetic field,  $B$  is described by

$$E = -\mu \cdot B. \quad (2.3)$$

For a quantum-mechanical system, the magnetic moment,  $\mu$ , may be replaced by the appropriate operator such that the corresponding *Hamilton* operator is obtained as

$$\mathcal{H} = g_e \mu_B \mathbf{S} \cdot \mathbf{B}. \quad (2.4)$$

For a free electron exposed to a magnetic field in  $z$ -direction with magnitude  $B_0$  this operator simplifies to

$$\mathcal{H} = g_e \mu_B S_z B_0. \quad (2.5)$$

$S_z$  is the only operator on the right-hand side of [Equation 2.5](#), so the eigenvalues of the Hamiltonian are multiples of the eigenvalues of itself

$$E = m_s g_e \mu_B \cdot B_0, \quad (2.6)$$

where  $m_s = \pm 1/2$  is the spin quantum number. Hence, there are two states which are degenerate in zero magnetic field,  $B_0$ . Upon application of a magnetic field, their energy separation,  $\Delta E$  increases linearly with  $B_0$

$$\Delta E = g_e \mu_B B_0, \quad (2.7)$$

which is referred to as *Zeeman* effect. The energy separation of two levels can be matched to the energy of a quantum of radiation  $hf$  which gives the resonance condition for a free electron

$$hf = g_e \mu_B B_0, \quad (2.8)$$

which forms the basis of EPR spectroscopy.

The absorption of radiation depends on transition probabilities between the two energy states, which in turn are a function of the population difference,  $\Delta N$ . In thermal equilibrium, relative populations may be described by *Boltzmann* statistics and is given by

$$N_+/N_- = e^{-\Delta E/k_B T}, \quad (2.9)$$

where  $N_+$  and  $N_-$  are the populations of the spin states,  $k_B$  is the Boltzmann constant,  $T$  is the temperature, and  $\Delta E$  as defined above. The population may be calculated from the relative populations and is given by

$$\frac{\Delta N}{N_s} = \frac{N_+ - N_-}{N_+ + N_-} = \frac{1 - e^{-\Delta E/k_B T}}{1 + e^{-\Delta E/k_B T}}, \quad (2.10)$$

where  $N_s$  is the total number of spins and  $\Delta N = N_+ - N_-$  is the population difference of the two spin states.



## 2.2 SPIN HAMILTONIAN

In the previous section, the Hamiltonian of an isolated free electron was discussed. This gives rise to an EPR spectrum with single resonance line fulfilling at the resonance condition of Equation 2.8. However, such free electrons are rarely observed in real-world paramagnetic species. Instead, they are influenced by magnetic interactions with their local environment such as hyperfine interaction (HFI) with nearby nuclear spins. These interactions may lead to many different energy states between which allowed transitions exist, resulting in a plethora of spectral lines. The energies of a spin system can be described by the so-called *spin Hamiltonian*. All paramagnetic species presented in this thesis can be described by a spin-1/2 system with HFI. Therefore, their spin Hamiltonian is given by [63]

$$\hat{H} = \hat{H}_{\text{EZ}} + \hat{H}_{\text{HF}}. \quad (2.11)$$

The first term describes the *electron Zeeman interaction*, while the HFI is described by the second. Other contributions such as nuclear quadrupole interaction or nuclear Zeeman interaction are neglected in Equation 2.11. Zero-field splitting only occurs for spin systems with a total spin  $> 1/2$  [64]. As the spin Hamiltonian concept exists since the dawn of EPR, it is described in many textbooks such as [65–69].

2.2.1 *Electron Zeeman interaction*

Equation 2.5 was derived assuming a free electron spin which was quantised along the external field  $\mathbf{B}$ . Usually, however, the electron spin is not free but bound in a material environment so that the  $g$ -factor deviates from the  $g$ -value of the free electron,  $g_e$ . While for organic radicals the deviation is usually smaller than 0.5%, the  $g$ -value for transition metal ions spans over a wide range of values [68]. The  $g$ -value can be used as a fingerprint of a material, similar to the chemical shift in nuclear magnetic resonance (NMR). The electronic Zeeman term of the spin Hamiltonian representing the interaction of the electron spin  $S$  with the external magnetic field  $B$  is described by [68]

$$\hat{H}_{\text{EZ}} = -\mathbf{B}\hat{\mu} = \mu_B\mathbf{B}^\top \mathbf{g}\hat{S}, \quad (2.12)$$

where  $\hat{\mu}$  and  $\hat{S}$  are the angular momentum and spin operator, and  $\mathbf{g}$  is the so-called  $g$ -tensor, formally a  $3 \times 3$  matrix, containing all spatial information from the environment. Generally, the  $g$ -tensor is anisotropic and only for cubic or higher symmetry reduces to a scalar.

Usually  $g$  is symmetric, so it can be diagonalised to its principal axes system and Equation 2.12 becomes

$$\hat{H}_{\text{EZ}} = \mu_{\text{B}} \begin{pmatrix} B_x & & \\ & B_y & \\ & & B_z \end{pmatrix} \begin{pmatrix} g_x & & \\ & g_y & \\ & & g_z \end{pmatrix} \begin{pmatrix} \hat{S}_x \\ \hat{S}_y \\ \hat{S}_z \end{pmatrix} = \mu_{\text{B}} \sum_{i=x,y,z} B_i g_i \hat{S}_i, \quad (2.13)$$

where  $g_x$ ,  $g_y$  and  $g_z$  are the principal values of the  $g$ -tensor. As mentioned above, for  $g_x = g_y = g_z$ , the tensor reduces to a scalar and is referred to as cubic or isotropic. If two principal values are equal, the  $g$ -tensor is referred to as axial. In absence of symmetry, i.e.,  $g_x \neq g_y \neq g_z$ , the  $g$ -tensor is referred to as rhombic.

### 2.2.1.1 $g$ -anisotropy

The extent of observed  $g$ -anisotropy depends on the state of the sample. [68] For samples with randomly oriented spins in a solid, e.g., frozen solutions or powder samples, all orientations of the paramagnetic centre with respect to the external magnetic field are equally probable. This leads to so-called powder spectra, where each orientation is observed. Simulation of such powder spectra can be performed with the function *pepper* of the *EasySpin* [70] software package.

For samples in solution, however, the molecules tumble so that they lose their fixed orientation with respect to the external magnetic field. This may lead to an averaging of the  $g$ -anisotropy depending on the rate of reorientation of the molecule compared to the timescale of the observation, i.e., the inverse of the microwave (MW) frequency. The time of reorientation may be described by a rotational correlation time,  $\tau_c$ . If  $\tau_c$  is much longer than the inverse MW frequency, the sample seems frozen and exhibits a powder-like spectrum. In the opposite case, i.e.,  $\tau_c \ll 1/f_{\text{mw}}$ , the  $g$ -anisotropy will be completely averaged out. In this case, the resonance will be observed at a magnetic field corresponding to  $g_{\text{iso}} = \frac{1}{3}\text{tr}(g)$  leading to a so-called isotropic fast motion spectrum. This can be simulated with the function *garlic* of the *EasySpin* software package [70]. Between the two extreme cases, a mixture of powder and fast-motion spectrum appears, which is called slow-motion spectrum. The latter can be simulated using *chili* of *EasySpin* [70]. In first order approximation, the rotational correlation time can be calculated from the Stokes-Einstein equation as [68]

$$\tau_c = \frac{4\pi\eta R^3}{3k_{\text{B}}T},$$

where  $\eta$  is the viscosity of the solution,  $R$  is the hydrodynamic radius,  $k_{\text{B}}$  is the Boltzmann constant, and  $T$  the temperature of the sample.

### 2.2.2 Hyperfine Interaction

The HFI arises from the magnetic interaction of the electron spin with nuclear spins in its close surroundings. Alongside the  $g$ -value, it is one of the most important sources of information in EPR spectroscopy allowing to identify paramagnetic centres and giving insights into the ligand sphere. As these interactions may result in complicated spectra overlaid by other interactions, sophisticated pulse methods such as electron-nuclear double resonance (ENDOR) [71], electron-electron double resonance (ELDOR)-detected NMR [72], and electron spin echo envelope modulation (ESEEM) [73] have been developed, which allow disentangling HFIs in great detail.

A detailed derivation of the HFI Hamiltonian is performed in many EPR textbooks including [65, 67], and only the most important results are stated here. The derivation uses the fact that the magnetic interaction corresponds to the classical dipole-dipole interaction between the magnetic moments of the electron and the nucleus placed at a distance  $r$  with respect to each other.

Using this approach, the Hamiltonian of the HFI of an electron spin  $S$  and a nuclear spin  $I$  is given by

$$\hat{H}_{\text{HF}}/h = \hat{S}^T \mathbf{A} \hat{I} = \begin{pmatrix} \hat{S}_x & \hat{S}_y & \hat{S}_z \end{pmatrix} \begin{pmatrix} A_{xx} & A_{xy} & A_{xz} \\ A_{yx} & A_{yy} & A_{yz} \\ A_{zx} & A_{zy} & A_{zz} \end{pmatrix} \begin{pmatrix} \hat{I}_x \\ \hat{I}_y \\ \hat{I}_z \end{pmatrix}, \quad (2.14)$$

where  $A$  is the so-called hyperfine-coupling tensor in units of MHz,  $\hat{S}$  and  $\hat{I}$  are the spin operators for the electron and nuclear magnetic moments, respectively. The hyperfine-coupling tensor can be split apart into the isotropic Fermi contact interaction ( $r = 0$ ) and the electron-nuclear dipolar interaction ( $r > 0$ ) as

$$\mathbf{A} = a_{\text{iso}} \mathbf{I}_3 + \mathbf{T} \quad (2.15)$$

where  $a_{\text{iso}}$  is the isotropic hyperfine-coupling constant,  $\mathbf{I}_3$  is the  $3 \times 3$  identity matrix, and  $\mathbf{T}$  is the anisotropic dipolar coupling tensor. The isotropic hyperfine-coupling constant is given by [67]

$$a_{\text{iso}} = \frac{2}{3} \mu_0 g_e \mu_B g_N \mu_N |\Psi_0(0)|^2, \quad (2.16)$$

where  $\mu_0$  is the magnetic constant,  $g_N$  and  $\mu_N$  denote the nuclear  $g$  value and nuclear magneton, respectively, and  $|\Psi_0(0)|^2$  is the electron spin density at the position of the nucleus at  $r = 0$ .

The elements of  $\mathbf{T}$  of the electron-nuclear dipolar interaction take the form

$$T_{ij} = \frac{\mu_0}{4\pi} \mu_0 g_e \mu_B g_N \mu_N \left\langle \Psi_0 \left| \frac{3r_i r_j}{r^5} - \frac{\delta_{ij}}{r^3} \right| \Psi_0 \right\rangle, \quad (2.17)$$

where  $\Psi_0$  is the ground-state wave function and  $\delta_{ij}$  is Dirac's delta function. Usually,  $T$  can be diagonalised by a rotational transformation to its eigenframe as

$$\begin{aligned} T_{\text{diag}} &= \mathbf{R}^\top(\alpha, \beta, \gamma) \mathbf{T} \mathbf{R}(\alpha, \beta, \gamma) \\ &= \begin{pmatrix} T_x & & \\ & T_y & \\ & & T_z \end{pmatrix} = T \begin{pmatrix} -(1-\rho) & & \\ & -(1+\rho) & \\ & & 2 \end{pmatrix}, \end{aligned} \quad (2.18)$$

where the diagonal elements have been replaced by an axial component  $T = T_z/2$  and a rhombic component  $\rho = (T_x - T_y)/2$ . In this case, the HFI is characterised by the three parameters  $a_{\text{iso}}$ ,  $T$ , and  $\rho$ .

In this work, both hyperfine interactions with axial symmetry ( $A_\perp = A_x = A_y = a_{\text{iso}} - T$ ;  $A_\parallel = A_z = a_{\text{iso}} + 2T$ ) and rhombic symmetry ( $A_x = a_{\text{iso}} - T + \rho$ ;  $A_y = a_{\text{iso}} - T - \rho$ ;  $A_z = a_{\text{iso}} + 2T$ ) are considered for vanadyl ions and 4-hydroxy-2,2,6,6-tetramethylpiperidine-1-oxyl (tempol) in solution, respectively.

### 2.3 VECTOR PICTURE

Although the electron spin is a quantum mechanical quantity, the description with a semi-classical model using *Bloch's* equations can explain many effects of a spin system in an external magnetic field absorbing quanta of radiation. It is especially suited to obtain easily manageable equations for the so-called saturation behaviour explained later. Similarly to the theory of the spin Hamiltonian, the vector picture is described in many textbooks including [65, 66, 69, 74, 75].

#### 2.3.1 Motion of the magnetisation in a magnetic field

The magnetic moment  $\boldsymbol{\mu}$  of an electron spin in the presence of an arbitrary and possibly time-dependent magnetic field  $\mathbf{B}(t)$  experiences a torque described by the equation of motion as

$$\frac{d\boldsymbol{\mu}_e}{dt} = \boldsymbol{\mu}_e \times (\gamma \mathbf{B}(t)) \quad (2.19)$$

For an ensemble of  $N_S$  unpaired electron spins, the macroscopically measured quantity is the magnetisation  $\mathbf{M}$ , which is the magnetic moment per unit volume  $V$ . Thus, the magnetic moment in Equation 2.19 may then be replaced by the sum of magnetic moments and for a static magnetic field  $\mathbf{B}_0$  along  $z$  reads

$$\frac{d\mathbf{M}}{dt} = \mathbf{M} \times (\gamma \mathbf{B}_0) = |\gamma| \mathbf{B}_0 \times \mathbf{M}, \quad (2.20)$$

with

$$\mathbf{M} = \frac{1}{V} \sum_i^{N_S} \boldsymbol{\mu}_{e,i}. \quad (2.21)$$

resulting in a precession about  $\mathbf{B}_0$  with a frequency of

$$\omega_0 = |\gamma| B_0 \quad (2.22)$$

referred to as *Larmor* frequency.

The motion of the magnetisation in a static magnetic field,  $\mathbf{B}_0 = (0, 0, B_0)^\top$  and a time-varying magnetic field,  $\mathbf{B}_1(t)$ , is described by

$$\frac{d\mathbf{M}}{dt} = |\gamma| (\mathbf{B}_0 + \mathbf{B}_1(t)) \times \mathbf{M} = |\gamma| \mathbf{B}_0 \times \mathbf{M} + |\gamma| \mathbf{B}_1(t) \times \mathbf{M}. \quad (2.23)$$

In the case of a circularly polarised magnetic field,  $\mathbf{B}_1$ , with a (MW) frequency  $\omega = 2\pi f$  described by

$$\mathbf{B}_1(t) = B_1 \begin{bmatrix} \cos \omega t \\ \sin \omega t \\ 0 \end{bmatrix} \quad (2.24)$$

Equation 2.23 describes a nutation, which is a superposition of two precessions about  $\mathbf{B}_0$  and  $\mathbf{B}_1(t)$  with their respective *Larmor* frequencies  $\omega_0$  and  $\omega_1 = |\gamma| B_1$ .

For simplicity, it is useful to transform Equation 2.20 and Equation 2.23 from the laboratory frame  $(x, y, z)$  to a so-called rotating frame  $(x', y', z')$  revolving with a frequency  $\omega$  about the  $z$ -axis. Using the conversion of infinitesimal changes of  $d\mathbf{M}$  to  $d'\mathbf{M}$  [74]:

$$d\mathbf{M} = d'\mathbf{M} + \omega dt \times \mathbf{M} \leftrightarrow \frac{d\mathbf{M}}{dt} = \frac{d'\mathbf{M}}{dt} + \omega \times \mathbf{M} \quad (2.25)$$

we can rewrite Equation 2.20 in the rotating frame as

$$\frac{d'\mathbf{M}}{dt} = |\gamma| \left( \mathbf{B}_0 - \frac{\omega}{|\gamma|} \right) \times \mathbf{M} = \mathbf{\Omega} \times \mathbf{M}, \quad (2.26)$$

where  $\mathbf{\Omega} = \omega_0 - \omega$  is the resonance offset describing the difference of the *Larmor* frequency to the rotation frequency,  $\omega$ . Comparing Equation 2.20 with Equation 2.26, it can be seen that the motion of the magnetisation in the rotating frame obeys same equation as in the laboratory frame if the magnetic field,  $B_0$ , is replaced by an effective field  $\mathbf{B}_0 - \omega / |\gamma|$ .

Taking the time-dependent magnetic field from Equation 2.24 into consideration, which is *time-independent* in the rotating frame, the effective magnetic field reads

$$\mathbf{B}_{\text{eff}} = \mathbf{B}_1 + \mathbf{B}_0 - \frac{\omega}{|\gamma|}. \quad (2.27)$$

Thus, the effective magnetic field is time-independent in the rotating frame. Therefore, the magnetisation precesses about  $\mathbf{B}_{\text{eff}}$  with a frequency of

$$\omega_{\text{eff}} = |\omega_1 + \mathbf{\Omega}| = \sqrt{\omega_1^2 + \Omega^2}, \text{ where } \Omega = \omega_0 - \omega. \quad (2.28)$$

Resonance occurs for  $\Omega = 0$ , which is the equivalent to the resonance condition expressed in Equation 2.8. In this case, the *Larmor* frequency and the rotation frequency,  $\omega$  coincide and  $\mathbf{B}_{\text{eff}} = \mathbf{B}_1$ . Then, the magnetisation precesses only about  $\mathbf{B}_1$  at a frequency  $\omega_1 = |\gamma| B_1$ . Far away from resonance, the effective magnetic field is either nearly parallel ( $\Omega \gg 0$ ) or anti-parallel ( $\Omega \ll 0$ ) to  $\mathbf{B}_0$ . Specifically, the angle inclined by  $\mathbf{M}$  and  $\mathbf{B}_{\text{eff}}$  may be written as

$$\theta_{\text{eff}} = \arctan(\omega_1/\Omega). \quad (2.29)$$

The equation of motion was derived with the assumption of a circularly-polarised microwave, the solutions obviously only apply for these. Common EPR spectrometers, however, usually use linearly polarised microwaves, e.g.  $B_1 = (2B_1 \cos \omega t, 0, 0)^T$  [66]. Linearly-polarised waves may be decomposed in two circularly-polarised waves with equal magnitude and opposite directions:

$$\begin{aligned} \mathbf{B}_{1,\text{lab}} &= \mathbf{B}_{1,\text{lab}}^r (+) + \mathbf{B}_{1,\text{lab}}^l (-) \\ &= B_1 (\cos(\omega t)\hat{e}_x + \sin(\omega t)\hat{e}_y) \\ &\quad + B_1 (\cos(\omega t)\hat{e}_x - \sin(\omega t)\hat{e}_y), \end{aligned} \quad (2.30)$$

where  $\hat{e}_x$  and  $\hat{e}_y$  are unit vectors in  $x$ - and  $y$ -direction. In the rotating frame, the right-hand polarised field behaves as described before and is time-independent. The left-hand polarised field, however, is still time-dependent<sup>1</sup> and off-resonant by approximately  $2\omega$ . Usually  $2\omega \gg \omega_1$ , so that the left-hand polarised field may be neglected. Hence, the solutions are also valid for linearly polarised microwaves.

### 2.3.2 Relaxation and Bloch equations

As explained in Section 2.3.1, the magnetisation,  $\mathbf{M}$  precesses about the effective field in the rotating frame, which may be considered an equilibrium position. If the magnitude or direction of this field is suddenly changed, the magnetisation will adapt to an equilibrium position in a certain time. For instance, if the effective field changes to zero, the magnetisation will return to its equilibrium position,  $\mathbf{M}_0$ . This process is called *relaxation* and will be discussed in the following. When including relaxation rates in the equations describing the motion of the magnetisation (cf. Equation 2.23), we obtain the famous *Bloch* equations first introduced by Felix Bloch in 1946 [76]. These rates merely explain phenomenologically the behaviour of the relaxation of the magnetisation and may be caused by a number of different processes. A general overview of relaxation mechanisms may be found in ref. [77], while comprehensive discussions of quantum-mechanical relaxation theory may be found in refs. [65, Chapter 8] and [66, Chapter 8].

<sup>1</sup>  $\mathbf{B}_{1,\text{rot}}^l = B_1 (\cos(2\omega t), \sin(2\omega t), 0)^T$

The relaxation of the  $z$ -component of  $\mathbf{M}$  is called spin-lattice or longitudinal relaxation and described may be described with a time constant,  $T_1$ . Here, an energy exchange between the spin system and the 'lattice' establishing thermal equilibrium, which can be described by

$$\frac{dM_z(t)}{dt} = -\frac{M_z(t) - M_0}{T_1}. \quad (2.31)$$

In the early days of EPR spectroscopy, relaxation studies were mainly investigating crystalline solids, so that the term 'lattice' meant crystal lattice. Nowadays, however, the 'lattice' is a more general term describing whatever surrounds the unpaired electron [77].

The relaxation in the  $xy$ -plane is called spin-spin or transversal relaxation and is described by a relaxation time,  $T_2$ . In thermal equilibrium, i.e., without field,  $M_x$  and  $M_y$  are zero since individual spins have no phase coherence. On resonance ( $\Omega = 0$ ), however, the magnetisation is turned about  $x'$  in the rotating frame leading to a phase coherence which results in a magnetisation component in the  $xy$ -plane. After excitation this phase coherence is lost due to local interactions between the individual spins. For this reason, the transverse magnetisation decays to zero, which can be expressed by

$$\frac{dM_x(t)}{dt} = -\frac{M_x(t)}{T_2} \quad \text{and} \quad \frac{dM_y(t)}{dt} = -\frac{M_y(t)}{T_2}. \quad (2.32)$$

Introducing the expressions for relaxation of [Equation 2.31](#) and [Equation 2.32](#) into the equation of motion in the rotating frame leads to the famous *Bloch* equations:

$$\frac{dM_x}{dt} = -\Omega M_y - \frac{M_x}{T_2} \quad (2.33a)$$

$$\frac{dM_y}{dt} = \Omega M_x - \omega_1 M_z - \frac{M_y}{T_2} \quad (2.33b)$$

$$\frac{dM_z}{dt} = \omega_1 M_y - \frac{M_z - M_0}{T_1}. \quad (2.33c)$$

These equations are a set of coupled ordinary differential equations that may be solved numerically to investigate the dynamics of spin-1/2 systems.

For a sufficiently slow scan of either magnetic field,  $\mathbf{B}_0$ , or MW frequency,  $\nu_{\text{mw}} = 2\pi\omega$ , compared to the relaxation rates, an equilibrium between relaxation and MW absorption occurs such that a steady

state emerges. Under these conditions, that is  $d\mathbf{M}/dt = 0$ , the *Bloch* equations in Equation 2.33 have a straightforward solution:

$$M_x = M_0\omega_1 \frac{\Omega T_2^2}{1 + \Omega^2 T_2^2 + \omega_1^2 T_1 T_2} = \frac{\chi'(t)B_1}{\mu}, \quad (2.34a)$$

$$M_y = -M_0\omega_1 \frac{T_2}{1 + \Omega^2 T_2^2 + \omega_1^2 T_1 T_2} = \frac{\chi''(t)B_1}{\mu}, \quad (2.34b)$$

$$M_z = M_0 \frac{1 + \Omega^2 T_2^2}{1 + \Omega^2 T_2^2 + \omega_1^2 T_1 T_2}, \quad (2.34c)$$

where  $M_0 = \chi_0 B_0 / \mu$  is the equilibrium magnetisation with the static magnetic susceptibility  $\chi_0$  and the permeability  $\mu = \mu_r \mu_0$ .

In Equation 2.34, the dynamic transverse susceptibility  $\chi = \chi' + i\chi''$  with the dispersive part  $\chi'$  and the absorptive part  $\chi''$  of the complex susceptibility has been introduced:

$$\chi' = \chi_0 \frac{\omega_0 \Omega T_2^2}{1 + \Omega^2 T_2^2 + \omega_1^2 T_1 T_2} \quad (2.35a)$$

$$\chi'' = \chi_0 \frac{\omega_0 T_2}{1 + \Omega^2 T_2^2 + \omega_1^2 T_1 T_2} \quad (2.35b)$$

In resonator-based CW-EPR with a reflection cavity (cf. Chapter 4), the spin system absorbs MW energy on resonance, which modifies the impedance of the cavity. The real (dispersive) part of the transverse magnetic susceptibility (Equation 2.35a) changes the inductance leading to a frequency change of the cavity, while the imaginary (absorptive) part of the transverse magnetic susceptibility changes the resistance of the cavity resulting in a phase shift. Usually, an automatic frequency control (AFC) is used to remove the frequency shift caused by the dispersive part and only the absorptive part is measured [66, 78].

To record an EPR spectrum, either the static magnetic field,  $B_0$ , or the frequency of the MW,  $f = 2\pi\omega$ , are swept, such that either the *Larmor* frequency or the MW frequency becomes a function of time, respectively.

Additionally, in absence of saturation, that is  $\omega_1^2 T_1 T_2 \ll 1$ ,  $\chi'$  and  $\chi''$  have fixed relationship described by the so-called *Kramers-Kronig* relation [79], which is given by

$$\chi'(\omega) = \frac{1}{\pi} P \int_{-\infty}^{+\infty} \frac{\chi''(\omega')}{\omega' - \omega} d\omega', \quad (2.36a)$$

$$\chi''(\omega) = -\frac{1}{\pi} P \int_{-\infty}^{+\infty} \frac{\chi'(\omega')}{\omega' - \omega} d\omega', \quad (2.36b)$$

where  $P$  denotes the Cauchy principle value. This relation allows to convert an absorption spectrum to a dispersion spectrum and vice versa.



### 2.3.3 Line broadenings

The lineshapes observed in EPR spectroscopy are not infinitely sharp but are broadened by different mechanisms. In absence of saturation, the absorptive part of the susceptibility,  $\chi''$ , displays a *Lorentzian* lineshape with a peak-to-peak linewidth in magnetic field units of the first derivative spectrum of

$$\Gamma = \Delta B_{\text{pp}} = \frac{2}{\sqrt{3}\gamma T_2}. \quad (2.37)$$

Since this quantity can directly be read off absorption spectra, it is common to state this value instead of the full width at half maximum (FWHM). This broadening is due to dephasing of the spins in the  $xy$ -plane and is referred to as *homogeneous broadening* or *Lorentzian broadening*.

So-called *inhomogeneous broadening* may be caused for instance by a distribution of  $g$ - and  $A$ -values. These distributions may often be described by a *Gaussian* distribution of the respective value. Therefore, this broadening is also called *Gaussian broadening*. Such distributions of the  $g$ -value may be found in amorphous materials such as amorphous silicon (a-Si), which will be used in the course of this thesis.

For paramagnetic species in solution so-called *concentration broadening* may be observed upon increasing its concentration. The first observation of such a broadening is reported in ref. [80] for Fremy's salt in aqueous solution. The effect may be described by Heisenberg exchange, also known as electron-spin exchange [65, 69], which was first suggested in ref. [81]. In dilute solutions, the paramagnetic species are well separated so that they do not interact. For solutions with a high concentration of paramagnetic species, however, this is not the case any longer. Due to diffusion, occasional collisions between the paramagnetic species occur. Upon such a collision, the exchange interaction is "switched on" for a short time allowing an exchange of their spin states. In this case, the electron repulsion gets significant and leads to an exchange contribution to the energy, which may be described by a Hamiltonian as

$$\hat{H}_{\text{HE}} = -2J\mathbf{S}_1 \cdot \mathbf{S}_2, \quad \text{with} \quad (2.38)$$

$$J = \langle \Psi_a(1) \Psi_b(2) | (e^2/r_{12}) | \Psi_a(1) \Psi_b(1) \rangle, \quad (2.39)$$

where  $\Psi_{1,2}$  are the wave functions of electron 1 and 2, respectively,  $e$  is the electron charge, and  $r_{12}$  is the distance between the electrons. This leads to a linewidth contribution in the EPR spectrum, which depends on the concentration.

## 2.4 RESONATOR-BASED CONTINUOUS-WAVE EPR

In this section, a very brief overview of the most important parts of resonator-based EPR spectrometers are given. A short review about

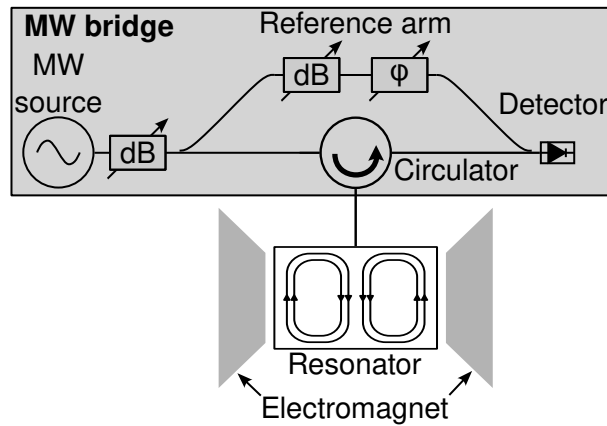


Figure 2.1: Simplified schematic of a resonator-based reflection-type CW-EPR spectrometer with homodyne detection. In the MW bridge, usually a Gunn diode is used as an MW source. An attenuator is used to reduce the MW power. The source is connected to the high-Q resonator through a circulator. The resonator couples the MW magnetic field component,  $B_1$ , to the magnetic susceptibility,  $\chi$ , of the sample. The reflected MW is detected by a detector diode, which is connected through the same circulator. The circulator ensures a unidirectional coupling of source to resonator to detector. The reference arm is used to bias the detector diode ensuring its operation in the linear regime. The external magnetic field,  $B_0$ , is swept using an electromagnet while keeping the MW frequency constant to obtain an EPR spectrum.

EPR instrumentation is presented in ref. [82], while a comprehensive treatise is published in ref. [78].

A simplified schematic of a resonator-based EPR spectrometer with homodyne detection is depicted in Figure 2.1. They typically employ MW bridges containing an MW source and detector (diode) in combination with an MW resonator (volume  $\sim \text{cm}^3$ ) with a large quality factor,  $Q$ , to enhance the signal-to-noise ratio (SNR). The resonator couples the MW magnetic field component,  $B_1$ , to the magnetic susceptibility,  $\chi$ , of the paramagnetic sample. A circulator is used to connect the resonator to the source as well as to the detector. This ensures a unidirectional coupling of the MW, i.e., the MW source is not influenced by the magnetic resonance. Commonly, a reference arm is used to bias the detector with some low power MW such that it operates in the so-called linear regime. To obtain an EPR spectrum, the external magnetic field,  $B_0$ , is swept using an electromagnet while keeping the MW frequency constant.

Usually, cavity resonators or dielectric ring resonators are employed, which serve two purposes. First, the MW power is “concentrated” at the sample position enhancing the SNR. Second, because standing waves are formed in the resonator, the electric,  $E_1$ , and magnetic field component,  $B_1$ , of the MW are exactly out of phase, i.e., the maximum  $B_1$  occurs at position where  $E_1$  is at a minimum and vice versa. This is

particularly useful for samples with a high dielectric constant, as these tend to absorb MW non-resonantly via the electric field component. The quality factor ( $Q$ ) of a resonator describes how efficient MW are stored and is defined as the ratio of the energy stored and the energy losses per MW cycle. The quality factor may also be defined by the ratio of the MW frequency and its bandwidth. For a  $Q$  of 1000 in the X-band ( $\sim 10$  GHz), the bandwidth is 10 MHz.

To improve the SNR, CW-EPR spectra are usually recorded using phase-sensitive detection (PSD). To this end, the static magnetic field is modulated using small modulation coils attached to the resonator. The spectrum is then recorded with a lock-in amplifier (LIA). The modulation frequency is usually up to 100 kHz and the modulation amplitude chosen so small such that the lineshape is not distorted [12, Section 4.8]. Due to the modulation, the first derivative of the spectrum is recorded.

#### 2.4.1 Quantitative EPR

EPR can be used as a quantitative method providing the absolute number of spins or concentration of the sample. While ref. [12] provides a comprehensive overview over quantitative EPR and its difficulties, only a short treatise is given here. The signal voltage of a reflection-type resonator-based EPR spectrometer depends on different experimental parameters as [12, 78, 83]

$$V_{\text{res}} = \chi'' \eta Q \sqrt{P_{\text{mw}} Z_0}, \quad (2.40)$$

where  $\chi''$  is the absorptive component of the magnetic susceptibility of Equation 2.35b,  $P_{\text{mw}}$  is the applied MW power, and  $Z_0$  is the characteristic impedance of the transmission line,  $\eta$  is the filling factor, and  $Q$  is the quality factor of the resonator. The filling factor,  $\eta$ , describes the ratio of magnetic energy stored in the sample to the magnetic energy stored in the resonator and is defined as

$$\eta = \frac{\int_{V_s} B_1^2 dV}{\int_V B_1^2 dV}. \quad (2.41)$$

The static magnetic susceptibility per unit volume,  $\chi_0$ , used in Equation 2.35b may be described by Curie's law as [65]

$$\chi_0 = \frac{\mu_0 N g^2 \mu_B^2 S(S+1)}{3k_B T}, \quad (2.42)$$

where  $N = N_s/V_s$  is the number density,  $k_B$  is the Boltzmann constant,  $T$  is the temperature.

To obtain the number of spins in the sample, the spectrum needs to be integrated to obtain the signal intensity due to the finite width of the spectrum. When using PSD as described before, the first-derivative

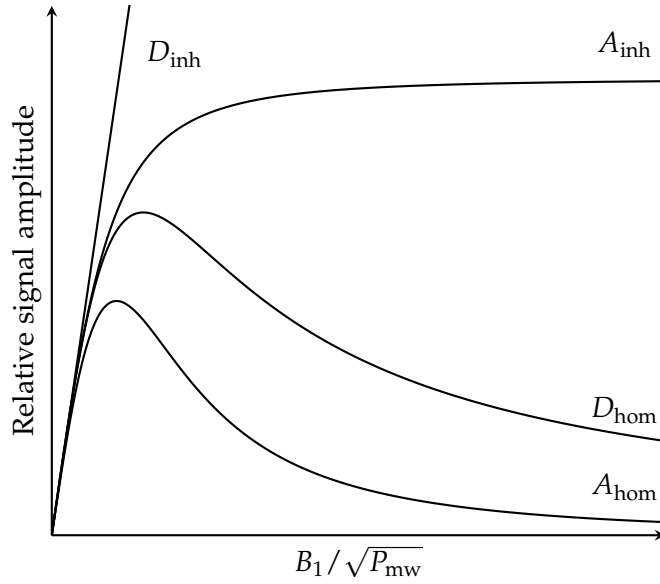


Figure 2.2: Saturation behaviour of the signal amplitude of homogeneously (hom) and inhomogeneously broadened (inh) absorption (A) and dispersion (D) first-order EPR spectra.

spectrum needs to be integrated twice, which is commonly referred to as double integral (DI). As seen in Equation 2.40, the signal voltage depends on many experimental and sample parameters that need to be taken into consideration for calculating the number of spins, which are explicitly given in ref. [12, Section 11.2].

#### 2.4.2 Microwave power

According to Equation 2.9, the population of the energy levels in thermal equilibrium is described by a Boltzmann distribution. This equilibrium is maintained if the excitation of spins from the lower lying energy level by the MW can be compensated by the spin-lattice relaxation time,  $T_1$ . In the vector picture, this means that the precession frequency  $\omega_1$  is small enough such that the magnetisation vector,  $\mathbf{M}$ , is only moderately deflected from its equilibrium value,  $\mathbf{M}_0$ , and returns to this value at each measurement point.

In resonator-based EPR, the magnitude of  $\omega_1 = |\gamma| B_1$  depends on the resonator conversion efficiency,  $C$  and the MW power,  $P_{\text{mw}}$  as [83]

$$B_1 = C\sqrt{P_{\text{mw}}}. \quad (2.43)$$

If  $B_1$  is too large relative to the relaxation times,  $\mathbf{M}$  is deflected from its equilibrium value. In this case, the population difference of the energy states of Equation 2.10 equalises and the EPR signal decreases. This is called MW *saturation*.

In ref. [84, Section 1.4], the saturation behaviour of homogeneously, i.e., *Lorentzian*, and inhomogeneously, i.e. *Gaussian*, broadened EPR

spectra is discussed based on *Bloch's* equations for both dispersion and absorption, which is displayed in [Figure 2.2](#). It is found that the signal amplitude of inhomogeneously broadened (first-derivative) dispersion spectra,  $D_{\text{inh}}$  is linearly increasing with  $B_1$  as

$$D_{\text{inh}} = \text{const.} \frac{B_1}{b_0}, \quad (2.44)$$

where  $b_0$  is the width of the inhomogeneously broadened (*Gaussian*) line. No saturation can occur in this case. This equation is the reason for the common believe in the EPR community that dispersion spectra never saturate, which is correct only for inhomogeneously broadened lines. For homogeneously broadened first-derivative dispersion spectra, saturation may occur, on the other hand. Its signal amplitude,  $D_{\text{hom}}$ , may be described by

$$D_{\text{hom}} = \text{const.} \frac{B_1 T_2^2}{1 + \sigma}, \quad (2.45)$$

where  $\sigma = 1/4\gamma^2 B_1^2 T_1 T_2$  is the saturation term of *Bloch's* equations. Similarly, the signal amplitude of homogeneously and inhomogeneously broadened first-derivative absorption spectra,  $A_{\text{hom}}$  and  $A_{\text{inh}}$ , respectively, may be described by

$$A_{\text{hom}} = \text{const.} \frac{B_1 T_2^2}{(1 + \sigma)^{3/2}} \quad (2.46)$$

$$A_{\text{inh}} = \text{const.} \frac{1}{b_0} \frac{B_1}{(1 + \sigma)^{1/2}}. \quad (2.47)$$

This shows that inhomogeneously broadened EPR spectra are less likely to saturate than homogeneously broadened ones. Moreover, dispersion spectra are less likely to saturate compared to their absorption spectra with the same broadening mechanism.

In addition to the decrease of the signal amplitude with increasing  $B_1$ , a line broadening may be observed, referred to as *saturation broadening*. For homogeneously broadened absorption spectra, the peak-to-peak linewidth described by [Equation 2.37](#) may be modified to include the dependence on  $B_1$  as [[78](#), Section 13C]

$$\Delta B_{\text{pp}} = \frac{1}{\sqrt{s}} \frac{2}{\sqrt{3} T_2} \frac{\hbar}{g \mu_B}, \quad \text{with } s = \frac{1}{1 + \gamma^2 B_1^2 T_1 T_2}. \quad (2.48)$$

For  $\gamma^2 B_1^2 T_1 T_2 \gg 1$ , i.e., for saturation, the one in the denominator of  $s$  may be neglected. The peak-to-peak linewidth then depends inversely linearly on  $B_1$ .

### 2.4.3 Spin sensitivity

The spin sensitivity or limit of detection (LOD) of a measurement may be defined [[85](#)] as

$$N_{\text{min}} = \frac{3}{\text{SNR}} \cdot \frac{NV_s}{\sqrt{\Delta f}}, \quad (2.49)$$

where SNR is the signal-to-noise ratio of the measurement,  $N$  is the spin density of the sample,  $V_s$  is the sample volume, and  $\Delta f$  is the equivalent noise bandwidth (ENBW) of the measurement. The equation can be transformed to calculate the concentration sensitivity, if  $NV_s$  is replaced with the concentration of the sample,  $c_s$ . With this equation, a theoretical lower limit of the detectable number of spins may be defined. For this, the spectrum of a sample with a known number of spins / concentration and with “good” SNR is used. In the case of a CW-EPR experiment, the SNR is determined from the spectrum as follows: The peak-to-peak amplitude of the first-derivative spectrum is divided by the noise floor as calculated from the standard deviation (STD) of a baseline region of the spectrum. The ENBW,  $\Delta f$ , is dominated by that of the LIA and therefore

$$\Delta f = \Delta f_{\text{LIA}}. \quad (2.50)$$

It depends on the time constant,  $\tau_{\text{LIA}}$ , and filter order and is typically of the order of  $\sim 1/\tau$ . The first fraction of Equation 2.49 is then used to calculate the number of spins that would be observed with an SNR of 3. The number 3 is introduced by [85] quite arbitrarily to account that for SNR below 3 the signal cannot be readily distinguished from noise. In addition, the number of spins is normalised to 1 s of measurement time by consideration of the ENBW,  $\Delta f$ , to account for different measurement times. Commonly, the LOD is normalised to a linewidth of 1 G = 0.1 mT to account for different linewidths.

**WHAT WE CAN LEARN FROM THIS EQUATION** Generally, the LOD may be used to compare different spectrometers with another. The calculated number should, however, not be over-intellectualised for a number of reasons. The LOD does not recognise the extent of the spectrum. It is rather a “binary” measure of an EPR-induced signal vs. a signal without EPR (no signal). It, therefore, does not return a number that is useful as an actual measure for the spin / concentration sensitivity for obtaining a full EPR spectrum but instead for a sensor that measures if there is a signal or not. Therefore, a statement like

The spin sensitivity is  $1 \times 10^8$  spins  $\text{Hz}^{-0.5}$ .

does not mean that we can obtain an EPR spectrum with a sample containing  $1 \times 10^8$  spins in a reasonable amount of measurement time. Furthermore, it is assumed that the signal amplitude scales linearly with the number of spins / concentration. For solutions, a broadening of the EPR lineshape may be observed with increasing concentration due to spin-spin interaction as described in Section 2.3.3. In this case, the signal intensity but not the signal amplitude increases linearly with concentration.

## 2.5 RAPID-SCAN EPR

In remainder of this chapter, the theoretical foundation to understand frequency-swept RS-EPR will be laid by firstly explaining rapid passage effects. Then the adiabaticity and its different definitions will be elaborated. At the end, the deconvolution process will be explained.

To improve the SNR of EPR especially for samples with long relaxation times, the rapid scan (RS) technique may be used [77]. By rapidly scanning the magnetic field or MW frequency over the EPR spectrum, the time spent on resonance is reduced, which results in an altered saturation behaviour such that higher  $B_1$  may be applied. In contrast to PSD used by CW-EPR, the transient EPR signal is recorded by means of a high-speed digitiser. So far, most of the RS experiments have been performed as field sweeps due to the limited bandwidth of the utilised MW resonators. In this thesis, non-adiabatic rapid frequency-swept EPR will be shown. Such frequency-swept RS-EPR has been discussed in only a few references [57, 86–88].

### 2.5.1 *Rapid passage signal*

In the master's thesis of Jannik Möser, in my opinion the most comprehensive review and best explanation of non-adiabatic rapid field scan EPR based on Bloch's equations may be found [89]. However, as such theses are commonly not published in Germany, the content is not readily available to the public. Here, only a feeble attempt can be made to adapt the theoretical considerations presented in said thesis for non-adiabatic rapid frequency scans.

The terminology of rapid scan EPR is ambiguous in the history of EPR. Many older EPR spectrometers have so-called rapid scan coils, which were used for field continuous wave (CW) scans that were much faster, i.e., "rapid", compared to the typical slow CW-EPR sweeps. In the following, however, the focus lies on the rapid passage regime as defined in ref. [76, 90]. In this regime, the scan rate, that is the rate of change of the static magnetic field or that of the MW frequency,  $f_{\text{mw}} = \omega / (2\pi)$ , is much faster than the relaxation times of the sample. To derive a quantitative criterion for this regime, it is useful to recollect the vector picture of the spin magnetisation discussed in Section 2.3.1. In literature, commonly field scans were considered to derive the criterion for the rapid passage regime. In this work, however, the same relations are derived for frequency scans. A change of the static magnetic field leads to a rotation of the effective magnetic field,  $B_{\text{eff}}$ , in the rotating frame. To investigate a change of the MW frequency, the rotating frame with a constant angular velocity equal to that of the MW frequency is not sufficient. In this case, an accelerated rotating frame, also known as frequency frame needs to be considered [91]. This frame rotates about  $z$  with the same angular velocity  $\omega(t)$  as the varying MW



frequency of the frequency scan. Usually,  $B_1$  is arbitrarily chosen to be along  $x^*$  (similar to the rotating frame). The axes of this frequency frame are denoted as  $x^*$ ,  $y^*$  and  $z^*$ . As before, the effective magnetic field may be defined as  $\mathbf{B}_{eff} = B_1 \hat{e}_{x^*} + (B_0 - \omega / |\gamma|) \hat{e}_{z^*}$ . Similar to the rotating frame, a change of the MW frequency leads to a rotation of the effective field about  $y^*$ . Specifically, the angle between the effective magnetic field,  $\mathbf{B}_{eff}$ , and the static magnetic field,  $\mathbf{B}_0$ , is defined as before as<sup>2</sup>

$$\theta_{eff}(t) = \arctan \left( \frac{B_1}{B_0 - \omega(t) / |\gamma|} \right). \quad (2.51)$$

The time-dependence of  $\omega$  has been made explicit. The angular velocity,  $d\theta_{eff}/dt$ , of the rotation of  $\mathbf{B}_{eff}$  around the  $y^*$ -axis may be calculated as

$$\frac{d\theta_{eff}}{dt} = \frac{\frac{d}{dt} \left[ \frac{B_1}{B_0 - \omega(t) / |\gamma|} \right]}{1 + \left[ \frac{B_1}{B_0 - \omega(t) / |\gamma|} \right]^2} \quad (2.52a)$$

$$= \frac{B_1}{[B_0 - \omega(t) / |\gamma|]^2 + B_1^2} \cdot \frac{1}{|\gamma|} \cdot \frac{d\omega(t)}{dt} \quad (2.52b)$$

$$= \frac{B_1}{B_{eff}^2} \cdot \frac{1}{|\gamma|} \cdot \frac{d\omega(t)}{dt} \quad (2.52c)$$

Consequently, the rapid passage regime may be defined in terms of the angular velocity  $d\theta_{eff}/dt$  being large in relation to the mean relaxation time  $\sqrt{T_1 T_2}$ . On resonance, the effective magnetic field is equal to  $B_1$ . Hence, the condition for the rapid passage regime [76, 92] is given by

$$\left| \frac{d\theta_{eff}}{dt} \right| = \frac{1}{|\gamma| B_1} \cdot \frac{d\omega}{dt} \gg \frac{1}{\sqrt{T_1 T_2}}, \quad \text{or } \frac{d\omega}{dt} \gg \frac{|\gamma| B_1}{\sqrt{T_1 T_2}}. \quad (2.53)$$

With this condition, scans may be divided in the slow-scan and rapid-scan region. This is not the only differentiation of types of sweep. A second classification of sweeps is the adiabaticity, which will be discussed below.

### 2.5.1.1 Adiabatic rapid passage

Similar to the term ‘‘rapid’’, the term ‘‘adiabaticity’’ is ambiguously used in the EPR community. The adiabaticity used throughout this thesis is based on the quantum mechanical definition as used by Powles [93], Weger [92], Schweiger and Jeschke [66] and others. In an adiabatic process in the Ehrenfest sense, the change of the spin system is sufficiently slow such that it can adapt its configuration, i.e., the quantum numbers are conserved during the process [94]. The second

<sup>2</sup> Please note that we refrain from redefining all variables in the frequency frame as the outcome will be the same as in the rotating frame.



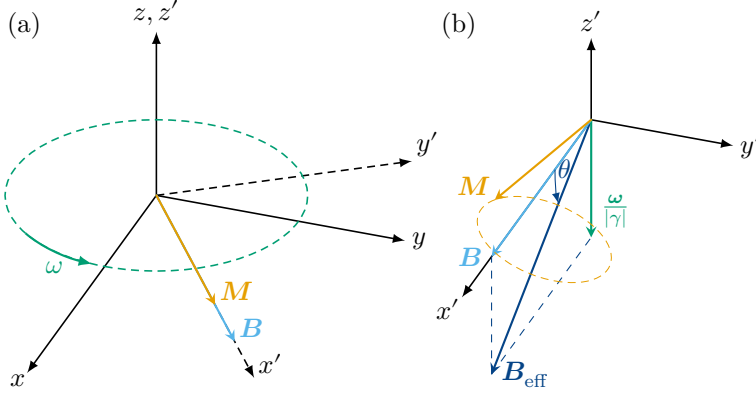


Figure 2.3: Trajectory of the magnetisation in the adiabatic rapid passage condition. **(a)** The magnetic field,  $\mathbf{B}(t)$  rotates about the  $z$ -axis with an angular frequency of  $\omega = \omega \hat{e}_z$ . The magnetisation,  $\mathbf{M}$ , is initially aligned along  $\mathbf{B}$ . The laboratory frame is indicated by the solid coordinate system denoted with  $x, y$  and  $z$ . The rotating frame with the angular frequency of  $\omega$  is indicated by the dashed coordinate system with  $x', y'$  and  $z'$ . **(b)** In the rotating frame depicted by  $x', y'$  and  $z'$ , the magnetisation,  $\mathbf{M}$ , precesses about the effective field,  $\mathbf{B}_{\text{eff}} = \mathbf{B} - \omega / |\gamma|$ .

definition for an adiabatic scan is communicated by the Hyde group in ref. [95].<sup>3</sup>

In an adiabatic rapid frequency scan, the scan rate, that is the change of the MW frequency, is small compared to the Larmor frequency of the magnetisation vector,  $\mathbf{M}$ . Then, the magnetisation will follow the direction of the effective magnetic field, which will be shown below. The derivation is based on ref. [93].

To derive the condition for adiabaticity, we first examine the trajectory of a magnetisation vector,  $\mathbf{M}$ , in presence of an arbitrary time-dependent magnetic field,  $\mathbf{B}(t)$ , rotating about the  $z$ -axis with an angular frequency,  $\omega = \omega \hat{e}_z$ . We assume that  $\mathbf{M}$  is initially aligned along  $\mathbf{B}$  in the laboratory frame. For scan rate fulfilling the condition for a rapid scan as defined in the previous section, the relaxation times may be ignored. Consequently, the equation of motion of the magnetisation in the rotating frame is given by (cf. Equation 2.26)

$$\frac{d\mathbf{M}}{dt} = (|\gamma| \mathbf{B} - \omega) \times \mathbf{M} = \mathbf{B}_{\text{eff}} \times \mathbf{M}. \quad (2.54)$$

As before,  $\mathbf{B}_{\text{eff}}$  is time-independent in the rotating frame. Hence,  $\mathbf{M}$  will precess about  $\mathbf{B}_{\text{eff}}$  with a frequency of  $\omega_{\text{eff}} = |\gamma| B_{\text{eff}}$ . The angle

<sup>3</sup> The definition communicated by the Hyde group is given by  $|(d/dt)(B_0 - \omega/\gamma)| \gg H_1/T_1$  [95]. This definition is very similar to the slow scan regime as defined in Equation 2.53. The sole difference is that here only  $T_1$  is used instead of the mean relaxation time  $\sqrt{T_1 T_2}$ . Therefore, in the nomenclature defined in ref. [95] the RS shown in this thesis are in the adiabatic regime, while they are actually in the non-adiabatic regime as defined by [92].

between  $\mathbf{B}$  and  $\mathbf{B}_{\text{eff}}$ ,  $\theta_{\text{eff}}$  may be calculated from trigonometric considerations shown in [Figure 2.3](#). It is given by  $\tan \theta_{\text{eff}} = \omega / (|\gamma| B)$ . Assuming  $\mathbf{M}$  to be initially aligned with  $\mathbf{B}$ , it will stay within an angle of  $2\theta_{\text{eff}}$  with respect to  $\mathbf{B}$ . In the adiabatic regime, that is if  $\omega$  is much smaller than the Larmor frequency  $|\gamma| B$ ,  $\theta_{\text{eff}}$  may be approximated by a Taylor expansion around zero, such that  $2\theta_{\text{eff}} \approx 2\omega / (|\gamma| B) \ll 1$ . In this case, the magnetisation stays approximately collinear with  $\mathbf{B}_{\text{eff}}$ .

To apply this consideration to the common geometry used in Bloch's equations,  $\mathbf{B}_0 = B_0 \hat{e}_{z^*}$  needs to be added to [Equation 2.54](#). According to [Equation 2.52](#), a change of  $d\omega$  leads to a rotation of  $\mathbf{B}_{\text{eff}}$  about the  $y^*$ -axis by  $d\theta_{\text{eff}}$  in the frequency frame. Please note that  $\theta_{\text{eff}}$  denotes the angle between the effective magnetic field and  $\mathbf{B}_0$  and  $\mathbf{B}_{\text{eff}} = \mathbf{B}_1 + \mathbf{B}_0 - \omega(t) / |\gamma|$  as defined in [Equation 2.27](#) which is time-dependent in the frequency frame. Consequently, the condition for adiabaticity is given by

$$\frac{d\theta_{\text{eff}}}{dt} \ll \omega_{\text{eff}}(t) = |\gamma| B_{\text{eff}}(t). \quad (2.55)$$

Using [Equation 2.52](#) yields

$$\frac{d\theta_{\text{eff}}}{dt} = \frac{B_1}{B_{\text{eff}}^2} \cdot \frac{1}{|\gamma|} \cdot \frac{d\omega}{dt} \ll |\gamma| B_{\text{eff}}(t), \text{ or } \frac{d\omega}{dt} \ll \frac{\gamma^2 [B_{\text{eff}}(t)]^3}{B_1} \quad (2.56)$$

As  $B_1 \leq B_{\text{eff}}$  at all times, [Equation 2.57](#) may be replaced by

$$\frac{d\omega}{dt} \ll \gamma^2 B_1^2. \quad (2.57)$$

This equation is commonly referred to as the condition for an adiabatic rapid sweep [[92](#), [93](#)]. For a frequency sweep in negative direction, i.e., from  $\omega \gg \omega_0$  to  $\omega \ll \omega_0$  (according to [Equation 2.28](#)), the magnetisation will qualitatively behave as follows. At the start of the sweep,  $\mathbf{B}_{\text{eff}} \approx \mathbf{B}_0$  and therefore the magnetisation  $\mathbf{M}$  precesses about  $\mathbf{B}_0$ . Consequently,  $\mathbf{M} \approx M_0 \hat{e}_{z^*}$ . During the sweep,  $\mathbf{B}_{\text{eff}}$  is rotated from its initial direction almost parallel  $z^*$  to  $-z^*$ . Since the precession of  $\mathbf{M}$  about the effective field is much faster than its rotation, the magnetisation "follows" the effective field, such that at  $\mathbf{M} \approx -M_0 \hat{e}_{z^*}$  at the end of the sweep. [Figure 6 \(b\)](#) in ref. [[91](#)] illustrates the reversal of the magnetisation for an adiabatic frequency sweep in the frequency frame.

### 2.5.2 Non-adiabatic rapid passage

In the non-adiabatic case, i.e., if

$$\frac{d\omega}{dt} \gg \gamma^2 B_1^2, \quad (2.58)$$

the precession of the magnetisation about the effective field will be much slower than the rotation of the effective field about  $y^*$ . In this case, the magnetisation will *not* “follow” the effective field, and therefore it remains close to thermal equilibrium,  $\mathbf{M} = M_0 \hat{e}_{z^*}$ . This regime is sometimes also referred to as *fast passage* [66]. The  $xy$ -component of the magnetisation may be approximated by [90, Equation 8]

$$M_{xy} \approx -M_0 \frac{\omega_1 T_2 [1 - i\Omega(t) T_2]}{1 + [\Omega(t) T_2]^2} \quad (2.59a)$$

$$- A \exp \left[ -\frac{t}{T_2} - i \int_b^t dt'' \Omega(t'') \right], \text{ with}$$

$$A \approx i\omega_1 M_0 \int_{-\infty}^{t_1} dt' \exp \left[ \frac{t'}{T_2} + i \int_b^{t'} dt'' \Omega(t'') \right] \cdot \frac{d\Omega/dt'}{[1/T_2 + i\Omega(T')]^2}, \quad (2.59b)$$

where  $b$  is an arbitrary integration limit. This equation can be explained as follows. The first term describes the usual slow passage behaviour that depends only on the resonance offset,  $\Omega$ . The second term, however, superimposes a damped free oscillation on the slow passage behaviour, which is induced by the passage of resonance. This damped free oscillation may be seen as an free induction decay (FID) with changing precession frequency (*Larmor*) for a field sweep. For a frequency sweep, however, the *Larmor* precession is constant according to Equation 2.22 but the angular velocity of the rotating frame changes.

### 2.5.3 Sinusoidal frequency scans

Different waveforms may be used in RS-EPR to achieve non-adiabatic rapid scans, such as triangular, sawtooth, trapezoidal or sinusoidal scans. In ref. [88], sawtooth and triangular excitation has been discussed. In this work, however, sinusoidal frequency scans will be used for the RS experiments, similar to those used in ref. [86]. While in this reference, only the central part of the scan was used for analysis, so that a linear scan may be assumed, here, the complete sinusoidal waveform is used.

The excess<sup>4</sup> instantaneous MW frequency,  $f_i$ , is defined as

$$f_i = -\Delta f_{rs} \cos(2\pi f_{rs} t), \quad (2.60)$$

where  $\Delta f_{rs} = \Delta\omega_{rs}/(2\pi)$  is the modulation amplitude in Hz, and  $f_{rs} = \omega_{rs}/(2\pi)$  is the rapid scan frequency in Hz. The former defines the scan width of the experiment, which is equal to  $2 \cdot \Delta f_{rs}$ , while the latter may be referred to as the repetition rate. The MW frequency is the sum of the central MW frequency around which the MW is modulated and the instantaneous excess MW frequency as

$$f_{osc}(t) = f_{osc,c} + f_i(t) = f_{osc,c} - \Delta f_{rs} \cos(2\pi f_{rs} t). \quad (2.61)$$

4 I.e., in excess of the MW frequency

The scan rate of a sinusoidal frequency sweep may be defined as the change of the MW frequency as

$$\frac{df_{\text{osc}}}{dt} = \frac{df_i}{dt} = \underbrace{2\pi\Delta f_{\text{rs}}f_{\text{rs}}}_{\alpha_{\text{rs}}} \sin(2\pi f_{\text{rs}}t), \quad (2.62)$$

where  $\alpha_{\text{rs}}$  is the maximum scan rate in a sinusoidal frequency sweep. Due to the sinusoidal scan, resonance is achieved twice per period,  $T_{\text{rs}} = 1/f_{\text{rs}}$ . If the scan is centred around the resonance position, resonance is achieved at  $t = T_{\text{rs}}/4$  and at  $t = 3T_{\text{rs}}/4$ . At these positions, the sinus is approximately linear, so that  $\alpha_{\text{rs}}$  may be used instead of  $d\omega/dt$ . So, the criteria for non-adiabatic rapid frequency scans may be simplified as follows. The rapid scan regime is reached, if

$$\alpha_{\text{rs}} \gg \frac{|\gamma| B_1}{\sqrt{T_1 T_2}}. \quad (2.63)$$

The condition for non-adiabaticity can be rewritten as

$$\alpha_{\text{rs}} \gg \gamma^2 B_1^2. \quad (2.64)$$

Rapid scan transients may be simulated by numerically solving Bloch's equations displayed in Equation 2.33 for arbitrary excitations, which is computationally relative expensive. For sinusoidal excitation, however, a computationally efficient analytical solution was presented in ref. [96]. This is implemented in the function *blochsteady* of *EasySpin* [70], which will be used in Section 7.2.3.

#### 2.5.4 Fourier deconvolution

To recover the slow-scan EPR spectrum, the RS-EPR transients, need to be deconvolved, which is discussed in detail in ref. [97] for rapid sinusoidal scans. The main assumption is that the spin system may be described as a linear system. This is the case if the amplitude of the oscillating magnetic field  $B_1$  is small enough to avoid saturation. Then, the response of a spin system  $y(t)$  to the excitation  $d(t)$  can be expressed as

$$r(t) = (h * d)(t) = \int_{-\infty}^{\infty} h(\tau) d(t - \tau) d\tau, \quad (2.65)$$

where  $h(t)$  is the impulse response of the spin system, which is the FID, and  $*$  denotes the convolution operator. For a frequency sweep  $d(t)$  is defined as

$$d(t) = \exp[i\phi(t)], \quad (2.66)$$

in which  $\phi(t)$  is the instantaneous phase of the MW. The angular MW frequency  $\omega_{\text{mw}}$  is the derivative of the phase, so  $d(t)$  becomes

$$d(t) = \exp\left[i \int_0^t \omega_{\text{mw}}(\tau) d\tau\right]. \quad (2.67)$$

In the frequency domain, the convolution in [Equation 2.65](#) is a multiplication as

$$R(\omega) = H(\omega)D(\omega), \quad (2.68)$$

where  $R(\omega)$ ,  $H(\omega)$ , and  $D(\omega)$  denote the *Fourier* transforms of  $r(t)$ ,  $h(t)$ , and  $d(t)$ , respectively. Hence, the slow-scan EPR spectrum may be calculated as

$$H(\omega) = R(\omega)/D(\omega). \quad (2.69)$$

Similar to the simulation of the transients, the Fourier deconvolution for sinusoidal excitation based on the theory presented in ref. [97] is implemented in *EasySpin* with the function *rapidscan2spc*. This function, however, expects baseline-corrected and properly aligned transients as input, which is crucial for a successful deconvolution (c.f [Section 7.2.3](#)).



## ELECTRON PARAMAGNETIC RESONANCE ON A CHIP

---

This chapter deals with the theoretical background of the EPR-on-a-Chip (EPRoC) required to understand the experimental data in the subsequent chapters. First, a short overview of unconventional detection methods using microresonators is presented. A qualitative description of the working principle of the EPRoC is presented, before a more quantitative approach to model the EPRoC is shown. Closed-form expressions for both the continuous wave (CW) dispersion-like and absorption-like signals are discussed. In addition, the transient detection will be shortly explained. The theoretical spin sensitivity is calculated for the EPRoCs used in this thesis. At last, a short treatise about the fundamental differences between field and frequency sweeps as well as field and frequency modulation is given.

### 3.1 WORKING PRINCIPLE

Common EPR spectrometers are typically optimised for relatively large samples (greater than  $1 \text{ mm}^3$ ) using cavity resonators with volumes of several  $\text{cm}^3$ . The sample is inserted into a capillary tube within the cavity. Within the cavity, the microwave (MW) forms a standing wave, resulting in exactly out-of-phase magnetic and electric field components. The sample is positioned at the centre of the cavity, where the magnetic field amplitude is maximum and the electric field amplitude is minimum. The requirement for the microwave frequency to coincide with the resonance frequency of the resonator imposes a relation between the cavity dimensions and the microwave frequency. Consequently, resonators used at X-band frequencies have volumes several times larger than the sample, resulting in relatively weak microwave fields at the sample.

The dependence of the magnetic field amplitude,  $B_1$ , on the volume,  $V$ , may be derived by calculating  $B_1$  from the energy  $W$  stored in the resonator. The energy stored in the electromagnetic field is given by

$$W = \int_{\text{cavity}} (w_{\text{el}} + w_{\text{mag}}) dV, \quad (3.1)$$

where  $w_{\text{el}}$  and  $w_{\text{mag}}$  represent the electric and magnetic field components of the energy density, respectively. Assuming spatially uniform magnetic field variation for simplicity, the magnetic part of the field

energy density is  $w_{\text{mag}} = W/(2V) = \mu_0 B_1^2$ . Consequently, the  $B_1$  field amplitude can be expressed as

$$B_1 = \sqrt{\frac{W}{2V\mu_0}} = \sqrt{\frac{PQ}{2V\mu_0 f}} \quad (3.2)$$

where  $W = P\tau = PQ/f$  represents the energy stored in the cavity,  $P$  is the power of the MW entering the cavity,  $\tau$  is the storage time,  $Q$  is the quality factor of the resonator, and  $f$  is the MW frequency.

Hence, the efficiency of converting MW power into  $B_1$  decreases with increasing cavity dimensions. By reducing the size of the resonator, the conversion efficiency may be enhanced. This relationship is typically quantified in terms of the filling factor,  $\eta$  (cf. Equation 2.41) defined as the fraction of microwave interacting with the sample. Therefore, the filling factor is inherently low for common EPR spectrometers. As explained in Section 2.4, the measured signal is linearly proportional to  $\eta$ . Consequently, the sensitivity for small samples is suboptimal due to the small filling factor. The filling factors of cavity resonators may be increased by means of low-loss ferroelectric or dielectric inserts [98–100] with a large dielectric constant,  $\epsilon$ , which reduce the resonator volume by approximately  $1/\epsilon^2$  [101]. Instead of cavity resonators, dielectric resonators with an intrinsically large  $\eta$  may be used [102–104].

In addition, resonant or non-resonant microstructures with dimensions smaller than the wavelength of the MW may be used. By design, the filling factor of such microstructures is much larger than that of cavity resonators. Since the microwave wavelength is much smaller than the diameter of the coil, the sample is in the near-field. Consequently, the magnetic field  $B_1$  is predominantly determined by  $\nabla \times \mathbf{B}_1 = \mu_0 \mathbf{J}$ , where  $\mu_0$  is the vacuum permeability and  $\mathbf{J}$  is the current density in the coil [105]. This field is independent of the electric field  $E_1$ , allowing for independent minimisation of  $E_1$ , thereby reducing unwanted non-resonant absorption in the sample. As a result, samples with a high dielectric constant may be investigated more effectively than with resonator-based spectrometers.

Typically, these microstructures employ inductive detection inspired by nuclear magnetic resonance (NMR) spectrometers [56, 106]. One simple approach to estimating the sensitivity is *Faraday's* law of induction. The precession of the magnetisation induces a voltage  $v$  in an inductor loop according to  $v = d\Phi/dt$ , with  $\Phi$  being the magnetic flux due to the spins. The magnetic field of a point dipole decreases with  $r^{-3}$ , with  $r$  being the distance from the point dipole, while the integration over the surface increases with  $r^2$ . Consequently, the signal of a point dipole decreases with  $r^{-1}$  as the coil size increases. This model suggests that small resonators should have higher sensitivity, a trend confirmed experimentally [107]. Another approach to derive sensitivity is using the principle of reciprocity [108, 109]. Several designs



of non-resonant microcoils have been presented in refs. [110–113]. Similarly, various designs of microresonators have been published such as planar ones with an  $\Omega$ -, r- [101, 107] or butterfly shape [114] as well as inverse anapole resonators [115], loop gap resonators [116, 117], three-dimensional solenoidal microcoils [118], and microstrip resonators [119, 120]. In ref. [121], two interwoven microcoils on a single microchip are used to generate the MW and detect the magnetic resonance. In all these designs, the microwave is typically produced by an (external) source uni-directionally coupled to the resonator. This ensures that the MW source is not affected by the magnetic resonance, similar to the common resonator-based EPR spectrometers discussed in Section 2.4.

The EPRoC, on the other hand, utilises a planar single inductor of an LC oscillator integrated on a single microchip to generate and detect the MW at the same time, which was firstly proposed in ref. [51]. The design is inspired by several NMR and EPR spectrometers developed from the 1950s to 1980s [56, 122–125]. In contrast to the previous designs, the MW is generated by the oscillations of the LC oscillator, so that a dedicated MW bridge is not required. Due to this design principle, the MW source and the spin system are bi-directionally coupled. Figure 3.1 (a) depicts a special type of LC oscillator, a voltage-controlled oscillator (VCO). The VCO comprises two parts: A lumped (R)LC resonator also referred to as LC tank ( $R_{\text{coil}}$ ,  $L_{\text{coil}}$ ,  $D_1$  and  $D_2$  act as a varactor with capacity  $C \propto V_{\text{tune}}$ ) and a cross-coupled transistor pair ( $M_1$  and  $M_2$ ). The latter is often referred to as ‘active pump circuit’ and acts as a negative resistance compensating for the losses in the LC tank. In this way, stable oscillations at MW frequencies may be achieved.

Qualitatively, the detection of the magnetic resonance may be explained as follows. A paramagnetic sample is placed on the coil of the VCO and a suitable static magnetic field,  $B_0$ , is applied such that the energy levels of the spin system are split. Far away from resonance, the inductor of the VCO generates the MW with a certain frequency,  $\omega_{\text{osc}} \approx 1/\sqrt{L_{\text{coil}}C(V_{\text{tune}})}$ , and magnitude,  $B_1$ . By changing  $B_0$  the resonance condition of Equation 2.8 may be achieved. Then, the  $B_1$  disturbs the spin system, that is the macroscopic magnetisation, which may be described by Bloch’s equations (cf. Section 2.3.1). This in turn changes the inductance as well as the resistance of the inductor of the VCO. A change of the inductance will change the oscillation frequency as seen above. Therefore, detecting the change of the oscillation frequency will provide some kind of dispersion signal. The change of the resistance, on the other hand, will reduce the oscillation amplitude, which provides an absorption signal. The same behaviour is obtained by keeping  $B_0$  constant and changing the oscillation frequency by varying the tuning voltage to the varactor to a frequency such that the resonance condition is fulfilled.

In the early publications discussing the EPRoC, LC oscillators with a fixed capacitance was used [51, 52], while ref. [55] extended the technology to include VCOs, which allowed performing frequency sweeps. This in turn enabled the development of the first battery-operated EPR spectrometer [55]. A comprehensive analysis of the EPRoC in general and noise analyses in particular are provided in refs. [126, 127]. Embedding the VCO in a low-bandwidth phase-locked loop (PLL) (cf. Section 4.2.2) allows to precisely control the phase and frequency of the VCO and with that also of the MW. This allows to compensate for process, voltage and temperature variations. In addition, rapid-scan EPR (RS-EPR) experiments were made possible as a precisely defined MW phase is required for a successful deconvolution (cf. Section 2.5.4 and Chapter 7). EPRoCs with on-chip PLLs with large bandwidths were presented in refs. [128, 129] enabling pulsed EPR as well as high-speed RS-EPR experiments. Experimental data of the former were shown in [130]. The usage of arrays of EPRoCs was already proposed in ref. [51], but only realised by injection locking 8 VCOs in ref. [61] ten years later (cf. Section 3.4). Other EPRoCs array are comprised of 12, 14 and more VCOs injection-locked [128, 131, 132].

### 3.2 MODELLING OF THE EPROC

In the following, approximate closed-form expressions for the oscillation frequency and amplitude of the EPRoC in presence of spin resonance will be discussed. The detailed derivation may be found in reference [127] for the oscillation frequency and in reference [133] for the oscillation amplitude. Generally, the derivations are structured as follows.

Firstly, the inductance and resistance of a coil filled with a paramagnetic material with certain macroscopic magnetic susceptibility,  $\chi$ , is calculated. To model the macroscopic susceptibility, the *Bloch* equations explained in Equation 2.35 are used. Secondly, the amplitude and frequency of the LC tank oscillator as depicted in Figure 3.1 (a) in absence of EPR are calculated using the equivalent circuit diagram shown in Figure 3.1 (b). Finally, the results from the first two steps are combined, i.e., the influence of the inductance and resistance due to EPR on the frequency and amplitude of the LC tank oscillator are calculated. Please note that the equivalent circuit diagram in Figure 3.1 (b) is simplified by omitting noise sources compared to the ones in references [127, 133], where detailed noise analyses of the phase, frequency and amplitude noise were performed.

#### 3.2.1 Coil filled with paramagnetic material

The change of inductance,  $L_{\text{spin}}$ , and resistance,  $R_{\text{spin}}$ , of an inductor filled with paramagnetic material due to spin resonance may be calcu-

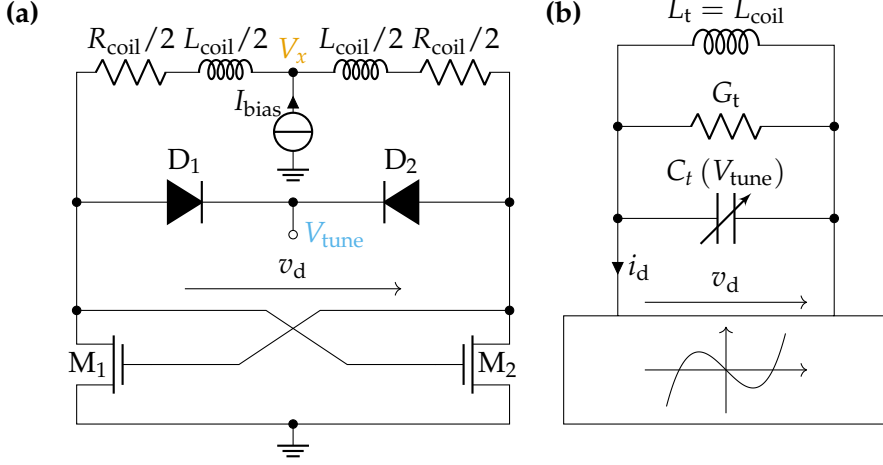


Figure 3.1: **(a)** Schematic of the complementary metal-oxide-semiconductor (CMOS) LC tank VCO. The two diodes  $D_1$  and  $D_2$  act as a varactor with a capacity proportional to  $V_{\text{tune}}$ .  $M_1$  and  $M_2$  are the cross-coupled transistors.  $R_{\text{coil}}$  and  $L_{\text{coil}}$  are the resistance and inductance of the coil, respectively. The bias current,  $I_{\text{bias}}$ , is applied to the tap of the coil. **(b)** Equivalent circuit diagram of the schematic of the CMOS LC tank VCO. Reproduced with permission from SNCSC from ref. [127].

lated from a magnetic energy based approach in combination with the steady-state solution of Bloch's equations. The complete derivation is published in detail in ref. [127, Section 3] and only the results are shown here.

If an inductor is filled with a paramagnetic sample, its inductance,  $L_{\text{coil,spin}} = L_{\text{coil}} + L_{\text{spin}}$ , and resistance,  $R_{\text{coil,spin}} = R_{\text{coil}} + R_{\text{spin}}$ , will change as compared to an unfilled coil. The change is described by  $L_{\text{spin}}$  and  $R_{\text{spin}}$  (eq. 18a and 18c in [127]) as

$$L_{\text{spin}} = \gamma T_2^2 \Delta\omega \cdot \int_{V_s} \frac{M_0 (B_{1xu}^2 + B_{1yu}^2)}{1 + \Delta\omega^2 T_2^2 + \gamma^2 T_1 T_2 (B_{1x}^2 + B_{1y}^2)} dV \quad (3.3a)$$

$$R_{\text{spin}} = -\gamma T_2 \omega_{B_1} \cdot \int_{V_s} \frac{M_0 (B_{1xu}^2 + B_{1yu}^2)}{1 + \Delta\omega^2 T_2^2 + \gamma^2 T_1 T_2 (B_{1x}^2 + B_{1y}^2)} dV, \quad (3.3b)$$

where  $V_s$  is the sample volume,  $B_{1xu}$  and  $B_{1yu}$  as well as  $B_{1x}$  and  $B_{1y}$  are the  $x$ - and  $y$ -components of the unitary  $B_{1u}$  as well as the  $B_1$  field, respectively,  $M_0$  is the steady-state sample magnetisation,  $\Delta\omega = \omega_{B_1} - \omega_L$  is the resonance offset,  $\omega_L = -\gamma B_0$  is the Larmor frequency, and  $\omega_{B_1}$  is the frequency of the  $B_1$  field produced by the inductor. Please note that in this derivation the static magnetic field,  $B_0$ , is assumed to be parallel to  $z$  and all components of  $B_1$  perpendicular to this field are considered.

In the non-saturated case, i.e., for  $1 \gg T_1 T_2 \gamma^2 (B_{1x}^2 + B_{1y}^2)$ , we can simplify Equation 3.3 by introducing the non-saturated version of the complex susceptibility discussed in Equation 2.35 (extended to two dimensions). In this case the susceptibility is independent of  $B_1$  and the volume integral may be replaced by the filling factor as

$$\begin{aligned} L_{\text{spin}} &= \frac{\chi'}{\mu_0} \int_{V_s} B_{1xu}^2 + B_{1yu}^2 dV \\ &= \chi' \cdot \frac{\int_{V_s} B_{1xu}^2 + B_{1yu}^2 dV}{\int_V B_{1xu}^2 + B_{1yu}^2 dV} \cdot \frac{1}{\mu_0} \cdot \int_V B_{1xu}^2 + B_{1yu}^2 dV \\ &= \chi' \cdot \eta \cdot L_{\text{coil}} \end{aligned} \quad (3.4a)$$

$$\begin{aligned} R_{\text{spin}} &= -\frac{\chi'' \omega_{B_1}}{\mu_0} \int_{V_s} B_{1xu}^2 + B_{1yu}^2 dV \\ &= -\chi'' \eta \omega_{B_1} \cdot L_{\text{coil}}, \end{aligned} \quad (3.4b)$$

where  $L_{\text{coil}} = 1/\mu_0 \int_V \mathbf{B}_u^2 dV$  is the conventional inductance of the inductor when filled with air/vacuum,  $B_{1xu}$  and  $B_{1yu}$  are the  $x$ - and  $y$ -components of the unitary  $B_1$  field, respectively,  $\mu_0$  is the free-space permeability,  $V_s$  is the sample volume,  $V$  is the entire space, and  $\omega_{B_1}$  is the frequency of the  $B_1$  field. Specifically, the filling factor of the coil  $\eta$  is defined as

$$\eta = \frac{\int_{V_s} B_{1xu}^2 + B_{1yu}^2 dV}{\int_V B_{1xu}^2 + B_{1yu}^2 dV}. \quad (3.5)$$

For resonator-based EPR, the filling factor is commonly approximated by  $\eta \approx V_s/V$ . The spin-induced changes in inductance and resistance shown in this section are valid for any coil filled with a paramagnetic sample placed in a static magnetic field and is not limited to the EPRoC. Hence, in the following the oscillator of the EPRoC will be described.

### 3.2.2 Non-linear oscillator modelling

The schematic of an LC tank oscillator used in the experiments conducted within this thesis is shown in Figure 3.1 (a). The lossy (R)LC tank (denoted with LC tank) is connected to a cross-coupled transistor pair (denoted with  $M_1$  and  $M_2$ ), which acts as a negative resistance compensating the energy loss of the LC tank. The two diodes  $D_1$  and  $D_2$  act as a varactor whose capacitance is a function of  $V_{\text{tune}}$ .

To obtain analytical expressions for the frequency and amplitude of the LC tank oscillator, the equivalent circuit diagram shown in Figure 3.1 (b) is used. The equivalent tank conductance,  $G_t$ , is calculated from  $R_{\text{coil}}$  and the quality factor of the coil  $Q_{\text{coil}}$ , as

$$G_t \approx \frac{1}{R_{\text{coil}} Q_{\text{coil}}^2}. \quad (3.6)$$

Please note that the noise sources discussed in refs. [127, 133] are not included in the diagram for simplicity reasons as we will not discuss the noise behaviour in detail. The non-linear I-V-characteristic of the cross-coupled transistor pair may be approximated with a third order polynomial according to ref. [134] as

$$i_d \approx -\frac{G_{m0}}{2}v_d + \frac{G_{m0}^3}{16I_{bias}^2}v_d^3, \quad (3.7)$$

where  $G_{m0} = \sqrt{\beta I_{bias}/n}$  is the gate transconductance of a single transistor,  $n$  is the transistor slope factor,  $\beta$  is the transfer parameter of a single transistor,  $I_{bias}$  is the oscillator bias current, and  $v_d$  is the differential tank voltage. Here, each transistor is assumed to be in strong inversion and saturation [134]. Using Kirchhoff's current law to node 1 and using the differential tank voltage as the state variable  $x = v_d$ , the oscillator behaviour may be described by an ordinary differential equation (ODE) as

$$\ddot{x} + \omega_{LC}^2 x = -\epsilon \frac{1}{C} \left( \frac{1}{\epsilon} \left[ G_t - \frac{G_{m0}}{2} \right] + \frac{x^2}{I_{bias}^2} \right) \dot{x}, \quad (3.8)$$

where  $\epsilon = 3G_{m0}^3 / (16n^2)$  and  $\omega_{LC} = 1/\sqrt{L_{coil}C}$  is the oscillation frequency of the LC tank. Using Linsted's method [135, Section 5.9] to find periodic solutions to the ODE leads to the first-order estimates of the oscillation frequency [127] and amplitude [133] of the LC tank oscillator as

$$\omega_{osc} = \omega_{LC} \left( 1 - \frac{(\alpha_{od} - 1)^2}{16 \cdot Q_{coil}^2} \right) \quad (3.9a)$$

$$A_{osc} = 4\sqrt{\frac{2}{3}} \frac{nI_{bias}}{G_{m0}} \sqrt{1 - \frac{1}{\alpha_{od}}}, \quad (3.9b)$$

where  $\alpha_{od} = G_{m0} / (2G_t)$  is the overdrive parameter, which needs to be larger than unity to achieve stable oscillations. The overdrive parameter relates the gate transconductance of both transistors to the total equivalent conductance of the LC tank, i.e., roughly speaking it describes the ratio of the "negative" resistance of the active pump circuit to the "positive" resistance of the LC tank.

To include magnetic resonance in Equation 3.9a and Equation 3.9b, all parameters depending on the previously shown change of inductance,  $L_{spin}$ , and resistance,  $R_{spin}$ , need to be replaced. Explicitly, the parameters depending on the spin-induced inductance and resistance are the quality factor as

$$Q_{coil,spin} = \frac{\omega_{osc,spin} L_{coil,spin}}{R_{coil,spin}}, \quad (3.10)$$

the equivalent tank conductance as

$$G_{t,spin} \approx \frac{1}{R_{coil,tot} Q_{coil,spin}^2} \approx C \frac{R_{coil,tot}}{L_{coil,tot}}, \quad (3.11)$$

and following the overdrive parameter as

$$\alpha_{\text{od,spin}} = \frac{G_{\text{m0}}}{2G_{\text{t,spin}}}. \quad (3.12)$$

Consequently, the oscillation frequency and amplitude in presence of magnetic resonance may be described by

$$\omega_{\text{osc,spin}} = \frac{1}{\sqrt{(L_{\text{coil}} + L_{\text{spin}}) C}} \left( 1 - \frac{(\alpha_{\text{od,spin}} - 1)^2}{16Q_{\text{coil,spin}}^2} \right) \quad (3.13a)$$

$$A_{\text{osc,spin}} \approx 4 \sqrt{\frac{2}{3}} \frac{nI_{\text{bias}}}{G_{\text{m0}}} \sqrt{1 - \frac{2G_{\text{t,spin}}}{G_{\text{m0}}}} \quad (3.13b)$$

To derive a complete numerical model for signal calculation all spin-dependencies need to be considered as discussed in ref. [127, Section 5.1] in detail. As both  $L_{\text{spin}}$  and  $R_{\text{spin}}$  are functions of the oscillation amplitude through  $B_1$  and  $\omega_{\text{osc,spin}}$  through  $\Delta\omega$  and vice versa, Equation 3.13a and Equation 3.13b are in fact fixed-point equations representing the bidirectional coupling of the spin system with the oscillator. This means that the oscillator frequency and amplitude is influenced by the spin system and vice versa. This finding is very important as it is fundamentally different from resonator-based EPR, where the MW source is uni-directionally coupled to the spin system by means of a circulator. This bidirectional coupling can be made more obvious by writing

$$B_{1,\text{spin}} = f_1(\omega_{\text{osc,spin}}, B_{1,\text{spin}}) \quad (3.14a)$$

$$\omega_{\text{osc,spin}} = f_2(\omega_{\text{osc,spin}}, B_{1,\text{spin}}). \quad (3.14b)$$

These fixed-point equations can only be solved numerically with a proper choice of starting values for  $B_{1,\text{spin}}$  and  $\omega_{\text{osc,spin}}$ .

In the following, however, we will not go into detail about the numerical simulation but simplify Equation 3.13a and Equation 3.13b to obtain closed-form expressions for the frequency-sensitive (FM) and amplitude-sensitive (AM) signal of the EPROC.

### 3.2.3 Continuous wave frequency-sensitive detection (FM signal)

Equation 3.13a can be considerably simplified if the weak spin-dependence of  $\alpha_{\text{od}}$  and  $Q_{\text{coil}}$  is ignored as

$$\omega_{\text{osc,spin}} = \frac{1}{\sqrt{(L_{\text{coil}} + L_{\text{spin}}) C}} \left( 1 - \frac{(\alpha_{\text{od}} - 1)^2}{16Q_{\text{coil}}^2} \right). \quad (3.15)$$

Typically, in EPR experiments, the change of the inductance,  $L_{\text{spin}}$ , is much smaller than  $L_{\text{coil}}$ . Hence, to compute spin-induced inductance

$L_{\text{spin}}$  we can replace the  $\omega_{B_1}$  in  $\Delta\omega = \omega_{B_1} - \omega_L$  used in Equation 3.3a by  $\omega_{\text{osc},0}$  as

$$\omega_{\text{osc},0} = \omega_{\text{osc,spin}} (L_{\text{spin}} = 0), \quad (3.16)$$

which is the oscillation frequency in absence of spin resonance. This step essentially stops the fixed-point iteration after the first step. Then, Equation 3.15 may be further simplified into a first-order Taylor series in  $L_{\text{spin}}$  about  $L_{\text{coil}}$ . We are interested in the frequency change of the oscillator due to spin resonance as this is the measured signal, i.e.,

$$\Delta\omega_{\text{osc,spin}} = \omega_{\text{osc,spin}} - \omega_{\text{osc},0} \quad (3.17a)$$

$$\approx -\frac{1}{2}\omega_{\text{osc},0}\frac{L_{\text{spin}}}{L_{\text{coil}}}. \quad (3.17b)$$

This equation describes the so-called FM signal of oscillator-based EPR and is valid for extended samples including saturation and possible  $B_1$  inhomogeneity.

In the non-saturated case ( $1 \gg \gamma^2 T_1 T_2 (B_{1x}^2 + B_{1y}^2)$ ), Equation 3.17 can considerably be simplified by utilising the filling factor as defined in Equation 3.5 to

$$\Delta\omega_{\text{osc,spin}} \approx -\frac{1}{2}\omega_{\text{osc},0} \cdot \eta \cdot \chi'. \quad (3.18)$$

As seen by Equation 3.18, the EPRoC FM signal is a dispersion-like signal depending only on  $\chi'$  of the complex susceptibility if the paramagnetic sample is unsaturated. To simulate such dispersion-like spectra with EasySpin [70], the microwave phase may be adjusted in the simulation by providing *mwPhase* of  $\pm\pi/2$  to the corresponding simulation.

### 3.2.4 Continuous wave amplitude-sensitive detection (AM signal)

The oscillation amplitude in presence of spin resonance is obtained by inserting  $L_{\text{spin}}$  and  $R_{\text{spin}}$  from Equation 3.3 into Equation 3.13b and reads

$$A_{\text{osc,spin}} \approx 4\sqrt{\frac{2}{3}}\frac{nI_{\text{bias}}}{G_{\text{m}0}}\sqrt{1 - \frac{2CR_{\text{coil,spin}}}{G_{\text{m}0}L_{\text{coil,spin}}}}, \quad (3.19)$$

This is still a fixed-point equation considering the bidirectional coupling. In the next step,  $L_{\text{spin}}$  and  $R_{\text{spin}}$  are replaced by their simplified versions of Equation 3.4, neglecting saturation. Hence, Equation 3.19 simplifies to

$$A_{\text{osc,spin}} \approx 4\sqrt{\frac{2}{3}}\frac{nI_{\text{bias}}}{G_{\text{m}0}}\sqrt{1 - \frac{2CR_{\text{coil}}(1 + Q_{\text{coil}}\eta\chi'')}{G_{\text{m}0}L_{\text{coil}}(1 + \eta\chi')}}. \quad (3.20)$$

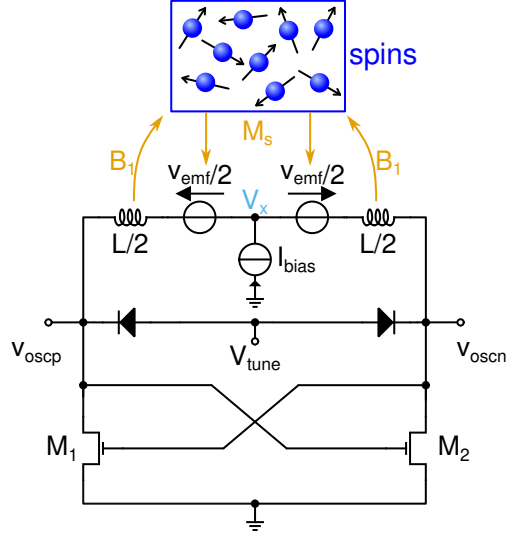


Figure 3.2: Interaction of spin system with EPROC used for the transient detection model. The VCO coil produces a magnetic field,  $B_1$ , acting on the spin system with macroscopic magnetisation  $M_s$ . The spin system in turn acts on the VCO by inducing a voltage,  $v_{emf}$ , in the coil windings.

Additionally, as before  $L_{spin} \ll L_{coil}$  and  $R_{spin} \ll R_{coil}$  is assumed allowing to simplify the equation even further. Again, this means that the fixed-point iteration is stopped after the first step. Here, we are interested in the change of the oscillation amplitude due to spin resonance as this is the measured signal, i.e.,

$$\Delta A_{osc,spin} = A_{osc,spin} - A_{osc,0} \quad (3.21a)$$

$$\approx 4\sqrt{\frac{2}{3}} \frac{nI_{bias}}{G_{m0}} \sqrt{1 - \frac{1}{\alpha_{od}}} \cdot \frac{\eta(Q_{coil}\chi'' - \chi')}{2(\alpha_{od} - 1)} \quad (3.21b)$$

Hence, we observe an absorption-like signal with a slight admixture of dispersion depending on  $Q_{coil}$  for an unsaturated spin system. In resonator-based EPR, where the absorption and dispersion of the signal can be recorded in quadrature, this admixture would correspond to a phase shift, which can easily be modelled with EasySpin by providing the parameter *mwPhase* to the experimental settings. For large  $Q_{coil}$ ,  $\chi''$  dominates the signal and only a small asymmetry may be seen.

### 3.2.5 Transient detection

The equations derived in the previous section are valid only for CW excitation/detection. For transient detection, a different model needs to be used as described in [136]. The interaction of the VCO and the spin system is depicted in Figure 3.2. The  $B_1$  produced by the coil of the VCO acts on the spin system, which in turn acts on the VCO by inducing a voltage,  $v_{emf}$ , in the coil windings by means of the (time-



dependent) macroscopic spin magnetisation,  $M_s$ . The magnetisation is given by *Bloch's* equations. Similar to before, the analytical expressions are obtained from a magnetic energy based approach. The induced voltage may then be calculated by

$$v_{\text{emf}} = -\frac{d}{dt} \int_{V_s} [\mathbf{B}_u(\mathbf{r}) \cdot \mathbf{M}_s(\mathbf{r}, t)] dV, \quad (3.22)$$

where  $\mathbf{B}_u$  is the unitary magnetic field of the inductor and  $V_s$  is the sample volume. Using the reciprocity principle [109], the same relation may be obtained. The oscillation amplitude changes induced by spin resonance may be derived using a perturbation theory based approach presented in [137], resulting in

$$\delta \dot{A}(t) = - \underbrace{(\alpha_{\text{od}} - 1)}_{\omega_p} \frac{\omega_{\text{osc}}}{Q_{\text{coil}}} \delta A - \omega_{\text{osc}} v_{\text{emf}}(t) \sin(\omega_{\text{osc}} t). \quad (3.23)$$

The parameter  $\omega_p$  is very large, so the oscillation amplitude changes due to magnetic resonance may be described by

$$\delta A(t) \approx -\frac{Q_{\text{coil}}}{\alpha_{\text{od}} - 1} \sin(\omega_{\text{osc}} t) \frac{d}{dt} \int_{V_s} [\mathbf{B}_u(\mathbf{r}) \cdot \mathbf{M}_s(\mathbf{r}, t)] dV. \quad (3.24)$$

Equation 3.24 describes a modulation of the oscillation amplitude with a frequency that corresponds to the difference of the precession frequency of the spin magnetisation  $M_s$  and  $\omega_{\text{osc}}$ .

### 3.2.6 Dependence of the EPR-on-a-Chip signal on the bias current

While in resonator-based EPR the dependence of the signal amplitude / intensity on the applied MW power /  $B_1$  – the so-called saturation behaviour – is well-understood as discussed in Section 2.4.2, the behaviour of EPRoC on a change of the bias current, which is equivalent to the MW power in resonator-based EPR, is more complicated. Therefore, the saturation behaviour of the EPRoC will be discussed in the following using the analytical expressions of the FM and AM signal of Equation 3.18 and Equation 3.21b, respectively. As these equations were derived assuming unsaturated samples, that is  $\chi'$  and  $\chi''$  are independent of  $B_1$ , the obtained results will show the “chip”-related part of the dependence of the FM and AM signal on a change of the bias current.

The chip-related parameters dependent on the bias current are identified in the following. The gate transconductance of a single transistor introduced in Equation 3.7 depends on the bias current as

$$G_{\text{mo}} = \sqrt{\beta I_{\text{bias}} / n}, \quad (3.25)$$

which leads to a dependence of the overdrive parameter on the bias current as

$$\alpha_{\text{od}} = \frac{G_{\text{mo}}}{2G_t} = \frac{\sqrt{\beta I_{\text{bias}} / n}}{2G_t}. \quad (3.26)$$

Inserting the overdrive parameter into the analytical solution of the FM signal of Equation 3.18 yields

$$\Delta\omega_{\text{osc,spin}} \approx -\frac{1}{2}\omega_{\text{osc},0}(I_{\text{bias}})\eta\chi' \quad (3.27a)$$

$$\propto 1 - \frac{\left(\frac{\sqrt{\beta I_{\text{bias}}/n}}{2G_t} - 1\right)^2}{16Q_{\text{coil}}^2}, \quad (3.27b)$$

The filling factor,  $\eta$ , is independent of the bias current. Therefore, the chip-related change of the FM signal depends on the parameters  $\beta$ ,  $n$ ,  $G_t$ , and  $Q_{\text{coil}}$ .

The AM signal of Equation 3.19 depends on the bias current and indirectly via the gate transconductance and the overdrive parameter as

$$\Delta A_{\text{osc,spin}} \approx 4\sqrt{\frac{2}{3}}\frac{nI_{\text{bias}}}{G_{m0}(I_{\text{bias}})}\sqrt{1 - \frac{1}{\alpha_{\text{od}}(I_{\text{bias}})}} \cdot \frac{\eta(Q_{\text{coil}}\chi'' - \chi')}{2(\alpha_{\text{od}}(I_{\text{bias}}) - 1)} \quad (3.28a)$$

$$\propto \sqrt{\frac{n^2 I_{\text{bias}}}{\beta}}\sqrt{1 - \frac{1}{\alpha_{\text{od}}(I_{\text{bias}})}} \cdot \frac{1}{2(\alpha_{\text{od}}(I_{\text{bias}}) - 1)} \quad (3.28b)$$

Again,  $\chi'$ ,  $\chi''$  and  $\eta$  are independent of the bias current. As before, the chip-related change of the AM signal on the bias current depends on its parameters. The change of both FM and AM signal may be quantified using typical parameters. The optimal value for the overdrive parameter that minimises the noise contribution from the active tank [126, P. 202] is given by  $\alpha_{\text{od,opt}} = 1.5$ . The slope factor typically ranges between 1.2 and 1.5 [126, P. 51], while the gate transconductance is of the order of several mS [126, P. 186]. Assuming that  $G_{m0} = 1$  mS and  $n = 1.2$  for a bias current of 5 mA,  $\beta$  may be calculated. This in turn allows a calculation of the change of the AM signal as function for the bias current. For the FM signal, a value of  $Q_{\text{coil}}$  of 2, 5 and 10 were assumed. The change of the FM and AM signal on the bias current is shown in Figure 3.3.

For the FM signal, a decrease of the signal amplitude is seen with increasing bias current, the change of which strongly depends on  $Q_{\text{coil}}$ . For  $Q_{\text{coil}}$  of 2, the decrease of the FM signal is  $\sim 8\%$  when increasing the bias current from 5 to 25 mA, while for quality factor ( $Q$ )-values above 5 the change over the same range is  $\sim 1\%$ . The strong dependence on  $Q_{\text{coil}}$  arises from the  $Q_{\text{coil}}^2$  in the denominator of Equation 3.27. The change of the AM signal, on the other hand, exhibits a non-linear behaviour on the bias current. Here, the decrease is  $\sim 30\%$  for the parameters when increasing the bias current from 5 to 25 mA. If the overdrive parameter is larger than the optimal value, the change of the FM signal gets larger and that of the AM signal gets smaller.

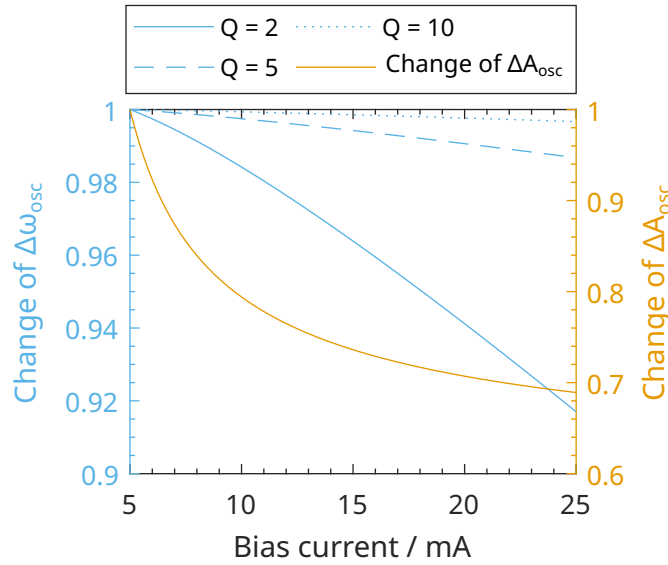


Figure 3.3: Change of the FM (left  $y$ -axis) and AM signal (right  $y$ -axis) as a function of the applied bias current assuming  $G_{m0} = 1$  mS,  $n = 1.2$  and different  $Q_{coil}$  of 2, 5 and 10. The latter only influences the FM signal amplitude.

In this section, we have seen that the dependence of the FM and AM signal amplitude on the bias current of the EPRoC – we could call it saturation behaviour of the EPRoC – is more complicated than the dependence of absorption and dispersion signal in resonator-based EPR on the MW power, since the EPRoC itself reacts on a change of the bias current.

### 3.3 THEORETICAL SPIN SENSITIVITY / LIMIT OF DETECTION

The absolute spin sensitivity / limit of detection (LOD) of the EPRoC may be estimated from the closed-form expressions of FM and AM signal discussed in Section 3.2.3 and Section 3.2.4 in combination with a model of the frequency and amplitude noise, respectively. In this thesis, we will not investigate this, as this has been performed in great detail in [126, 127, 134] for the FM signal and [133] for the AM signal. Instead, we will only discuss the main ideas of the derivation and its results. As it will turn out that the theoretical spin sensitivity for both FM and AM is the same as shown in [126], we will not treat them separately here.

To model the frequency and amplitude noise, two sources of noise are considered: the voltage noise introduced by the coil resistance and current noise introduced by the cross-coupled transistor pair. For both processes a white noise process is assumed. In [127], also the  $1/f$  noise of the cross-coupled pair is analysed but not used for the calculation of the LOD, because the commonly used field/frequency modulation reduces the  $1/f$  noise such that it can be neglected. The  $S/N(B_1, \omega_{osc})$

in a bandwidth of  $\Delta f = 1$  Hz may be calculated from the FM/AM signal and its respective noise. For the FM/AM signal, the magnetic susceptibility including saturation of Equation 2.35 is used. Hence, the  $S/N$  depends on  $T_1$  and  $T_2$ , too. The optimal  $\omega_{\text{osc}}$  and  $B_1$  maximising the  $S/N$  are then determined by taking the partial derivatives of  $S/N$  with respect to  $\omega_{\text{osc}}$  and  $B_1$  and equating them to zero, resulting in a maximum  $S/N_{\text{max}}$  for  $2T_1 = T_2$  at  $\omega_{\text{osc}} \approx \omega_0$ . The static susceptibility presented in Equation 2.35a and Equation 2.35b is calculated from Curie's law for a spin-1/2 system as  $\chi_0 = \mu_0 n \gamma^2 \hbar^2 / (4k_B T)$ , with  $n = N_{\text{spin}}/V_s$  being the spin density of the sample. Using the definition of the spin sensitivity / LOD of Equation 2.49, we can calculate the theoretical spin sensitivity of the EPRoC as

$$N_{\text{min}} = \frac{3N_{\text{spin}}V_s}{S/N_{\text{max}}} \quad (3.29a)$$

$$= \frac{12k_B^{3/2}T^{3/2}\sqrt{(1 + \alpha_{\text{od}}\gamma_{\text{nD}})R_{\text{coil}}}}{\gamma^3\hbar^2B_uB_0^2}, \quad (3.29b)$$

where  $k_B$  is the Boltzmann constant,  $T$  is the absolute temperature,  $\alpha_{\text{od}}$  is the overdrive parameter,  $\gamma_{\text{nD}}$  is the gate excess noise factor of the transistors,  $\gamma$  is the gyromagnetic ratio,  $\hbar$  is the reduced Planck's constant,  $R_{\text{coil}}$  is the resistance of the coil,  $B_0$  is the static magnetic field and  $B_u$  is the unitary magnetic field of the coil. Assuming  $B_u$  is uniform and produced by a circular coil, it may be approximated from the diameter of the coil,  $d_{\text{coil}}$ , as

$$B_u \approx \frac{\mu_0}{d_{\text{coil}}} \quad (3.30)$$

In addition,  $\gamma_{\text{nD}} \approx 1$  for a transistor in strong inversion [127, P. 75] and for a reasonable choice of  $\alpha_{\text{od}} = 3$  [127], Equation 3.29b may be simplified according to

$$N_{\text{min}} = \frac{24k_B^{3/2}T^{3/2}\sqrt{R_{\text{coil}}}}{\gamma^3\hbar^2B_uB_0^2}. \quad (3.31)$$

For the EPRoCs used within this thesis operating at approximately 14 GHz corresponding to a  $B_0$  of approximately 500 mT at room temperature ( $T = 300$  K) with a coil diameter of  $d_{\text{coil}} = 200$   $\mu\text{m}$  and a coil resistance of  $R_{\text{coil}} = 6.8$   $\Omega$ , we obtain a spin sensitivity of

$$N_{\text{min}} \approx 2 \times 10^8 \text{ spins}/\sqrt{\text{Hz}}. \quad (3.32)$$

### 3.4 ARRAYS OF INJECTION-LOCKED VCOS

As mentioned above, the EPRoC with a single VCO is designed for volume-limited samples with dimensions of a few hundred micrometres due its coil size. For concentration-limited samples, cavity resonators with their large sample volume are much better suited. To

optimise the EPRoC for such samples, the sample volume needs to be enlarged. To this end, arrays of  $N$  injection-locked VCOs, from now on called  $N$ -coil EPRoC array, have been developed [61, 128]. In these devices, the array is locked to a joint oscillation frequency. By the injection-locking the phase noise of the joint oscillation frequency is lowered by  $\sqrt{N}$ . In addition, the readout complexity for the complete array is reduced to a single FM signal. The lowering of the phase noise can intuitively be explained by a correction force between the injection-locked VCOs, i.e., whenever a single VCO in the array tries to perturb the joint phase from its nominal value, the  $N - 1$  VCOs will exert a correction force on the single VCO.

Furthermore, the sample volume is increased by  $N$ . Intuitively, one would assume that the signal amplitude, that is the frequency shift, would also increase by  $N$ , as more sample is available in the sensitive volume of the EPRoC. This, however, is not the case as will be explained below. If only  $n$  coils of the VCOs of the  $N$ -coil VCO array are covered with sample, i.e.,  $n$  VCOs experience an EPR-induced frequency shift (the FM signal), the same correction force – or rather restoring force in this context – acts on the joint oscillation frequency. To understand the concept of the restoring force, we consider first a single coil VCO EPRoC. If the coil of the VCO is completely filled with paramagnetic sample, the frequency shift will be maximal. If this coil is now in an injection-locked  $N$ -coil VCO array, the remaining  $N - 1$  non-filled VCOs exert a restoring force on the one VCO with the sample, effectively lowering the frequency shift of the one VCO (compared to a single VCO). Since the joint oscillation frequency is measured, it will be only slightly deviated from the equilibrium value. The restoring force is reduced when more and more coils of VCOs are covered with sample until it completely vanishes if all coils are filled. Then, the frequency shift in each coil and the joint frequency shift are the same which was confirmed by simulations in ref. [61, Figure 3 left]. It is important to note that the frequency shift per coil does not get larger (compared to a single VCO), but the restoring force gets smaller. Hence, there is no gain in frequency shift when filling all coils compared to a single VCO, but only the phase noise gets smaller.

In summary, the spin sensitivity is improved by  $\sqrt{N}$  by utilising an injection-locked VCO array. This effect could be called *spatial averaging*, similar to *temporal averaging*, which scales with  $\sqrt{T}$ , where  $T$  is the total measurement time.

### 3.5 PHASE-SENSITIVE DETECTION WITH FREQUENCY MODULATION

For applications of the EPRoC, the simplest solution is to employ a permanent magnet in combination with an frequency swept (FS) EPRoC sensor to avoid electromagnets for field sweeps. To enable phase-sensi-

tive detection (PSD) and avoid additional coils for modulating the static magnetic field (BM), frequency modulation (FM) of the MW carrier may be used. Apart from a simpler sensor setup, frequency modulated (FM) offers additional advantages compared to field modulated (BM). First, mechanical vibrations, so-called microphonics, from the modulation field are completely avoided and, secondly, the FM is homogeneous throughout the sample, which may be beneficial for a larger signal intensity [138–140]. The main technical difference between BM and FM is the “transfer of modulation” principle, a term introduced in ref. [141]. This principle means that modulation should be transferred to the MW carrier only when magnetic resonance occurs, which is obviously violated for FM where the MW carrier is directly modulated. If FM is used, the noise characteristics of the MW components are transferred to the modulation frequency, which is then detected with an lock-in amplifier (LIA). In ref. [142], the effects of modulation were theoretically and experimentally investigated in detail. It was found that if the modulation frequency exceeds the linewidth of the EPR spectrum, modulation sidebands appear in the spectrum, which can be assigned to multi-photon transitions. In addition, it was proven that BM and FM are mathematically and physically not equivalent. While only BM spectra were presented in ref. [142], in ref. [140], spectra obtained with BM and FM of lithium phthalocyanine exhibited different lineshapes, which could be reproduced in a simulation. However, [143] summarised the findings of the above-mentioned articles such that the differences between BM and FM are negligible for “normal” conditions in EPR experiments, i.e. modulation frequencies of up to 100 kHz.

## MATERIALS AND METHODS

---

In this chapter, the experimental configurations as well as preparation and characterisation of the standard samples used within the scope of this thesis will be discussed. Firstly, commercial resonator-based EPR instrumentation is shortly described. Then, the EPR-on-a-Chip (EPRoC) instrumentation and the different measurement modes are discussed. At the end, the preparation and characterisation of the standard samples are described.

### 4.1 RESONATOR-BASED EPR INSTRUMENTATION

For most of the resonator-based CW-EPR spectra shown in this thesis, commercial spectrometers have been used, a detailed description of which may be found in literature [12, 82, 144]. In particular, a Bruker ElexSys E580 X-/Q-band continuous wave (CW)- and pulsed spectrometer and a Magnettech Miniscope MS5000 CW spectrometer both located in the Berlin Joint EPR Laboratory at the Helmholtz-Zentrum Berlin (HZB) were utilised.

The Bruker spectrometer uses a 10" iron magnet (Bruker ER 073, maximum field 1.45 T) in combination with an X-band CW and pulsed microwave (MW) bridge (Bruker E580-1010). The maximum MW power of the Gunn diode is  $\sim 160$  mW which can be attenuated by up to  $-60$  dB, i.e., to  $\sim 0.16$   $\mu$ W. The sample is placed inside a dielectric-ring MW resonator (Bruker ER 4118X-MD5, conversion factor:  $0.42$  mT W $^{-0.5}$ ), which in turn is mounted in a continuous-flow helium cryostat (Bruker ER 4118CF). In this work, the cryostat has not been utilised for the experiments and was merely used as a holder for the probehead. The magnetic field is measured with a fourier transform NMR (FT-NMR) teslameter (Bruker ER 036TM), placed outside the cryostat. Magnetic field offsets were determined by EPR calibration measurements of standard samples with known  $g$ -values such as  $\alpha,\gamma$ -bisdiphenylene- $\beta$ -phenylallyl (BDPA) or nitrogen-atom-endohedral C<sub>60</sub> (N@C<sub>60</sub>).

The Magnettech MS5000 spectrometer is a benchtop device with a cavity resonator (conversion factor:  $0.12$  mT W $^{-0.5}$ ) and a small electromagnet with a maximum field of 650 mT. The MW power can be adjusted between 1  $\mu$ W and 100 mW. Hence, the available  $B_1$  range is smaller than that of the Bruker spectrometer in combination with the ER 4118X-MD5 resonator. For temperature-dependent measurements, a liquid nitrogen variable temperature controller (TCH04) with a range of 93 to 493 K may be used. Similarly, magnetic field offsets were de-



terminated by EPR calibration measurements of standard samples with known  $g$ -values such as BDPA or  $\text{N@C}_{60}$ .

## 4.2 EPR-ON-A-CHIP INSTRUMENTATION

The working principle of the EPRoC and the influence of the magnetic resonance signal on its oscillation frequency and amplitude was explained in [Section 3.2.3](#) and [Section 3.2.4](#), respectively. The following section deals with control of the MW frequency and the actual readout of both the change of the oscillation frequency and amplitude in the experimental setup.

### 4.2.1 Experimental configuration

Most of the EPRoC experiments were performed at the home-built EPRoC spectrometer in the Berlin Joint EPR Laboratory at HZB. A sketch of the setup of the EPRoC is shown in [Figure 4.1](#) (a). Each EPRoC is integrated into the *Bruker ESP300* spectrometer. However, only the electromagnet (*Bruker B-E 25*) generating  $B_0$  and its controller are used for the experiment. It is powered by a *Bruker ER 083* power supply and is capable of delivering a direct current (DC) magnetic field from 10 mT to 1.4 T. Its magnitude is controlled using a feedback loop with a Hall probe attached in the centre of the magnet.

The different iterations of the EPRoC are located on custom-designed PCBs discussed in [Section 4.2.4](#), which are placed in the centre between the pole shoes of the magnet, such that  $B_0$  and the surface of the EPRoC are perpendicular.

There are different power supplies for the different EPRoC printed circuit boards. From the applied bias current,  $I_{\text{bias}}$ , the  $B_1$  magnitude on the chip is defined. The particular current sources are described in [Section 4.2.4](#).

The reference frequency,  $f_{\text{ref}}$ , is provided by either a signal generator (either *Rohde & Schwarz SMB100A* or *Rohde & Schwarz SMB100B*) with an output frequency range from 1.1 kHz to 1 GHz. The  $f_{\text{ref}}$  inputs of all PCBs are terminated with  $50\Omega$  and need a power of  $\sim 1$  mW. Due to a 32-divider used in the PLL as described in [Section 4.2.2](#), the signal generator needs to provide a reference frequency of approximately  $13.44\text{ GHz}/32 = 420\text{ MHz}$ . The signal generator is capable of a frequency modulation of  $f_{\text{ref}}$  with a low frequency, which is used as modulation frequency,  $f_{\text{mod}}$ , for phase-sensitive detection in CW operation with a maximum modulation frequency of 1 MHz. The modulation amplitude of the modulation is set by the parameter *FM deviation*,  $\Delta f$ . The frequency deviation, which is seen on the EPRoC, is also multiplied by the factor of 32. Depending on the model of the signal generator, the maximum FM deviation at  $\sim 420$  MHz is either 2 MHz (*Rohde & Schwarz SMB100A* (R&S SMB100A)) or 5 MHz (*Rohde*



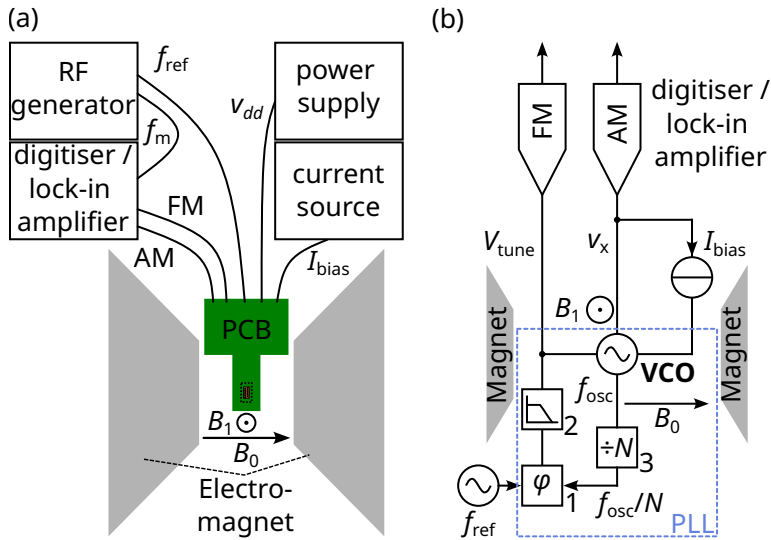


Figure 4.1: Schematic of the EPRoC setup. **(a)** Sketch of the experimental setup. The EPRoC is located on a printed circuit board (PCB) which is placed between the pole shoes of an electromagnet providing the static magnetic field,  $B_0$ . The power supply provides electricity for the components on the PCB. The current source provides the bias current,  $I_{bias}$ , to the EPRoC, generating  $B_1$ . The printed circuit board is placed such that the  $B_1$  perpendicular to the surface of the EPRoC is perpendicular to  $B_0$ . The radio frequency (RF) generator supplies the reference frequency for the phase-locked loop (PLL). The FM and AM signal are recorded either with a lock-in amplifier (LIA) or a digitiser for CW and RS operation, respectively. **(b)** Block diagram of the closed-loop EPRoC setup used. The voltage-controlled oscillator (VCO) of the EPRoC is embedded in a PLL marked by the dashed rectangle. In the PLL, the phase comparator (1) and loop filter (2) and the divider (3) ensure that the frequency,  $f_{ref}$ , of the RF generator and the oscillation frequency,  $f_{osc}/N$ , of the EPRoC is the same by adapting  $V_{tune}$ .  $N = 32$  is the divider on the EPRoC. The recorded signals are  $V_{tune}$  for the FM signal and  $V_x$  for the AM signal.

& Schwarz SMB100B (R&S SMB100B)). With that the maximum peak-to-peak modulation amplitude ( $\Delta f_{\text{mod,pp}} = 2 \times 32 \times \Delta f$ ) on the chip is 128 MHz (4.58 mT) and 320 MHz (11.42 mT), respectively. In practise, such large modulation frequency and amplitudes are not useful for CW operation, as many samples would be over-modulated and passage effects may be observed.

**CONTINUOUS WAVE OPERATION** For the CW detection, a two-channel dual-phase LIA (*Anfatec Instruments AG - eLockIn 203*), is used. Its input impedance is 1 M $\Omega$ . The device supports modulation frequencies between 10 mHz and 250 kHz. The modulation frequency, however, is supplied by the signal generator, which is connected to the reference input of the LIA. For the experiments, the FM output of the PCB is usually connected to input 1 while the AM output is connected to input 2. With that, both the frequency modulated (FM) and the amplitude modulated (AM) signal may be detected simultaneously. CW-EPRoC spectra are either recorded by sweeping the external magnetic field,  $B_0$ , while keeping the oscillation frequency,  $\omega_{\text{osc}}$ , constant which is controlled by the reference frequency or vice versa. The whole experimental setup is controlled by a home-written *LabVIEW* software.

**RAPID SCAN OPERATION** For RS operation, the same frequency modulation of the reference frequency as of the CW operation is used. The terms modulation frequency and modulation amplitude, however, have a different meaning here. The modulation amplitude corresponds to the repetition rate of the experiment,  $f_{\text{rs}}$ , while the peak-to-peak modulation amplitude corresponds to the sweep range of the experiment,  $\Delta f_{\text{rs}}$ . The scan rate,  $\alpha_{\text{rs}}$ , of the RS experiment may be calculated from the repetition rate and the sweep width (cf. [Section 2.5.3](#)).

For the RS-EPRoC detection, the 12 bit 1.8 GSa s<sup>-1</sup> *Zurich Instruments* UHFLI digitiser was used. Both, FM and AM signal are fed into the digitiser. The sampling rate is set to 450 MHz to suppress high frequency noise. RS-EPRoC transients are recorded at a constant external magnetic field,  $B_0$ , and constant centre oscillation frequency,  $\omega_{\text{osc}}$ , with frequency modulation. The whole experimental setup is controlled by a home-written *LabVIEW* software. For the read-out of the digitiser, however, a home-written Python programme was used due to a bug in the driver for *LabVIEW* leading to excessive memory usage.

#### 4.2.2 FM detection via phase-locked loops

The EPRoC is commonly embedded in a PLL to control and stabilise its oscillation frequency via an external (low noise) reference frequency supplied by an RF generator. This is called the closed-loop setup and is depicted in [Figure 4.1](#) (b) as opposed to the open-loop setup in which

the EPRoC is not embedded in any feedback loop for control of the frequency, i.e., a free-running oscillator. For all the EPRoC measurements shown in this thesis, a closed-loop setup was used. The PLL serves two purposes for the EPRoC. Firstly, the phase and hence the frequency of the VCO(s) of the EPRoC is precisely controlled. Secondly, the PLL serves as a frequency-to-voltage converter that allows the measurement of the change of the frequency of the EPRoC due to magnetic resonance, i.e., the FM signal. The PLL provides a downconverted FM signal at the modulation frequency. Generally, there are different ways to convert the frequency change of the VCO to a voltage such as quadrature downconversion. Embedding the VCO of the EPRoC in a PLL was first discussed in ref. [145] for CW experiments and in ref. [131] for RS experiments.

A sketch of the working principle of a PLL is explained below, while a detailed discussion of phase-lock loops is presented in ref. [146]. An elementary PLL consists of phase detector (1), a loop filter (2), and a VCO (in our case the VCO of the EPRoC) connected in a loop as depicted in Figure 4.1 (b). The divider (3) is not strictly necessary but is utilised by the EPRoC to divide the oscillation frequency by a factor of  $N$ . Assuming that the PLL is locked, and the phase detector is linear, its output voltage is proportional to the phase difference of the reference signal and the VCO signal (divided by  $N$ ). The loop filter (2) suppresses noise and high-frequency components in the output of the phase detector and returns the so-called tuning voltage,  $V_{\text{tune}}$ , to the VCO, which determines its frequency. Deviations from the centre frequency may be described by  $\Delta f = K_0 V_{\text{tune}}$ , where  $K_0$  is the so-called VCO gain factor. As the frequency is the derivative of the phase, this equation relates  $V_{\text{tune}}$  with the phase of the (divided) VCO signal and if the PLL is locked both reference signal and VCO oscillate in phase. For an ideal VCO,  $V_{\text{tune}}$  is proportional to its frequency and hence, can be used to measure the change of the oscillation frequency of the EPRoC due to magnetic resonance, which is called *FM signal*. To recover the actual change of the oscillation frequency due to magnetic resonance with the correct unit Hz, the measured tuning voltage needs to be converted by means of the VCO gain factor. Commonly VCOs exhibit a slightly non-linear behaviour of their oscillation frequency as a function of the tuning voltage. Additionally, the VCO gain changes with bias current, among other things. Therefore, a calibration curve for each state is required, an example of which is shown in Figure 4.2. The left  $y$ -axis displays the DC tuning voltage as a function of the oscillation frequency / MW frequency. Because the first derivative of an EPR spectrum is recorded due to phase-sensitive detection (PSD) with the LIA, the first derivative of the DC calibration curve is required. To reduce numerical errors, the DC was fitted with a third-order polynomial, of which the first two coefficients were used to calculate the derivative. This conversion is not strictly required for field sweeps with

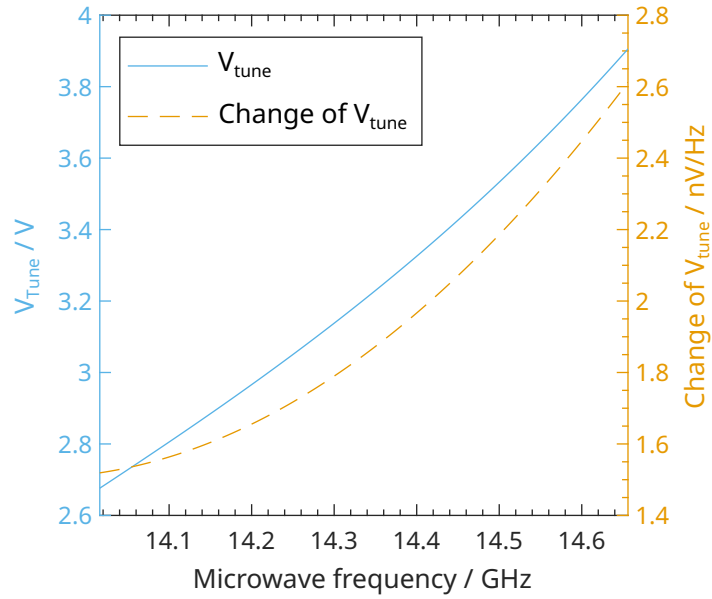


Figure 4.2: Exemplary tuning voltage as a function of the MW frequency used to convert  $V_{\text{tune}}$  to  $\Delta\omega_{\text{osc,spin}}$  of the single-coil EPRoC dipstick board submersed in water at a bias current of 4 mA. Left  $y$ -axis: DC tuning voltage. Right  $y$ -axis: First derivative of the DC tuning voltage.

a constant oscillation frequency, since the conversion factor is constant. For frequency sweeps, however, the conversion must be performed. Otherwise, the spectral shape of the resulting spectrum is distorted. If the absolute value of the change of the oscillation frequency is not required, the on-resonance spectrum may be divided by an off-resonance spectrum recorded with the same acquisition parameters.

#### 4.2.3 AM detection

Similar to the downconversion of the frequency change of the EPRoC, a downconversion of the oscillation amplitude of the EPRoC is required, too. For this, an implicit demodulation of the oscillation amplitude is provided at the centre tap of the differential tank inductor ( $V_x$  in Figure 3.1) when current biasing the VCO as depicted in Figure 4.1 (b) leading to the so-called *AM signal*. This method is discussed in general for complementary metal-oxide-semiconductor (CMOS) LC oscillators in ref. [147] and in particular for the EPRoC in refs. [133, 136, 148].

#### 4.2.4 Iterations of the EPR-on-a-Chip

In the course of this thesis, three different EPRoC designs have been used which will be described in the following.

#### 4.2.4.1 12-coil array EPR-on-a-Chip

This EPRoC design utilises 12 injection-locked VCOs similar to the one presented in [61]. As discussed in Section 3.4, the injection locking lowers phase noise of the joint array frequency by  $\sqrt{12}$ . The octagonally-shaped coils of the VCOs with an outer diameter (OD) of 200  $\mu\text{m}$  are arranged in a zipper-like fashion on the EPRoC in two rows of 6 coils each. The distance of the coils is 200  $\mu\text{m}$  in the rows, while the two rows are  $\sim 225 \mu\text{m}$  apart. The traces of the coils are 8.5  $\mu\text{m}$  wide.

The 12-coil VCO EPRoC array PCB is powered by DC power supply PCB built by Anh Chu mounted to the EPRoC PCB. It consists of two current sources powering AM1 and AM2 as well as one voltage source powering the remaining ten VCO. The PCB itself is powered by a *Keysight E3646A* two channel DC power supply with 15 V and 5.5 V ( $V_{dd}$ ) to ground. An additional *LabVIEW* program is used to control the power supply PCB. Voltages between 0.45 V and 1.5 V and bias currents between 2 mA and 24 mA per coil (AM1/AM2) can be set.

The frequency sweep range of this EPRoC extends from 12 to 14.4 GHz (sweep width 2.4 GHz or 85.6 mT). A 32-divider is used on the chip, so that the reference frequency is in the range of  $\sim 420$  MHz. The PLL utilised in this PCB has an approximate bandwidth of 10 MHz, which is large enough that it may be used for both CW and RS operation. This PCB is inserted horizontally between the pole shoes of the magnet, so that solid-state samples or liquid samples in capillaries may be placed directly onto its surface.

#### 4.2.4.2 Single-coil dipstick EPR-on-a-Chip

This EPRoC design utilises a single VCO presented in [130]. Similar to the 12-coil EPRoC array, the octagonally-shaped coil of the VCOs has an OD of 200  $\mu\text{m}$  and a thickness of the traces of 8.5  $\mu\text{m}$ . A Keithley 6221 current source is used for the dipstick PCB. The VCO of the EPRoC oscillates from about 2 mA to approximately 24 mA.

The frequency sweep range of this EPRoC extends from 13.8 to 14.4 GHz (sweep width 1.6 GHz or 57.1 mT). A 32-divider is used on the chip, so that the reference frequency is in the range of  $\sim 420$  MHz. The PLL utilised in this PCB has an approximate bandwidth of 10 MHz, which is large enough that it may be used for both CW and RS operation. There are two features of this EPRoC PCB design that make it unique to previous designs. Firstly, the tip of this EPRoC PCB, on which the actual EPRoC is located, is detachable, so that in case of failure of the EPRoC it can quickly be replaced. Secondly, the said tip is coated with a 10 to 12  $\mu\text{m}$  thick film of parylene C.<sup>1</sup> This coating allows to submerge the tip of the EPRoC PCB into a sample solution. Therefore, this PCB is inserted vertically between the pole shoes of the magnet. The sample

<sup>1</sup> The coating was applied by Diener Electronic; Michal Kern and Anh Chu investigated the coating and communicated with the company.

solution is placed in a 10 mL beaker into which the tip of the dipstick PCB is lowered.

**12-COIL DIPSTICK EPR-ON-A-CHIP** A similar parylene C coated dipstick PCB with the 12-coil EPRoC as described in [Section 4.2.4.1](#) was manufactured and is located at the Max-Planck-Institut für chemische Energiekonversion. It features a detachable tip as the single-coil EPRoC dipstick.

### 4.3 SAMPLE PREPARATION AND CHARACTERISATION

For a detailed understanding of the spectra obtained with the EPRoC, a set of samples was prepared that was thoroughly investigated mainly using “standard” resonator-based EPR and other techniques. Different sample classes were used for this purpose. The first class are stable organic radicals in powder form. In this thesis, BDPA and 2,2-diphenyl-1-picrylhydrazyl (DPPH) were used as typical representatives and are described in [Section 4.3.1.1](#) and [Section 4.3.1.2](#), respectively. The second type are solid state thin films, in our case a thin film of amorphous silicon (a-Si) on a Quartz substrate described in [Section 4.3.1.3](#). The third type of samples investigated are stable organic radicals in polar solution. For this, 4-hydroxy-2,2,6,6-tetramethylpiperidine-1-oxyl (tempol) in water was used, which is described in [Section 4.3.2.1](#).

#### 4.3.1 Solid state samples

##### 4.3.1.1 $\alpha,\gamma$ -bisdiphenylene- $\beta$ -phenylallyl (BDPA)

BDPA is a crystalline stable organic radical first synthesised in 1957 [149] and is commonly used as an EPR standard. In resonator-based EPR at X-band, BDPA exhibits an intense single EPR line at  $g = 2.003$  with a linewidth of about 0.07 mT [150]. It is, therefore, commonly used for the development of new methods studying unpaired electrons [151–153] and also seems ideally suited as a standard sample for the EPRoC.

The density of BDPA is  $1.220 \text{ g cm}^{-3}$  [154]. With a molecular weight of  $495.63 \text{ g mol}^{-1}$  [155], a spin density of  $1.5 \times 10^{21} \text{ spins cm}^{-3}$  is obtained.

The relaxation times were first determined by Goldsborough et al. to be  $T_1 = 110 \text{ ns}$  and  $T_2 = 100 \text{ ns}$  [156]. In ref. [157] it was found that although commercial BDPA is crystalline, the individual particles used for the investigation are not single crystals. In the same work, Mitchell et al. found an intra-particle distribution of  $T_2$  between 80 to 160 ns with RS-EPR [157] of different particles from the same batch.

For the experiments with the EPRoC, BDPA with benzene (1:1) in powder form was used as obtained from Sigma Aldrich. Small grains with sizes smaller than the diameter of the EPRoC coil were selected

by a comparison with a printed microscale. They were subsequently placed onto the surface of the EPRoC under a light microscope by means of a sharpened toothpick.

**ESTIMATION OF THE VOLUME AND MASS** The mass of the samples was determined from its sample volume assuming a homogeneous distribution of the mass density. For the experiments shown in chapters 5 and 7 the sample volume was determined after its placement onto the EPRoC, while the volume estimation for the  $B_1$  mapping experiments in Chapter 6 was performed prior to the placement of the sample on the sample holder. To determine the volume of the investigated sample, its planar dimensions were determined from (multiple) photographs of the sample by comparison with the dimensions of the coils on the EPRoC or with the printed microscale. The out-of-plane dimension was estimated from the size of the shadow of the sample. For that, lighting from different sides was used so that the shadow could readily be distinguished from the sample. The volume was then calculated from the dimensions assuming a cuboid. While the planar dimensions may be determined with a relatively small error of  $\sim 10\%$  from the micrograph, the estimation of the out-of-plane dimension from the shadow has a large error of up to  $50\%$ . This results in a total relative error of the sample volume of  $\sim 82\%$ . In addition, the assumption of a cuboid sample may be invalid, too. In this case, the error may be even larger than previously estimated.

#### 4.3.1.2 *2,2-diphenyl-1-picrylhydrazyl (DPPH)*

DPPH is a commercially available stable nitrogen-centred radical. The X-band EPR spectrum of DPPH in powder form at room temperature consists of a single exchange-narrowed line at  $g = 2.0036 \pm 0.0002$  [158] with a linewidth between 0.15 to 0.81 mT [159] depending on the solvent from which it has been crystallised. It is commonly used in EPR method development and for the calibration of the modulation amplitude of commercial EPR spectrometers [158].

In ref. [133], the average density of DPPH powder was determined from refs. [160–163] and reads  $1.41 \text{ g cm}^{-3}$ . In combination with the molecular weight of  $394.32 \text{ g mol}^{-1}$  [164], the spin density of DPPH is calculated as  $2.1 \times 10^{21} \text{ spins cm}^{-3}$ .

#### 4.3.1.3 *Amorphous silicon thin film on Quartz glass*

To investigate the EPRoC array chip and for better sensitivity estimation, a thin film sample of a-Si was used. It belongs to most studied semiconductor materials in the last decades. An extensive review of (hydrogenated) a-Si may be found in [8]. For the purposes of this thesis, however, the most important properties are described below. Pure (unhydrogenated) a-Si finds very little application for technolo-



gical applications due to its poor electronic quality [165], such as low photoconductivity. The main reason for this is the high number of structural defects in a-Si, the so-called dangling bond (DB). A DB is an under-coordinated site in the a-Si network, where one of four Si valence electrons cannot form a bond with a neighbour and is left alone (i.e. *dangling*). In hydrogenated a-Si, these DB are compensated by H atoms, leading to a better electronic quality.

The first investigation of unhydrogenated a-Si performed by Brodsky and Title [166] found a *Lorentzian*-shaped line at  $g = 2.0055$ , which they attributed to the DB. Later research concentrated on hydrogenated a-Si and confirmed the existence of dangling bonds [167], and refined the  $g$ -tensor. A multifrequency EPR study by Fehr et al. [4] found a rhombic  $g$ -tensor for the DB, which was in good agreement with density functional theory calculations. In this work, a thin film of unhydrogenated a-Si is used, where we make use of the large number of DB since they give rise to an intense EPR signal. Due to the high concentration of DB in the sample (cf. [paragraph 4.3.1.3](#)), the  $g$ -tensor is not observed due to a strong exchange coupling. Therefore, instead of the rhombic  $g$ -tensor mentioned above, the isotropic  $g$ -value determined in ref. [166] is used.

**SAMPLE PREPARATION** A 15  $\mu\text{m}$  thick film of a-Si was e-beam evaporated in the Von Ardenne cluster at PVcomB of HZB [168] (emission current: 560 mA,  $T = 680^\circ\text{C}$ , deposition rate between 400 and 450  $\text{nm min}^{-1}$ , sample rotation 15 rpm) on a  $5 \times 5 \text{ cm}^2$  and 500  $\mu\text{m}$  thick Quartz (CrysTec GmbH) substrate. The thickness was confirmed by investigating the edge of the sample where the sample holder was placed with a confocal microscope. At this position, a  $\sim 15 \mu\text{m}$  step was present. The  $5 \times 5 \text{ cm}^2$  sample was cut into several  $1 \times 2 \text{ mm}^2$  and  $1 \times 5 \text{ mm}^2$  small pieces using a dicing saw (DISCO DAD3220).

**SPIN QUANTIFICATION** The number of spins of one of the  $1 \times 5 \text{ mm}^2$  samples was determined with a calibrated spectrometer (*Lyra*) at Freie Universität Berlin by means of quantitative EPR at X-band (MW power:  $6.3 \times 10^{-2} \text{ mW}$ , modulation amplitude: 0.1 mT, modulation frequency: 100 kHz, time constant: 1 s, number of scans: 1, Q-factor: 7440) to be  $1.8 \times 10^{15}$ . With a volume of  $5 \times 1 \times 0.015 \text{ mm}^3 = 8 \times 10^{-5} \text{ cm}^3$ , the spin density reads

$$\rho_{\text{a-Si film}} = 2.4(5) \times 10^{19} \text{ spins cm}^{-3}.$$

Here, the relative error for each length is assumed to be 10 %, resulting in a relative error for the sample volume of 18 %. The average distance of two DB is then calculated to be  $\sim 3.4 \text{ nm}$ .

**LINESHAPE AND LINEWIDTH** [Figure 4.3](#) shows the spectra of the a-Si film at S-band (a), X-band (b) and Q-band (c). The spectra at S-



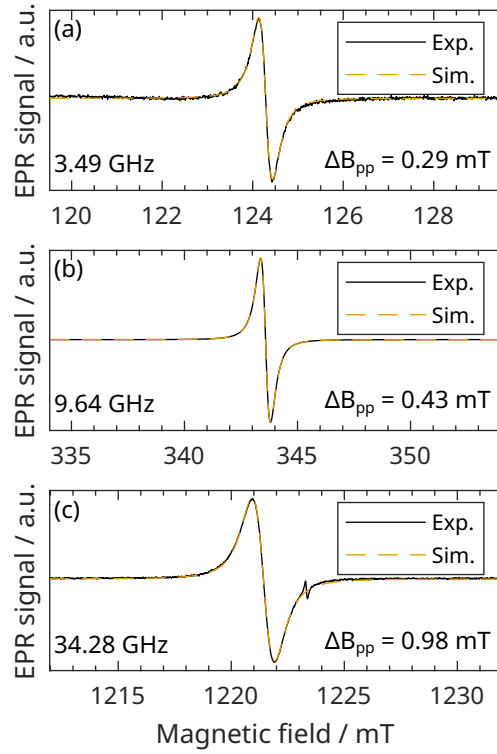


Figure 4.3: EPR spectra of the 15  $\mu\text{m}$  thick a-Si film on Quartz glass obtained at (a) S-band (Bruker ER 4118S-MS5,  $P_{\text{mw}} = 0.22$  mW,  $n_{\text{avg}} = 190$ ,  $f_{\text{mod}} = 100$  kHz,  $B_{\text{mod}} = 0.05$  mT,  $\tau = 58.59$  ms), (b) X-band (Bruker ER 4118X-MD5,  $P_{\text{mw}} = 2.53$  mW,  $n_{\text{avg}} = 1$ ,  $f_{\text{mod}} = 100$  kHz,  $B_{\text{mod}} = 0.1$  mT,  $\tau = 29.3$  ms), and (c) Q-band (Bruker ER 5106Q-TW,  $P_{\text{mw}} = 12.5$  mW,  $n_{\text{avg}} = 8$ ,  $f_{\text{mod}} = 100$  kHz,  $B_{\text{mod}} = 0.1$  mT,  $\tau = 10.24$  ms). Each spectrum was simulated using *pepper* of the *EasySpin* software package.

and X-band exhibit a single line, while at Q-band a small second line is visible, too. The second line most likely originates from the Quartz substrate, which overlaps in S- and X-band with the spectrum of the DB in the a-Si. All spectra were simulated with *pepper* of the *EasySpin* software package [70]. For the simulation, a spin-1/2 system with a convolutional broadening with both *Gaussian*,  $\Delta B_{\text{pp,G}}$ , and *Lorentzian*,  $\Delta B_{\text{pp,L}}$ , contributions was assumed for the DB in a-Si. The second line in the Q-band spectrum was simulated assuming a spin-1/2 with convolutional *Lorentzian* broadening only. While the spectrum at S-band mainly has a *Lorentzian* shape ( $\Delta B_{\text{pp,G}}/\Delta B_{\text{pp,L}} = 3.2\%$ ), the *Gaussian* contribution increases towards X-band (16.7%) and Q-band (51.3%). This MW frequency dependent change of lineshape may be attributed to *g*-strain, which has a stronger influence at larger MW frequencies and magnetic fields. The total linewidth of the a-Si film sample exhibits a linear behaviour on the MW frequency.

**RELAXATION TIMES** Due to the high defect density, the relaxation times of the sample could not be determined using standard pulsed

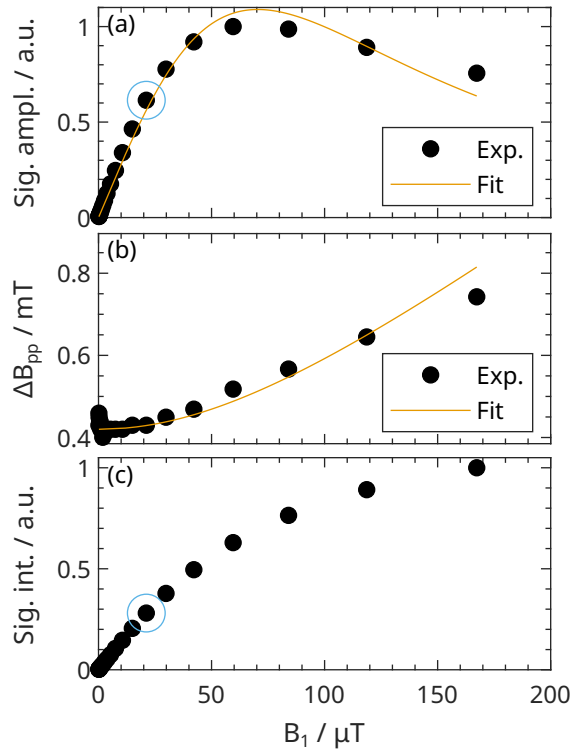


Figure 4.4: Saturation analysis at X-band of the  $15 \mu\text{m}$  thick a-Si film on Quartz glass. **(a)** Peak-to-peak amplitude of the EPR spectra with fit assuming a *Voigt* lineshape. The spectrum obtained at  $B_1$  marked with the open circle is used for further analysis. **(b)** Experimental peak-to-peak linewidth obtained from the spectra with fit. **(c)** Signal intensity (double integral) of the EPR spectra. The spectrum obtained at  $B_1$  marked with the open circle is used for further analysis.

EPR methods. The high defect density of the sample leads to a large dipole-dipole interaction between the spins, which leads to spin-spin relaxation times that are lower than the instrument dead time of the EPR spectrometer.

Therefore, the relaxation times are estimated by a fit of the saturation curve shown in Figure 4.4 using the method described in [169]. Instead of using the *Bloch* equations which assume a *Lorentzian* lineshape only, here, a *Voigtian* lineshape is assumed. This lineshape reflects the spectrum of the a-Si to a good extent. The calculation estimates  $B_1$  from the MW power using the conversion factor,  $C$ , of the cavity. The saturation analysis was performed at X-band since the resonator conversion factor for the Q-band probehead is much lower ( $C = 0.006 \text{ mT W}^{-0.5}$ ), such that no saturation could be seen at Q-band. To maximise the  $B_1$  range of the saturation measurement, the ER 4118 X-MD5 probehead was used since it has the largest conversion factors

of the commercial *Bruker* probeheads of  $C = 0.42 \text{ mT W}^{-0.5}$  [170]. The estimated spin-spin ( $T_2$ ) and spin-lattice ( $T_1$ ) relaxation times are

$$T_1 \approx 200 \text{ ns} \quad \text{and} \quad T_2 \approx 20 \text{ ns}.$$

These relaxation times are much faster compared to hydrogenated amorphous silicon (a-Si:H), which exhibits  $T_1$  in the range of  $\mu\text{s}$ . However, the high defect density quenches the relaxation times of the sample.

#### 4.3.2 Solution samples

##### 4.3.2.1 Dissolved 4-hydroxy-2,2,6,6-tetramethylpiperidine-1-oxyl

As a solution test sample, a series of 4-hydroxy-2,2,6,6-tetramethylpiperidine-1-oxyl (tempol) /  $\text{H}_2\text{O}$  solutions with concentrations of (0.01, 0.1, 1 and 10)  $\text{mmol L}^{-1}$  were used. Tempol is a commercially available air stable nitroxide radical. There are many nitroxides commonly employed in EPR research, but they share one property which is the unpaired electron that is coupled to a nitrogen (N) nucleus. Usually, they are covalently or non-covalently introduced into different materials as micro-probes to study the local environment. The accessible parameters of the samples through the nitroxide probes among others are pH, viscosity, polarity, H-bond networks, transition temperatures, local dynamics, and distances toward other nitroxide probes [171].

**SAMPLE PREPARATION** Tempol was bought from Sigma-Aldrich (97%, LOT #BCCB3715) and used as obtained. The  $10 \text{ mmol L}^{-1}$  starting solution was prepared by dissolving an appropriate amount of the sample in 50 mL de-ionised water. Lower concentrations were obtained by dilution of the  $10 \text{ mmol L}^{-1}$  starting solution.<sup>2</sup>

**QUANTITATIVE EPR WITH THE MAGNETTECH MS5000** To obtain quantitative EPR data of multiple samples, the amount of sample in the resonator as well as the sample position need to be reproducible. Due to the high dielectric constant of water, a measurement of the solutions in the standard 4 mm EPR capillaries is not possible. Therefore, the samples were filled in open-ended  $50 \mu\text{L}$  capillaries (Hirschmann ringcaps, inner diameter (ID): 1.02 mm) and sealed with Kritoseal at both ends. The filling height was from one end without the green marking until the black mark in the centre of the capillary, such that the filling height is larger than the resonator. For the sample alignment in the Magnettech MS5000 spectrometer the capillary guidance tube (Magnettech F120/1.5 3.6 mm) was used as explained in the user

<sup>2</sup> In homoeopathic terms, the lower concentrated solutions would correspond to “potencies” of D<sub>1</sub>, D<sub>2</sub> and D<sub>3</sub> compared to the starting solution. The samples were, however, not properly shaken to be considered homoeopathic “medication”.

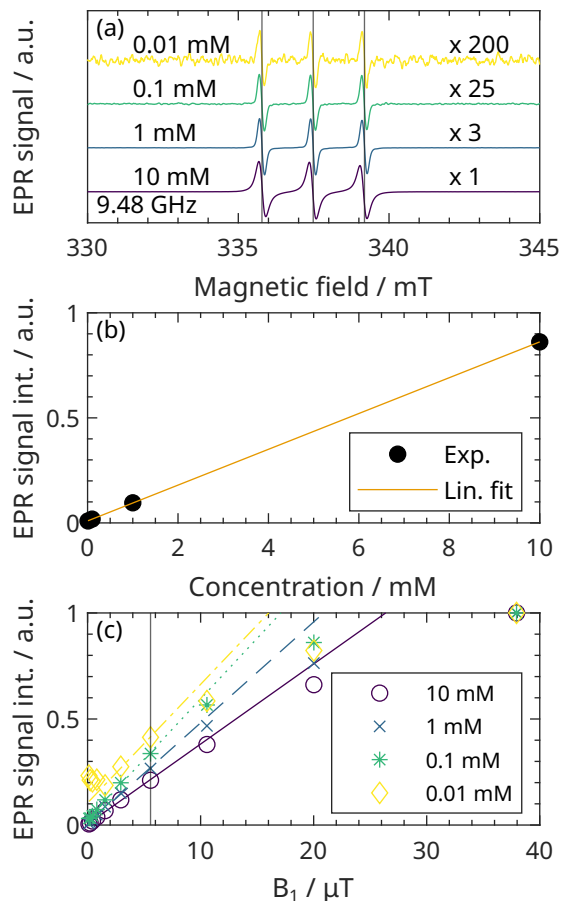


Figure 4.5: Tempol /  $\text{H}_2\text{O}$  solutions with concentrations of (0.01, 0.1, 1 and 10)  $\text{mmol L}^{-1}$ . **(a)** Resonator-based EPR spectra. Each spectrum is multiplied by the number on the right of the respective spectrum to ensure similar scaling in the plot. The vertical lines mark the hyperfine splitting caused by the N nucleus. **(b)** EPR signal intensity (double integral (DI)) as a function of the tempol concentration obtained from the spectra above. A linear behaviour is observed. **(c)** Saturation analysis obtained from the DI shows saturation at a  $B_1$  above about  $5.6 \mu\text{T}$ . The lines (solid, dashed, dotted, dash-dotted) are linear fits to the data at low power. The EPR spectra in (a) were acquired at the  $B_1$  marked with the vertical line corresponding to  $5.6 \mu\text{T}$ .

manual, i.e., the top of the guidance tube was on the same height as the plastic capillary holder. The samples were inserted to the bottom of the guidance tube for investigation. This procedure ensures the same experimental conditions for all samples.

Figure 4.5 (a) displays the spectra of the tempol solutions in X-band obtained with the Magnettech MS5000 spectrometer with a modulation frequency of 100 kHz, a modulation amplitude of 0.07 mT and an MW power of 2.15 mW (5.6  $\mu$ T). All spectra exhibit three lines due to the hyperfine splitting by the N. In addition, the samples are in the isotropic limit, which can be seen by the fact that the three lines almost have the same intensity [171]. In this regime, the anisotropic solid state interactions are averaged out and only an isotropic average of the magnetic interactions can be observed. Therefore, the isotropic hyperfine splitting parameter  $A_N$  may be read-off the spectrum as shown in Figure 4.5 (vertical lines in the plot) and reads  $\sim 47.7$  MHz, which is similar to literature values for tempol in solution. Earlier findings, however, did mostly not investigate tempol in pure water, but in other solvents. In ref. [172], the dependence of the hyperfine splitting of tempol and other nitroxides was investigated for different solvents. For solvents containing a Hydroxy-group, such as alcohols, a linear dependence of  $A_N$  on the dielectric constant,  $\epsilon$ , from about 15 to 33 was found. Considering water a solvent with a Hydroxy-group, too, and extrapolating  $A_N$  to  $\epsilon = 80$ , a hyperfine splitting of 46.9 MHz is obtained. In addition, Clark et al. [173] found a value of 47.6 MHz for tempol in water, which is in agreement with the findings presented here.

The 10 mmol L<sup>-1</sup> spectrum exhibits a broadening of the three lines compared to the lower concentrations due to the high concentration as explained in Section 2.3.3. Therefore, the signal amplitude is only about a factor of 3 larger than the 1 mmol L<sup>-1</sup> sample. If there was no exchange broadening, the signal amplitude should scale linearly with the concentration of the solutions, i.e., it should be 10 times larger for a 10 times higher concentration. The samples with 0.01, 0.1 and 1 mmol L<sup>-1</sup> show this behaviour approximately. The EPR signal intensity, however, is not affected by a change of the lineshape and shows a linear relationship between the doubly-integrated EPR signal and the concentration as seen in Figure 4.5 (b).

The saturation behaviour of the tempol solutions is shown in Figure 4.5 (c). It is plotted here as the EPR signal intensity (DI of the first-absorption EPR spectrum) as a function of  $B_1$ . All solutions exhibit a similar saturation behaviour. The part of each saturation curve at low power is linearly fit to obtain the onset of the saturation. The approximate non-saturating  $B_1$  can be extracted from the fits and the experimental data. It is depicted with the vertical line in Figure 4.5 (c) at the non-saturating power of about 5.6  $\mu$ T. The spectra in Figure 4.5 (a) were obtained at this MW power.



## PRACTICAL CONSIDERATIONS FOR EPR SPECTROSCOPISTS

---

### 5.1 INTRODUCTION

This chapter is mainly written for EPR spectroscopists who got hold of one of the EPR-on-a-Chip (EPRoC) printed circuit boards (PCBs) and want to use it for their research. It is thought to facilitate the understanding of the EPRoC technology for potential users and may therefore, be described as “materials and methods-ish”. The purpose of this chapter is to understand the FM and AM spectra in detail. At the same time, it lays the foundation for the subsequent chapters, in which certain aspects of the EPRoC will be investigated in more detail. Some presented experimental data are currently not fully understood, but may be interpreted in the future.

The understanding of the spectra recorded by the EPRoC is of utmost importance to enable the EPRoC technology to be used as a spectroscopic tool. While for resonator-based EPR, many analyses about the EPR signal have been performed since its dawn, discussed e.g. in refs. [78, 83], an in-depth analysis of actual EPRoC spectra recorded with the EPRoC is incomplete. Therefore, this chapter contains detailed analyses of both FM and AM spectra of the solid-state and solution-state samples described in [Chapter 4](#). The spectra are simulated and compared to resonator-based EPR with their differences highlighted. One unique advantage of the EPRoC over resonator-based EPR is the ability to record frequency-swept spectra in addition to field-swept spectra especially at “low” microwave (MW) frequencies, i.e. up to Q-band. This generally allows the use of permanent magnets instead of the commonly used electromagnets, which in turn may lead to a complete miniaturisation of the whole EPRoC spectrometer and not only of its MW components [55, 59]. Here, the difference of field- and frequency-swept spectra are discussed. The uniqueness is further used for a proof-of-principle frequency-domain magnetic resonance (FDMR) experiment that is usually only possible in dedicated resonator-free high-field / high-frequency EPR spectrometers.

The sensitivity is a very important quantity for any spectroscopy. For resonator-based EPR, this was analysed in detail mainly by Feher [83]. A detailed analysis for the EPRoC similar to that of resonator-based EPR may be found in refs. [126, 127, 133]. Yet, such theoretical consider-

---

Some parts of this chapter are from S. Künstner, J. E. McPeak, A. Chu, M. Kern, M. Wick, K.-P. Dinse, J. Anders, B. Naydenov, K. Lips, Microwave Field Mapping for electron paramagnetic resonance (EPR)-on-a-Chip Experiments. *Science Advances* 2024, 10 (33), ead05467. DOI: [10.1126/sciadv.ad05467](https://doi.org/10.1126/sciadv.ad05467).

ations sometimes only have a limited value for the actual experiment. Therefore, absolute spin sensitivities determined experimentally with solid-state samples will be discussed in this chapter and compared to previously published results.

Many samples especially for medical or biological applications contain paramagnetic species dissolved in aqueous solutions. Such solutions of solvents with a high dielectric constant – so-called lossy solvents – pose a major challenge to EPR spectroscopists [174–176]. Because these samples absorb the MW in the resonator non-resonantly via the electric field. Thin capillaries or so-called flat cells [12, 177] are therefore commonly used to investigate such samples. In this case, excessive non-resonant MW absorption is avoided both by reducing the sample volume in the resonator and by placement of the sample in parts of the resonator with low electric field. For the EPRoC technology, different means of investigation of paramagnetic species in aqueous solution are employed, including placement of the sample in capillaries with different geometries. The EPRoC dipstick approach, however, allows submersing the EPRoC into a sample solution, which brings the investigation of such samples to a new level drastically simplifying sample handling. This approach is similar to those presented using a dipstick micro-resonator [47] or a non-resonant near-field probehead [49]. The absolute spin sensitivity of the EPRoC dipstick determined with aqueous solutions is similar to that determined with powder samples. In addition, the usefulness of the values of the concentration sensitivity is verified.

The influence of the dielectric constant of many solvents on the sensitivity of resonator-based EPR spectrometers was investigated in refs. [175, 176]. Although this thesis does not provide such an in-depth analysis, the effect of the dielectric constant is analysed with two samples with a low and high dielectric constant, respectively.

The MW saturation of the sample is another important parameter for EPR spectroscopists as spectra recorded under saturating conditions are often discarded due to possible lineshape broadening. While the saturation behaviour of paramagnetic species in resonator based EPR has been studied in depth [84, 178–180], a detailed analysis of these parameters is missing for the EPRoC.

This chapter is structured as follows. First, the materials and methods are described. This includes the samples, experimental configurations, acquisition parameters and post-processing steps. The simulation procedures for both FM and AM spectra are outlined. Second, the results are presented and discussed. In this part, the FM and AM spectra of solid state samples,  $\alpha,\gamma$ -bis(diphenylene)- $\beta$ -phenylallyl (BDPA) and amorphous silicon (a-Si), are shown. These are then used to determine the absolute spin sensitivity. Subsequently, the difference between field- and frequency-swept spectra is discussed and an FDMR experiment is presented. Thereafter, the investigation of solution-state samples,



tempol in water and ethanol, with the EPRoC is discussed. This comprises placement of solutions in capillaries of varying geometry as well as submersing the complete EPRoC in the sample solution. In the last part of this chapter, the saturation behaviour and the effect of varying frequency modulation amplitudes will be discussed. The chapter concludes with a summary and outlook.

## 5.2 MATERIALS AND METHODS

### 5.2.1 *Experiment*

For the experiments in this chapter, all iterations of the EPRoC described in [Chapter 4](#) were used. The experiments on the solid-state samples were performed with the 12-coil EPRoC array placed horizontally between the pole shoes of the electromagnet. Most of the spectra of solution-state samples were recorded with the single-coil EPRoC dipstick, which was vertically inserted. In both configurations,  $B_0$  and the component of  $B_1$  perpendicular to the surface of the EPRoC are orthogonal.

### 5.2.2 *Samples*

In this chapter, all samples described in [Section 4.3](#) were used. Spectral comparisons with X-band EPR were performed with a grain of BDPA, a thin-film a-Si sample as well as tempol dissolved in water and ethanol, respectively.

BDPA with benzene (1:1) in powder form was used as obtained from Sigma Aldrich. The experimental data of BDPA was obtained with the same grain that has been used in [\[131\]](#) and will be described in detail in [Chapter 7](#). The sample handling and volume estimation is described in detail in [Section 4.3.1.1](#). The BDPA sample was placed in coil AM1 of the 12-coil EPRoC array. The sample volume is approximately 0.7 nL with an estimated amount of spins of  $1.0(2) \times 10^{15}$  spins. A  $1 \times 2 \text{ mm}^2$  a-Si sample (cf. [Section 4.3.1.3](#)) was attached to a sample holder and placed such that all coils of the 12-coil EPRoC array were covered with the sample. Samples of tempol in water with varying concentrations ranging from  $10 \mu\text{mol L}^{-1}$  to  $10 \text{ mmol L}^{-1}$  were used described in [Section 4.3.2.1](#).

### 5.2.3 *Acquisition parameters and post-processing*

#### 5.2.3.1 *Solid state samples*

The 12-coil EPRoC array board was used for the investigation of the solid state samples, BDPA and a-Si. The field-swept FM and AM spectra of the BDPA sample used for the comparison with literature values

were recorded at a constant MW frequency,  $f_{\text{MW}} = 13.44$  GHz, and a constant bias current,  $I_{\text{bias}} = 5$  mA. Phase-sensitive detection (PSD) with frequency modulation ( $f_{\text{mod}} = 100$  kHz) and a peak-to-peak modulation amplitude,  $\Delta f_{\text{pp}} = 0.96$  MHz, was used. The time constant,  $\tau_{\text{LIA}}$ , and filter order of the lock-in amplifier (LIA) were 50 ms and  $24 \text{ dB oct}^{-1}$ , respectively. One scan ( $n_{\text{avg}} = 1$ ) was recorded.

The same settings were used for the experiments with varying bias current (cf. Section 5.3.4.3). The modulation amplitude was set to 1.92 MHz to achieve a slightly larger signal-to-noise ratio (SNR). The bias current was varied between 5 and 18 mA.

For the field sweep of the a-Si sample the following parameters were used:  $f_{\text{MW}} = 13.44$  GHz,  $I_{\text{bias}} = 5$  mA,  $n_{\text{avg}} = 1$ ,  $f_{\text{mod}} = 100$  kHz,  $\Delta f_{\text{pp}} = 5.312$  MHz,  $\tau_{\text{LIA}} = 100$  ms ( $24 \text{ dB oct}^{-1}$ ). The same settings were used for the experiments with varying bias currents (cf. Section 5.3.4.3). The range of the bias current was 5 to 24 mA.

For the comparison of the a-Si spectra acquired with the EPRoC to resonator-based EPR, S-, X-, and Q-band data discussed in detail in Section 4.3.1.3 were used.

**X- AND Q-BAND SATURATION** The field-swept continuous wave (CW) X- ( $f_{\text{MW}} = 9.642$  GHz) and Q-band ( $f_{\text{MW}} = 34.28$  GHz) saturation data were acquired with a Bruker ElexSys E580 spectrometer with the ER 4118 X-MD5 ( $C = 0.42 \text{ mT W}^{-0.5}$ ) and the ER 5016 Q-TW resonator ( $C = 0.006 \text{ mT W}^{-0.5}$  [181]), respectively. For both datasets, PSD with field modulation was employed with  $f_{\text{mod}} = 100$  kHz and  $\Delta B_{\text{mod,pp}} = 0.1$  mT. The time constant of the LIA was 29.3 ms and 10.24 ms for X- and Q-band, respectively. In total, 1 average per MW power was recorded for the X-band data, and 8 for the Q-band data.

### 5.2.3.2 Solution samples

Most of the spectra of solution samples were acquired with the single coil EPRoC dipstick board. Each of the following paragraphs corresponds to a section with the same name in the results and discussion section, so that the experimental parameters may easily be assigned.

**FIELD- AND FREQUENCY SWEEPS** For the FM and AM spectra of the  $10 \text{ mmol L}^{-1}$  tempol/ $\text{H}_2\text{O}$  sample the following parameters were used:  $I_{\text{bias}} = 2$  mA,  $n_{\text{avg}} = 5$ ,  $f_{\text{mod}} = 90$  kHz,  $\Delta f_{\text{pp}} = 3.2$  MHz,  $\tau_{\text{LIA}} = 100$  ms ( $24 \text{ dB oct}^{-1}$ ). The resulting experiments are discussed in Section 5.3.2.

**LOW FIELD FREQUENCY-DOMAIN EPROC** For the low-field frequency-domain EPRoC map, 26 FM and AM spectra with a frequency sweep range from 12.8 to 14.4 GHz at varying magnetic field ranging from 460 to 510 mT were recorded. The following acquisition parameters were used:  $I_{\text{bias}} = 2$  mA,  $n_{\text{avg}} = 1$ ,  $\tau_{\text{LIA}} = 100$  ms ( $24 \text{ dB oct}^{-1}$ ),

$f_{\text{mod}} = 91.111 \text{ kHz}$ ,  $\Delta f_{\text{pp}} = 3.2 \text{ MHz}$ . For each spectrum, an off-resonance spectrum at 200 mT was recorded. The discussion of these experiments may be found in [Section 5.3.2.1](#).

**RECTANGULAR CAPILLARIES** The 12-coil EPRoC array was used to obtain the field-swept FM spectra of the  $10 \text{ mmol L}^{-1}$  tempol/ $\text{H}_2\text{O}$  solution in the rectangular capillaries (*VitroCom*). The experimental parameters are as follows:  $f_{\text{MW}} = 13.44 \text{ GHz}$ ,  $I_{\text{bias}} = 5 \text{ mA}$ ,  $n_{\text{avg}} = 1$ ,  $f_{\text{mod}} = 75 \text{ kHz}$ ,  $\Delta f_{\text{pp}} = 3.2 \text{ MHz}$ ,  $\tau_{\text{LIA}} = 200 \text{ ms}$  ( $24 \text{ dB oct}^{-1}$ ). The experiments are discussed in [paragraph 5.3.3.1](#). Three capillaries with different geometries were used for the experiment. The relevant geometry is defined by the wall thickness,  $d_{\text{wall}}$ , the inner height,  $d_{\text{ID}}$ , the inner width,  $d_{\text{width}}$ . The values are as follows: *VitroCom* 5004 ( $d_{\text{wall}} = 28 \text{ }\mu\text{m}$ ,  $d_{\text{ID}} = 40 \text{ }\mu\text{m}$ ,  $d_{\text{width}} = 0.4 \text{ mm}$ ), *VitroCom* 5005 ( $d_{\text{wall}} = 35 \text{ }\mu\text{m}$ ,  $d_{\text{ID}} = 50 \text{ }\mu\text{m}$ ,  $d_{\text{width}} = 0.5 \text{ mm}$ ), *VitroCom* 5015 ( $d_{\text{wall}} = 50 \text{ }\mu\text{m}$ ,  $d_{\text{ID}} = 50 \text{ }\mu\text{m}$ ,  $d_{\text{width}} = 1 \text{ mm}$ ). The length of all capillaries was 50 mm.

**USEFUL CONCENTRATION SENSITIVITY** To determine the concentration sensitivity, a set of tempol/ $\text{H}_2\text{O}$  samples with concentrations of 10, 100 and  $1000 \text{ }\mu\text{mol L}^{-1}$  were used. The acquisition parameters for field and frequency sweeps were the same, as follows:  $I_{\text{bias}} = 2 \text{ mA}$ ,  $\tau_{\text{LIA}} = 100 \text{ ms}$  ( $24 \text{ dB oct}^{-1}$ ),  $f_{\text{mod}} = 90 \text{ kHz}$ ,  $\Delta f_{\text{pp}} = 3.2 \text{ MHz}$ . The number of averages was varied for the different concentrations:  $1 \text{ mmol L}^{-1}$ :  $n_{\text{avg}} = 5$ ;  $100 \text{ }\mu\text{mol L}^{-1}$ :  $n_{\text{avg}} = 25$ ;  $10 \text{ }\mu\text{mol L}^{-1}$ :  $n_{\text{avg}} = 50$ ; The MW frequency for the field sweeps was  $14.336 \text{ GHz}$  and the magnetic field was  $509.3 \text{ mT}$  for the frequency sweeps. For the latter, off-resonant spectra were acquired at a magnetic field of  $400 \text{ mT}$ . The discussion of the experiments may be found in [paragraph 5.3.3.3](#).

**INFLUENCE OF THE DIELECTRIC CONSTANT** The experiments used to investigate the influence of the dielectric constant on the EPRoC signal discussed in [Section 5.3.4.1](#) were performed by Takuma Sato at the Max-Planck-Institut für chemische Energiekonversion with an identically-constructed EPRoC setup with a 12-coil array dipstick board. The frequency-swept FM and AM spectra of the  $1 \text{ mmol L}^{-1}$  tempol /  $\text{H}_2\text{O}$  and of the  $1 \text{ mmol L}^{-1}$  tempol / ethanol solution were acquired with the following acquisition parameters:  $B_0 = 500 \text{ mT}$  on resonance  $n_{\text{avg}} = 50$ ,  $f_{\text{mod}} = 90 \text{ kHz}$ ,  $\Delta f_{\text{pp}} = 3.2 \text{ MHz}$ ,  $\tau_{\text{LIA}} = 10 \text{ ms}$  ( $24 \text{ dB oct}^{-1}$ ). The off-resonance field was  $100 \text{ mT}$ . This board uses a single current source for all voltage-controlled oscillators (VCOs), which was set to  $15 \text{ mA}$ . This results in  $15 \text{ mA}/12 = 1.25 \text{ mA}$  of bias current per coil.

The X-band data of the tempol /  $\text{H}_2\text{O}$  and tempol/ethanol solutions were acquired with a Magnettech MS5000 spectrometer. In total, 4 averages were recorded for each spectrum with field modulation

( $f_{\text{mod}} = 100 \text{ kHz}$ ,  $\Delta f_{\text{mod}} = 0.01 \text{ mT}$ ). The sweep time per average was 60 s. For both samples, the MW frequency was 9.45 GHz.

**INFLUENCE OF THE FREQUENCY MODULATION AMPLITUDE** A 10 mmol L<sup>-1</sup> tempol/H<sub>2</sub>O sample was used for these experiments. Field-swept FM spectra were obtained at different frequency modulation amplitudes at a fixed MW frequency of 14.34 GHz. One spectrum per modulation amplitude was recorded with a modulation frequency of 90 kHz. The LIA filter time constant was 100 ms (24 dB oct<sup>-1</sup>).

### 5.2.3.3 Post processing

All shown spectra apart from the resonator-based EPR spectra are filtered with a 2<sup>nd</sup> order *Savitzky-Golay* filter with a filter width chosen such that the spectrum was not broadened by the filtering procedure.

### 5.2.4 Spectral simulations

The spectral simulations are described in the following. For least-square fitting of the simulations of the experimental data, the unfiltered spectra were used.

#### 5.2.4.1 Powder spectra

For spectral simulations, the *EasySpin* software package (version 6.0.0-dev.53) was used [70]. The function *pepper* was used for the simulations of the BDPA and a-Si FM spectra. The asymmetry of the AM spectra was accounted for with a special simulation function based in *pepper*, which returns a mixture of absorption and dispersion spectra based on Equation 3.21b such that the resulting spectrum was calculated by  $\chi'' - Q_{\text{coil}}\chi'$ . The parameters of the simulations were adapted by least-square fitting of the simulation to the experimental data. The total spin of both samples is 1/2. For the simulations, the scalar *g*-value of BDPA and a-Si was taken from literature and may be found in Sections 4.3.1.1 and 4.3.1.3, respectively. To account for possible offsets of the magnetic field, a field offset parameter is used. Convolutional *Lorentzian* and pseudo-*Voigtian*, i.e., *Gaussian* and *Lorentzian*, broadening was assumed for BDPA and a-Si, respectively. For the FM spectrum, a dispersion spectrum is simulated by setting the MW phase (*mwPhase*) in the simulation to  $\pi/2$ . The fit parameters for the FM spectra are the convolutional broadening(s) and the field offset, while for the AM spectra  $Q_{\text{coil}}$  was varied, too, in addition to the aforementioned fit parameters.

For the extraction of the peak-to-peak linewidth as well as the calculation of the double integral (DI) in Section 5.3.4.3, only *Lorentzian* broadening was assumed.

#### 5.2.4.2 Fast-motion spectra

The function *garlic* of *EasySpin* is used for the simulation of the tempol solutions discussed in Section 5.3.4.1. This function may be used for radicals in solution with small hyperfine interaction (HFI). This is the case for the tempol solutions. The function calculates the resonance fields/frequencies (stick spectrum) using the Breit-Rabi equation for  $S = 1/2$  with an arbitrary nuclear spin [182]. Tempol in solution in the isotropic limit is best described by a spin-1/2 system isotropic  $g$ -value of 2.0059 [173] with a nitrogen nucleus  $I = 1$ , with isotropic HFI,  $A_{\text{iso}}$ . Similar as for the solid state samples, convolutional pseudo-Voigtian broadening is applied. As before, the MW phase was set to  $\pi/2$  for the simulation of the FM data. Due to relatively symmetric spectra about the resonance fields/frequencies, the AM data was simulated as an absorption spectrum. The parameters that were varied in the least-square fit of the simulation to the experiment were the isotropic HFI, the *Gaussian* and *Lorentzian* broadening as well as a field offset. The EPR absorption spectrum was simulated in the same way as the AM spectrum.

#### 5.2.5 Extraction of EPR data from literature

In the course of this chapter, spectral simulations of EPR spectra presented in literature are performed. To perform the simulations, the spectra are digitised using the free software *WebPlotDigitizer* [183]. This software allows to (manually) extract the numerical data from a variety of plot types, including EPR spectra. The  $x$ -axis of the extracted data is usually non-linearly spaced, so that an interpolation of the data is required to perform the spectral simulations.

### 5.3 RESULTS AND DISCUSSION

#### 5.3.1 Investigation of solid state samples

The spectral comparison is performed with two powder samples: BDPA and a thin-film a-Si sample both of which are described in detail in Sections 4.3.1.1 and 4.3.1.3.

##### 5.3.1.1 $\alpha,\gamma$ -bis(diphenylene)- $\beta$ -phenylallyl (BDPA)

Figure 5.1 shows first-derivative dispersion-like FM (top) and absorption-like AM spectra (bottom) of a grain of BDPA placed in coil AM1 with respective spectral simulations performed with *EasySpin* [70]. A slight asymmetry is observed in the FM spectrum, while resonator-based EPR spectra of BDPA in powder form do not exhibit an asymmetry. A similar asymmetry, however, is observed in all VCO-based FM

spectra recorded over the years [51, 52, 55, 61, 184–186].<sup>1</sup> According to the analytical solution of Equation 3.18, the FM signal should be symmetric for a spin-1/2 system. The analytical solution, however, lacks the consideration of the bi-directionality of VCO and spin system. In addition, it is derived assuming a non-saturated sample. Hence, this may lead to an asymmetric spectrum. Further data about the asymmetry of FM spectra is given in Section 5.3.4.3.

The AM spectrum of the BDPA sample is shown in Figure 5.1 bottom. As expected from Equation 3.20, this spectrum is asymmetric due to a dispersive component [133] in addition to the (main) absorptive lineshape.

Both BDPA spectra were simulated using the *EasySpin* software package [70], assuming a spin-1/2 system with an isotropic  $g$ -value of 2.003 obtained from literature [150]. Convolutional *Lorentzian* broadening was applied in the simulation. Its peak-to-peak linewidth<sup>2</sup> was determined through least-square fitting of the experimental spectra as described earlier in Section 5.2.4. While the peak-to-peak linewidth is the only fit parameter for the simulation of the FM spectrum, the AM spectrum was simulated with an additional asymmetry parameter, that is  $Q_{\text{coil}}$ . The *Lorentzian* peak-to-peak linewidth of both FM and AM spectra is  $\sim 0.096$  mT. For the AM spectrum  $Q_{\text{coil}} = 1.4$ . This value is much smaller than simulated values for other EPRoC designs.

For direct spectral comparison with a resonator-based EPR spectrometer, an experiment with the same grain of BDPA or of a similar BDPA sample is necessary. However, the former is not possible due to the small grain size which does not allow retrieval of the sample once it is placed on the EPRoC. In addition, in a previous study [157], an intra-grain distribution of  $T_2$  for BDPA grains with dimensions of a few 100  $\mu\text{m}$  from one batch was reported. Hence, using a different grain of BDPA could lead to false interpretations due to different linewidths. The reported  $T_2$  ranged from 80 to 160 ns in X-band. Assuming the linewidth of BDPA to be only determined by relaxation, it may be calculated using Equation 2.37. The calculated linewidths in X-band are within the range of 0.04 to 0.08 mT. This is about 60 to 20 % smaller than that observed in the experimental BDPA data. Several factors may contribute to the observed broadening, including inhomogeneity of the static magnetic field, MW frequency-dependent mechanisms such as disorder-induced  $g$ -strain and saturation effects.

An inhomogeneous static magnetic field could cause a broadening of the spectra of the solid-state samples. Typically, the homogeneity of the commonly used (large) electromagnets is of the order of  $1 \times 10^{-5}$  in

<sup>1</sup> An internal report from Bruker of the EPRoC project states that the asymmetry of the FM signal may be correlated with the sample size.

<sup>2</sup> Please note that the linewidths presented in this work always correspond to the peak-to-peak linewidths of a first-derivative EPR absorption spectrum, adhering to the conventional practice in the EPR community. Therefore, these linewidths cannot be directly read off the displayed spectra.



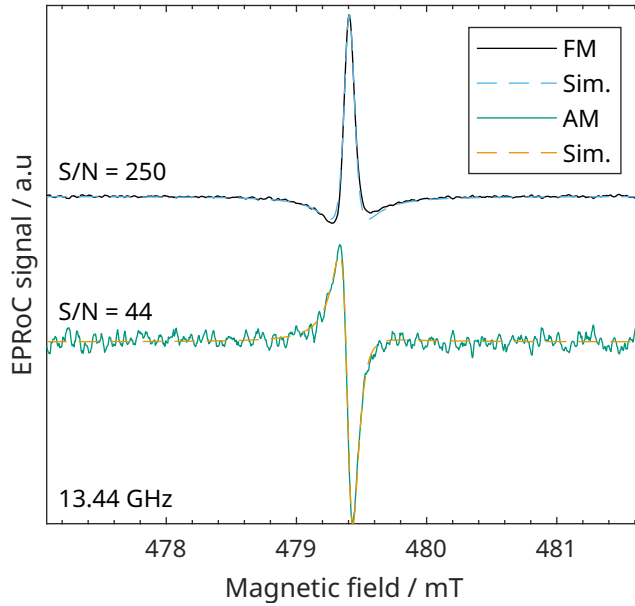


Figure 5.1: Field-swept EPRoC spectra of a grain of BDPA (sample volume:  $\sim 0.7(2)$  nL; mass:  $0.8(2)$   $\mu$ g; number of spins:  $1.0(2) \times 10^{15}$  spins) with spectral simulations. **Top:** FM signal. **Bottom:** AM signal. The central MW frequency of 13.44 GHz is indicated.

a spherical volume of  $1 \text{ cm}^3$  [82] if there is no ferromagnetic material in the vicinity of the pole shoes. This results in an absolute deviation of the magnetic field of  $\sim 0.005$  mT for the MW frequencies and magnetic fields used for the EPRoC. Because the sample volumes of the BDPA grain is much smaller ( $1 \times 10^7$ ) than the specified volume for the homogeneity, it is expected that the homogeneity within the sample is even smaller than the value mentioned above. However, ferromagnetic parts of the holder and PCB could cause some  $B_0$  inhomogeneity. The holder was built from commercially-available optomechanical parts from *Thorlabs*, which were tested to be non-magnetic. The PCB is most likely manufactured from FR4 material with conducting paths, which is also expected to be non-magnetic. Therefore, an inhomogeneity of the static magnetic field is unlikely to be the main cause of the observed broadening. In addition, the broadening caused from inhomogeneities of the magnetic field would result in a *Gaussian* distribution, which is not seen for the BDPA sample, which is best simulated with *Lorentzian* broadening only. Similarly, frequency-dependent broadening such as *g*-strain would usually also result in *Gaussian* broadening. In addition, as spectra of BDPA obtained at Q-band do not exhibit any major broadening compared to X-band, the latter is unlikely to be a contribution to the broadening.

Saturation could be a contributing factor, particularly given the relatively large and inhomogeneous  $B_1$  values expected for microoscillator-based EPR. The inhomogeneity of  $B_1$  inherent for microcoils does not lead to lineshape broadening in CW spectra but merely changes the sig-

nal amplitude/intensity if the sample is unsaturated at each point in space. EPR spectra obtained by the saturation transfer technique, however, may suffer from lineshape distortions [187]. Yet, if portions of the sample within the sensitive volume experience saturation, lineshape broadening is very well possible as the total EPR signal is the volume integral over the sample in the sensitive volume. The distribution of  $B_1$  of the 12-coil EPRoC array will be discussed in detail in Chapter 6. To a first approximation, the  $B_1$  in the centre of the coil generated perpendicular to the surface of the EPRoC may be estimated by means of *Biot-Savart's* law for a circular inductor loop with a radius,  $R$ , equal to that of the coils, 100  $\mu\text{m}$ . The current in the loop,  $I_{\text{coil}}$ , may be calculated from the bias current,  $I_{\text{bias}}$ , using the square-root law proposed in [131] and described in detail in Section 7.3.2. In this case,  $B_1$  is given by

$$B_1 = \frac{1}{2}\mu_0 \frac{a + b\sqrt{I_{\text{bias}}}}{2R}, \quad (5.1)$$

for which  $a$  and  $b$  are empirical constants of the square-root law. The additional factor  $1/2$  in the equation takes into account that only half the magnitude of the MW is available for EPR excitation due to the two counter-rotating MW fields in the rotating frame. Using a bias current of 5 mA,  $B_1 \approx 27 \mu\text{T}$  in the centre of the coil at its surface.  $B_1$  increases towards the traces of the coil, yet, already at  $27 \mu\text{T}$ , it is plausible that the sample experiences saturation when possessing a  $T_1$  value of 110 ns from ref. [156] and  $T_2$  in the range mentioned earlier. This could lead to saturation-induced broadening, which could explain the increased peak-to-peak linewidth compared to X-band.

The SNR of both spectra is calculated as the ratio of the peak-to-peak amplitude and the standard deviation (STD) of the baseline regions of the spectrum. For the FM spectrum the SNR is 250 which is approximately  $5 \times$  larger than that of the AM spectrum of 44. Although, FM and AM signal should in theory exhibit the same spin sensitivity [133], the AM signal is detected using an intrinsic demodulator with poor noise characteristics as discussed in [131] and [133], which may lead to a degradation of the SNR of the AM spectrum.

### 5.3.1.2 Amorphous silicon

As the results obtained with a BDPA sample are not easily comparable to resonator-based EPR spectra, a thin-film a-Si sample will be discussed in the following. Furthermore, the mean relaxation time of this sample is shorter than that of BDPA by approximately a factor of  $\sim 2$  using the values provided in Section 4.3.1.3 for the a-Si and literature values for BDPA stated in Section 4.3.1.1. Therefore, if the BDPA sample was saturated as discussed, the a-Si sample may be unsaturated or at least less strongly saturated. The sample is a 15  $\mu\text{m}$ -thick film of a-Si on



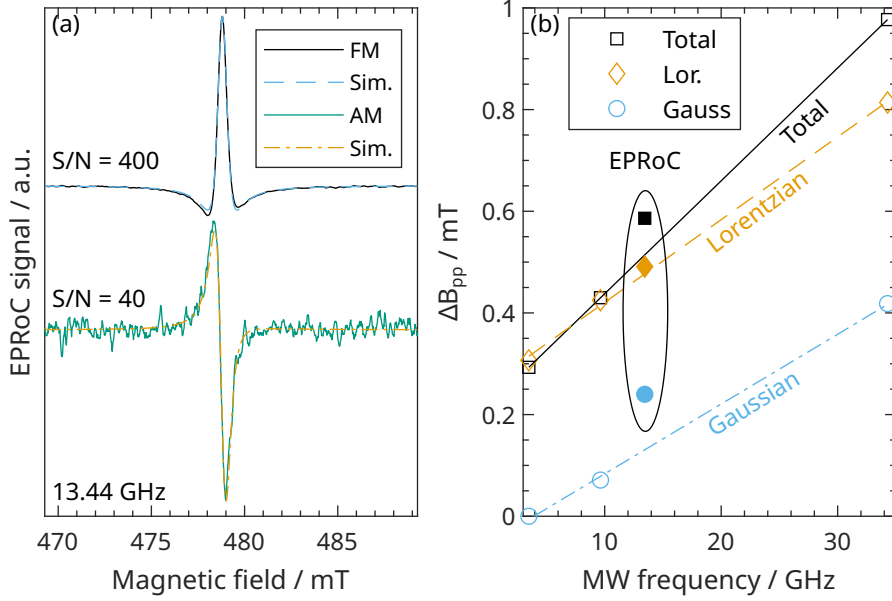


Figure 5.2: **(a)** Field-swept EPRoC spectra of the a-Si sample with spectral simulations. Top: FM signal. Bottom: AM signal. **(b)** Peak-to-peak linewidth,  $\Delta B_{pp}$ , of the a-Si sample as a function of MW frequency as obtained from the experimental spectra (total), *Lorentzian* (Lor.) and *Gaussian* (Gauss) contribution to the linewidth obtained from simulations of the EPR absorption spectra at S-, X- and Q-band and of the FM spectrum at K<sub>u</sub>-band. The open symbols represent the data obtained with a resonator-based EPR spectrometer, while the filled symbols represent the data obtained with the EPRoC. Linear fits of the resonator-based EPR data are shown as solid, dashed and dash-dotted lines for the total, *Lorentzian* and *Gaussian* linewidth, respectively.

Quartz glass with spatial dimensions of  $2 \times 1 \text{ mm}^2$ , i.e., all 12 coils can be covered with the sample.

Figure 5.2 (a) shows the first-derivative dispersion-like FM (top) and absorption-like AM spectra (bottom) of an a-Si sample at 13.44 GHz. Similar to the FM spectrum of the BDPA sample, the FM spectrum exhibits a slight asymmetry compared to EPR absorption spectra at S-, X- and Q-band shown in Figure 4.3 and discussed in Section 4.3.1.3, which exhibit no asymmetry.

Similarly, the AM spectrum is asymmetric due to a dispersive component [133] as expected from Equation 3.20. Both spectra were simulated using the *EasySpin* software package [70] assuming a spin-1/2 system with a  $g$ -value of 2.0055 [166] with convolutional *Gaussian* and *Lorentzian* broadening with a similar procedure as discussed in Section 5.3.1.1. For a comparison with linewidth values obtained with resonator-based EPR, the experimental peak-to-peak linewidths of absorption spectra and the respective *Gaussian* and *Lorentzian* contribution for S-, X- and Q-band obtained from simulations of the corresponding spectra (cf. Section 4.3.1.3) are displayed in Figure 5.2

(b), together with linear fits of the resonator-based EPR linewidths. At S- ( $\sim 3.5$  GHz) and X-band (9.6 GHz), the sample exhibits mainly a *Lorentzian* lineshape as expected from literature [166]. At Q-band (34.3 GHz), a mixture of *Gaussian* and *Lorentzian* is seen, most likely due to *g*-strain [8]. Assuming a linear increase of the peak-to-peak linewidth of the sample from S-band to Q-band, the projected linewidths at 13.44 GHz would be 0.52 mT, 0.13 mT and 0.48 mT for the total experimental peak-to-peak linewidth, the *Gaussian* and the *Lorentzian* contribution, respectively. The linewidths obtained from the simulation of the EPRoC signals are 0.59 mT, 0.21 mT and 0.50 mT for the total peak-to-peak linewidth, the *Gaussian* and the *Lorentzian* contribution, respectively (cf. Figure 5.2 (b)). This corresponds to a  $\sim 13\%$  broadening in the spectrum recorded with the EPRoC compared to the that recorded with resonator-based EPR. The broadening can mainly be attributed to the *Gaussian* contribution as it is about 62% larger than expected from the linear fit, while the *Lorentzian* contribution fits well to the linear fit. The *Gaussian* broadening may partly be explained by saturation broadening of the sample at the sample positions close the trace of the coils, where the  $B_1$  magnitude is much larger than in the centre of the coil. In addition, the asymmetry of both FM and AM spectrum may also introduce complications in the fitting routine used, resulting in an increased amount of perceived broadening due to discrepancies between the fit and the experimental data. Possibly, the assumption of a linear increase of the linewidth may be invalid since only three points, two of which lie relative closely (S- and X-band). Yet, obtaining EPR data in the range between X- and Q-band, e.g., at  $K_u$  (14 GHz) or K-band (24 GHz) was not possible due to a lack of access to K-band spectrometers. Dietmar Stehlik's K-band spectrometer at Freie Universität Berlin described in ref. [188] was disassembled years ago. Also, Carlos Graeff's K-band spectrometer at Universidade Estadual Paulista "Júlio de Mesquita Filho" [189] was not available in time for this dissertation. A home-built  $K_u$ -band spectrometer at 14 GHz with a cavity resonator was described in refs. [101, 107].

The SNR of the AM spectrum of 40 is  $10 \times$  lower than that of the FM signal (400), which may be explained as follows. First, the AM spectrum was recorded only in one coil (AM1), while the FM signal detects all 12 coils of the EPRoC array taking advantage of the noise improvement of the injection-locking (cf. Section 3.4). Second, the AM signal is detected using an intrinsic demodulator with poor noise characteristics as mentioned above. The ratio of the SNRs (FM/AM) of the a-Si sample is approximately twice as large as that of the BDPA sample, which may be explained by the fact that the BDPA sample was present in coil AM1 only.

### 5.3.1.3 Absolute spin sensitivity determined with powder samples

From the previously shown EPRoC spectra of BDPA and a-Si, the spin sensitivity may be determined from the number of spins in the samples, the SNR of the spectra and the equivalent noise bandwidth (ENBW) of the experiment as explained in Section 2.4.3. The latter may be calculated from the time constant and roll-off of the LIA. The volume of the BDPA sample placed in coil AM1 was 700 pL resulting in spin sensitivities of approximately  $5 \times 10^{12}$  and  $3 \times 10^{13}$  spins  $G^{-1} Hz^{-0.5}$  for FM and AM signal, respectively. This was determined with a field sweep. The value for the AM sensitivity is similar within the error margin to the value determined with a frequency sweep of the same sample in ref. [131] (cf. Section 7.3.1). In the reference, the AM spin sensitivity is compared to the FM sensitivity of this EPRoC, determined at Universität Stuttgart (USTUTT) with a (likely) much smaller<sup>3</sup> DPPH sample compared to the BDPA sample that was used for determining the AM sensitivity. The stated value of the FM sensitivity is  $5 \times 10^9$  spins  $G^{-1} Hz^{-0.5}$ , showing approximately a four order of magnitude worse AM sensitivity than FM sensitivity. The discrepancy of the AM and FM spin sensitivities was explained by a lower FM noise floor of  $\sqrt{12} \approx 3.5$  as well as by the sensitivity and the degradation of the noise floor of the implicit AM demodulator of around 1/6 and approximately 20 dB, respectively, obtained from simulations in [133]. In total, a 210-fold degradation of the AM sensitivity compared to the FM sensitivity was found.

This is in contrast to the sensitivity determined with the FM spectrum of the same BDPA sample of  $5 \times 10^{12}$  spins  $G^{-1} Hz^{-0.5}$ . For comparison with previous publications utilising single-coil EPRoC sensors, this number needs to be corrected to account for the injection-locking of the EPRoC array. In ref. [61, Figure 3 left], it was shown that an EPRoC array with a certain number of spins in each coil,  $n_{\text{spin}}$ , and a single-coil EPRoC with the same number of spins,  $n_{\text{spin}}$ , exhibit the same signal amplitude. As the sample was placed in only one coil of the 12 VCOs in the experiment, the signal amplitude of the FM signal is lowered by approximately 1/12 compared to a sample that is evenly distributed over all coils as discussed in Sections 3.4 and 6.3.3. In addition, the noise floor of the EPRoC array is expected to be lower than that of a single-coil EPRoC by approximately  $\sqrt{12}$  due to the injection locking. Hence, the correction factor for the FM spin sensitivity is  $1/\sqrt{12}$ . Therefore, the corrected FM spin sensitivity determined with the BDPA sample is then given by  $2 \times 10^{12}$  spins  $G^{-1} Hz^{-0.5}$ .

For the a-Si sample, the spin sensitivities are  $3 \times 10^{10}$  and  $3 \times 10^{11}$  spins  $G^{-1} Hz^{-0.5}$  for FM and AM, respectively. The sample volume of the a-Si within the sensitive volume of the EPRoC was calculated to be  $\sim 2700$  pL. The sensitive volume was calculated from the sensitive

<sup>3</sup> Speculated is 2 orders of magnitude with a 2,2-diphenyl-1-picrylhydrazyl (DPPH) sample placed in the centre of one of the coils.

area determined with the  $B_1$  mapping of [Section 6.3.1](#) and the film thickness of  $15\ \mu\text{m}$  from the sample. In summary, the ratios of the FM and AM sensitivities for both the BDPA and the a-Si sample are approximately one order of magnitude. This is much smaller than the four orders of magnitude discussed in ref. [\[131\]](#).

In ref. [\[133\]](#), an AM spin sensitivity<sup>4</sup> of  $9 \times 10^{10}$  spins  $\text{Hz}^{-0.5}$  was determined from a field-swept spectrum with frequency modulation with  $f_{\text{mod}} = 10$  kHz. For this, a 14 pL DPPH sample with  $\sim 2.8 \times 10^{13}$  spins was used. The experiment was using a single-coil EPRoC configuration ( $d_{\text{coil}} = 300\ \mu\text{m}$ ) presented in ref. [\[55\]](#). The experimentally determined value was compared to the theoretically predicted value of  $N_{\text{min}} = 2 \times 10^8$  spins  $\text{G}^{-1} \text{Hz}^{-0.5}$  (cf. [Section 3.3](#)), showing a difference in the AM sensitivities of experiment and theory of almost 3 orders of magnitude. This difference is explained by suboptimal  $B_1$  in the experiment in addition to the sensitivity and increased noise floor of the AM demodulator obtained from simulations, in total accounting for most of the difference. Furthermore, in ref. [\[190\]](#), an FM spin sensitivity  $2 \times 10^{10}$  spins  $\text{G}^{-1} \text{Hz}^{-0.5}$  was determined with a similarly-sized DPPH sample (5.4 pL) with the same generation of single-coil EPRoC as in refs. [\[55, 133\]](#). In [\[55\]](#), the FM spin sensitivity was determined with a BDPA sample (frequency sweep) without further information about the sample size and experimental parameters to be  $4 \times 10^9$  spins  $\text{Hz}^{-0.5}$ .

[Table 5.1](#) summarises the many spin sensitivity values from above, which range from about  $5 \times 10^9$  to  $2 \times 10^{13}$  spins  $\text{G}^{-1} \text{Hz}^{-0.5}$  for both FM and AM signal.

In the following, possible reasons for the discrepancy of the determined spin sensitivities are explained. As BDPA and DPPH in powder form exhibit similar relaxation times of the order of 40 to 160 ns [\[156, 157, 191\]](#), their saturation behaviour is similar. Hence, this could only contribute a small effect to the determination of the spin sensitivity for samples of the same size. The linewidth of DPPH, however, is approximately twice as large as that of BDPA, so that the signal amplitude of the latter is about twice as large as for the former. The main difference, however, is the volume of the samples used to determine the spin sensitivity. This differs by a factor of  $\sim 48$  with the sample volume of the BDPA sample used here being  $\sim 0.7$  nL ( $\sim 700$  pL) and the DPPH sample  $\sim 14$  pL used in ref. [\[133\]](#). Due to the different spin densities of BDPA and DPPH (cf. [Section 4.3.1.1](#) and [Section 4.3.1.2](#)), the number of spins in the samples differ by a factor of  $\sim 67$ . As the estimation of the sample volume from photographs is considerably inaccurate, the sample volumes have relative errors of approximately 82 % (cf. [paragraph 4.3.1.1](#)). In combination with uncertainties of the densities of the sample and of the spin density, the relative error for the number

<sup>4</sup> In the references, the spin sensitivity is not always normalised to a linewidth of 1 G. The samples used for the determination of the sensitivity are always BDPA or DPPH with linewidths of up to 2 G. Hence, the determined sensitivities do not change drastically and stay within the same order of magnitude even after normalisation.

Table 5.1: Experimentally-determined spin sensitivities of different iterations of the EPRoC. The reference (Ref.), the sample used, the sample volume ( $V_s$ ), the spin sensitivity of the FM and AM signal are provided. N/A indicates that the sensitivity was not determined or published.

Ref.	Sample	$V_s$ pL	FM sens. spins $G^{-1} Hz^{-0.5}$	AM sens.
[133]	DPPH	14	N/A	$9 \times 10^{10}$
[61]	DPPH	4	$8 \times 10^9$	N/A
[190]	DPPH	5	$2 \times 10^{10}$	N/A
[131] <sup>1</sup>	*	*	$5 \times 10^9$	N/A
[131] <sup>2</sup>	BDPA	700	N/A	$2 \times 10^{13}$
PhD	BDPA	700	$2 \times 10^{12}$	$3 \times 10^{13}$
PhD	a-Si	2800	$3 \times 10^{10}$	$3 \times 10^{11}$

<sup>1</sup>Determined at USTUTT

<sup>2</sup>Determined at HZB

\*Unspecified

of spins is 84 %, so that the total error of the ratio of the number of spins is 118 %.

Owing to the comparably large sample size of the grain of BDPA used here, the  $B_1$  experienced by the sample, especially close to the trace of the coil, is much larger than that in the centre as discussed in Section 6.3.1.1. At the positions close the trace, the sample may be strongly saturated, and the signal amplitude is much smaller than anticipated as seen in Section 6.3.1.2 and Section 6.3.1.3. This may have led to an overestimation of the number of spins that are actually sensed by the EPRoC based on the sample volume alone in ref. [131]. Instead, the sample geometry and  $B_1$  distribution of the EPRoC need to be taken into consideration. To test this hypothesis, the spin density determination could be performed with differently-sized particles. These experiments, however, would be rather tedious.

For a more precise estimation of the sample volume, single crystals of DPPH grown from a diethyl ether solution may be used [192]. In this case, the DPPH single crystal grows in a needle-shape. Hence, needles with varying lengths may be used to determine the spin sensitivity. Such samples have actually been used for experiments with the EPRoC in ref. [184] and [193].

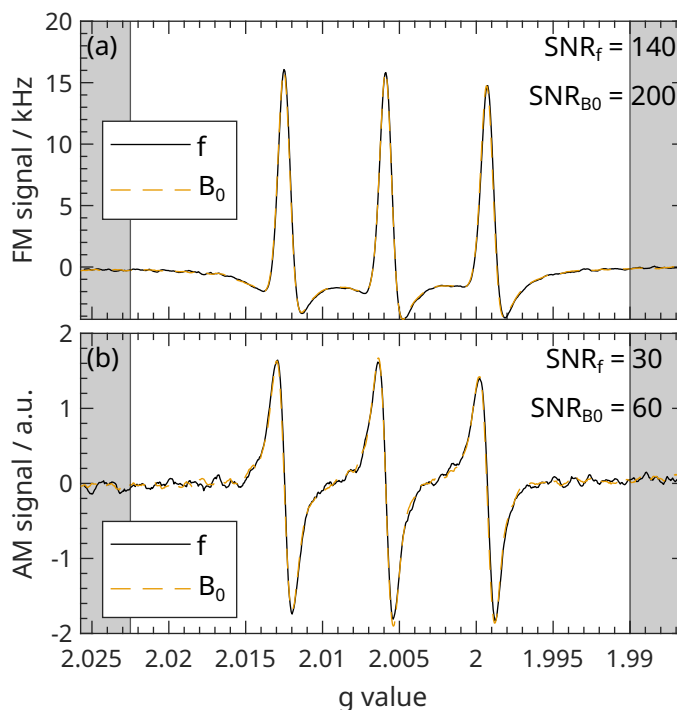


Figure 5.3: Field- (dashed, denoted with  $B_0$ ) and frequency-swept (solid, denoted with  $f$ ) EPRoC spectra of a  $10 \text{ mmol L}^{-1}$  tempol/ $\text{H}_2\text{O}$  solution obtained with the single-coil EPRoC dipstick board at a fixed MW frequency of  $14.34 \text{ GHz}$  and fixed  $B_0$  of  $509.25 \text{ mT}$ , respectively. **(a)** FM signal. **(b)** AM signal. The noise level used for equating the SNR is calculated from the baseline regions of the spectra, which are indicated by a grey shading.

### 5.3.2 Field and frequency sweeps

In this section, we will slightly jump ahead and discuss data of a  $10 \text{ mmol L}^{-1}$  tempol/ $\text{H}_2\text{O}$  solution obtained with an EPRoC dipstick board, which will be discussed later in [Section 5.3.3.2](#). For this discussion, however, the aggregate phase does not matter. Instead, the wider three-line spectrum of the sample compared to the previous samples allows for more insight in the EPRoC technology. Field and frequency sweeps are fundamentally different due to the field-dependent *Boltzmann* factor. This factor is constant throughout a frequency sweep, while it changes during the field sweep as it is linearly proportional to the  $B_0$  in the high-temperature approximation. The change over the width of a field sweep is, however, negligible and is only relevant for experiments acquired in different MW bands. To investigate difference of both field and frequency sweeps, two spectra of a  $10 \text{ mmol L}^{-1}$  tempol/ $\text{H}_2\text{O}$  solution were obtained with a field and a frequency sweep, respectively. The data were acquired with the same experimental settings. Especially, the field and frequency step size was chosen such they were equal. To this end, the frequency step size of  $419.2 \text{ kHz}$  was calculated from the field step of  $0.015 \text{ mT}$  using the resonance



condition from Equation 2.8. To obtain the frequency-swept spectra shown in Figure 5.3, an off-resonant spectrum ( $B_0 = 400$  mT) was subtracted from the on-resonant spectrum ( $B_0 = 509.25$  mT) as explained in Section 4.2.2 for both FM (a) and AM (b) signal. In addition, the FM spectrum needs to be corrected due to the non-linear behaviour of the MW frequency of the EPRoC on the tuning voltage as explained in Section 4.2.2. For the correction, a calibration curve as shown in Figure 4.2 was used.

In Figure 5.3 FM (a) and AM (b) spectra are displayed exhibiting, a three-line spectrum originating from the hyperfine interaction of the Nitrogen atom with  $I = 1$  with the electron spin of  $S = 1/2$  in the fast-motion limit, where the anisotropic terms in the spin Hamiltonian interactions of the sample are averaged out due to the fast motion of the spin species. Both spectra perfectly overlap. As observed before, the SNR of the FM signal is always larger than that of the AM signal. In addition, the SNR of the frequency sweep is lower than that of the field sweep of the same signal.

#### 5.3.2.1 Low-field frequency-domain EPRoC

In the following, we will extend the field and frequency sweep capabilities of the EPRoC to obtain FDMR / frequency-domain EPR maps as it is commonly done at specialised high-field / multi-high-frequency EPR experimental configurations such as described in refs. [194, 195]. The benefit of these FDMR maps is that they make the energy level diagram of the spin system under investigation directly discernible and allows for investigation of samples such as single-molecule-magnets with large zero-field splitting [196]. It is only possible to obtain such a map since these experimental configurations work without an MW resonator enabling frequency sweeps in addition to field sweeps. At frequencies up to Q-band, high-Q resonators are commonly used to record EPR spectra such that it is impossible to obtain FDMR maps due to the low bandwidth of these resonators. With the EPRoC, this limitation does not exist, and it is possible to record such a map at low field. Figure 5.4 shows a proof-of-principle FDMR map obtained at 14 GHz with a 10 mmol L<sup>-1</sup> tempol/H<sub>2</sub>O solution. The map was obtained from 26 frequency sweeps with 5001 points. As expected, three transitions are visible in this map originating from the hyperfine interaction of the Nitrogen atom with  $I = 1$  with the electron spin of  $S = 1/2$  with a linear increase of the Zeeman splitting by the magnetic field,  $B_0$ . The transitions are indicated by dash-dotted lines in the plot. The FDMR map of the FM signal shows an increase of the noise floor at frequencies above  $\sim 14.2$  GHz, which arise from the upper limit of the lock-range of the phase-locked loop (PLL) as explained in Section 4.2.2, where it is not as stable as for lower MW frequencies. The AM FDMR map shown in Figure 5.4 (b) is not affected by this instability and does not exhibit an increase in the noise floor towards higher MW frequen-

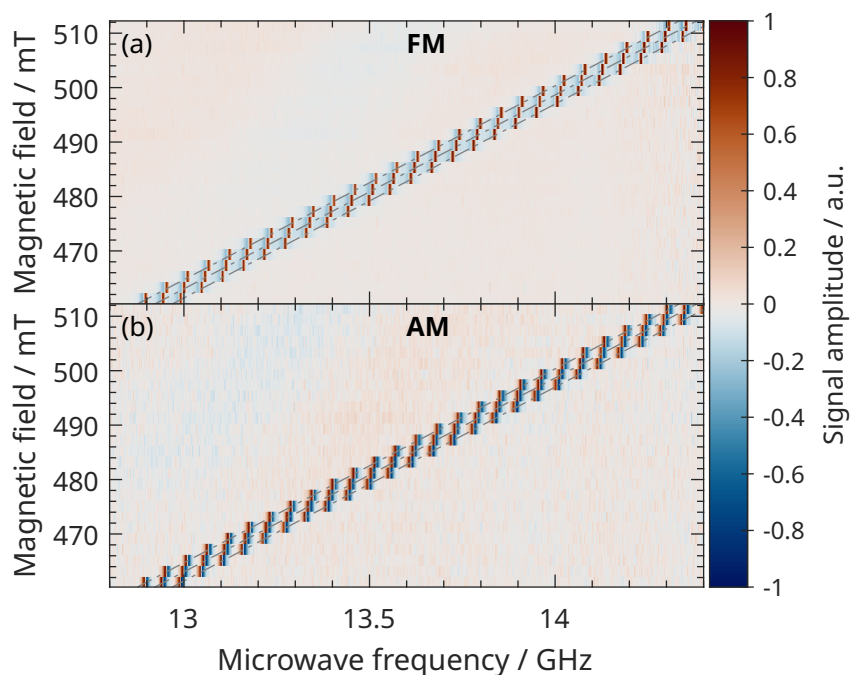


Figure 5.4: 1.6 GHz wide frequency-domain magnetic resonance (FDMR) map of a  $10 \text{ mmol L}^{-1}$  tempol/ $\text{H}_2\text{O}$  solution obtained with the single-coil EPRoC dipstick board. **(a)** FM signal. **(b)** AM signal. The dash-dotted lines show the transitions calculated from the spin system.

cies. However, the AM data are in general more noisy compared to the FM data possibly due to the utilised intrinsic demodulator for the AM signal of the EPRoC [131, 133]. Please note, that this proof-of-principle experiment does not allow to show the potential of such FDMR maps due to the relatively simple spin system.

### 5.3.3 Investigation of paramagnetic species in solution

In the following section, different options to investigate paramagnetic species in solution, their sensitivities and the sample handling will be discussed. First, solutions in round and rectangular capillaries are revisited, which resembles the standard sample handling of resonator-based EPR, where the sample is put in the spectrometer. Second, we will discuss the inverse option, where the EPRoC is submersed in the solution – the EPRoC dipstick – with three different iterations. To comply with previous experiments in literature, the experiments and sensitivity analyses shown in this section were performed with solutions of tempol in  $\text{H}_2\text{O}$ .



### 5.3.3.1 Solutions in capillaries

**ROUND CAPILLARIES** The straight-forward way to investigate solution state samples with the EPRoC is the usage of round capillaries in which the sample solution is placed. Such round capillaries are commonly used in commercial EPR spectrometers with different diameters dependent on the MW frequency and desired sample volume. The capillary may be placed such that the wall of the capillary is parallel to the surface of the EPRoC. As the round capillary wall does not fit well to the planar surface of the EPRoC, the capillary needs to be attached by means of a holder or glue.

In ref. [126], tempol / H<sub>2</sub>O solutions with concentrations of 10, 3 and 1 mmol L<sup>-1</sup> were investigated in plastic capillaries (inner diameter (ID): 150 μm; outer diameter (OD): 162 μm) at about 26 GHz. However, the concentration sensitivity was not calculated in this work. In ref. [190], experimental data of a 10 mmol L<sup>-1</sup> tempol/H<sub>2</sub>O solution in a round capillary (ID: 500 μm, wall thickness: ~100 μm) on a single-coil EPRoC at 14 GHz is discussed. Revisiting the data shown in [190], the concentration sensitivity may be calculated from the concentration of the sample, the SNR of the spectra and the ENBW of the experiment as explained in Section 2.4.3. For the data shown in ref. [190], a concentration sensitivity of the FM signal of about 530 μmol L<sup>-1</sup> G<sup>-1</sup> Hz<sup>-0.5</sup> was found. The usage of an 8-coil EPRoC array at 14 GHz improves the concentration sensitivity to about ~30 μmol L<sup>-1</sup> G<sup>-1</sup> Hz<sup>-0.5</sup> (calculated from 200 μmol L<sup>-1</sup> Hz<sup>-0.5</sup> with the linewidth normalised to 3 × ~0.2 mT), which was determined with a 5 mmol L<sup>-1</sup> tempol/H<sub>2</sub>O solution [61].

**RECTANGULAR CAPILLARIES** A simpler sample alignment may be achieved by using open-ended rectangular capillaries. In the following experimental data tempol solutions in such capillaries from *VitroCom* with different geometries is presented. The geometry and its relevant parameters are shown in Figure 5.5 (a). The capillaries differ in wall thickness,  $d_{\text{wall}}$ , sample thickness or distance between the walls,  $d_{\text{ID}}$ , and the width. The rectangular capillaries may be placed directly onto the surface of the EPRoC, without requiring a support structure such as glue. Figure 5.5 (b) shows FM spectra of a 10 mmol L<sup>-1</sup> tempol/H<sub>2</sub>O solution placed in different rectangular capillaries. Two of the capillaries (5015, 5005) have the same ID,  $d_{\text{ID}}$  of 50 μm, while the third capillary (5004) has a  $d_{\text{ID}}$  of 40 μm. The spectra of the two thicker capillaries (5015, 5005) exhibit a similar lineshape, i.e., all three lines show the same amplitude, while the thinner capillary shows a reduced third line. This difference may be explained by a longer rotational correlation time exhibited by the sample in the thinner capillary. This may be caused by stronger capillary forces in the thinner capillary compared to the thicker ones, effectively slowing down the rotation of the tempol molecules in the solution.

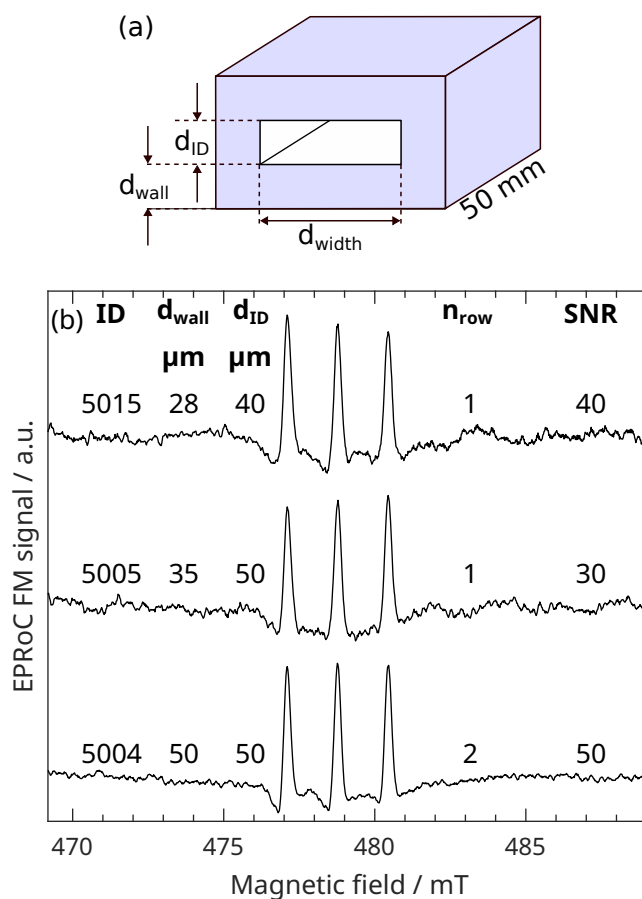


Figure 5.5: **(a)** Sketch of the geometry of the rectangular capillaries with the relevant parameters affecting the sample volume. Please note that the length of the capillaries (50 mm) is much larger than the other parameters and also much larger than the dimensions of the EPRoC. **(b)** EPRoC spectra of a  $10 \text{ mmol L}^{-1}$  tempol/ $\text{H}_2\text{O}$  solution placed in different rectangular capillaries recorded with the 12-coil EPRoC array. **Top:** *VitroCom* 5004 with a wall thickness of  $d_{wall} = 28 \mu\text{m}$ , inner diameter of  $d_{ID} = 40 \mu\text{m}$  and a width of  $d_{width} = 0.4 \text{ mm}$  covering one row of the coils,  $n_{row}$ . **Middle:** *VitroCom* 5005 ( $d_{wall} = 35 \mu\text{m}$ ,  $d_{ID} = 50 \mu\text{m}$ ,  $d_{width} = 0.5 \text{ mm}$ ) covering one row of the coils. **Bottom:** *VitroCom* 5015 ( $d_{wall} = 50 \mu\text{m}$ ,  $d_{ID} = 50 \mu\text{m}$ ,  $d_{width} = 1 \text{ mm}$ ) covering both rows of the coils.

Due to the width of the capillary, the number of covered rows of coils of the 12-coil EPRoC array,  $n_{\text{row}}$ , differs in the experiment. The widest capillary (5015) covered both rows of coils, while the other two (5004 and 5005) cover only one row of six coils. This, in turn, has an effect on the probed sample volume which is about 24 nL, 12 nL, and 9.6 nL for capillary 5015, 5005 and 5004, respectively.<sup>5</sup> The spectrum of the sample in capillary 5015 exhibits the largest SNR of about 50, while spectra of the sample in capillary 5005 and 5004 exhibit an SNR of about 30 and 40, respectively. From these values, the respective concentration sensitivities of about 40, 60 and 50  $\mu\text{mol L}^{-1} \text{G}^{-1} \text{Hz}^{-0.5}$  (5015, 5005, 5004) may be calculated. The difference of the SNRs may be explained by the difference in volume and wall thickness. While 5015 has the thickest wall of 50  $\mu\text{m}$ , reducing the  $B_1$ , it covers both rows of coils, increasing the signal amplitude. For 5005 and 5004, the reduced wall thickness seems to compensate for the lower ID, such that the SNR is equal.

In summary, the rectangular capillaries provide an easier sample handling experience, and, in theory, a larger filling factor compared to the round capillaries discussed above. However, the concentration sensitivity for tempol in  $\text{H}_2\text{O}$  is in the same order of magnitude as in the previous experiments.

**HOLEY EPROC** This experiment was not performed within the scope of the thesis and is only referenced here for completeness. To improve the filling factor of the EPRoC with round capillaries, a hole was drilled in an EPRoC via focussed ion beam. Round capillaries may be inserted in this hole. This effectively extends the sensitive volume into the substrate of the EPRoC. Detailed information about the holey EPRoC is given in ref. [130]. For this single-coil EPRoC at 14 GHz, a concentration sensitivity of 70  $\mu\text{mol L}^{-1} \text{G}^{-1} \text{Hz}^{-0.5}$  (normalised to 1 G linewidth from 450  $\mu\text{mol L}^{-1} \text{Hz}^{-0.5}$ ) was found. The idea to use round capillaries inserted in holes in planar microresonators originated from ref. [107]. In their work, the scaling of the sensitivity of different planar  $\Omega$ -shaped and R-shaped microresonators with varying inductor dimensions was investigated. A 3 mmol  $\text{L}^{-1}$  tempol/ $\text{H}_2\text{O}$  solution in a capillary with an OD 400  $\mu\text{m}$  (ID: 300  $\mu\text{m}$ , wall thickness: 50  $\mu\text{m}$ ) was investigated. The capillary was inserted in the hole in the substrate of a  $\Omega$ -shaped microresonator with a diameter of 500  $\mu\text{m}$ . The results were compared to a measurement of the same sample at a similar MW frequency in a cavity with a transverse electric (TE)-102 mode. The SNR [107, Figure 6] of the  $\Omega$ -shaped resonator was much higher than that of the cavity experiment despite the  $\sim 43 \times$  larger sample volume in the cavity resonator. However, no estimation of the concentration sensitivity was given.

<sup>5</sup> The sample volume assumed for one coil is the square of the diameter of the coil times the ID of the capillary.

### 5.3.3.2 Submersible EPRoC dipstick

In the preceding section, different geometries of capillaries filled with sample solution were investigated. In this section, however, the sample placement is reversed in a sense that the sample is not placed onto or into the EPRoC, but the EPRoC is submersed into the solution under investigation, as proposed in [131] - the so-called EPRoC dipstick. In the following, different attempts of the dipstick approach will be discussed. First, the EPRoC array of Chapter 6 was submerged without a protective coating. Second, the single-coil EPRoC board investigated in ref. [190] and coated with superglue was examined. Third, a dedicated dipstick single-coil EPRoC coated with parylene C was tested.

**NO COATING** The first dipstick test was performed with the 12-coil EPRoC array board as described in Section 4.2.4.1. Prior to the measurements, only the electrical surface-mounted devices on the PCB, the bonding wires to and pads of the EPRoC were covered with additional epoxy resin (UHU Plus Schnellfest). No protective layer was applied to the chip, as it was expected that the passivation layers SiO<sub>2</sub> (some nm) and SiN (200 to 300 nm) as well as an isolating polyimide layer (~5 μm) on the surface of the EPRoC, applied during manufacturing (cf. Section 6.2.2.2), would be sufficient to protect the EPRoC from damage. The first dipstick experiment was performed as follows. Before submersion, the EPRoC turned on as usual with frequency modulation. It was then slowly submersed in a 10 mmol L<sup>-1</sup> tempol/H<sub>2</sub>O solution while observing the current draw of the power supply for the whole EPRoC PCB. Changes in the current draw could indicate electrical shorts caused by the aqueous solution. Initially, the EPRoC was operational, and the current draw did not change considerably. After approximately 30 min, however, the EPRoC stopped working. This duration may be called survival time for the EPRoC. The defective EPRoC was investigated with scanning electron microscopy to search for cracks on the surface. However, the results were inconclusive. After this somewhat disappointing first experiment, different coatings to protect the EPRoC were investigated as discussed in the next sections.

**SUPERGLUE COATING** From the previous dipstick experiment, it became clear that a protective coating of the EPRoC is needed to protect it from being destroyed upon submersion. Therefore, the EPRoC board used in ref. [190] was coated with a thin film of cyanoacrylate adhesive (superglue - UHU Blitzschnell Präzision with Ethyl cyanoacrylate) by Peter Fischer. The superglue was manually applied to the both sides of the tip of the EPRoC PCB with the following procedure. A line of superglue was applied to the PCB which was dispersed onto the surface of the PCB and the EPRoC by means of a sharp edge of a small piece of rubber. In the presence of humidity in air, the cyanoacrylate polymerises by forming long strong chains such that a thin inhomogeneous

layer of superglue develops. This coating effectively protected this EPRoC for about 75 h submersed in aqueous solution before it suffered the same fate as the uncoated EPRoC from the previous section. It, however, effectively improved the survival time by a factor of more than 150. Speculations for the failure include a disintegration of the cyanoacrylate coating by elevated temperatures of the EPRoC due to a low thermal conductivity of the coating or by the aqueous solution itself as well as diffusion of water into the cyanoacrylate.

In theory, infrared (IR) imaging could be used to investigate the coverage of the coating due to the distinct triple bond between Nitrogen and Carbon in the polymer. IR imaging performed on the EPRoC was, however, inconclusive due to the inhomogeneous thickness of the coating, resulting in varying IR signal amplitudes.

**PARYLENE C COATING** The most stable coating for the EPRoC dipstick that was investigated is a thin layer of parylene C. This material is commonly used as a moisture barrier as well as corrosion resistant coating for medical and other applications [197]. By means of chemical vapour deposition, a 10 to 12  $\mu\text{m}$  parylene C layer was deposited on a specially-designed EPRoC dipstick PCB described in [Section 4.2.4.2](#). This PCB features a replaceable daughterboard on which the actual EPRoC is located. In a case of a failure of the EPRoC, only the daughterboard needs to be replaced. The concentration sensitivity of this EPRoC design was determined with a 1  $\text{mmol L}^{-1}$  tempol/ $\text{H}_2\text{O}$  solution and is given by 2 and 12  $\mu\text{mol L}^{-1} \text{G}^{-1} \text{Hz}^{-0.5}$  for the FM and AM signal, respectively.

### 5.3.3.3 Concentration sensitivity

In the following, the concentration sensitivities determined with the different approaches are discussed. Please note that the concentration sensitivity determined for the EPRoC dipstick is well-defined since the sample volume is much larger than the sensitive volume so that the filling factor is maximal. In [Table 5.2](#), the concentration sensitivities are summarised. The sensitivities were obtained with differently concentrated solutions, with different EPRoC boards and different acquisition parameters. Hence, for a correct comparison of the determined concentration sensitivities, all parameters affecting the signal amplitude need to be considered such that the values may be normalised to certain standard measurement conditions. The parameters mostly influencing the signal amplitude include the sample concentration, the modulation amplitude and the bias current, which determines  $B_1$ .

For samples with a low concentration of paramagnetic species, the signal amplitude increases linearly with the concentration. However, at a sample concentration of 10  $\text{mmol L}^{-1}$ , for instance, the EPR spectrum is exchange broadened (cf. [Section 2.3.3](#)) and therefore the signal amplitude increases sub-linearly as a function of the concentration

Table 5.2: Concentration sensitivities of FM,  $c_{\min,FM}$ , and AM detection,  $c_{\min,AM}$ , determined with tempol/H<sub>2</sub>O solutions with different sample alignment. Round cap. || means sample in a round capillary placed parallel to the surface of the EPRoC. In Rect. cap. ||, the sample resides in a rectangular capillary placed parallel to the surface of the EPRoC. Round cap.  $\perp$  describes the holey EPRoC with a round capillary. The number of coils,  $n_{\text{coil}}$ , and the concentration of the sample solution,  $c_s$ , are given. Please note that the uncoated and superglue-coated EPRoC dipstick are not included since they can not be considered stable experimental configurations.

	$c_{FM}$	$c_{AM}$	$n_{\text{coil}}$	$c_s$	Ref.
	$\mu\text{mol L}^{-1} \text{G}^{-1} \text{Hz}^{-0.5}$		1	$\text{mmol L}^{-1}$	
Round cap.	30	-	8	5	[61]
Rect. cap.	40	-	12	10	[131]
Round cap. $\perp$	70	-	1	10	[130]
Dipstick	2	12	1	1	-

above  $\sim 3 \text{ mmol L}^{-1}$ . This can be observed in the spectra of 10 and 1  $\text{mmol L}^{-1}$  tempol/H<sub>2</sub>O solution in Figure 4.5 in Section 4.3.2.1, in which the signal amplitude of the 10  $\times$  higher concentrated sample only shows a  $\sim 3 \times$  larger signal amplitude. This effect is partly compensated by the normalisation to a linewidth of 1 G (corresponding to 2.8 MHz).

Similarly, the modulation amplitude affects both linewidth and signal amplitude. The former is again compensated by the normalisation if the modulation amplitude is larger than the natural linewidth. If the modulation amplitude is not optimised, i.e., much lower than the natural linewidth, the signal amplitude may be lower than optimal. While the modulation amplitude of the experiments with the rectangular capillaries and the dipstick was 3.2 MHz (corresponding to 0.1 mT), the modulation amplitudes used in the experiments to estimate the concentration sensitivities of the round capillary of ref. [61] and of the holey EPRoC of ref. [130] are not stated. Therefore, the sensitivity values are not normalised to the modulation amplitude as the normalisation factor for the holey EPRoC is missing. The other experiments were performed under the same conditions.

The most critical parameter is the applied bias current and the corresponding  $B_1$  magnitude. For the experiments, however, different EPRoCs were used. As the conversion from bias current to  $B_1$  of each EPRoC is individual and unknown unless exactly determined, it is impossible to calculate the exact  $B_1$  for each experiment. In ref. [131], for instance, the  $B_1$  values were obtained from an analysis of the rapid scan data of a saturation experiment, which revealed a square-root dependence of  $B_1$  on the bias current, which will be discussed in detail in



[Section 7.3.2](#). In addition, the  $B_1$  distribution as discussed in [Chapter 6](#) does also play an important role. Therefore, the possibly different  $B_1$  magnitudes and distributions cannot be taken into consideration. Taking the different signal amplitudes due to the sample concentration, the values for the round and rectangular capillaries as well as the holey EPRoC need to be corrected by 2 to 3, i.e., divided. Even after correction, using capillaries to investigate samples in solution leads to lower concentration sensitivities by approximately one order of magnitude than the dipstick approach. This can mainly be attributed to a smaller accessible sensitive volume due to the wall thicknesses (28 to 50  $\mu\text{m}$ ) and wall curvature of the capillaries compared to the thickness of the parylene C coating ( $\sim 10 \mu\text{m}$ ).

The best concentration sensitivity was obtained with the parylene C coated EPRoC dipstick and is 2 and 12  $\mu\text{mol L}^{-1} \text{G}^{-1} \text{Hz}^{-0.5}$  for the FM and AM signal, respectively. The concentration sensitivity of the FM signal is a factor of  $\sim 6$  better than for the AM signal as seen before for the a-Si and BDPA samples discussed in [Section 5.3.1](#). From the concentration sensitivity and the sensitive volume of the EPRoC ( $\sim 1.6 \text{ nL}$ ), which will be discussed in detail in [Chapter 6](#), the absolute sensitivity of the EPRoC may be calculated. The absolute spin sensitivity of  $2 \times 10^9 \text{ spins Hz}^{-0.5}$  determined from the concentration sensitivity is of same order of magnitude as the absolute spin sensitivities determined from powder samples of BDPA ( $4 \times 10^9 \text{ spins Hz}^{-0.5}$ ) [55] and DPPH ( $8 \times 10^9 \text{ spins Hz}^{-0.5}$ ) [61]. This finding is important for several reasons. First, the thickness of the coating seems to be negligible compared to the total sensitive volume. Second, the solvent in general and its dielectric constant in particular seems to have only little effect on the sensitivity of the EPRoC in contrast to resonator-based EPR. The effect of the dielectric constant of the sample will be discussed in detail in [Section 5.3.4.1](#). Third, due to the increased absorption of the solvent, the absolute value of the  $B_1$  may be decreased especially close to the trace of the coil (cf. *Maxwell's* equations). This reduction may be helpful as the generally large  $B_1$  of tens of  $\mu\text{T}$  saturates most samples as discussed earlier (cf. [Section 5.3.1](#) and [Section 7.2.3](#)). It could thus lead to a lower degree or no saturation of the investigated sample.

Even the lowest, i.e., best, concentration sensitivity of the EPRoC of a few  $\mu\text{mol L}^{-1}$  is much worse than the concentration sensitivities for cavity-based EPR spectrometer. For instance, the specified concentration sensitivity for the Magnettech MS5000 spectrometer is 20  $\text{pmol L}^{-1}$  [198] without further information about its determination. Generally, the concentration sensitivity of cavity-based EPR will be much better than that of the EPRoC due to the much larger probed volume in the resonator. Therefore, the concentration sensitivities determined for similar micro-EPR approaches seem to be a fair comparison. The near field non-resonant EPR probehead exhibited a concentration sensitivity  $\sim 20 \text{ mmol L}^{-1} \text{Hz}^{-0.5}$  [49], while that of the pulsed EPR “dipstick” was

$37 \mu\text{mol L}^{-1} \text{ Hz}^{-0.5}$  [47]. The latter was determined from the fourier transform EPR spectrum of a  $1 \text{ mmol L}^{-1}$  trityl radical in water.

Therefore, the concentration sensitivity of the EPRoC dipstick seem to be better by approximately one order of magnitude compared to similar approaches published previously.

**USEFUL CONCENTRATION SENSITIVITY** The statement of an absolute or concentration sensitivity determined from the SNR of a sample with a high number of spin / high concentration may be of limited use for spectroscopists as the acquisition time is not taken into consideration, as discussed in Section 2.4.3. To challenge the concentration sensitivity value determined in the previous section, a series of tempol/ $\text{H}_2\text{O}$  solutions with concentrations of  $10 \mu\text{mol L}^{-1}$ ,  $100 \mu\text{mol L}^{-1}$  and  $1 \text{ mmol L}^{-1}$  were investigated.

Both field- and frequency-swept spectra acquired with the same experimental parameters are shown in Figure 5.6. In each plot, the SNR and the number of averages are indicated. The number of points of the spectra is the same such that the effective acquisition time as defined in Equation 7.8 differs only by the number of averages. The experimental acquisition time<sup>6</sup> to acquire one average of a field-swept spectrum was approximately 500 s, while it was approximately half for a frequency-swept spectrum. Because an off-resonant spectrum is required for baseline correction of the frequency-swept spectra, the experimental acquisition time is doubled, so that by chance, the experimental acquisition times are the same for both field and frequency sweep. The spectra of both field and frequency sweeps of the  $1 \text{ mmol L}^{-1}$  and  $100 \mu\text{mol L}^{-1}$  sample as well as the field-swept spectrum of the  $10 \mu\text{mol L}^{-1}$  sample exhibit the expected three-line spectrum of a rapidly tumbling nitroxide in solution. The frequency-swept spectrum of the  $10 \mu\text{mol L}^{-1}$  solution, however, shows a residual baseline. The SNRs of the field-swept spectra are always larger than that of the frequency-swept spectra by a factor of 1.7 to 3.3 ( $1 \text{ mmol L}^{-1}$ ,  $100 \mu\text{mol L}^{-1}$ ). This may be attributed to a larger noise floor / baseline. The absence of an EPRoC spectrum in the frequency sweep of the  $10 \mu\text{mol L}^{-1}$  sample may be explained by the low SNR of the field sweep of  $\sim 11$ . Since the SNR would be even lower for the frequency sweep, it is not observable.

The experimental acquisition time of the spectrum of the tempol solution with a concentration of  $10 \mu\text{mol L}^{-1}$  with its SNR of 11 was  $\sim 6.5 \text{ h}$ . Hence, the experimentally determined value of the concentration sensitivity with a sample of relatively high concentration, is approximately equal to that which can actually be recorded with averaging.

<sup>6</sup> That is the real measurement time.



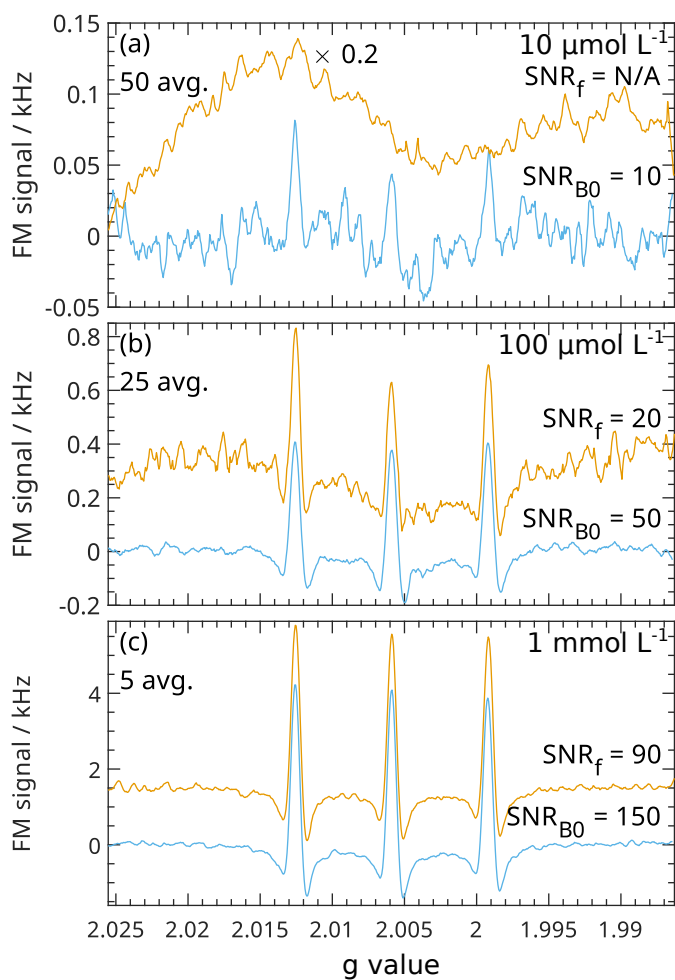


Figure 5.6: Field- (bottom) and frequency-swept (top) FM spectra of tempol/ $\text{H}_2\text{O}$  solutions with concentrations of  $10 \mu\text{mol L}^{-1}$  (a),  $100 \mu\text{mol L}^{-1}$  (b), and  $1 \text{ mmol L}^{-1}$  (c). The spectra are vertically shifted by (a): 0 kHz, (b): 0.3 kHz, (c): 1.5 kHz for better visibility. The SNR, the number of averages and the concentration are indicated in each figure.

## 5.3.4 Influence of sample and experimental parameters

In this section, the influence of certain sample and experimental parameters on the EPRoC signal is investigated. First, the influence of the dielectric constant of the sample is discussed. Second, the influence of the bias current on the signal amplitude and shape is explained. The section concludes with a discussion of the modulation amplitude and its effect on the SNR.

## 5.3.4.1 Influence of the dielectric constant of the sample on the EPRoC

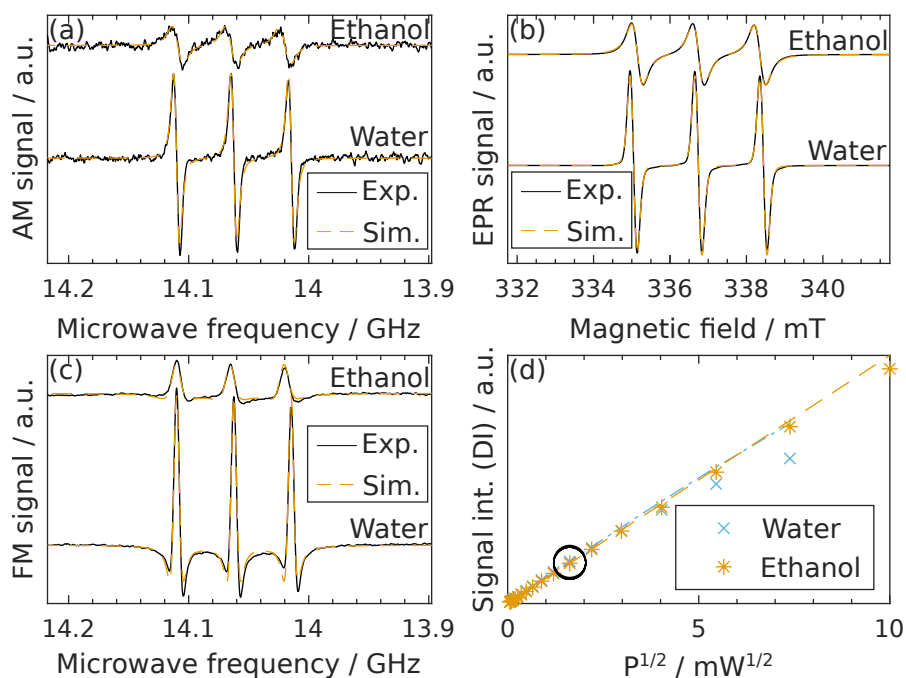


Figure 5.7: EPRoC and EPR spectra of 1 mmol L<sup>-1</sup> tempol dissolved in water and ethanol, respectively, with spectral simulations. (a) EPRoC AM signal. (b) EPR absorption signal recorded with a resonator-based EPR spectrometer at an MW power of 2.64 mW. (c) EPRoC FM signal. (d) EPR saturation recorded with a resonator-based EPR spectrometer. The black circle depicts the MW power that was used to record the spectra in (b).

Samples with large dielectric constants such as water, which are so-called lossy samples, usually challenge EPR spectroscopists due to the non-resonant MW absorption of these samples via the electric field. The amount of absorption depends on the complex part of the dielectric constant,  $\epsilon''$ . In addition, the real part of the dielectric constant may lead to a phase shift in the measured EPR spectrum resulting in a mixture of absorption and dispersion. The effect of such lossy samples has intensively been studied since the dawn of EPR especially by the Eaton group [175, 176, 199, 200]. For the EPRoC, however, such an analysis is missing. Therefore, the influence of the

dielectric constant of the sample on the EPRoC signal was investigated with tempol dissolved in water and ethanol with a concentration of  $1 \text{ mmol L}^{-1}$ , respectively.

In Figure 5.7 AM (a), FM (c) and EPR spectra (b) with respective simulations of both spectra are shown. As expected, isotropic fast-motion three-line spectra are observed for both samples due to the HFI of the  $^{14}\text{N}$  nucleus of tempol with the electron spin. The signal amplitudes of the FM, AM and EPR spectra of the water sample are larger than that of the ethanol sample. On first sight, this finding is quite counter-intuitive. It would be expected that the water sample exhibits a lower signal amplitude than the ethanol sample due to the lower  $Q$ -factor which was smaller by approximately 2 in the resonator-based EPR spectrometer. A lower  $Q$ -factor was also found in ref. [175]. A sensitivity reduction by a factor of  $\sim 2$  for a grain of DPPH was found in [200, Figure 6 A], when changing from ethanol to water. However, DPPH not dissolved but in powder form with aliquots of different solvents present in a separate sample tube. Similar experiments were performed in ref. [176], in which the signal amplitude of DPPH or irradiated  $\text{SiO}_2$  was lower when water was inserted in the cavity compared to ethanol. In our experiments, on the other hand, tempol is *dissolved* in ethanol and water, respectively. This may lead to different parameters in the spin Hamiltonian.

While the signal amplitude is relevant for calculation of the sensitivity, the signal intensity obtained from DI of the spectra, gives quantitative information about the concentration of the samples.<sup>7</sup> The signal intensities of both samples recorded with the resonator-based EPR spectrometer with the same acquisition parameters and normalised to the  $Q$ -value of the experiment are equal as seen in the saturation plot in Figure 5.7 (d). Hence, the concentration of tempol in both samples is the same.

To gain insight into the spin Hamiltonians, all spectra were simulated with *garlic* of the *EasySpin* software package assuming a spin-1/2 system in solution with an isotropic  $g$ -value of 2.0059, with isotropic HFI caused by the  $^{14}\text{N}$  nucleus of the tempol and convolutional *Gaussian* and *Lorentzian* broadening. For the simulations, the isotropic hyperfine-coupling constant,  $a_{\text{iso}}$  as well as the *Gaussian* and *Lorentzian* broadening were adjusted in a least-square fit of the spectrum to the experimental data. The simulation parameters of the X-band EPR spectra and similar samples from literature are shown in Table 5.3. The hyperfine splitting of the water sample (47.7 MHz) is slightly larger than that of the ethanol sample (45.0 MHz). While the *Gaussian* contribution of the line broadening ( $\Delta B_{\text{pp,G}} = 0.16 \text{ mT}$ ) of the water sample is larger than the *Lorentzian* broadening ( $\Delta B_{\text{pp,L}} = 0.05 \text{ mT}$ ), the ethanol sample exhibits similar values of both *Gaussian* ( $\Delta B_{\text{pp,G}} = 0.15 \text{ mT}$ ) and *Lorentzian* broadening ( $\Delta B_{\text{pp,L}} = 0.23 \text{ mT}$ ).

<sup>7</sup> Assuming the same sample volume.

Table 5.3: Fit parameters of 1 mmol L<sup>-1</sup> tempol in water and ethanol.  $c_s$  is the sample concentration,  $a_{\text{iso}}$  is the isotropic hyperfine coupling constant,  $\Delta B_{\text{pp,G}}$  and  $\Delta B_{\text{pp,L}}$  are the peak-to-peak linewidths of the *Gaussian* and *Lorentzian* broadening, respectively.

Solvent	Water		Ethanol	
	This work	[201]	This work	[202]
$c_s / \text{mmol L}^{-1}$	1	0.1	1	0.5
$a_{\text{iso}} / \text{MHz}$	47.7	47.3	45.0	44.2
$\Delta B_{\text{pp,G}} / \text{mT}$	0.16	0.18	0.15	0.16
$\Delta B_{\text{pp,L}} / \text{mT}$	0.05	0.03	0.23	0.20
$Q$	1220	N/A	2170	N/A

For comparison with experimental data of similar samples from literature, EPR spectra from the respective references were digitised as described in Section 5.2.5 and subsequently simulated. In ref. [201, Figure 1 (a)] the X-band EPR spectrum of a 100  $\mu\text{mol L}^{-1}$  tempol water solution and its stability over 30 days is presented. The simulation of the spectrum revealed that the hyperfine splitting ( $a_{\text{iso}} = 47.3 \text{ MHz}$ ) as well as the *Gaussian* ( $\Delta B_{\text{pp,G}} = 0.18 \text{ mT}$ ) and *Lorentzian* broadening ( $\Delta B_{\text{pp,L}} = 0.03 \text{ mT}$ ) is comparable to the 1 mmol L<sup>-1</sup> sample discussed here. In addition, in ref. [172] an  $a_{\text{iso}}$  of 45.1 MHz was found for a concentration of 200  $\mu\text{mol L}^{-1}$  tempol in ethanol, which is also similar to the value found here. Similarly, for the ethanol sample, a simulation of the X-band spectrum of 500  $\mu\text{mol L}^{-1}$  tempol in ethanol<sup>8</sup> [202, Figure 1 (a)] showed similar values as the 1 mmol L<sup>-1</sup> tempol/water solution:  $a_{\text{iso}} = 44.2 \text{ MHz}$ ,  $\Delta B_{\text{pp,G}} = 0.16 \text{ mT}$  and  $\Delta B_{\text{pp,L}} = 0.20 \text{ mT}$ .

The results of the spectral simulations of the FM signal of both samples and the AM signal of the water sample are equal within the accuracy of the simulation to those obtained from the EPR spectra displayed in Table 5.3. Small deviations are observed from the simulations of the AM spectrum of the ethanol solution. Here,  $a_{\text{iso}}$  is  $\sim 0.3 \text{ MHz}$  smaller and  $\Delta B_{\text{pp,G}}$  is larger by  $\sim 0.04 \text{ mT}$  than obtained from the FM and the EPR spectrum. These deviations may be explained by the fact that the simulation was performed without taking the admixture of dispersion to the absorption signal into consideration (cf. Section 5.3.1) and by the relatively low SNR of  $\sim 20$  of the AM spectrum.

As mentioned above, the signal amplitude of the water sample is larger than that of the ethanol sample by a factor of  $\sim 4.8$  for the FM spectrum,  $\sim 4$  for the AM spectrum and  $\sim 2.9$  for the EPR spectrum.

In the following, speculations about the origin of the different signal amplitudes are presented, as the experiments shown here do not allow

<sup>8</sup> 95 % ethanol/5 % water. This mixture corresponds to the commonly used ethanol.

drawing final conclusions about the influence of the dielectric constant and are for that reason preliminary.

The signal voltage of a resonator-based EPR spectrometer may be described by [12, 78, 83]

$$V_{\text{res}} = \chi'' \eta Q \sqrt{P Z_0}, \quad (5.2)$$

where  $P$  is the MW power, and  $Z_0$  is the characteristic impedance of the transmission line. The linear dependence of the signal voltage on  $Q$  is the reason why the signal intensities of different samples need to be normalised to this value for a comparison as mentioned above. Similarly, the EPR spectra shown in Figure 5.7 (b) may also be corrected by  $Q$  listed in Table 5.3. Then, the signal amplitudes of the spectra would correspond to the values that would be obtained for the same quality factor ( $Q$ ). The ratio of the  $Q$ -values of the water and ethanol spectrum is  $\sim 1.8$ , so that the signal amplitude of the water sample would be  $\sim 5.2$  larger than that of the ethanol sample. This value is similar to that obtained from the EPRoC FM spectra 4.8. Hence, it seems that EPRoC FM signal is *insensitive* to the dielectric constant of the sample. These findings may intuitively be explained as follows. In resonator-based EPR, the  $Q$ -factor is defined as

$$Q = \frac{2\pi \text{ energy stored}}{\text{energy dissipated per cycle}}. \quad (5.3)$$

The stored energy of a cavity resonator is constant for the same MW frequency. However, for a lossy sample with a large dielectric constant such as water, the energy dissipated per cycle is much larger than for a sample with a small dielectric constant, such as ethanol. Hence, the  $Q$  is lower for water than for ethanol as observed in the EPR data shown before. For the EPRoC, on the other hand, the definition of the  $Q$ -factor is somewhat different. We may speak of an apparent  $Q$ , as the losses of the LC tank are compensated by the active pump circuit discussed in Section 3.2.2. Therefore, in the presence of a lossy sample, the denominator of Equation 5.3 may indeed decrease compared to a non-lossy sample. The numerator, the energy stored, is increased by the same amount due to the compensation by the active pump circuit, so that  $Q$  may be independent of the dielectric constant of the sample.

The former hypothesis is supported by the frequency dependence of the complex dielectric constant of water and ethanol,  $\epsilon = \epsilon' + i\epsilon''$ . Its complex part,  $\epsilon''$ , determines the amount of MW absorption, while the real part,  $\epsilon'$ , leads to a frequency shift. The complex dielectric constant of water and ethanol was calculated using a *Debye* model with parameters as described in [203, Eq. 1 and Tab. 1] for an X-band frequency of 9.46 GHz and for a  $K_u$ -band frequency of the EPRoC of 14.2 GHz. For water, it is given by  $\sim 28.6$  at X-band and  $\sim 34.5$  at  $K_u$ -band, while for ethanol it is  $\sim 2.4$  at X-band and  $\sim 1.9$  at  $K_u$ -band. At X-band, the complex component of the dielectric constant of water is  $\sim 12$

times larger than that of ethanol. Hence, the amount of non-resonant MW absorption via  $E_1$  is much larger, which can also be seen by the lower  $Q$ -value of the water sample at X-band compared to the ethanol sample (cf. Table 5.3). At  $K_u$ -band, the complex component of the dielectric constant of water is  $\sim 19 \times$  larger than that of ethanol. This would reduce the  $Q$ -value of the water sample even more compared to the ethanol sample. Using the ratio of the signal amplitudes at X-band as a reference, in an experiment with a resonator-based EPR spectrometer at  $K_u$ -band adhering to Equation 5.2, the ratio of the signal amplitudes of the water and ethanol spectra should decrease. With the EPRoC, however, the opposite is observed. At  $K_u$ -band the ratio of the signal amplitudes increases compared to X-band. Hence, the EPRoC signal seems to be insensitive to changes in the dielectric constant of the sample.

**A REMARK ON LINESHAPE BROADENING** Compared to the experiments performed with powder samples in Section 5.3.1, the spectra of the tempol samples do not exhibit a lineshape broadening. In the following, possible reasons for this difference are discussed. Saturation experiments recorded in X-band with resonator-based EPR instrumentation shown in Chapter 4 show that the a-Si sample saturates at about  $20 \mu\text{T}$ , while  $1 \text{ mmol L}^{-1}$  tempol in water saturates already at  $\sim 5 \mu\text{T}$ , which is 4 times lower. It would therefore be expected that the tempol sample would also exhibit saturation effects if acquired at the same bias current. By chance, the bias current used to record the tempol spectra is  $4 \times$  lower (1.25 mA) than that used to record the a-Si spectra (5 mA). Therefore, assuming that the lineshape broadening of the a-Si originates from (partly) saturating the sample, this should be observed for the tempol sample, too. However, while the a-Si sample was directly placed on the surface of the EPRoC, the 12-coil EPRoC dipstick array used to investigate the tempol solution has a  $\sim 10 \mu\text{m}$  thick parylene C coating. Hence, the solution is further away from the surface of the EPRoC, where the values of  $B_1$  are largest. In addition, the solvents used for the tempol samples could additionally attenuate  $B_1$ . Furthermore, the diffusion of tempol molecules in the solvent may also play a role. These effects could result in lower saturation experienced by the tempol samples compared to the a-Si sample.

#### 5.3.4.2 *Influence of the frequency modulation on the EPRoC signal*

In this section, the dependence of the FM and AM spectra on the frequency modulation amplitude will be discussed. For this investigation, field-swept FM and AM spectra of a  $10 \text{ mmol L}^{-1}$  tempol/ $\text{H}_2\text{O}$  sample were obtained at different frequency modulation amplitudes at fixed MW frequency of 14.34 GHz. Only the central line of each spectrum was analysed. One spectrum per modulation amplitude was recorded with a modulation frequency of 90 kHz. In Figure 5.8 (a), the FM and

AM baseline are displayed, which was obtained from the mean of the baseline regions of the spectra. Both FM and AM baselines exhibit a linear increase with the frequency modulation amplitude. For the FM signal, a linear dependence is expected as discussed in ref. [190, Appendix A]. It results from the utilisation of the PLL as a downconverter in combination with frequency modulation. The linear dependence of the AM baseline on the frequency modulation amplitude may have different reasons including some kind of cross-talk of the modulation on the EPRoC.

The noise floor of FM and AM signal is displayed in Figure 5.8 (b) calculated as the STD of the baseline regions. Here, both detection methods exhibit different behaviours. While the AM noise floor has no apparent dependence on the modulation amplitude, a linear increase of the FM noise floor for modulation amplitudes larger than 3 MHz is observed. This increase may be explained by a larger bandwidth of the FM signal in the time domain, resulting in noise integration by the PSD.

In Figure 5.8 (c), the peak-to-peak signal amplitude of the spectra is shown. Since the signal intensity is linearly proportional to the modulation amplitude [12], a linear increase of the signal amplitude is expected for modulation amplitudes lower than the linewidth, which is seen in the experimental data for modulation amplitudes lower than  $\sim 7$  MHz. For modulation amplitudes (much) larger than the linewidth, a broadening of the line is observed leading to a flattening of the increase of the signal amplitude. The SNR of the spectra is shown in panel (d) of Figure 5.8, which is calculated as the ratio of panels (c) and (d). Since there is no dependence of the AM noise on the modulation amplitude, the shape of the SNR as a function of the modulation amplitude resembles that of the signal amplitude. Due to the increase of the FM noise floor over the complete range of modulation amplitudes and the increase in FM signal amplitude at modulation amplitudes below 7 MHz, an initial increase of the SNR is seen below 7 MHz. At modulation amplitudes larger than 7 MHz, the SNR is reduced due to the larger noise floor and the sublinear increase of the signal amplitude.

#### 5.3.4.3 Dependence of the EPRoC signal on the bias current

The MW saturation of the sample is another important parameter for EPR spectroscopists as spectra recorded under saturating conditions are often discarded due to possible lineshape broadening.

In the previous sections, a lineshape broadening was observed for the BDPA and a-Si sample at a bias current of 5 mA used to record the spectra. A possible cause for this broadening may be MW saturation (cf. Section 2.4.2). As mentioned earlier, continuous wave EPR (CW-EPR) spectra need to be recorded under non-saturating conditions, i.e., at an MW power (which determines the value of  $B_1$ ) low enough such



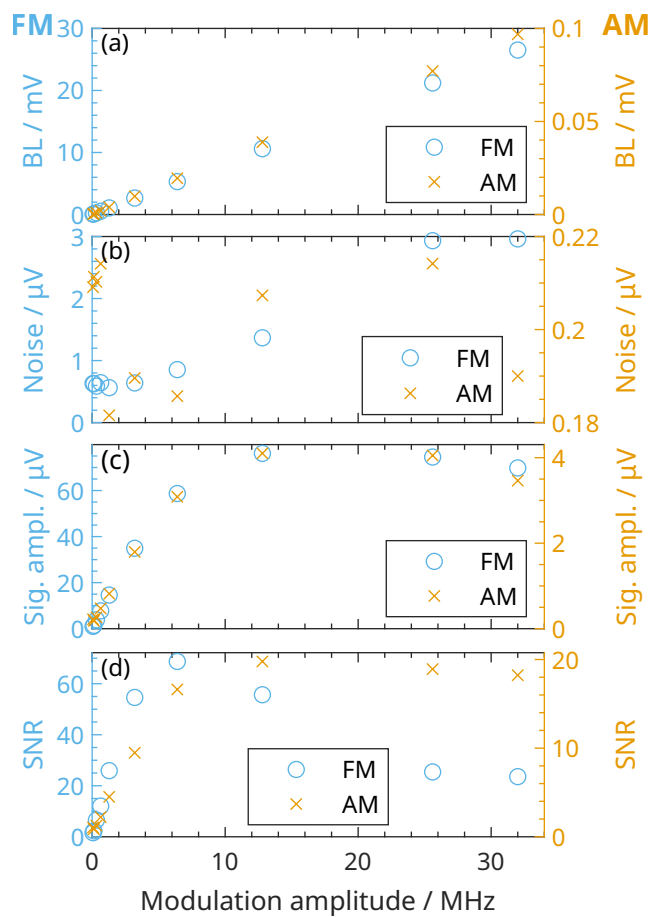


Figure 5.8: Response of the FM and AM signal on a variation of the frequency modulation amplitudes determined from spectra of a  $10 \text{ mmol L}^{-1}$  tempol/ $\text{H}_2\text{O}$  solution. (a) FM and AM baseline amplitude of the spectra calculated from the mean of the baseline of the spectra. (b) Standard deviation of the same baseline regions, i.e., noise. (c) Peak-to-peak signal amplitude. (d) SNR of FM and AM signal.



that the spin system stays in thermal equilibrium, to enable correct qualitative and quantitative analyses. In resonator-based EPR, a simple test to check if a spectrum has been recorded under non-saturating conditions may be performed as follows. The magnitude of  $B_1$  is controlled by the attenuation of the constant MW power of the source. When increasing the MW power by a factor of 4, i.e., by decreasing the attenuation by 6 dB, the peak-to-peak amplitude of the EPR absorption spectrum should increase by a factor of 2. If the increase is less than a factor of 2, the sample was saturated and a lower MW needs to be used. In resonator-based EPR spectrometers, MW sources with a fixed power of 100 to 200 mW at X-band in combination with variable attenuators are used to set the applied MW power to the desired value. Commonly, the attenuation ranges from 0 to 60 dB (sometimes even 80 dB), which corresponds a power attenuation of up to 6 orders of magnitude. Hence, the accessible MW power ranges between  $\sim 100$  mW and  $\sim 0.1$   $\mu$ W. For instance, this results in  $B_1$  magnitudes ranging between 0.15  $\mu$ T and  $\sim 150$   $\mu$ T for the Bruker ER 4118X-MD5 resonator.

As explained previously, using EPRoC, the coil current determines the magnitude of  $B_1$  (cf. Section 5.3.1.1). The coil current in turn depends on the bias current. For the conversion of bias current to coil current, the so-called square-root model with empirical parameters may be used for the 12-coil array [131]. For this configuration of the EPRoC, bias currents of up to  $\sim 25$  mA per coil may be applied which is limited by the heat dissipation capability of the EPRoC. A certain minimal bias current of a few mA is required to achieve a stably oscillating VCO. Consequently, the range of  $B_1$  is between  $\sim 30$  to  $\sim 150$   $\mu$ T in the centre of each coil. Because  $B_1$  can not as easily be attenuated as in resonator-based EPR, its magnitude may be too large for many (relatively) slowly relaxing paramagnetic species. For such samples, the rapid-scan EPR (RS-EPR) technique may be utilised instead, which will be discussed in detail in Chapter 7. Furthermore, in contrast to resonator-based EPR, the EPRoC itself and not only the spin system reacts to a change of the bias current as discussed in Section 3.2.6. While the saturation behaviour of resonator based CW-EPR has been studied in depth [84, 178–180], a starting point for a detailed analysis of the EPRoC response will be presented in this chapter. To gain insight, several properties of the recorded first-derivative FM and AM spectra are examined as a function of the bias current including peak-to-peak signal amplitude, asymmetry of the lineshapes and peak-to-peak linewidth.

The peak-to-peak signal amplitudes of the AM and FM detected spectra of the BDPA grain as well as the a-Si sample normalised to their respective maximum value are depicted in Figure 5.9 (a) and (b), respectively.

The AM signal amplitude (cf. Figure 5.9 (a)) for both samples increases with increasing bias currents and saturates at higher bias cur-

rents. This finding is similar to resonator-based EPR, where the detected EPR signal is the spin magnetisation which is proportional to  $B_1 \cdot \chi''$  [78, 83]. Due to the longer mean relaxation time of the BDPA sample ( $\sqrt{T_1 \cdot T_2} \sim 105 \mu\text{s}$ ) compared to the a-Si sample ( $\sqrt{T_1 \cdot T_2} \sim 63 \mu\text{s}$ ), the AM signal amplitude of the BDPA sample saturates at lower bias currents than the a-Si sample. For the latter, only slight saturation is observed at the largest accessible bias currents. Similarly, in ref. [186], the dependence of the AM amplitude of a BDPA sample on the bias current is shown. In this work, however, the range of the bias currents was extended to much lower values by utilising a single-coil EPRoC based on a Colpitts oscillator produced in a high electron mobility transistor technology, resulting in approximately  $30 \times$  lower  $B_1$  magnitudes. The signal amplitudes of the AM signal showed a linear increase with the bias current.

In Section 3.2.6, the change of the AM and FM signal on a varying bias current was calculated from the analytical expressions presented in Chapter 3. As these expressions are only valid for unsaturated samples, only the EPRoC-related change of the signals is calculated using design parameters of the EPRoC from literature. It was found that the AM signal would be maximal at the lowest bias current of 5 mA for unsaturated samples. If the sample could be described by Bloch's equations, the magnetic susceptibility,  $\chi$ , is maximal for the  $B_1 = 0$ . Hence, in total, a decrease of the signal amplitude is expected for the AM signal. This, however, contradicts the experimental findings presented in Figure 5.9. Possible origins of error include a wrong choice of the design parameters for the calculation of the change of the signal or a more complex interaction between the EPRoC and the spin system, that can not be modelled by the analytical expressions.

The dependence of the FM signal amplitude on the bias current is shown in Figure 5.9 (b). Here, the signal amplitude is maximum at the lowest bias current of 5 mA and decreases for larger bias currents for both samples. This behaviour is expected from the analytical expression of Equation 3.17, since the signal only indirectly depends on  $B_1$  via the real part of the magnetic susceptibility,  $\chi'$ . The decrease of the signal amplitude would be larger for the BDPA sample ( $\sim 50\%$ ) than for the a-Si sample ( $\sim 10\%$ ) due to the longer mean relaxation time of the BDPA sample.

On first sight, the behaviour of the FM signal is quite counter-intuitive compared to earlier findings on the dispersion EPR signal on different samples, such as F centres in potassium salt (KCl) [178], E' centres in irradiated fused  $\text{SiO}_2$  and NBS coal 1635 [204] – and in general the common belief in the EPR community that the dispersion signal does not saturate. However, in resonator-based EPR usually the spin magnetisation,  $B_1\chi'$ , and *not* the magnetic susceptibility is detected [84]. As mentioned above, the FM signal of the EPRoC detects the magnetic susceptibility, the factor  $B_1$  leading to an initial increase

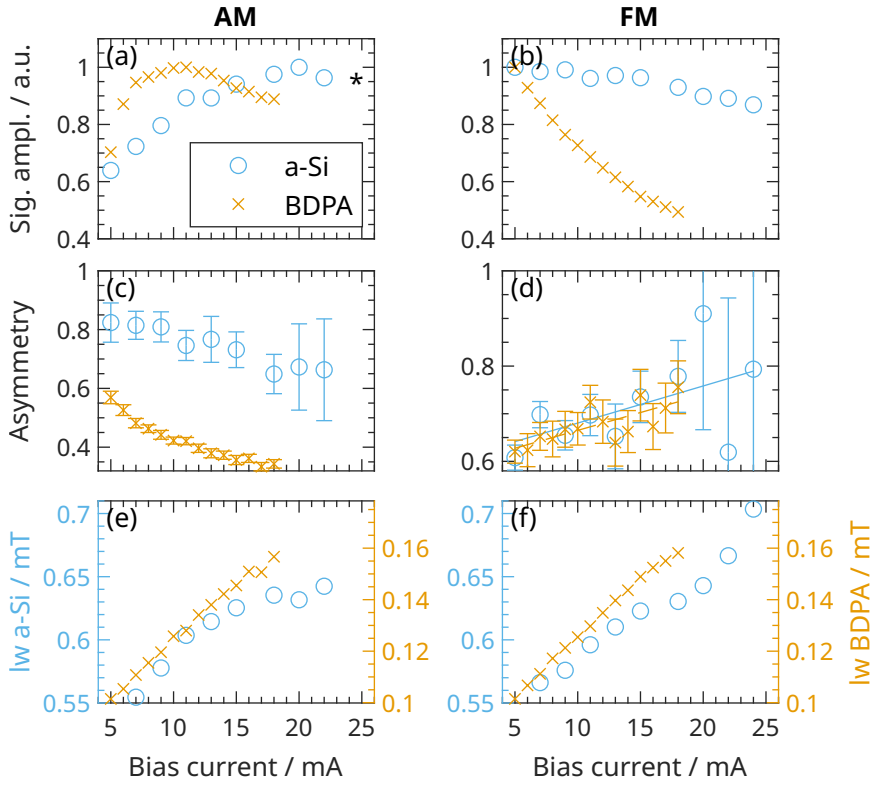


Figure 5.9: Dependence of the EPRoC signal of a BDPA sample and an a-Si sample on the bias current. **(a)** AM peak-to-peak signal amplitude normalised to the largest amplitude, calculated from the difference of global maximum and minimum of the spectra. **(b)** FM peak-to-peak signal amplitude normalised to the largest amplitude, calculated from the difference of global maximum and minimum of the spectra. **(c)** Degree of AM asymmetry of the spectrum calculated by the ratio of the magnitudes of maximum and minimum of the spectra. **(d)** Degree of FM asymmetry of the spectrum calculated by the ratio of the two minima on both sides of the resonance field/frequency. **(e)** and **(f)** Lorentzian peak-to-peak linewidth of the AM and FM spectra, respectively, as obtained from spectral simulations.

in the saturation curve is not present. The shape of the saturation curve depends on the line broadenings and is discussed in detail for dispersion and absorption signals in [84]. For the dispersion signal, it is found that inhomogeneously (*Gaussian*) broadened lines indeed do not saturate, while homogeneously (*Lorentzian*) broadened lines saturate with a certain dependence on  $B_1$ . The latter saturates similarly to the absorption signal of inhomogeneously broadened lines.

In Section 3.2.6, the dependence of the FM signal on the bias current was calculated from the analytical expression. It was found that the “EPRoC-related” change of the FM signal for an unsaturated sample strongly depends on the quality factor of the LC tank. While for a larger  $Q_{\text{coil}}$  of 10, the change of the signal amplitude over the range of bias currents of 5 to 25 mA, was approximately  $-8\%$ , for smaller

$Q_{\text{coil}} = 2$ , it reduces to  $-1\%$ . Hence, from these theoretical considerations, a decrease of the signal amplitude of the FM signal is expected.

In addition, in ref. [186], the FM signal of a BDPA sample did not change over the complete range of the bias current ( $B_1$ ) due to its much lower magnitude. The expected decrease in signal amplitude from the paramagnetic sample may be calculated from the magnetic susceptibility,  $\chi$ . In this experiment, the theoretical decrease was less than  $1\%$  (calculated from the relaxation times of BDPA stated above), which agrees well with the reported data.

Moreover, the asymmetry of the spectrum (cf. Figure 5.2) changes upon variation of the bias current. For the AM signal, the symmetry is calculated as the ratio of the absolute values of the maximum and minimum of each spectrum (cf. Figure 5.1 and Figure 5.2 (a), both bottom). The symmetry for the FM signal, on the other hand, is calculated as the ratio of the minimum signal amplitude below resonance and the minimum signal amplitude above resonance for the field sweep and vice versa for the frequency sweep. A symmetry value of 1 means that both values are the same and hence the spectrum is symmetric. The error of the symmetry value was calculated using error propagation from the STD of the baseline regions of the individual spectra. The baselines of the FM spectra of the a-Si sample at bias currents above 18 mA were relatively strong so that the values may be erroneous. Similarly, the AM signal of the a-Si sample showed much larger baselines above 18 mA than below.

The symmetry is shown in Figure 5.9 (c) and (d) for the AM and FM signal, respectively. For both samples, both the AM and FM symmetry is always below 1, indicating that all FM and AM spectra at the investigated bias currents are asymmetric at least to some extent.

The AM symmetry values are maximum at the lowest used bias current of 5 mA ( $\sim 0.85$  for a-Si and  $\sim 0.57$  for BDPA) and decrease non-linearly for larger values for both samples. For a-Si sample larger values of the symmetry and a slower decrease towards a minimum of approximately 0.65 at 22 mA are observed compared to the BDPA sample with a minimum of approximately 0.35 at 18 mA.

For the FM signal, the opposite behaviour of the symmetry is observed. Both samples exhibit a similar symmetry value of  $\sim 0.6$  at the lowest bias current, which increases towards larger bias currents. The increase of the BDPA sample is relatively linear which is confirmed by a fit of the experimental data.

In addition, the dependence of the linewidth of the spectra on the bias current is investigated. The linewidths are determined from spectral simulations of the EPRoC spectra with *EasySpin* utilising *pepper* as described in Section 5.2.4.1. For the FM spectra, dispersion EPR spectra were simulated neglecting the asymmetry discussed above. However, apart from the asymmetry, the rest of the spectrum is very well reproduced. The simulation of the AM spectrum included the asymmetry

by using a custom fitting function based on Equation 3.21b. Figure 5.9 (e) and (f), show the simulated linewidths for AM and FM signal, respectively. In contrast to the simulations shown in Section 5.3.1.2, only *Lorentzian* broadening was assumed, to obtain a single value for the peak-to-peak linewidth. In the plot, the linewidth of the a-Si sample is plotted on the left  $y$ -axis and that of the BDPA sample is plotted on the right  $y$ -axis. Please note that for easier comparison, the linewidth values of the BDPA sample were converted from frequency to field units. The resulting linewidths for both AM and FM signal were similar for each sample. An increase of the linewidth with increasing bias current for the AM signal as well as the FM signal is observed. This increase is rather linear for the BDPA sample. For the a-Si sample, a linear increase is seen below a bias current of 20 mA, while above that value the increase is sublinear. The latter may originate from false linewidth values due to the large baselines of the spectra in this region of the bias current as mentioned earlier. Generally, in EPR an increase of the linewidth in the spectra is observed if the sample is saturated.

The saturation behaviour of the AM signal of the a-Si sample was compared to that of resonator-based EPR at X- and Q-band as shown in Figure 5.10. For X- and Q-band,  $B_1$  was calculated from the MW power and the respective resonator conversion factor, while for the EPRoC it was calculated from the bias current using the square-root law. The peak-to-peak signal amplitudes of X-band and EPRoC AM shown in Figure 5.10 (a) are normalised to its respective maximum value. The Q-band peak-to-peak signal amplitude was normalised to the amplitude expected from the X-band saturation curve. For Q-band, no saturation is observed due to the low available microwave power and low conversion factor of the resonator with a maximum  $B_1$  magnitude of  $\sim 17 \mu\text{T}$ , lower than the minimum  $B_1$  magnitude obtained with the EPRoC. Hence, the signal amplitude increases linearly with  $B_1$ . At X-band, the signal amplitude increases linearly below  $\sim 20 \mu\text{T}$  and saturates above this value. The maximum signal amplitude is at  $\sim 60 \mu\text{T}$  and decreases to about 75 % of its maximum at  $\sim 160 \mu\text{T}$ . The EPRoC AM signal amplitude shows a linear increase up to  $\sim 100 \mu\text{T}$  after which it starts to saturate. As discussed before, the signal amplitude increases with increasing bias current for the AM signal, so the signal amplitude alone is not a good parameter to assess the degree of saturation.

Therefore, the signal intensities are shown in Figure 5.10 (b). The signal intensities of the X- and Q-band data were obtained from the DI. As the EPRoC spectra are asymmetric about the resonance field/frequency, a DI did not return reasonable results, i.e., it did not exhibit a sigmoid shape as would be expected. Therefore, the simulations from which the linewidths were extracted previously were used. For the AM signal, pure absorptive spectra with proper scaling were simulated using *EasySpin*, i.e., without accounting for

the asymmetry. Converting the FM signal by means of the *Kramers-Kronig* relation does not lead to meaningful results as it is not valid for saturated samples. Therefore, similarly, pure absorptive spectra were simulated using *EasySpin* from the fit parameters of the FM spectra with proper scaling. These simulations were then doubly integrated to obtain the signal intensity. For the X- and Q-band data, the normalisation was similar to before; for the former, the signal intensity was normalised to its maximum value, while for the latter the signal intensity was normalised to the expected signal intensity value at X-band. The EPRoC data was normalised similar to the Q-band data, namely to the signal amplitude value expected at X-band. The signal intensity of the FM signal increases linearly with increased  $B_1$  up to  $\sim 110 \mu\text{T}$ . The values above that value may be false due to a rather large baseline in the spectra. The signal intensity of the AM signal shows a different behaviour. It increases linearly up to  $\sim 65 \mu\text{T}$ . Above that value the signal intensity increases sub-linearly, i.e., saturation is observed. As before, the Q-band EPR signal intensities increase linearly with  $B_1$  due to their relatively low magnitudes. The EPR signal intensity at X-band increases linearly up to  $\sim 30 \mu\text{T}$ , above which it slightly saturates (cf. [Figure 5.10 \(b\)](#)). Considering that the signal intensity values obtained for the AM signal may introduce errors, for instance, due to imperfect overlap of simulation and experimental data, the dependence of the signal intensities of AM signal and X-band EPR signal on  $B_1$  seem to be similar. This is in contrast to the previous observation using the signal amplitudes. However, the linewidth at X-band is smaller than that a 13.44 GHz used by the EPRoC as discussed in [Section 5.3.1.2](#). Therefore, a line broadening due to saturation will affect the signal amplitude of the EPRoC at a larger  $B_1$  compared to X-band.

For the BDPA sample, a direct comparison of the EPRoC saturation behaviour to X- or Q-band is not possible for two reasons. Due to the small size of the samples, it is not possible to transfer the same BDPA grain from the EPRoC to a resonator-based spectrometer or vice versa. Using a different grain of BDPA likely leads to wrong results as an inter-grain distribution of the  $T_2$  relaxation times of BDPA from the same batch was observed in ref. [157]. The range of relaxation times was found to be between 80 to 160 ns. Hence, using different grains of BDPA are likely to exhibit varying relaxation times and cannot be compared.

As the results of this section were somewhat inconclusive, theoretical simulations and possibly more experiments are required. Here, an even faster relaxing sample should be used to probe the behaviour of the EPRoC and not that of the sample. In the meantime, to minimise the amount of saturation, the lowest bias current should be used for the acquisition of continuous wave EPR-on-a-chip (CW-EPRoC) spectra.

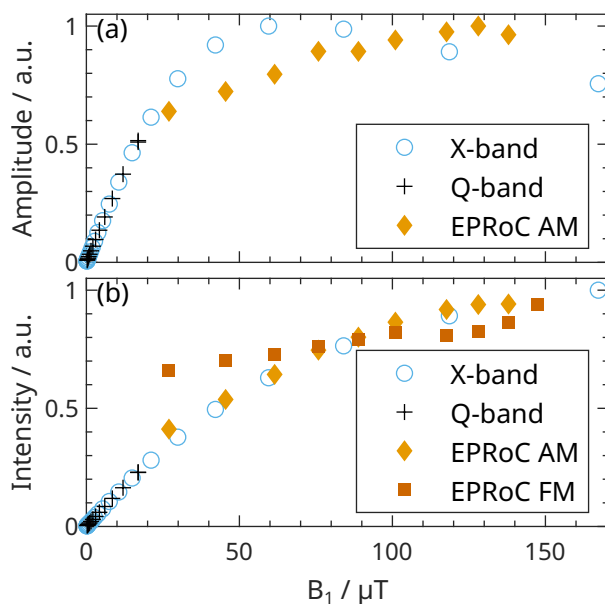


Figure 5.10: Saturation behaviour of the a-Si sample obtained with the EPRoC and with a resonator-based EPR spectrometer at X- as well as Q-band. **(a)** Normalised peak-to-peak amplitude of AM signal and EPR absorption signals in X- and Q-band. **(b)** Normalised signal intensity as obtained from the double integral of FM and AM spectra as well as absorption spectra at X- and Q-band. The normalisation procedure is explained in the text. The magnitude of  $B_1$  was calculated from the MW power and the resonator conversion factor for X- and Q-band. For the EPRoC,  $B_1$  was calculated from the bias current and the square-root law.



#### 5.4 CONCLUSIONS

Many important aspects of the EPRoC technology were introduced and discussed in this chapter. To this end, solid-state as well as solution samples were investigated. While the former samples were directly placed on the EPRoC, the submersible EPRoC dipstick allowed investigation of the latter directly in a beaker. EPRoC FM and AM spectra of a grain of BDPA, of a thin film of a-Si and of tempol dissolved in water as well as ethanol were compared to X-band spectra recorded with resonator-based EPR spectrometers. The spectra of the solid state samples exhibited a slight lineshape broadening compared to the expected linewidths at the used MW frequency determined by resonator-based EPR. The broadening was attributed to saturation effects due to large minimum  $B_1$  magnitudes of the EPRoC. For the examined solution-state samples, however, no broadening was observed. This difference may be explained on the one hand by the thin coating used to shield the EPRoC dipstick from the solvents. This effectively lowers the maximum  $B_1$  magnitudes that the samples experience for the same bias current. On the other hand, the  $B_1$  could be attenuated by the solvents.

Furthermore, it was found that field and frequency sweeps exhibit the same spectral shape and are therefore equivalent. It is not possible to record wide frequency-swept spectra with resonator-based EPR, i.e. more than a few hundred MHz due to the limited resonator bandwidth. Hence, this is one of the unique characteristics of the EPRoC. Generally, this allows the use of permanent magnets which would drastically reduce the experimental complexity and size. If an electromagnet is used, however, low-field FDMR may be utilised, of which a proof-of-principle experiment has been shown with tempol in water. With this method, multiple frequency-swept spectra are obtained at varying external magnetic fields allowing the direct visualisation of the spin Hamiltonian. Yet, the frequency-swept spectra exhibited a slightly lower SNR than the field-swept spectra possibly due to an inherent baseline in the frequency sweep.

In addition, the sensitivity of the EPRoC was discussed in this chapter. While there are issues with determining the absolute spin sensitivity possibly originating from inhomogeneous  $B_1$  and different sample sizes, the concentration sensitivity values of the EPRoC of  $2 \mu\text{mol L}^{-1} \text{ Hz}^{-0.5}$  are better than that of similar micro-resonator EPR by approximately one order of magnitude. The concentration sensitivity value was tested against a sample with similar concentration. Moreover, the dielectric constant of the sample seems to have no influence EPRoC spectra in contrast to resonator-based EPR.

Since saturation is a major concern for EPR, the dependence of the EPRoC FM and AM signal on the bias current was investigated. Here, however, the results were ambiguous and further experimental and



theoretical research may be required. To avoid (excessive) saturation of the recorded spectra, the EPRoC should be operated using RS-EPR techniques discussed in [Chapter 7](#).

In summary, this chapter laid the foundation for the following chapters, in which some aspects will be discussed in much greater detail.



## CONSIDERATIONS ON THE MICROWAVE MAGNETIC FIELD DISTRIBUTION

---

### 6.1 INTRODUCTION

In the previous chapter, we discussed general properties of the EPR-on-a-Chip (EPRoC), such as saturation and sensitivity. In this chapter, however, we will focus on another aspect for the development of EPRoC sensors. While in spectroscopy, the exact signal shape, i.e., the EPRoC spectrum is most important to elucidate the parameters of the spin system under investigation, sensors usually return a scalar describing a certain parameter of the specimen in question. Hence, the actual spectrum is of minor importance and instead the signal intensity/amplitude is the main source of information. Commercial resonator-based EPR is routinely used for sensor-like applications by means of *quantitative* EPR, where the paramagnetic centre in the specimen are quantified [12]. A common application is radiation dosimetry, in which EPR is used to quantify the radiation dose of alanine dosimeters for low dose applications [13]. In post-accident dosimetry, the radiation dose of the victims may be determined using their nails, tooth enamel, or bones [14–16] to determine the necessary treatment. Similarly, the radiation dose determined by EPR may be used to date archaeological objects or geological sites if the natural radiation rate is known with respect to the sample environment [17–19]. The so-called electron spin resonance (ESR) dating fills the gap between radiocarbon and Argon dating, i.e., between 60 000 and 200 000 years. Another field in which quantitative EPR has found significant application is food analysis and control. Here, EPR is used to investigate the effect of ionising irradiation on food stability [20, 21], to monitor the shelf life of beer [31] and to determine the stability of edible oils [32]. In environmental science, quantitative EPR may be used to determine the content and type of certain transition metal ions in water [22], the effect of pollutants such as SO<sub>2</sub> on lichens [23] and to evaluate crude oil contamination from sand and soil [24]. Additionally, the degradation of automobile lubrication oil may be investigated with quantitative EPR [205, 206]. The ability to obtain non-invasively the concentration of reactive oxygen species (ROS) as well as the pH and partial oxygen pressure (pO<sub>2</sub>) in blood and tissues places quantitative EPR in a clinical context as well [207, 208]. The level of

---

A significant portion of this chapter is from S. Künstner, J. E. McPeak, A. Chu, M. Kern, M. Wick, K.-P. Dinse, J. Anders, B. Naydenov, K. Lips, Microwave Field Mapping for EPR-on-a-Chip Experiments. Science Advances 2024, 10 (33), ead05467. DOI: [10.1126/sciadv.ad05467](https://doi.org/10.1126/sciadv.ad05467).

$pO_2$  for instance is the most significant pathophysiological variable in peripheral vascular disease, which is not easily accessible with other techniques. Likewise, the response of tumours to cytotoxic therapy, especially ionising radiation, is critically dependent on  $pO_2$ . Enhanced levels of ROS overwhelming the antioxidant defence system of the cell, otherwise known as oxidative stress, play a role in cardiovascular (i.e., ischemia-reperfusion), neurodegenerative (i.e., Parkinson, Alzheimer, Multiple Sclerosis), inflammatory diseases, and cancer [209]. Using spin traps, the concentration of ROS may be determined [33, 34]. In materials science, EPR is commonly used to quantitate paramagnetic defect concentrations in thin-film solar cell devices limiting their efficiency [3, 5, 25–27], to quantify the electron distribution between fullerene derivatives in ternary organic solar cells [28] and to assess the catalytic efficiency and degradation processes of energy-producing materials such as graphene oxide and carbon nitride [29, 30]. Quantitative EPR is also used in biochemical research, e.g., to determine the concentration of iron-sulphur complexes in whole cells [210] or the efficiency of the spin-labelling procedure for EPR protein structure analysis [211]. Commercial (benchtop) resonator-based EPR spectrometers such as the *Magnettech MS5000* are typically used for routine quantitative EPR measurements as they provide ease of use in combination with a relatively good concentration sensitivity (cf. Section 2.4.3). These spectrometers are usually calibrated with samples with a known number of spins or spin density, such as nitroxide solutions with well-known molar concentrations. In the optimal case, the  $B_1$  field of the microwave (MW) exciting spin resonance in the cavity resonator should be uniformly distributed, i.e., constant, over the entire sample. Yet, in practice, the sample may be (much) larger or (much) smaller than the effective  $B_1$  field<sup>1</sup>, complicating quantitative analyses [12]. To successfully quantify a sample larger than the effective  $B_1$  field, either a calibration sample with the same geometry and dielectric properties as well as a known number of spins is required to reduce the error introduced by the inhomogeneous  $B_1$  field distribution, or the spatial distribution of the  $B_1$  field of the resonator needs to be experimentally determined to account for the different signal amplitude caused by the inhomogeneous  $B_1$  distribution. While the spatial  $B_1$  distribution of cavity resonators may be analytically calculated, it is usually determined from the EPR signal intensity of a “point” sample such as  $\alpha,\gamma$ -bis(diphenylene)- $\beta$ -phenylallyl (BDPA) or 2,2-diphenyl-1-picrylhydrazyl (DPPH) at different positions within the cavity. This method, however, may be erroneous as the sample usually affects the  $B_1$  in the cavity [175, 212], so that using a calibration sample is usually preferable. For large samples, so-called *uniform field resonators* were developed by Hyde and co-workers [213] to improve  $B_1$  homogeneity

<sup>1</sup> The effective  $B_1$  field is “defined” here as  $B_1$  that is homogeneous, accessible and isolated from  $E_1$ .

over the entire sample. For extended samples, a further complication is caused by the inhomogeneity of the  $B_0$  field modulation amplitude [214] commonly employed for quantitative resonator-based continuous wave EPR (CW-EPR) due to the small size of the modulation coils as it affects the signal intensity, too.

As cavity resonators are typically designed for relatively large samples (100 to 1000  $\mu\text{L}$ ), their sensitivity for mass- or volume-limited samples is suboptimal due to their small filling factor,  $\eta$ , as discussed in Section 3.1. Therefore, dielectric and ferroelectric inserts, small solenoidal coils and other resonant structures [99, 110–113] have been developed for improved sensitivity for samples with volumes in the range of 1  $\mu\text{L}$ . Dedicated three-dimensional [116, 117, 215, 216] and planar, i.e., 2D, microresonators [101, 107, 115, 119, 120] have been developed for sub-microlitre samples such as protein crystals and thin films. Especially, the latter exhibit large  $B_1$  gradients over the sample volume complicating pulsed EPR and quantitative EPR experiments. While for the former pulse shaping may be used to compensate the inhomogeneous  $B_1$  at least to some degree [91, 217, 218], for the latter, detailed knowledge about the  $B_1$  distribution is required to obtain quantitative information about the sample [12].

The application of microresonators for routine quantitative EPR experiments is mainly limited due to the necessity for an MW bridge and the complicated coupling procedure to the MW source [219]. As the EPRoC does not need an external MW bridge and is “automatically” critically coupled, most of the aforementioned problems and limitations for routine quantitative EPR investigations may be circumvented, because coils of voltage-controlled oscillators (VCOs) are used for the generation and detection of the MW. In addition, instead of  $B_0$  field modulation for phase-sensitive detection (PSD), the MW carrier frequency is modulated. A theoretical consideration of field and frequency modulation is given in Section 3.5. The advantage here is that the spatial distribution of  $B_1$  is not relevant for the effectiveness of the modulation as compared to field modulation. Therefore, single coil EPRoC and EPRoC arrays seem ideally suited for sub-microlitre samples with sizes much smaller than the coil size and for thin films with lateral dimensions much larger than a single coil, respectively.

To achieve quantitative results using the EPRoC array for such samples, it is crucial to evaluate certain signal properties of the EPRoC array. This involves examining the dependence of the EPR signal on the sample position within a single coil by scanning the entire array in all spatial directions. Moreover, the behaviour of an EPRoC array with an inhomogeneously distributed sample must be assessed.

In this chapter, experimental data and simulations of the  $B_1$  field distribution of the 12-coil EPRoC array using “point”-like samples of BDPA and a homogeneous thin-film sample of amorphous silicon (a-Si) are discussed. With these experiments in combination with the finite-

element simulations of the  $B_1$  distribution, the sensitive volume of a single coil as well as the complete array is determined. In addition, the dependence of the EPRoC signal amplitude on the sample position as well as on partial coverage of the array coils is investigated.

The chapter is structured as follows. First, a short explanation about the samples and the utilised experimental setup including the mapping apparatus is given. Second, the simulations of the oscillatory magnetic and electric field, the spatial dependence of the signal amplitude and the dependence of an inhomogeneous distribution of sample is explained. Subsequently, the experimental results of the  $B_1$  mapping experiments of 1 and 3 coils of the 12-coil EPRoC array with a “point”-like sample of BDPA are presented and discussed. The dependence of the signal amplitude of a thin film of a-Si sample as a function of the distance of the sample to the EPRoC and the utilisation of a different number of coils of the EPRoC array is also discussed. Finally, the chapter concludes with a summary.

## 6.2 MATERIALS AND METHODS

In this section, a short description of the samples, the experimental configuration and parameters used within this chapter is given. Close attention is paid to mapping apparatus and the geometry of the coils producing  $B_1$  of the 12-coil EPRoC array. Then, the finite-element simulation of the oscillatory magnetic and electric field is explained, the results of which are used for the simulation of the spatial dependence of the EPR signal amplitude explained thereafter. This is followed by a description of the simulation using a circuit simulator of the signal amplitude of the EPRoC array when the sample is not covering all coils. At last, the electric field in a TE-102 cavity is calculated for comparison with the finite-element simulation of the oscillatory electric field of the EPRoC array.

### 6.2.1 Samples

For the experiments presented in this chapter, small grains of BDPA and a 15  $\mu\text{m}$  thick a-Si film sample ( $2 \times 1 \text{ mm}^2$ ) were used. A detailed explanation of the samples is given in [Section 4.3.1.1](#) for BDPA and in [Section 4.3.1.3](#) for the a-Si sample.

The sample size of the grains of BDPA were estimated prior to attaching to the sample holder from a comparison of their planar dimensions with a printed microscale. Samples with planar dimensions of tens of  $\mu\text{m}$  were selected for the experiments.

### 6.2.2 Experimental configuration

The 12-coil EPRoC array (cf. [Section 4.2.4.1](#)) was used for all experiments presented in this chapter in combination with a mapping apparatus described below allowing controlled positioning of the sample in all three spatial directions.

#### 6.2.2.1 Mapping apparatus

A home-built mapping apparatus was used to observe the EPRoC signal in position relative to the coils of the EPRoC. The grain of BDPA was attached to the tip of a flame-drawn borosilicate capillary (Hirschmann 50  $\mu\text{L}$  ringcaps with an inner diameter of 1.02 mm) with vacuum grease, which were inserted in a Bruker Flexline sample holder. This sample holder was mounted to a motorised 3-axis stage (Thorlabs PT3-Z8) such that the sample was floating above the EPRoC. To move the 3-axis stage, three actuators with a minimum repeatable incremental movement or step size of 0.2  $\mu\text{m}$ , a backlash smaller than 8  $\mu\text{m}$  and a bidirectional repeatability smaller than 1.5  $\mu\text{m}$  were used which allowed mapping with micrometre precision in the  $x$ -,  $y$ - and  $z$ -direction as defined in [Figure 6.1](#) (a). In this coordinate system, the static magnetic field,  $B_0$ , is parallel to the  $y$ -axis. The a-Si sample was attached to the opening of a 1.5 mm outer diameter EPR tube (Hirschmann 50  $\mu\text{m}$  ringcaps) with superglue which in turn was inserted in the above-mentioned Bruker sample holder. Two cameras were used to align the samples above the chip. The  $z$ -direction was monitored by a digital single lens mirrorless (DSLM) camera (Olympus OM-D E-M5II camera and Olympus M.Zuiko Digital ED 14-150 mm F4-5.6 II lens), while a USB microscope (TOOLCRAFT USB microscope) was used to observe the  $x$ - and  $y$ -direction. For the measurements with the BDPA samples, the sample was lowered carefully such that a distance of 10 to 20  $\mu\text{m}$  between the sample and the EPRoC was established, such that the sample did not touch the EPRoC. The a-Si sample, however, is quite robust and could be lowered to the EPRoC until the sample touched the surface. To ensure a parallel movement of the sample in the  $x$ - $y$ -plane of the EPRoC, i.e., to ensure a constant  $z$  while moving in the  $x$ - and  $y$ -direction, the EPRoC board was tilted using the four screws connecting the board to the sample holder. To align the EPRoC board, an iterative process was used. Here, the flame-pulled capillary without a sample was successively moved to the corners of the EPRoC (roughly  $2 \times 1 \text{ mm}^2$ ) and lowered until it touched the surface. Then, the screws were aligned to reduce the tilting. The procedure was repeated until the flame-pulled capillary would touch the surface after a 10  $\mu\text{m}$  step towards the surface in all four corners.

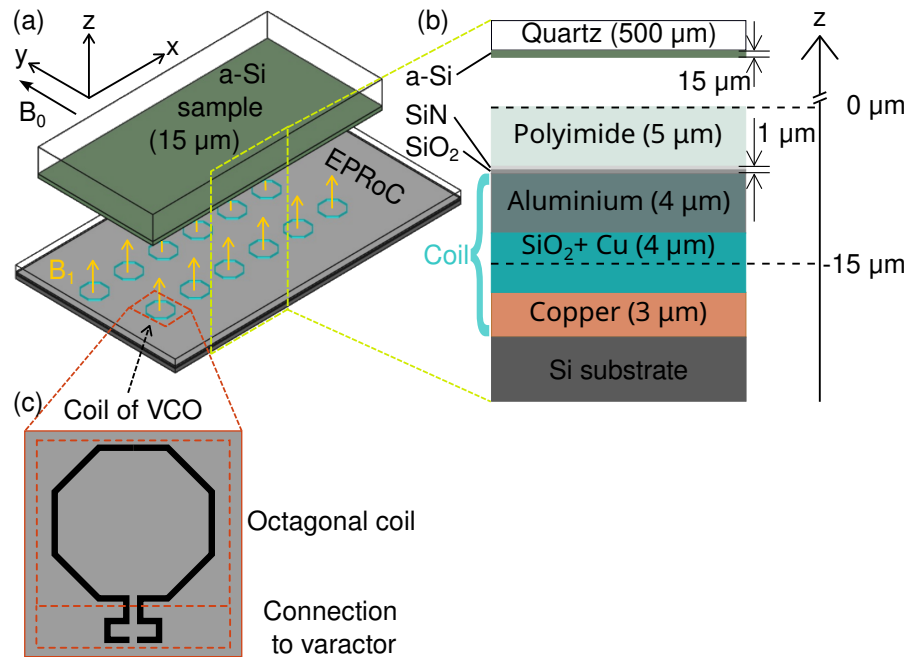


Figure 6.1: Sketch of the geometries of the 12-coil EPRoC array. **(a)** Sketch of the 12-coil array board with the directions of  $B_1$  and  $B_0$  indicated with the a-Si sample floating above. The direction of  $x$ ,  $y$  and  $z$  are indicated by the coordinate system in the top-left corner. **(b)** Layer structure of the coil of the EPRoC with indications about the approximate thickness of each layer. The layers of the coil were considered in the simulation of the oscillatory magnetic field. **(c)** The planar shape of a single coil of the EPRoC can be divided into the octagonal coil and the connection to the varactor of the VCO, which was taken into consideration in the simulation of the oscillatory magnetic field. Adapted from ref. [220] ©.



### 6.2.2.2 Geometry of the coils of the 12-coil EPR-on-a-Chip array

On the 12-coil EPRoC array, the 12 coils of the VCOs are arranged in a zipper-like fashion in two parallel rows of six coils each as shown in [Figure 6.1](#) (a) with the a-Si thin film sample hovering above the EPRoC. Within each row, i.e., in  $x$ -direction, the distance from the centre of each coil to its nearest neighbour is  $300\ \mu\text{m}$ . The distance of the two rows measured from the centre of the coils is in  $y$ -direction is  $\sim 425\ \mu\text{m}$ . In addition, the two rows are offset by  $150\ \mu\text{m}$  in  $x$ -direction. Each coil consists of two parts as shown in [Figure 6.1](#) (c); octagonally shaped coil and a rectangular part connecting the whole coil to the varactor. The octagonally shaped coil has an outer diameter of  $200\ \mu\text{m}$  and its trace has a (planar) thickness of  $8.5\ \mu\text{m}$ . The layer structure of the coils of the 12-coil EPRoC array is shown in [Figure 6.1](#) (b). The coils consist of a  $3\ \mu\text{m}$  thick copper layer and a  $4\ \mu\text{m}$  thick aluminium layer connected with a  $4\ \mu\text{m}$  thick via made of  $\text{SiO}_2$  and copper on top of a silicon substrate. The EPRoC is passivated by thin films of  $\text{SiO}_2$  and  $\text{SiN}$ . For chemical resistance, a  $\sim 5\ \mu\text{m}$  thick polyimide layer is placed on top. The chip was fabricated in a  $130\ \text{nm}$  complementary metal-oxide-semiconductor (CMOS) technology (CMRF8SF from GlobalFoundries).

### 6.2.3 Acquisition parameters and post-processing

All CW spectra were acquired as field sweeps with frequency modulation using a modulation frequency of  $75\ \text{kHz}$  and a peak-to-peak modulation amplitude of  $5.3\ \text{MHz}$  ( $0.19\ \text{mT}$ ) for the a-Si sample and  $6.4\ \text{MHz}$  ( $0.23\ \text{mT}$ ) for the BDPA sample. Please note that the modulation amplitude for BDPA was deliberately set to approximately twice the linewidth for improved signal-to-noise ratio (SNR) and to reduce the measurement time. To further improve the SNR, the recorded spectra were linearly baseline-corrected and smoothed with a 2<sup>nd</sup> order *Savitzky-Golay* filter. The filter window was chosen such that no visible broadening of the spectra occurred.

#### 6.2.3.1 Fit of the signal amplitude maps

The EPRoC signal amplitude maps of [Section 6.3.1.2](#) were least-square fitted with 2D *Gaussian* function as

$$I = b + a \exp \left( -\frac{(x - x_0)^2}{2c_x^2} - \frac{(y - y_0)^2}{2c_y^2} \right), \quad (6.1)$$

where  $b$  is a constant offset of the functions from 0, i.e., the baseline value,  $a$  is the maximum signal amplitude,  $x_0$  and  $y_0$  is the offset of the maximum value from the (0,0) and  $FWHM_x = 2\sqrt{2 \ln 2} c_x$  and  $FWHM_y = 2\sqrt{2 \ln 2} c_y$  determine the full width at half maximum (FWHM) of the function. All of the above parameters were adjusted to minimise the root mean square (RMS) error.

### 6.2.4 Simulations

#### 6.2.4.1 Simulation of the oscillatory magnetic and electric field

The simulation of the oscillatory magnetic,  $\mathbf{B}_1 = B_{1,x}\hat{e}_x + B_{1,y}\hat{e}_y + B_{1,z}\hat{e}_z$ , and electric,  $\mathbf{E}_1 = E_{1,x}\hat{e}_x + E_{1,y}\hat{e}_y + E_{1,z}\hat{e}_z$ , field was performed by Michal Kern and Markus Wick at University of Stuttgart with the finite-element simulation software COMSOL Multiphysics. For the simulation, the layer structure and shape of the coil as shown in [Figure 6.1](#) (b) and (c) was considered. To reduce computational time, however, the  $\mathbf{B}_1$  and  $\mathbf{E}_1$  fields of only one half-coil on an infinite Silicon substrate were simulated at 14 GHz with a coil current of 30 mA. These data were mirrored, translated and superimposed to obtain the  $\mathbf{B}_1$  and  $\mathbf{E}_1$  distribution of the complete 12-coil EPRoC array. To match the coil current of the simulations to that of the experiments, the simulated  $\mathbf{B}_1$  and  $\mathbf{E}_1$  were scaled using the square-root law proposed in ref. [131] relating the coil current to the bias current. The values of  $\mathbf{B}_1$  and  $\mathbf{E}_1$  are calculated on an unevenly spaced  $x$ - $y$ - $z$ - grid by COMSOL Multiphysics depending on the gradient of the field, i.e., the density of values is larger for a larger gradient at a particular position. This type of data is called *scattered* data as compared to *gridded* data where the points are evenly spaced. To plot maps of the  $\mathbf{B}_1$  and  $\mathbf{E}_1$  distributions and to calculate EPR signals from the  $\mathbf{B}_1$  distribution, the simulated data were linearly interpolated in  $x$ -,  $y$ - and  $z$ -direction using the function *scatteredInterpolant* of MATLAB which utilises a *Delaunay* triangulation of the scattered data points to perform the interpolation.

#### 6.2.4.2 Simulation of the spatial dependence of the signal amplitude of extended paramagnetic samples in inhomogeneous $B_1$ distributions

The simulation of the signal amplitude of extended samples as a function of its position was performed as described by the FM signal of [Equation 3.17](#). In this equation, the spin-induced change of the inductance,  $L_{\text{spin}}$ , as a function of the sample position was calculated using [Equation 3.3](#), for which the integral over the sample volume was replaced by a sum. As this simulation uses the steady-state solution of Bloch's equations, it is generally valid for EPR and not only for EPRoC. The simulation was performed as follows. The numerically simulated  $\mathbf{B}_1$  distribution of the EPRoC array discussed in [Section 6.2.4.1](#) was interpolated on a uniform grid in  $x$ -,  $y$ - and  $z$ -direction. For each point on this grid, the magnitude of  $\mathbf{B}_1$  perpendicular to  $\mathbf{B}_0 \parallel y$ , i.e.,  $B_{1,\perp} = |B_{1,x}\hat{e}_x + B_{1,z}\hat{e}_z|$  was calculated. This in turn was used to calculate EPR spectra described by  $L_{\text{spin}}(B_0, x, y, z)$  with the corresponding relaxation times. These spectra were numerically differentiated taking into account PSD of the EPRoC in the experiment. For simplification, a cuboid sample shape was assumed. All contributions from the

extended sample were used to determine the peak-to-peak signal amplitude.

#### 6.2.4.3 Simulation of the signal amplitude on partial utilisation of the EPRoC array

The simulation of the signal amplitude obtained by partial utilisation of the 12-coil EPRoC array was performed by Anh Chu with the *SpectreRF* Circuit Simulator (Cadence Design Systems) similar to simulations performed in ref. [61] for an 8-coil EPRoC array. In this simulation, the so-called steady-state spin model was used, which was first proposed in ref. [221, Section 3.3] for nuclear magnetic resonance (NMR) and then extended to EPRoC in refs. [133, 148]. The fundamental assumption of this model is that the spin system is unsaturated and may therefore be modelled as an RLC-circuit, which is coupled to the coil of the VCO of the EPRoC with a coupling constant  $K_{\text{spin}} = \eta\chi_0$ . The parameters of the RLC-circuit  $R_{\text{spin,sim}}$ ,  $L_{\text{spin,sim}}$  and  $C_{\text{spin,sim}}$  are determined by the transverse relaxation time,  $T_2$ , and  $B_0$ . For the former,  $T_2^*$  of the a-Si sample of 20 ns was determined in Section 4.3.1.3 and for the latter,  $B_0$  was equal to that of the experiments. The bias current was set to 5 mA equal to that used in the experiment. The sample volume per coil was calculated from the thickness of the a-Si sample of 15  $\mu\text{m}$  and the sensitive area determined in Section 6.3.1.2 and is given by  $V_s = 80 \times 62.5 \times 15 \mu\text{m}^3 = 2.34 \times 10^5 \mu\text{m}^3$ . The number of spins per coil was calculated from  $V_s$  the spin density of the a-Si sample (cf. Section 4.3.1.3), from which  $\chi_0$  was calculated using Curie's law using Equation 2.42. The detector volume [133] was calculated as

$$V_{\text{det}} \approx \frac{\mu_0}{B_{1,u}^2} L_0, \quad (6.2)$$

where  $L_0$  is the inductance of the coil in absence of EPR, and the unitary field,  $B_{1,u} = B_1/I_{\text{coil}}$  was calculated from *Biot-Savart's* law and is assumed to be constant over the sample. This is in contrast to the previous experiments, in which the simulated  $B_1$  distribution was used to calculate the EPR signal amplitude. Due to the cylindrical symmetry, an analytical solution exists for  $B_{1,z}$  in the centre axis of the current loop with a radius,  $R$ , with the current in the loop of  $I_{\text{coil}}$ :

$$B_{1,z,BS}(z) = \frac{1}{2} \frac{\mu_0 I_{\text{coil}}}{2} \frac{R^2}{(R^2 + z^2)^{3/2}} \quad (6.3)$$

with the vacuum permeability,  $\mu_0$ . Here,  $R = 100 \mu\text{m}$  is the radius of the coil of the EPRoC and  $I_{\text{coil}}$  is calculated from the bias current using the square-root law proposed in ref. [131]. The additional factor 1/2 in the equation takes into account that only half the magnitude of the MW is available for EPR excitation due to the two counter-rotating MW fields in the rotating frame. The filling factor,  $\eta = V_s/V_{\text{det}}$ , was

calculated from the sample and detector volume. The simulations were performed for sample present in 3, 6, 9 and 12 coils. For each number of coils with sample, a 0<sup>th</sup> order field-swept FM spectrum was calculated, i.e., without PSD by an lock-in amplifier (LIA), which were numerically differentiated considering the modulation amplitude of the experimental data to obtain the first-derivative FM spectrum (1<sup>st</sup> order) as recorded in the experiment with the LIA. The peak-to-peak signal amplitudes were determined from these first-derivative FM spectra, which show a linear increase as a function of the number of coils with sample.

### 6.2.5 Calculation of the electric field component of the microwave inside a TE-102 cavity resonator

The field components of the MW field,  $H_1$  and  $E_1$ , inside a rectangular cavity resonator with the transverse electric (TE)-102 mode with dimensions of  $a = 23.5$  mm ( $x$ ),  $b = 11.0$  mm ( $y$ ), and  $d = 42.0$  mm ( $z$ ) [222] may be calculated by [78, p. 132]

$$H_{1,x} = \frac{H_0}{\left[1 + (d/2a)^2\right]^{1/2}} \sin\left(\frac{\pi x}{a}\right) \cos\left(\frac{2\pi z}{d}\right) \quad (6.4a)$$

$$H_{1,z} = \frac{H_0}{\left[1 + (d/2a)^2\right]^{1/2}} \cos\left(\frac{\pi x}{a}\right) \sin\left(\frac{2\pi z}{d}\right) \quad (6.4b)$$

$$E_{1,y} = j \left(\frac{\mu_0}{\epsilon_0}\right)^{1/2} H_0 \sin\left(\frac{\pi x}{a}\right) \cos\left(\frac{2\pi z}{d}\right), \quad (6.4c)$$

where  $H_0$  is the amplitude of the MW magnetic field,  $\mu_0$  is the magnetic and  $\epsilon_0$  is the electric constant. In contrast to the coordinate system used in the experiments in this experiment, the static magnetic field  $B_0 \parallel z$  and the sample is inserted along the  $x$ -axis at  $z = d/2$  in the coordinate system used in ref. [78]. For allowed transitions, only the magnetic field component perpendicular to  $B_0$  is relevant, that is  $H_{1,x}$ , which gets maximal at  $x = a/2$  and  $z = d/2$ , which is in the centre of the cavity. At these positions the trigonometric functions have their maximum. Equation 6.4a may be rearranged assuming a certain  $H_{1,x,\max}$  to calculate  $H_0$  as

$$H_0 = H_{1,x,\max} \left[1 + (d/2a)^2\right]^{1/2}, \quad (6.5)$$

which is then used to calculate  $E_{1,y}$  from Equation 6.4c. This equation has its extrema at  $x = a/2$  and  $z = d/4$  or  $z = 3d/4$ , are about 10.5 mm away from the centre of the cavity in the  $z$ -direction using the dimensions above.  $E_{1,y}$  is sinusoidally increasing (from  $-E_{1,y}$  at  $z = 3d/4$ ) or decreasing (from  $E_{1,y}$  at  $z = 1d/4$ ) to 0 in the centre of the cavity at  $z = d/2 = 21$  mm. Using the same  $B_1 = 27 \mu\text{T}$  in the

centre of the cavity as realised in the EPRoC,  $H_{1,x,\max} = 2/\mu_0 B_1$  may be calculated, which in turn can be used to calculate the maximum of  $E_{1,y} = 21 \text{ kV m}^{-1}$ . To account for the two counter-rotating MW components, the factor of 2 was included.

### 6.3 RESULTS AND DISCUSSION

In this section, experimental and simulated results are presented and discussed. The section starts with a general remark on the definition of the sensitive volume in the EPR research community, which is followed by a simulation of the oscillatory magnetic and electric fields of the 12-coil array, from which a sensitive volume may be defined. The results of the mapping of the signal amplitude in three spatial directions with a “point”-like grain of BDPA are presented and discussed with respect to the results of the simulations. Subsequently, the dependence of the signal amplitude of the thin-film a-Si sample on its distance from the surface of the EPRoC is discussed. Finally, the signal amplitude of the thin-film a-Si sample as a function of the coverage of the EPRoC array is discussed and compared with the simulation results from a circuit simulator.

#### 6.3.1 Sensitive volume

In the EPR community, the terms “sensitive volume” or “active volume” refer to the region within a sample from which the EPR signal is predominantly detected. The sensitive volume may be defined from the  $B_1$  distribution of the resonator/coil. The idea of this approach is that the EPR signal of an unsaturated sample scales with  $B_1^2$ . An arbitrary cut-off value for  $B_1$  is then chosen that would give rise to a small EPR signal compared to a signal with the maximum  $B_1$  value.

It is important to note that in resonator-based EPR the MW from the MW source can be attenuated such that the sample is unsaturated independently of its relaxation times and the linear dependence of the signal as a function of  $B_1$  is upheld. For this reason, references describing the  $B_1$  distribution of different (micro-)resonators show  $B_1$  values normalised to the input power. For oscillator-based EPR such as the EPRoC, a certain minimum bias current is needed to ensure stable oscillations of the VCO as discussed before. This minimum bias current depends on the circuit design and the fabrication technology. While the bias current for CMOS EPRoCs is between 3 to 5 mA per coil for stable oscillations leading to  $B_1$  values of about 20  $\mu\text{T}$  in the centre of the loop, EPRoCs utilising high electron mobility transistor (HEMT) of ref. [186] need a lower bias current, leading to a  $B_1$  of only 0.4  $\mu\text{T}$  in the centre of the current loop. It is possible to apply the definition of the sensitive volume mentioned above to EPRoC, however, the requirement of an

unsaturated sample may not be valid depending on the relaxation times of the sample.

In addition, the maximum  $B_1$  of cavities such as the TE-102 (cf. [Section 6.2.5](#)) is in the centre and decays sinusoidally when moving away from the centre. In this case, the choice of the reference  $B_{1,\text{ref}}$  as the maximum  $B_1$  is quite unequivocal. For microresonators and -oscillators, this choice is not as straight forward due to the inhomogeneous  $B_1$  distribution depending on their geometry. For instance, in the case of the EPRoC with the octagonally-shaped planar coils, a certain “homogeneous” region of  $B_1$  in the centre of the loop ( $x = 0$ ,  $y = 0$ ) can be found with a  $B_1$  magnitude differing by 25 % from the maximum when close to the loop itself (cf. [Section 6.3.1.1](#)). A similar region of “good homogeneity”  $B_1$  was mentioned in [118] and called “active volume”. In ref. [115], on the other hand, discussing inverse anapole (micro-) resonators, the maximum  $B_1$  perpendicular to  $B_0$  was chosen as the  $B_{1,\text{ref}}$ . In this chapter, we will follow the latter definition. In summary, there is no strict definition of the term “sensitive volume”, and attention should be paid to the definitions in the literature if a comparison is required.

### 6.3.1.1 Simulation of the oscillatory magnetic field

[Figure 6.2](#) (b) shows the results of the numerically simulated distribution of the magnetic component of the MW ( $B_{1,\perp} = |B_{1,z}\hat{e}_z + B_{1,x}\hat{e}_x|$ ) of the 12-coil EPRoC array perpendicular to  $B_0 \parallel y$  with a bias current of 5 mA. Please note that  $B_{1,y} = B_{1,y}\hat{e}_y$  is not considered here as this component is parallel to  $B_0$  and hence would not result in an EPR signal for *Kramers'* systems with a half-integer spin. In the following, the designation  $B_1$  instead of  $B_{1,\perp}$  will be used to reduce notational clutter. Yet, the analysis of non-*Kramers'* systems with integer spin may benefit from the additional  $B_{1,y}$  component. The simulation was performed as described in [Section 6.3.1.1](#) such that only one half-coil was simulated, the result of which was mirrored, translated and superimposed. In this way, the mutual inductance between the coils is not considered, which may lead to erroneous values of  $B_1$  distribution especially between the coils<sup>2</sup>. Also, the  $B_1$  distribution inside the coils is marginally affected by the neighbouring coils since the magnitude of  $B_1$  of the nearest neighbour (along  $x$ ) is less than approximately 0.5 % of that in the centre of the coil and only about 10 % at the location of the coil trace. [Figure 6.2](#) (b) shows the  $B_1$  distribution at the surface of the EPRoC at  $z = 0$ . There,  $B_1$  is mainly concentrated inside the conductor loops with minimal absolute  $B_1$  outside the coils as expected. A close-up of the distribution for the top left coil is shown in [Figure 6.2](#) (c) with slices in the  $x$ - (e), the  $y$ - (d) and the  $z$ -direction (f) as indicated by

<sup>2</sup> When assuming two planar coils in a plane with currents flowing in the same spatial direction, the field at the midpoint of the distance between the centres of the adjacent coils should be zero due to symmetry.



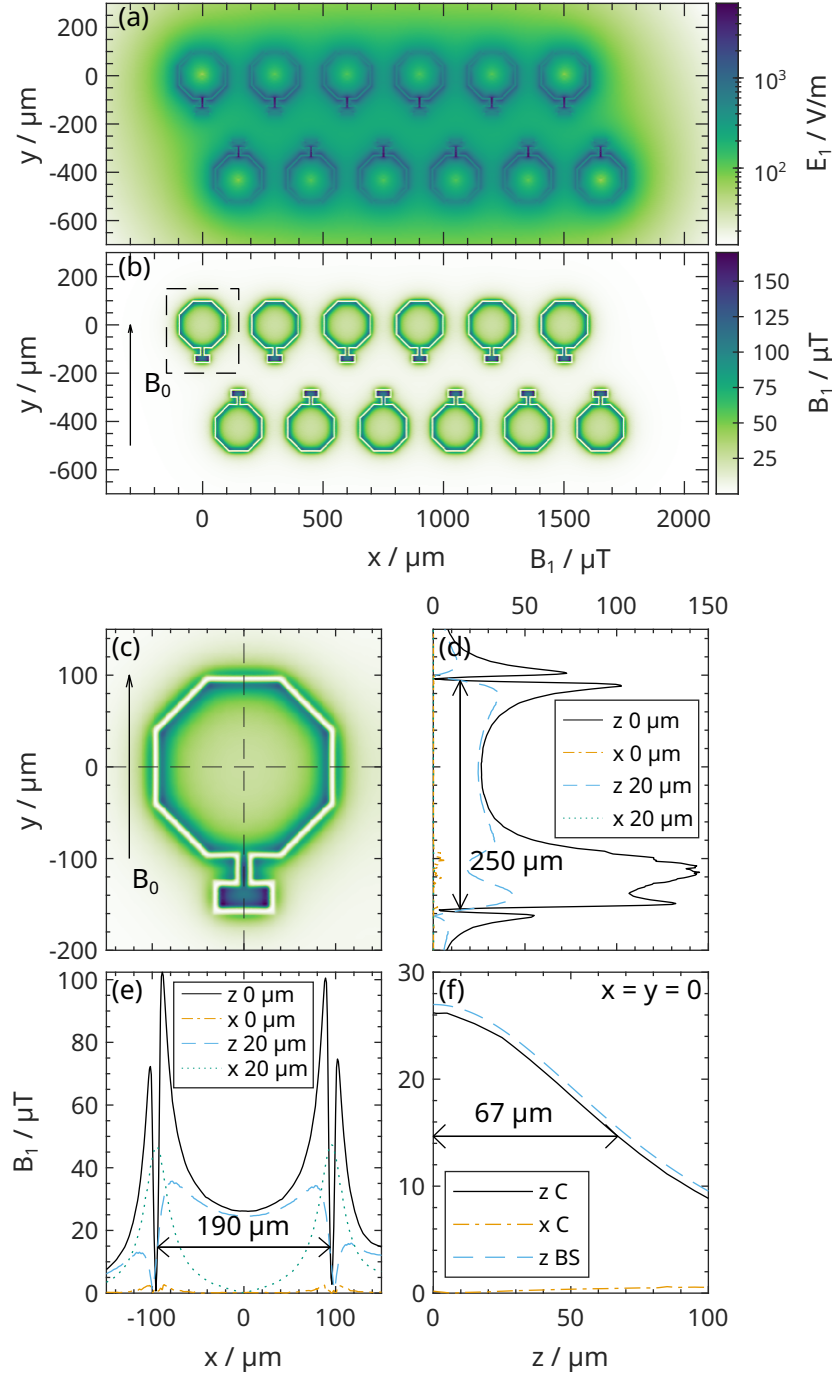



Figure 6.2: Simulated distribution of the electric and magnetic field of the 12-coil EPRoC array at its surface ( $z = 0$ ). **(a)** Magnitude of the electric field component,  $E_1 = |E_1|$ . **(b)** Magnitude of  $B_{1,\perp} = |B_{1,x}\hat{e}_x + B_{1,z}\hat{e}_z|$  ( $\perp$  to  $B_0$ ).  $B_0$  is parallel to  $y$ . The dashed rectangle indicates the section used shown in (c). **(c)** Magnitude of  $B_{1,\perp}$  of a single coil. **(d)** Slices of  $B_{1,z}$  and  $B_{1,x}$  as a function of  $y$  at  $z = 0 \mu\text{m}$  and  $z = 20 \mu\text{m}$ . **(e)** Slices of  $B_{1,z}$  and  $B_{1,x}$  as a function of  $x$  at  $z = 0 \mu\text{m}$  and  $z = 20 \mu\text{m}$ . **(f)** Slices of  $B_{1,z}$  and  $B_{1,x}$  as a function of  $z$  in the centre of the coil ( $x = y = 0$ ). Additionally,  $B_{1,z}$  calculated with *Biot-Savart's law* ( $z$  BS) for a circular conductor loop is indicated. Adapted from ref. [220] © .

dashed lines. As seen in the  $x$ -slice (Figure 6.2 (e)),  $B_1$  is mainly in the  $z$ -direction ( $B_{1,z}(z = 0)$  denoted with “ $z \ 0 \ \mu\text{m}$ ”) at  $z = 0$  with a maximum at the inner edges of the trace of the octagonal coil with values of approximately  $100 \ \mu\text{T}$ . It decreases towards the centre of the coil at a rate proportional to  $1/r$ , where  $r$  is the distance to the coil trace. Due to symmetry,  $B_{1,x}(z = 0)$  (denoted with “ $x \ 0 \ \mu\text{m}$ ”) along  $y$  at  $z = 0$ , should be small but non-zero due to the polyimide layer covering the surface as discussed in Figure 6.1. In the  $y$ -direction, the maximum of  $B_1$  is about  $150 \ \mu\text{T}$  at the connection to the varactor ( $y \sim -125 \ \mu\text{m}$ , cf. Section 6.3.1.1). At  $x = 0$  along  $y$ ,  $B_{1,x}(z = 0) = 0$  due to mirror symmetry of the coil, which is shown in (d).  $B_1$  in the  $z$ -direction at  $x = y = 0$  reaches a maximum at  $z = 0$  of about  $26 \ \mu\text{T}$  as seen in Figure 6.2 (f). In addition,  $B_{1,z}$  was calculated with the *Biot-Savart* law applied to a circular conductor loop for a comparison with the numerical simulation using Equation 6.3. As seen in Figure 6.2 (e), the numerical and analytical solution for  $B_z$  exhibit the same lineshape, shifted by less than  $1 \ \mu\text{m}$ , showing a good agreement of analytic solution and the numerical simulation. The  $B_1$  drops to  $\sim 10\%$  of its maximum value of  $\sim 150 \ \mu\text{T}$  observed at  $x = 0$  and  $y \sim -125 \ \mu\text{m}$  outside a volume of  $(190 \times 250 \times 67) \ \mu\text{m}^3 = 3.2 \ \text{nL}$  around the centre of the coil at  $x = y = 0$  as seen in Figure 6.2. This would correspond to a signal reduction by 99% assuming non-saturating conditions.

Additionally,  $B_{1,x}$  (denoted with “ $x \ 20 \ \mu\text{m}$ ”) and  $B_{1,z}$  (denoted with “ $z \ 20 \ \mu\text{m}$ ”) at a distance of  $z = 20 \ \mu\text{m}$  are shown in Figure 6.2 (d) and (e) as a function of  $y$  and  $x$ , respectively. Due to mirror symmetry of the coil,  $B_{1,x}(y)$  is 0 at  $x = 0$  and  $z = 20 \ \mu\text{m}$  in Figure 6.2, while  $B_{1,z}(y)$  shows a reduced maximum value of approximately  $40 \ \mu\text{T}$  and is generally more homogeneous.  $B_{1,x}(x) \perp B_0$  at  $z = 20 \ \mu\text{m}$ , however, shows values of up to  $65 \ \mu\text{T}$ , which needs to be taken into consideration as its magnitude exceeds that of  $B_{1,z}$  at the same  $z$ .

Figure 6.2 (a) shows the magnitude of the electric field component,  $|E_1|$ , of the 12-coil EPRoC array simulated for bias current of  $5 \ \text{mA}$ . To calculate the magnitude all spatial directions were considered. Because  $E_1$  varies over a wide range, the colour scale is logarithmic. A concentration of  $E_1$  is observed in the small gap between the trace with values up to  $3 \ \text{kV m}^{-1}$  where the connection to the varactor is located. Outside and inside the octagonal conductor loops,  $E_1$  is approximately one order of magnitude lower. A TE-102 rectangular cavity resonator with a  $B_1$  of  $27 \ \mu\text{T}$  similar to the EPRoC exhibits a maximum  $E_1$  of  $\sim 21 \ \text{kV m}^{-1}$  approximately  $10.5 \ \text{mm}$  away from the centre of the cavity as calculated in Section 6.2.5. This maximum value is approximately one order of magnitude larger than that of the EPRoC for the same  $B_1$ . Due to the large  $E_1$  sample tubes with diameters  $\ll 10.5 \ \text{mm}$  need to be used to avoid excessive non-resonant MW absorption through the electric field. Commonly,  $4 \ \text{mm}$  or  $3 \ \text{mm}$  outer diameter tubes are therefore used. However, even with these tubes,  $\sim 25\%$  of the



maximum  $E_1$  is present at the wall of the tubes. Due to the  $E_1$  values of the EPRoC inside the conductor loop of  $0.1 \text{ kV m}^{-1}$ , it is expected that samples smaller than the coil diameter placed inside the loop experience lower non-resonant MW absorption through  $E_1$  than larger and/or non-ideally positioned samples. Furthermore, extended lossy samples such as polar aqueous samples and generally samples with a large dielectric constant may profit from the overall lower  $E_1$  of the EPRoC compared to TE-102 cavity resonators. Examples of experiments of such samples are shown in [Section 5.3.3.2](#) and [Chapter 8](#).

### 6.3.1.2 Mapping of a single coil

In the following, the dependence of the FM signal amplitude on the sample position in a single coil of the EPRoC array will be discussed. For this, multiple EPRoC FM spectra of a single grain of BDPA ( $\varnothing \sim 35 \text{ }\mu\text{m}$ ,  $\sim 1 \times 10^{14}$  spins, cf. [Section 4.3.1.1](#)) were recorded with a step resolution of  $10 \text{ }\mu\text{m}$  in  $x$ -,  $y$ - and  $z$ -direction above one of the outermost coils of the EPRoC array, from which the peak-to-peak signal amplitude (cf. [Figure 5.2](#) (b) top in [Section 5.3.1](#)) was extracted. The mapping of the EPRoC FM signal is shown in [Figure 6.3](#) (a)-(f) for different heights from about  $10$  to  $60 \text{ }\mu\text{m}$ . For a comparison of the sizes of the coil and the sample, octagons representing the coil of the VCO with a diameter of  $200 \text{ }\mu\text{m}$  and a width of  $8.5 \text{ }\mu\text{m}$  are displayed to scale, while the cross gives an indication of the sample size.

The experimental data indicates that the EPRoC array is primarily sensitive inside the conductor loop. Outside the coil, the signal amplitude is minimal. The signal amplitude maps were least-square fit with a two-dimensional *Gaussian* profile to obtain information about the shape of the sensitive area. The *Gaussian* function was only taken for simplicity since it contains one parameter, the full width at half maximum, describing the width of the curve and has no further physical meaning.

A similar reduction of the signal amplitude when moving a BDPA sample away from the central position of an inverse anapole resonator was observed in ref. [[115](#), [Figure 3D](#)]. However, the investigated BDPA sample in their work was much larger than the sensitive region of the utilised resonator ( $15 \times 20 \times 5 \text{ }\mu\text{m}^3$ ) and is hence only partially comparable. This experiment is more similar to experiments that will be discussed in [Section 6.3.2](#) and [Section 6.3.3](#). As the sample was much larger than the sensitive region of the resonator, the sample occupied the complete sensitive volume when placed in the centre of the resonator, so that the filling factor was approximately unity. Upon displacement from the centre, the sensitive volume is not completely filled any longer, which effectively decreases the filling factor. Due to the unique design of the inverse anapole resonator, the  $B_1$  at the trace of the coil is lower than in its centre. Therefore, a displacement the sample from the centre reduces the filling factor even stronger.

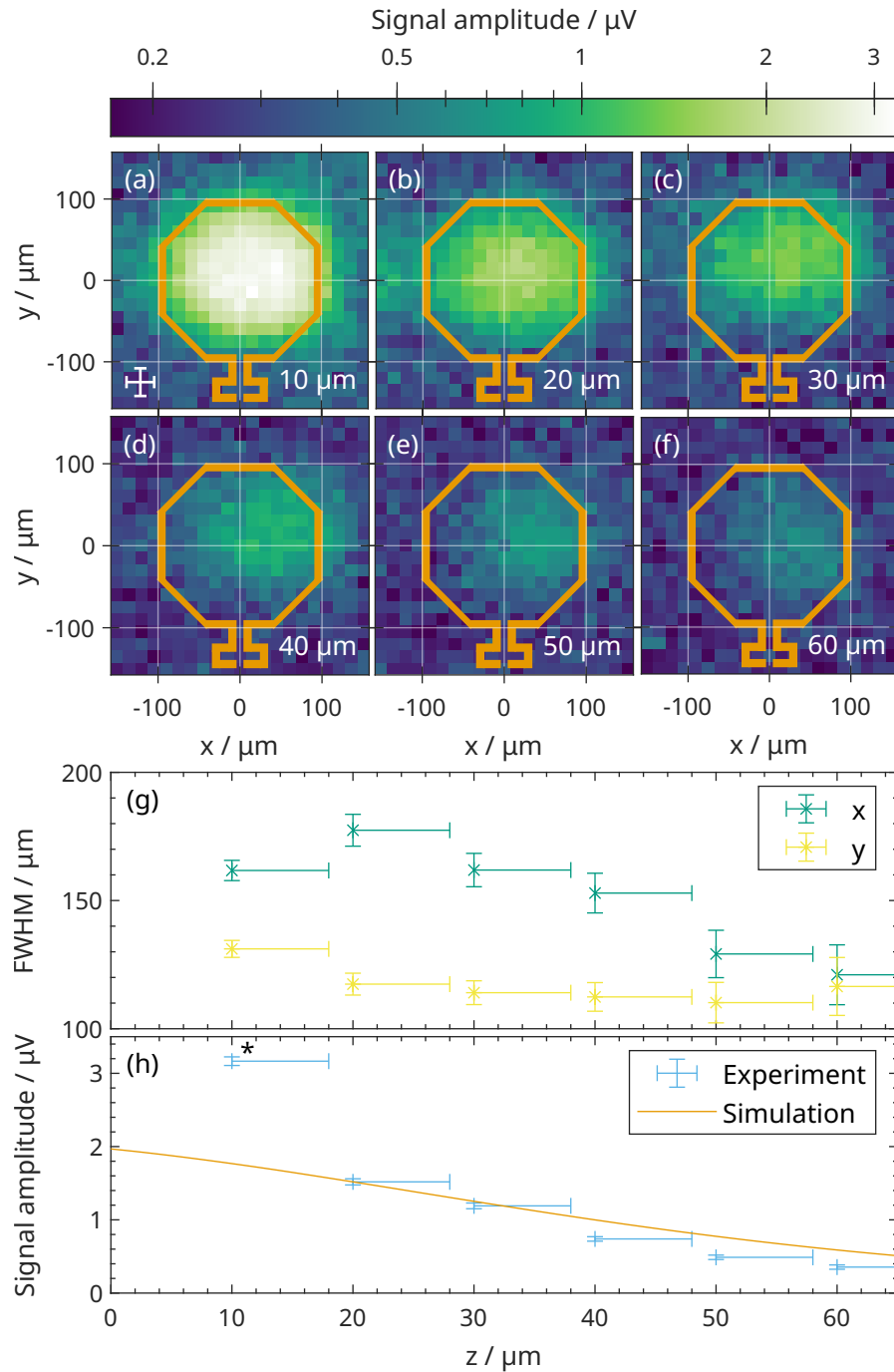


Figure 6.3: Mapping of the normalised peak-to-peak signal amplitude using a single grain of BDPA at a distance from the sample to the surface of the chip of (a) 10  $\mu\text{m}$ , (b) 20  $\mu\text{m}$ , (c) 30  $\mu\text{m}$ , (d) 40  $\mu\text{m}$ , (e) 50  $\mu\text{m}$ , (f) 60  $\mu\text{m}$ . The cross in (a) indicates the approximate sample size of 35  $\mu\text{m}$  in each direction containing approximately  $1 \times 10^{14}$  spins. The octagons illustrate the location of the conductor and are shown to scale with a diameter of 200  $\mu\text{m}$  and a thickness of 8.5  $\mu\text{m}$ . (g) FWHM in the  $x$ - and  $y$ -directions and (h) signal amplitude as obtained from the fit of the signal amplitude maps in (a)-(f) with a 2D Gaussian.

This lower  $B_1$  was confirmed by a saturation measurement at both positions.

In [Figure 6.3 \(h\)](#), the height dependence of the signal amplitude is shown, which was extracted from the *Gaussian 2D* fit of the maps in (a)-(f). The observed signal amplitude decreases non-linearly with increasing distance from the chip surface due to the lower  $B_1$ . Above  $60\ \mu\text{m}$ , the FM spectra could not be distinguished from the noise.

The relatively large error of the absolute values of the  $z$ -axis originates mostly from the determination of the distance as explained below. As the sample is easily lost when the tip touches the EPRoC, the experiment was performed as follows. The tip of the pulled quartz was carefully lowered towards the surface of the EPRoC while monitoring the approximate distance with a camera. With some experience, the tip of the pulled capillary with the sample can be lowered to a starting distance,  $z_{\text{start}}$ , of approximately  $20\ \mu\text{m}$ . At this distance the first map is recorded. Then, the direction of the movement of the tip is reversed in  $10\ \mu\text{m}$  steps, where maps were recorded, i.e., at approximate distances of  $z_{\text{start}} + 10, 20, 30, 40$  and  $50\ \mu\text{m}$ . At  $z_{\text{start}} + 60\ \mu\text{m}$ , the signal could not be distinguished from noise. At this distance, the direction of motion was reversed again and the sample lowered to  $z_{\text{start}} - 10\ \mu\text{m}$ , where again a signal amplitude map was recorded. Then, the tip with the sample was lowered to  $z_{\text{start}} - 20\ \mu\text{m}$ , where it came into contact the surface of the EPRoC. Hence,  $z_{\text{start}} - 20\ \mu\text{m}$  was defined as  $z = 0\ \mu\text{m}$  and the rest of the distances accordingly. Therefore, the approximate distances of the maps in the order of the experiment are  $z = 20, 30, 40, 50, 60$  and  $10\ \mu\text{m}$ . The  $z$ -error is mainly introduced by the determination of the distance in the last step where the sample is lowered from  $z = 10\ \mu\text{m}$  to  $0\ \mu\text{m}$  and is assumed to be as large as  $10\ \mu\text{m}$ . As the direction of motion was reversed twice in the experiment, the backlash of the translation stage acts in opposite directions and should approximately cancel. The relative  $\sim 10\ \mu\text{m}$  distance between maps recorded at  $30$  to  $60\ \mu\text{m}$ , however, is reliable due to the movement of the translation stage in the same direction, where the error is much smaller due to the minimum step size of  $0.05\ \mu\text{m}$  that may be achieved with the mapping apparatus.

In [Figure 6.3 \(h\)](#), the height dependence of the signal amplitude was simulated using the method discussed in [Section 6.2.4.2](#). The signal amplitude was calculated for a cubic sample with an edge length of  $35\ \mu\text{m}$  and with its centre in  $x$ - $y$ -direction coinciding with the coil centre at  $x = y = 0$ . In this case, the distance,  $z$ , is the distance from the bottom surface of the cube to the surface of the EPRoC. The cubical shape was merely used to simplify the simulation. The ratio of the volume of a sphere and of a cube with a diameter equal to the edge length, is  $\pi/6 \approx 0.52$ , which is comparable to the total error in the determination of the sample size. The relaxation times for BDPA of  $T_1 = 110\ \text{ns}$  and  $T_2 = 100\ \text{ns}$  necessary for the simulation were

taken from literature [156, 157]. For each point in the simulation, EPR spectra within the sample volume were calculated on a  $1 \times 1 \times 1 \mu\text{m}^3$ -grid, so that in total 42 875 first-derivative dispersion EPR spectra were summed per point. The peak-to-peak signal amplitude was calculated from each summed spectrum and is plotted in Figure 6.3 (h).

Similar to the experiment, the simulated signal amplitude decreases non-linearly with increasing distance from the chip surface. The first experimental data point of the signal amplitude at  $z = 10 \mu\text{m}$  is, however, approximately twice as large as expected from the simulation. This discrepancy can not alone be explained by the error of  $z$ -axis discussed above. Even after consideration of the  $z$ -error, the data point does not fit to the rest of the dataset. Therefore, the first experimental point in Figure 6.3 (h) was omitted and the simulation was instead normalised to the signal amplitude recorded at  $z = 20 \mu\text{m}$ . The simulated signal amplitudes are in good agreement with the amplitudes obtained from the experimental spectra even after consideration of the uncertainty in the absolute position of the  $z$ -axis. The decrease in signal intensity in the recorded spectra is relatively linear for  $z \geq 20 \mu\text{m}$ . The first point with its much higher signal amplitude, however, can not be explained by the presented theory, suggesting that it is incomplete.

As seen in Figure 6.3 (g), the values of the FWHM exhibit an asymmetry in the  $x$ - and  $y$ -directions with values of about  $160 \mu\text{m}$  in the  $x$ - and  $120$  to  $130 \mu\text{m}$  in the  $y$ -direction. While the FWHM in the  $y$ -direction does not change considerably, the FWHM in the  $x$ -direction decreases with increasing  $z$  to about  $120 \mu\text{m}$  FWHM at  $z = 60 \mu\text{m}$ . To investigate the origin of the asymmetry of FWHM in the  $x$ - and  $y$ -directions, signal amplitude maps shown in Figure 6.4 were simulated using the method described in Section 6.2.4.2 with the  $B_1$  distribution of the top-left coil (cf. Figure 6.2 (c)) discussed in Section 6.3.1.1 for a cubic sample of BDPA with an edge length of  $35 \mu\text{m}$ . Each point in the map in Figure 6.4 (a) represents the signal amplitude of a cubical sample with its  $x$ - $y$ -centre at the position of that point. As for the simulation of the height-dependent signal amplitude, a cubic sample with an edge length of  $35 \mu\text{m}$  was assumed with the aforementioned relaxation times. The maps were calculated in  $10 \mu\text{m}$  steps in the  $x$ - and  $y$ -directions and then interpolated. In the Figure 6.4, the simulations for two distances of the sample to the EPRoC ( $0$  and  $50 \mu\text{m}$ ) with different components of  $B_1$  are plotted.

If only the component of  $B_1$  perpendicular to the surface of the EPRoC is considered, i.e.,  $B_{1,z}\hat{e}_z$ , no asymmetry is observed in the signal amplitude map as shown in Figure 6.4 (a). To reproduce the asymmetry of the FWHM (cf. Figure 6.3 (g)), both  $B_{1,z}\hat{e}_z$  and  $B_{1,x}\hat{e}_x$ , perpendicular to  $B_0 \parallel y$  need to be considered in the simulation as seen in Figure 6.2 (b). A counter-check was performed by assuming  $B_1$  being composed of  $B_{1,z}\hat{e}_z$  and  $B_{1,y}\hat{e}_y$ , which does not correspond to an actual experiment, where the  $B_0$  would need to be along  $x$ . In this case

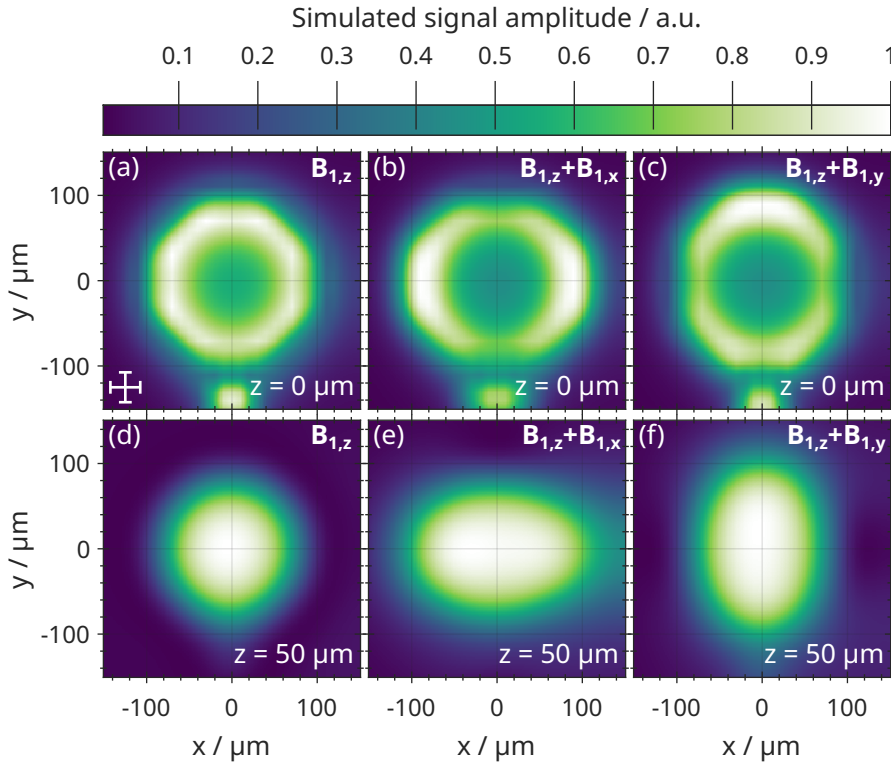


Figure 6.4: Simulation of the signal amplitude of a sample of BDPA with relaxation times  $T_1 = 110$  ns and  $T_2 = 100$  ns with a cubical shape with an edge length of  $35 \mu\text{m}$  at a distance of  $0 \mu\text{m}$  ((a), (b), (c)) and  $50 \mu\text{m}$  ((d), (e), (f)) to the surface of the EPRoC considering  $B_1$  composed of  $B_{1,z}$  ((a) and (d)),  $B_{1,z} + B_{1,x}$  ((b) and (e)), and  $B_{1,z} + B_{1,y}$  ((c) and (f)). The  $B_1$  arrangements in (b) and (e) correspond to the experiment where  $B_0 \parallel y$ . The maps in (c) and (f) would be observed if  $B_0$  was parallel to  $x$ . This would correspond to a rotation of the EPRoC of  $90^\circ$  about  $z$ .

the asymmetry is rotated by  $90^\circ$  as shown in Figure 6.4 (c). This would be expected if the EPRoC board was rotated by  $90^\circ$ , which was not possible due to geometrical restrictions imposed by the electromagnet.

The simulated maps exhibit a weak  $x$ - $y$ -asymmetry. This asymmetry may be explained by the residual  $B_1$  from the other coils of the VCO as the  $B_1$  distribution was extracted from the simulated  $B_1$  distribution of the 12-coil array shown in Figure 6.2 (c). Therefore, there is an increased  $B_1$  on the right-hand side due to the neighbouring coil.

All simulated maps at  $0 \mu\text{m}$  show an increase of the signal amplitude from the centre of the coil towards its trace. This is particularly pronounced in the direction of the additional component of  $B_1$  due to its increased magnitude, i.e., in Figure 6.4 (b) the increase of the signal amplitude from the centre towards the trace of the coil is stronger in  $x$ -direction where the  $B_{1,x}$  component is part of the total  $B_1$  and similarly in (c) in the  $y$ -direction. This increase of the signal amplitude is not seen in the experimental data in Figure 6.3 in contrast to experiments

performed in ref. [186] with an EPRoC design utilising HEMT instead of CMOS transistors. In the experiments in ref. [186], an increase of the signal amplitude by a factor of 100 was found when moving a small grain of BDPA from the centre of the coil ( $B_1 = 0.4 \mu\text{T}$ ) to the trace of the coil ( $B_1 = 4 \mu\text{T}$ ), i.e., a tenfold increase of  $B_1$ . As the magnitude  $B_1$  is smaller by  $\sim 65$  to  $\sim 35 \times$  compared to this EPRoC, the BDPA sample in their experiments was most probably not saturated so that the saturation factor,  $s = \gamma^2 B_1^2 T_1 T_2 \ll 1$ , in the denominator of Equation 3.3 may be neglected and the signal amplitude is expected to scale with  $B_1^2$ . In our simulations, the magnitude of  $B_1$  increases approximately three-fold along  $x$  at  $z = y = 0$  (cf. Figure 6.2 (e)), so that an increase of the signal amplitude by a factor of  $\sim 9$  is expected in the simulation. Yet, only an increase of approximately 2 to 3 is observed (cf. Figure 6.4 (b)), which can be attributed to the saturation of the BDPA sample in our experiments due to the larger  $B_1$  magnitude.

From simulations at  $z = 50 \mu\text{m}$  shown in Figure 6.4 (d), (e) and (f), a plateau of the signal amplitude is seen as observed in the experimental data. This suggests that the previously estimated absolute distance of the sample to the surface of the EPRoC is not correct. Previously, it was assumed that the sample was attached to the end of the tip such that this distance reflects the distance between sample and EPRoC. Apparently, this assumption seems to be invalid and the sample may be not exactly be attached to the end of the tip but at the side. Therefore, the  $z$ -axis may need to be corrected to reflect the actual sample position instead of the position of the end of the tip. Assuming that the maps obtained from the experiment and the respective simulations are correct, the distance of the map shown in Figure 6.3 (a) was not obtained at  $z = 10 \mu\text{m}$  as previously assumed but rather at  $z \sim 50 \mu\text{m}$  etc. Hence, the  $z$ -axis may be corrected by  $\sim 40 \mu\text{m}$ .

From the presented experimental data and the simulations, the sensitive volume of one of the coils of the 12-coil EPRoC array for BDPA may be estimated. For simplicity, we assume an ellipsoidal cylinder with a semi-major axis,  $a$ , of  $80 \mu\text{m}$ , semi-minor axis,  $b$ , of  $62.5 \mu\text{m}$  and a height,  $h$ , of about  $100 \mu\text{m}$ :

$$V_{\text{sens,coil}} = \pi ab \cdot h \approx 1.6 \text{ nL} \quad (6.6)$$

This value is about 50% smaller than the value determined from the  $B_1$  distribution alone in Section 6.3.1.1. The discrepancy may be explained by a combination of sample saturation and limited SNR in the experiment such that a 99% reduction of the signal amplitude as assumed the estimation of the sensitive volume in Section 6.3.1.1 may not be observable.

### 6.3.1.3 Mapping of three coils

Having determined the sensitive volume and  $B_1$  profile for a single VCO, it is necessary to investigate the behaviour of the FM signal of



the EPRoC array in different coils. To this end, a mapping experiment similar to the one described in Section 6.3.1.2 was performed over three coils of the 12-coil EPRoC array board. A similar sized grain of BDPA was used for this experiment, with similar settings for the acquisition of the FM signal. The step size in the  $x$ - and  $y$ -directions were  $10\ \mu\text{m}$  and  $25\ \mu\text{m}$ , respectively. The latter was chosen to reduce the total acquisition time to about 36.4 h. The spectra were acquired in a serpentine-like fashion starting at  $(-125\ \mu\text{m}, -125\ \mu\text{m})$  in positive  $x$ -direction. At the maximum  $x$ , the  $y$ -position was changed by  $-25\ \mu\text{m}$  to  $-100\ \mu\text{m}$ , after which  $x$  was moved in negative direction etc. The peak-to-peak signal amplitude of the FM signal at a distance of the sample to the surface of the chip of about  $20\ \mu\text{m}$  ( $60\ \mu\text{m}$ , when considering the offset determined previously) is shown in Figure 6.5 (a). The cross displayed on the bottom left represents the sample size while three coils of the VCO with a diameter of  $200\ \mu\text{m}$  are indicated by octagons with widths ( $8.5\ \mu\text{m}$ ) shown to scale to represent the thickness of the conductors in the EPRoC device. The experimental data show that the EPRoC array is primarily sensitive inside the coils as was observed in before in Section 6.3.1.2 and is *independent* of sample placement given that the FM signal is recorded in all coils. Outside the coils, the EPR signal is minimal. For further insight, a slice through the map at  $y = 0$  is shown in Figure 6.5 (b) as a function of  $x$ . Inside the coils, a plateau is seen with a width of about  $120\ \mu\text{m}$  and an amplitude of about  $7\ \mu\text{V}$  with a coefficient of variation in each plateau being less than 3%. Although we expected to observe the same signal amplitude and FWHM in all coils, we see small differences in these values originating from slight misalignments in the sample placement. The signal amplitude in between the coils decreases to about  $1\ \mu\text{V}$ . As before, the signal amplitude was fit with three 2D *Gaussian* functions of Equation 6.1 to determine the FWHM in the  $x$ - and  $y$ -directions. As observed previously, the FWHM are asymmetric with values of  $\sim 180\ \mu\text{m}$  and  $\sim 140\ \mu\text{m}$  in the  $x$ - and  $y$ -directions, respectively. The values are slightly larger than determined in Section 6.3.1.2, possibly due to the larger signal amplitude, which is about  $\sim 3.5$  larger compared to the mapping of one coil. This larger signal amplitude may further be explained by a large error originating from the estimation of the sample volume, since for this only a picture obtained with a light microscope was used.

From the data presented here and in Section 6.3.1.2, the sensitive volume of the EPRoC array may simply be calculated by the number of coils and the sensitive volume determined for one coil, such that the coils of the EPRoC array may be regarded as independently functioning detectors with respect to the  $B_1$ . For the complete array with 12 coils ( $n_{\text{coil}}$ ), the sensitive volume is therefore estimated as:

$$V_{\text{sens,array}} = n_{\text{coil}} V_{\text{sens,coil}} \approx 19.2\ \text{nL}.$$

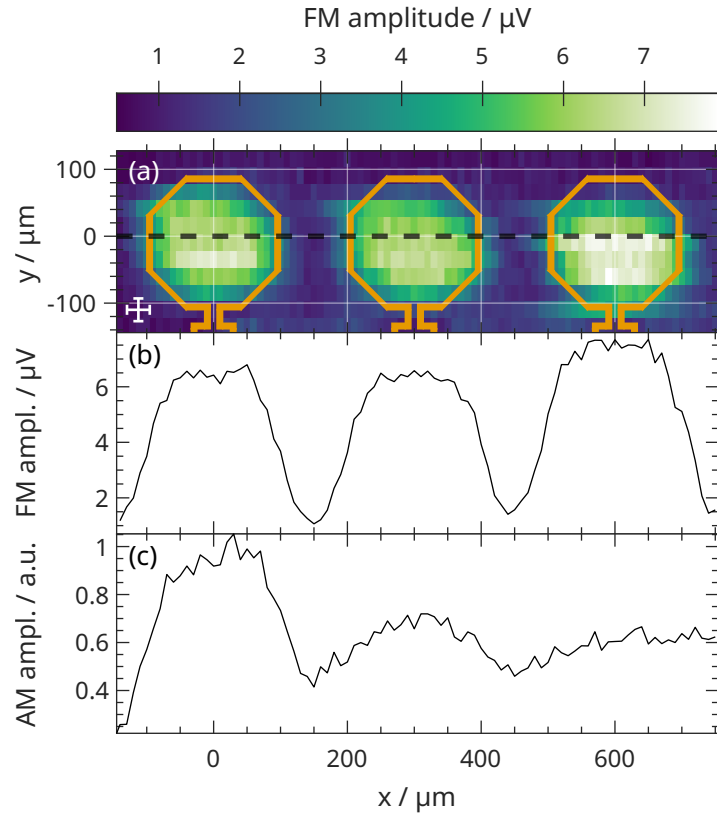


Figure 6.5: Mapping of three coils VCO array at about  $20\ \mu\text{m}$  above the EPRoC. **(a)** Map of the normalised peak-to-peak FM amplitude of three coils of the 12-coil EPRoC array. The cross (bottom-left) indicates the approximate sample size of  $35\ \mu\text{m}$  in each direction containing approximately  $1 \times 10^{14}$  spins. The octagons illustrate the conductors each with a diameter of  $200\ \mu\text{m}$  and a thickness of  $8.5\ \mu\text{m}$ . **(b)** Cross section of the map in the centre of the three coils (indicated by the black dashed line in (a)). All three coils show similar signal amplitude. **(c)** AM signal amplitude recorded with a line scan at  $y = 0$  with a grain of BDPA with a diameter of  $\sim 63\ \mu\text{m}$ .

In previous refs. such as [61], the sensitive volume was calculated as a cube with an edge length of the diameter of the coil. Using the diameter of the utilised coils of  $200\ \mu\text{m}$ , the sensitive volume for a single coil of  $8\ \text{nL}$  and consequently  $96\ \text{nL}$  for the complete 12-coil array was estimated, which is about  $\sim 5 \times$  larger than experimentally determined with BDPA.

In summary, this and the previous section showed the EPRoC is mainly sensitive inside the conductor loops with asymmetric shape of the signal amplitude inside each conductor loops. In addition, the FM signal amplitude is independent of the placement of the sample inside each coil as expected from the global nature of this signal. The asymmetry of the signal amplitude observed in the experimental and simulated data shown in this and the previous section (Section 6.3.1.2)



originating from the inhomogeneous  $B_1$  distribution suggests that all relevant contributions to the total  $B_1$ , i.e., perpendicular to  $B_0$  need to be considered even for “point”-like samples, the dimensions of which are much smaller than that of the coil.

It should be noted that the sensitive volume of the EPRoC is generally sample specific as it depends on the relaxation times of the sample due to saturation at different positions in space as seen from [Equation 3.3](#). The change of the inductance of the coil is modelled here by a volume integral over the whole sample. Two contributions dependent on  $B_1$  compete at each point in space. While the contribution of the unitary  $B_{1,u}(x, y, z)$  in the numerator only depends on the geometry of the coil, the contribution of the saturation factor in the denominator,  $s = \gamma^2 B_1^2(x, y, z) T_1 T_2$  depends additionally on the relaxation times  $T_1$  and  $T_2$  of the sample. Consequently, the sensitive volume is larger for samples with (very) short relaxation times than for samples with long relaxation times, which readily saturate. In the latter case, the spectra may be relaxation-broadened so that the signal amplitude does not increase linearly with  $B_1$ .

**CROSSTALK OF THE AM SIGNAL** Compared to the independently functioning detectors for the FM signal, the AM signal shows quite a different behaviour when moving from one coil to another coil. Please note that the only AM signal of the top-left coil ( $x = 0, y = 0$ ) in [Figure 6.2](#) (b) is extracted. This is not a global signal from all coils as the FM signal, but only detected in this coil. Instead of a complete mapping of a single or three coils, the AM signal was recorded along  $x$  at  $y \sim 0$  and  $z \sim 20 \mu\text{m}$ . As only the  $x$ -position was changed in this experiment, this procedure is called line scan. As the AM signal exhibits a lower SNR than the FM signal, a much larger BDPA sample with an edge length of about  $63 \mu\text{m}$  has been used for this experiment to be able to observe an AM signal. In addition, the experiment was not as optimal as in the previously shown experiments. The main problem of the dataset was the alignment of sample and EPRoC, such that motion of the sample was not parallel with the surface of the EPRoC. Therefore, the plateaus in the FM signal of this dataset (cf. [Section 6.3.1.3](#)), which should show the same signal amplitude as in seen in [Figure 6.5](#) were linearly decreasing due to the increased distance between sample and EPRoC at larger  $x$ . To remove this “baseline”, a polynomial of first order was fitted to the FM data to obtain the slope signal amplitude due to the misalignment. A first order polynomial with the same slope was also subtracted from the AM data to obtain the normalised AM signal of a line scan in the centre of the top row of coils along three coils as shown in [Figure 6.5](#) (c). Although the AM signal is only extracted from the top-left coil at  $x = 0$ , an EPR signal is observed in this coil even if the sample is placed in the second ( $x = 300 \mu\text{m}$ ) and even third coil ( $x = 600 \mu\text{m}$ ) along

the line, i.e., there is a crosstalk between the coils. Electrically, the second coil is the second-nearest neighbour to the first coil, since the coils are connected in a zipper-like fashion along  $x$  (cf. Section 6.2.2.2). Hence, the attenuation between the coils is  $\sim 3$  dB coil $^{-1}$ . This finding confirms previous findings of ref. [61] using a similar EPRoC array as used in this work, where the AM signal could be extracted from one coil only, while the FM signal was a global signal of all coils. In their experiment, a grain of BDPA and a grain of solid tempol were placed on two different coils of the EPRoC array. While the BDPA sample was placed in the coil where the AM signal was detectable, the tempol sample was placed in a different coil. In the resulting AM spectrum, signals from both samples could be identified due to their different  $g$ -value. While the FM signal showed similar signal amplitudes for both samples, the AM signal showed a significantly reduced amplitude ( $\gg 10 \times$ ) of the tempol signal.

### 6.3.2 Sensitive height determined with a thin-film sample

So far, the spatial properties of the FM and AM signal with a “point” sample much smaller than a coil were discussed. Effectively, this utilised only one coil of the EPRoC array at a time. In the following, the dependence of the FM signal on the sample positioning when utilising all coils at a time will be rationalised. The dependence of the FM signal amplitude of the thin-film a-Si sample with a thickness of  $15 \mu\text{m}$  on the distance between the sample and the surface of the EPRoC array,  $z$ , is shown in Figure 6.6. In this experiment, the  $2 \times 1 \text{ mm}^2$  a-Si thin film sample covered all coils of the EPRoC with its lateral dimensions being larger than the extent of the coils of the EPRoC. For the experiment, multiple FM spectra at different distances from the EPRoC were recorded from which the peak-to-peak signal amplitude were extracted to determine the sensitive height of the EPRoC array as plotted in Figure 6.6. The a-Si sample was in direct contact with the EPRoC VCO array at  $z = 0$ , which was confirmed using a DSLM camera placed approximately 50 cm away from the EPRoC and outside of the field of the electromagnet. At above about  $110 \mu\text{m}$ , the EPR signal is indistinguishable from the baseline noise yielding a sensitive height for the a-Si sample of about  $110 \mu\text{m}$ . This value agrees well with the that determined with the grain of BDPA as discussed in Section 6.3.1.2.

A comparison of the experimental data with the theoretical considerations presented in Section 3.2.3 is also shown in Figure 6.6. The expected FM signal amplitude of the a-Si sample was simulated using the  $B_1$  distribution discussed in Section 6.3.1.1 using Equation 3.15 as before. For the simulation an a-Si sample with a cuboid shape ( $2 \times 1 \times 0.015 \text{ mm}^3$ ) with relaxation times of  $T_1 = 200 \text{ ns}$  and  $T_2 = 20 \text{ ns}$  was assumed as determined from the saturation analysis and linewidth as discussed in Section 4.3.1.3. The voxel size for the

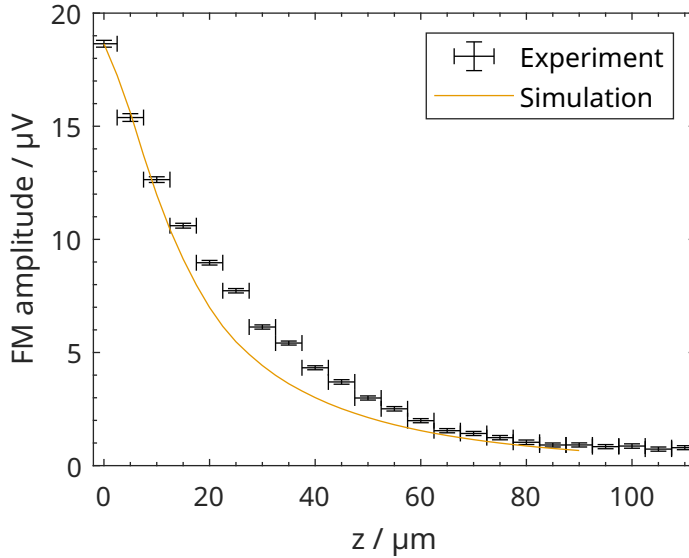


Figure 6.6: Dependence of the FM signal amplitude of the a-Si sample utilising all coils of the EPRoC array on the distance,  $z$ , between the sample and the surface of the EPRoC. The simulation was normalised such that the first point of the experimental data coincides with the simulation at the same height.

simulation was  $2.5 \times 2.5 \times 2.5 \mu\text{m}^3$  for calculation of the first-derivative dispersion EPR spectra. As before, the spectra were summed, and subsequently the peak-to-peak amplitude was obtained from the composite spectrum for each sample position in the  $z$ -direction. The simulated signal amplitude was normalised to coincide with the first datapoint at  $z = 0$  in Figure 6.6.

The simulation shows a good agreement with experimental data. However, slight discrepancies between  $\sim 20$  to  $60 \mu\text{m}$  are observed, where the simulated signal amplitude is lower than the experimental data. This effect could be explained by a slightly tilted sample whose surface is not exactly parallel to the surface of the EPRoC, so that one edge would be closer to the sensor area than expected. This effect would produce a larger signal amplitude. Generally, the absolute  $z$  values should be seen as a “rough” estimate due to its indirect determination. The absolute distance between the EPRoC and the sample can only be determined by a combination of high-resolution photographs of the sample in comparison to the experiment and from the motor positions.

### 6.3.3 EPR signal dependence on partial utilisation of the EPRoC array

The dependence of the signal amplitude on the coverage of the active area of the EPRoC array was investigated by moving the a-Si thin film sample along the long edge, i.e., along  $x$ , of the EPRoC array. Through the movement of the sample only parts of the active area

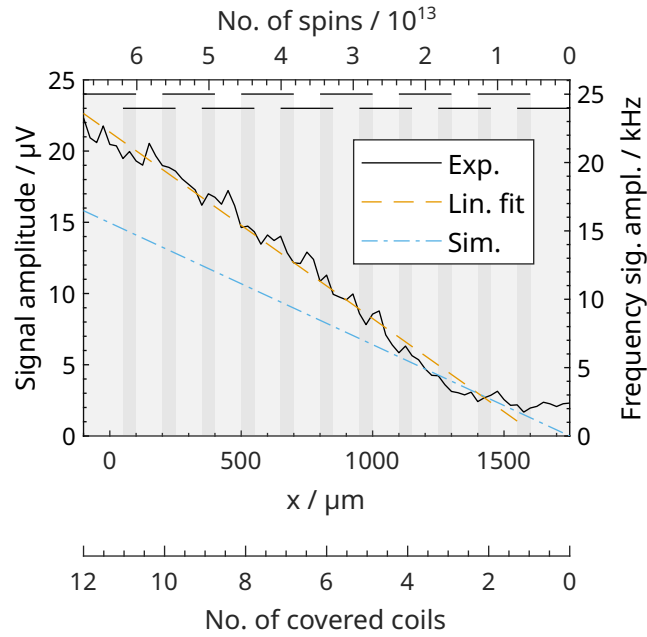


Figure 6.7: Dependence of the signal amplitude (peak-to-peak amplitude of the integrated first-derivative FM spectrum) on the number of occupied coils obtained by moving the a-Si sample along the long side ( $x$ ) of the EPRoC. The top  $x$ -axis displays the approximate number of spins in the sensitive area of the sensor assuming that no signal is detected outside the coils. The horizontal lines at the top represent the coils on the EPRoC array. The number of coils covered by the sample decreases from the left (12) to the right, where no coil is covered by the sample.

(the coils) were covered with the a-Si thin film sample, while recording the spectra. The results of this experiment are shown in Figure 6.7. The sample was positioned such that its centre coincided with  $y = 0$ . At  $-100 \mu\text{m}$ , the sample covered all 12 coils while at  $1750 \mu\text{m}$  no coils were covered (see second  $x$ -axis at the bottom. Due to the overlap of the coils in  $x$ -direction as indicated by the dark grey areas, this axis is not strictly linear, but the error is negligible.). From the number of covered coils, the approximate total number of spins in the active area (top  $x$ -axis) is calculated using the active area of the EPRoC determined in Section 6.3.1.2 ( $A_{\text{sens,coil}} = \pi \times 80 \times 62.5 \mu\text{m}^2$ ), the spin density of the a-Si sample and its thickness of  $15 \mu\text{m}$  (see Section 4.3.1.3 for more information). For simplicity, the active area was assumed to be a cylinder with an elliptical ground plane with the semi-minor and -major axes as determined before and a height of the a-Si sample ( $15 \mu\text{m}$ ). For each point in the figure, an EPR spectrum was recorded, from which the signal amplitude ( $y$ -axis) was calculated.

The signal amplitude of the FM signal in units of Hz of the VCO array (right  $y$ -axis) caused by the EPR resonance is calculated from the signal amplitude of the FM signal in V and the VCO gain of about  $1.04 \text{ GHz V}^{-1}$  (cf. Section 4.2.2).

If more than approximately two coils are covered, a linear increase in the signal amplitude is seen. When all coils are covered with the sample, corresponding to  $\sim 6.7 \times 10^{13}$  spins, the signal amplitude of the VCO in frequency units due to the EPR signal is about 22.3 kHz. Accordingly, each spin contributes approximately 0.33 pHz to the total FM signal. This means, that the oscillation frequency of the EPRoC is changed by this amount per spin present.

A simulation of the amplitude FM signal in frequency units as a function of the utilised VCOs of the injection-locked 12-coil array, i.e., the number of the covered coils, was performed with the harmonic balance-based periodic steady state (PSS) analysis of the circuit simulator *SpectreRF* utilising the same simulation procedure described in ref. [61] for an 8-coil EPRoC array. The results of the simulation are shown in Figure 6.7. The simulation was performed as a field sweep with the same parameters as for the experiment (MW frequency, bias current). The sample was modelled by Bloch's equations with the properties of the a-Si sample (relaxation times, spin density, sample volume). Please see Section 6.2.4.3 for a detailed explanation of the simulation. A linear increase of the frequency as a function of the utilised coils is found similar to the experimental data with a maximum peak-to-peak frequency signal amplitude of approximately 16.5 kHz when all coils are covered, which corresponds to  $0.24 \text{ pHz spin}^{-1}$ .

For a qualitative explanation of the behaviour of the signal amplitude on the number of covered coils, two contributing factors need to be considered, namely, the filling factor of each coil and the injection-locking of the VCO in the EPRoC array. According to the Curie law, the magnetic susceptibility,  $\chi_0$  depends linearly on the number of paramagnetic centres in the sample (cf. Section 2.4.1). As the FM signal is proportional to  $\chi_0$ , a linear increase of the FM signal upon covering the coils is expected. The effect of the injection-locking on the signal amplitude was discussed in Section 3.4. In ref. [61], a simulation of this effect was performed revealing a reduced signal amplitude of the global FM signal if not all coils are covered with sample. Therefore, the total frequency signal amplitude of a single VCO and an injection-locked array is similar, if the same amount of sample per coil is present. In the experiment, the contribution of both the filling of the coils and the injection-locking is observed, while for the simulation only the latter was considered. With the same experimental settings and parameters for the a-Si sample, we find that the frequency signal amplitude is approximately 35% smaller in the simulation than in the experiment. This discrepancy may partly be explained as follows. In the simulation, neither the  $B_1$  distribution nor the saturation of the sample could be taken into account. Furthermore, the sample volume was determined using the sensitive area of the BDPA sample.

#### 6.4 CONCLUSIONS

In summary, we have demonstrated the three-dimensional distribution of the  $B_1$  for a VCO-based EPRoC array detector, which is crucial for the development of quantitative EPRoC applications. We used a “point”-like grain of BDPA and a thin-film sample of a-Si to map the effective  $B_1$ . Our experiments revealed that the sensitive area of a single VCO is approximately cylindrical with an elliptical ground plane, having a semi-major axis of  $80\ \mu\text{m}$ , a semi-minor axis of  $62.5\ \mu\text{m}$ , and a sensitive height of around half the coil diameter ( $100\ \mu\text{m}$ ). The sensitive volume of each coil is approximately  $1.6\ \text{nL}$ . Our experimental data were compared to simulations using the steady-state solution of Bloch's equations and finite-element simulations of the  $B_1$  distribution, which were found to be in good agreement. We also found that the contribution of  $B_{1,x}$  to the total  $B_1$  cannot be ignored, which explains the deviations from purely cylindrical distributions observed in the recorded data.

Additionally, the dependence of the FM signal was examined when only partially covering the sensor. It was observed that there was a linear increase in the signal amplitude, indicating that even when the EPRoC array is not fully covered with a sample, quantitative EPR is still achievable if the spatial distribution of the sample is known. Furthermore, the signal amplitude of the FM signal if all coils of the EPRoC sensor were covered was found to be in good agreement with simulations, taking into account the number of spins in the sample.

## RAPID-SCAN EPR USING AN EPR-ON-A-CHIP SENSOR

---

### 7.1 INTRODUCTION

In [Chapter 5](#), the saturation behaviour of  $\alpha,\gamma$ -bisdiphenylene- $\beta$ -phenylallyl (BDPA) in powder form and the amorphous silicon (a-Si) thin film sample was discussed in [Section 5.3.4.3](#). It was found that the linewidth of the BDPA sample was approximately 20 to 60 % larger than expected assuming a relaxation-determined linewidth with  $T_2$  between 80 to 160 ns, which may be attributed to saturation due to the inherently large magnitude of  $B_1$  of the EPR-on-a-Chip (EPRoC) due to a certain minimum bias current required to achieve stable oscillations. Even at the lowest possible bias currents of 2 mA, the  $B_1$  in the centre of the coil is of the order of tens of  $\mu\text{T}$ , easily saturating many samples. Closer to the coil, the magnitudes of  $B_1$  are even higher as discussed in [Section 6.3.1.1](#). Thus, even samples with a relatively short spin-lattice relaxation time of  $\sim 100$  ns may easily be saturated when investigated with the EPRoC. Generally, the EPR signal intensity/amplitude depends on the population difference between the resonant spin states of the spin system in the steady-state under continuous wave (CW) microwave (MW) irradiation. As MW absorption induces transitions between the spin states, their populations tend to be equalised bringing the spin system out of thermal equilibrium. The MW absorption depends on the MW intensity, i.e.,  $B_1$  and the time spent on resonance. The spin-lattice relaxation time counterbalances the equalisation of the spin states. Hence, the saturation behaviour depends on  $B_1$ ,  $T_1$ ,  $T_2$  and the time spent on resonance. Thus, to enable the acquisition of unsaturated EPR spectra of samples with moderately long relaxation times  $\geq 100$  ns with the EPRoC, either the magnitude of  $B_1$  of the EPRoC needs to be lowered or the time on resonance needs to be shortened such that the spin system stays in thermal equilibrium. The former would require a complete redesign of the EPRoC and a possible change of production techniques as shown in [[186](#), [223](#)], where the high electron mobility transistor technology was used instead of complementary metal-oxide-semiconductor (CMOS) to produce an LC Colpitts oscillator. This oscillator has a minimum magnitude of  $B_1$  of 0.4  $\mu\text{T}$  at 300 K, which is about a factor of 100 smaller than that of the presented EPRoC. As a complete redesign of the EPRoC is very time-consuming

---

A significant portion of this chapter is from S. Kunstner, A. Chu, K.-P. Dinse, A. Schnegg, J. E. McPeak, B. Naydenov, J. Anders, K. Lips, Rapid-Scan Electron Paramagnetic Resonance Using an EPR-on-a-Chip Sensor. *Magnetic Resonance* 2021, 2 (2), 673–687. DOI: [10.5194/mr-2-673-2021](https://doi.org/10.5194/mr-2-673-2021).



and requires extensive testing, the so-called rapid-scan EPR (RS-EPR) technique may be used instead of CW-EPR utilising the rapid frequency sweep capabilities of the EPRoC. By scanning the MW frequency (or the magnetic field) with a rate large enough so that the time spent on resonance is short compared to the relaxation times, saturation effects can be avoided even using large  $B_1$  as found in our device. Hence, higher  $B_1$  may be used before saturation effects deteriorate the EPR signal. Instead of the common phase-sensitive detection (PSD) of CW operation with a lock-in amplifier (LIA), the RS-EPR transient is recorded with an oscilloscope or digitiser. Depending on the sample, passage effects, so-called wiggles, may appear on the trailing edge of the signal, which can be removed by *Fourier* deconvolution. These wiggles were first reported in water in the very early days of nuclear magnetic resonance (NMR) spectroscopy by Bloembergen et al. in 1948 [224]. The explanation of their shape was given shortly thereafter by Jacobsohn and Wangsness for linear sweeps [90] and by Salpeter for sinusoidal sweeps [225]. For a short time, RS was used for enhanced sensitivities in NMR [226–228], however, it soon became obsolete with the invention of Fourier transform NMR. The first observation in EPR of rapid passage effects from  $F$  centre in alkali halides and from donor states in silicon was reported by Portis in 1955 [229]. Also, Beeler et al. [230] observed passage effects in ammonia solutions of metallic sodium. A comprehensive treatise of rapid passage experiments was given by Weger [92] in 1960. RS-EPR then led a niche existence until its reinvention by the Eaton group in the early 2000s mainly as a field-swept experiment.

The first RS experiments after the reinvention was performed on the  $E'$  defect in irradiated vitreous  $\text{SiO}_2$  at X-band at that time labelled with the somewhat cryptic term “Out-of-Phase Rapid-Passage EPR” [231]. The more intuitive term “rapid scan EPR” was chosen for later publications of experiments studying lithium phthalocyanine at 250 MHz [232] and in X-band to study nitroxyl radicals [157], irradiated quartz [233] and BDPA [234].

Special coils and coil drivers [235, 236] were developed to achieve higher scan rates, which were in the meantime commercialised by Bruker. In addition, *Fourier* deconvolution algorithms for triangular [237] and sinusoidal scans [97] as well as algorithms for baseline-correction [238, 239] were developed.

Improvement of the signal-to-noise ratio (SNR) for different samples classes such as spin-trapped radicals [240], nitroxyl radicals [234],  $\gamma$ -irradiated organic solids [241] and samples with long relaxation times, such as hydrogenated amorphous silicon (a-Si:H), nitrogen-atom-endo-hedral  $\text{C}_{60}$  ( $\text{N@C}_{60}$ ) and  $N_S^0$  vacancies in diamond [5, 242] were reported. Additionally, RS-EPR was used in a high-frequency system to determine spin relaxation times where pulsed EPR (P-EPR) techniques were not applicable [86].



In most of the aforementioned experiments, field-swept RS-EPR in “conventional” resonator-based spectrometers were employed. Sweeping magnetic fields rapidly over a large range is technically demanding and needs special coils and amplifiers [235] restricting the sweep width to about 20 mT at tens of kHz. This in turn limits the application of RS-EPR to the narrow-spectrum sample classes mentioned above. Many samples, such as transition metal ion (TMI) states in biological samples or other samples, however, have a much wider spectrum. For faster scan rates, i.e., higher repetition rates, the sweep width is limited even more. Additionally, strong background signals may appear due to vibrations and eddy currents generated in the metallic parts of the cavity, which may be especially large for fast, wide scans [243].

To apply RS-EPR for samples with wider spectra, special techniques such as field-stepped direct detection (FSDD) or non-adiabatic rapid sweep (NARS) may be used [95, 244]. In these techniques, multiple RS-EPR transient signals are recorded while the field is stepped in small increments. The complete spectrum is obtained by combining the signals in post-processing. These techniques were applied to samples with wider spectra, such as copper complexes and  $\text{Mn}^{2+}$  in CaO [244, 245], lanthanides [246] as well as nitroxides [95]. Both techniques are similar to frequency swept electron spin echo detection in pulsed EPR, where multiple echoes are recorded while sweeping the magnetic field to obtain a complete spectrum. Using FSDD or NARS, however, complicates and prolongs the data acquisition and post-processing considerably.

Sweeping the MW frequency instead of the magnetic field may be another way of increasing the sweep width [86, 88, 131]. However, in resonator-based EPR, the high quality factor ( $Q$ ) cavity resonators usually employed limit the sweep width due to their low bandwidth, which is optimised for CW-EPR. To increase the bandwidth, the cavity could be overcoupled, which would lower the  $Q$  value proportional to the bandwidth. However, as the conversion of MW power to MW field would be lowered accordingly, this method is not of much use. Hence, the advantage of RS-EPR to increase the signal amplitude by using higher MW powers cannot be used.

As mentioned above, using the EPRoC, however, it is possible to utilise frequency-swept RS-EPR experiments over large sweep widths of more than 1.8 GHz (63 mT) without the constraints of resonator-based EPR [136]. Hence, it may be used for the investigation of samples exhibiting  $g$  and  $A$  anisotropy, samples with large hyperfine splitting and/or long relaxation times, such as transition metal ions complexes at cryogenic temperatures. In ref. [184], RS operation with single-chip integrated detectors was initially proposed but no details of the resulting EPR signal were provided. Using a voltage-controlled oscillator (VCO) to produce fast frequency ramps was used before to perform RS-EPR at high field/high frequencies [86]. In this report,

however, the VCO was only used to provide the rapid frequency ramps and not for detection.

With EPRoC, however, also detecting the transient change in sample magnetisation using a VCO-based EPRoC detector is an interesting possibility first proposed in [136]. First transient RS-EPRoC signals were already reported in 2017 [136]. Yet, it was not possible to deconvolve these transients to obtain EPR spectra due to the not precisely known phase of the exciting microwave needed for the *Fourier* deconvolution. Embedding the VCO in a phase-locked loop (PLL) allows for precise definition of the phase and frequency of  $B_1$  from an external reference, even in the presence of fluctuations in e.g. the temperature [145]. In combination with the implicit, high-bandwidth amplitude modulated (AM) demodulator built directly into the VCO as suggested in [136], EPRoC allows to detect the RS-EPRoC AM signal with a bandwidth on the order of a few hundred MHz. In the following, proof-of-concept frequency-swept RS-EPRoC experiments with a sweep width of 128 MHz (4.57 mT) of BDPA using an EPRoC detector are reported. As the findings in this chapter lay the foundation for future RS experiments with the EPRoC, certain aspects, which are obtained under various conditions, are discussed in detail to simplify the analyses of RS-EPRoC transients.

This chapter is organised as follows. Firstly, the materials and methods are explained including the instrumental configuration, samples and post-processing of the RS transients. Then, the results and discussion follows with the comparison of an RS and CW spectrum of the same BDPA sample, its saturation analysis, a sensitivity analysis and an outlook for further improvements the RS-EPRoC technique. At last, the chapter is summarised.

## 7.2 MATERIALS AND METHODS

In this section, a short description of the experiment used for the experiments in this chapter is given. Then, the relation of the bandwidth of the transient RS-EPRoC signal to the PLL bandwidth is discussed. A large part of this section deals with the deconvolution of the transient RS-EPRoC signal and the necessary post-processing steps. At last, the utilised sample described.

### 7.2.1 Experiment

Figure 7.1 depicts a schematic of the experiment. The EPRoC is located on a printed circuit board (PCB) which in turn is inserted between the poles of an electromagnet (Bruker B-E 25). In these experiments, the sweeping capabilities of the electromagnet were not used and, in principle, a permanent magnet could be used instead. Suitable prototypes of such magnets are discussed in refs. [130, 247]. The

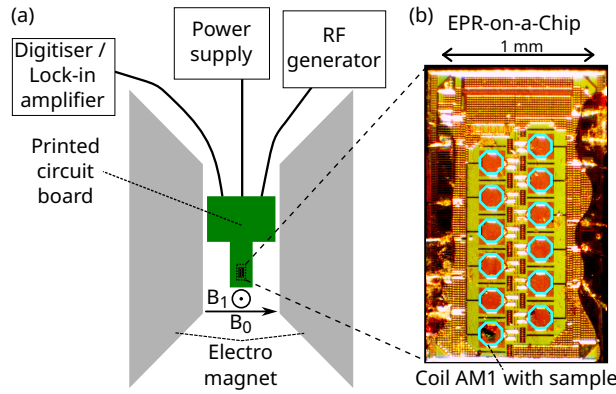


Figure 7.1: Depiction of the EPRoC setup. **(a)** The EPRoC is mounted on a printed circuit board (PCB) located between the coils of the electromagnet. The power supply powers the active components on the PCB and the power delivery board for the EPRoC. The radio frequency (RF) generator provides the reference frequency,  $f_{\text{ref}}$ , to the PLL on the PCB. A LIA is used for CW detection and a digitiser is used for RS detection. **(b)** Micrograph of the EPRoC chip with the particle of BDPA used for the experiments. The octagons depict the 12 coils of the EPRoC sensor of which only the bottom-left (depicted with Coil AM1) is used for the actual RS-EPRoC experiments. The sample is located in this coil, from which the AM signal is detected. Adapted from [131] © ⓘ.

12-coil EPRoC array was used for the experiments, which is similar to the design presented in ref. [61], and is discussed in detail in Section 4.2.4.1.

The FM signal was not used in the following experiments due to the relatively narrow bandwidth of the PLL of 10 MHz limiting the detection bandwidth for the FM signal. This in turn could distort the RS-EPRoC transient signal at large scan rates as discussed in the following section (Section 7.2.2). The AM signal, on the other hand, may be extracted from the VCO with the implemented implicit wide-band demodulator in the LC tank VCO, considerably reducing the experimental complexity as suggested in ref. [136]. As discussed in Section 3.2.5, the transient change of the oscillation amplitude of the VCO,  $\delta A(t)$ , by a paramagnetic sample in resonance is given by Equation 3.24 [136]. If the oscillation frequency,  $\omega_{\text{osc}}$ , is close to the Larmor frequency of the electron spin ensemble,  $\omega_L$ , i.e.,  $\omega_{\text{osc}} \approx \omega_L$ , then Equation 3.24 contains two components of the spin magnetisation in the rotating frame,  $M_{s,\text{rot}}$ : one low-frequency component at  $\omega_{\text{osc}} - \omega_L$  and one at twice the Larmor frequency. The low-frequency component is extracted by the implicit AM demodulator ( $V_x$  in Figures 3.1 and 3.2). As suggested in [186], an external AM demodulator could be used instead. The AM detection scheme is implemented in two separate VCOs inside the injection-locked VCO array (cf. Section 4.2.4.1), one of which is used as the EPR detector for all EPRoC experiments shown

in this chapter. More specifically, the sample was placed in the coil denoted with AM1 as shown in [Figure 7.1 \(b\)](#).

A Rohde & Schwarz SMB100A (R&S SMB100A) RF generator was used as reference for the PLL to control the MW frequency of the VCO of the EPRoC. The AM1 output providing the AM signal was recorded with either an LIA (Anfatec eLockIn 203) or a high-speed digitiser (Zurich instruments UHF-LIA, 12 bit vertical resolution,  $1.8 \text{ GSa s}^{-1}$ ) with the sampling rate set to 450 MHz, for CW and RS-EPR operation, respectively.

In contrast to the previous chapter, where most of the EPR experiments were performed as a field sweep, all EPR experiments shown in this chapter were performed as a frequency sweep around a central MW frequency of 13.44 GHz and with a static external magnetic field of  $B_0 = 479.4 \text{ mT}$ . A non-resonant transient RS background signal was subtracted from the experimental transient RS-EPRoC for background correction. For CW, no experimental background subtraction was performed.

The maximum modulation amplitude in the RS-EPRoC operation is limited by the RF generator (R&S SMB100A) providing a frequency-modulated reference signal at 420 MHz to the EPRoC via the PLL. Due to the 32-divider<sup>1</sup> on the chip, this frequency corresponds to 13.44 GHz on the chip. At this frequency, the maximum modulation amplitude at 420 MHz is 2 MHz, corresponding to  $\Delta f_{\text{rs}} = 32 \cdot 2 \text{ MHz} = 64 \text{ MHz}$  (2.28 mT) at the VCO. While for CW-EPRoC using phase-sensitive detection, this limitation poses no substantial restriction for most of the samples, RS-EPRoC with this particular RF generator suffers from a limited sweep width as only approximately 5% of the total available sweep width of 2.4 GHz ( $\Delta f \approx 1.2 \text{ GHz}$ , sweep width 85.6 mT) could be used in the experiments. The maximum modulation frequency of this RF generator is 1 MHz. Hence, the maximum scan rate for a sinusoidal scan as defined in [Equation 2.62](#),  $\alpha = 2\pi f_{\text{rs}} \Delta f_{\text{rs}}$ , is limited to  $402.1 \text{ THz s}^{-1}$ , corresponding to  $14.4 \text{ kT s}^{-1}$ .

### 7.2.2 Bandwidth relations of the RS-EPRoC transient and PLL

The bandwidth of a transient RS-EPR signal for a single *Lorentzian* line can be estimated from the scan rate,  $\alpha$ , in  $\text{Hz s}^{-1}$  and the effective transverse relaxation time,  $T_2^*$ , [[234](#)]

$$\Delta\nu_{\text{signal}} \approx N\alpha T_2^* = 2\pi N f_{\text{rs}} \Delta f_{\text{rs}} T_2^*. \quad (7.1)$$

The factor,  $N$ , determines the extent of lineshape broadening in the deconvolved spectrum and is usually chosen in a range of 3 to 5

<sup>1</sup> The 32-divider on the chip is placed such that the oscillation frequency is divided by 32, which is then compared to the reference frequency in the phase-frequency comparator. As the reference is frequency modulated, the modulation amplitude will be *multiplied* by the same number.

[248, Section 2.10.2]. The signal bandwidth of the transient RS-EPR signal is determined by frequency components of the “wiggles” on the trailing edge of the RS-EPR signal, depending on the resonance offset, the modulation amplitude ( $\Delta f_{rs}$ ), and the modulation frequency ( $f_{rs}$ ). For a constant  $T_2^*$  and a constant  $f_{rs}$ , the spacing of the “wiggles” on the trailing edge gets smaller with increasing modulation amplitude due to the larger resonance offset. The linear relationship between the signal bandwidth and  $T_2^*$  can be explained by the prolonged visibility of “wiggles” for a larger  $T_2^*$ . Since the resonance is passed twice within one full RS cycle, only half of the available bandwidth of any detection system can be utilised for the signal present in each half cycle. Therefore, the bandwidth of the detection system ( $\Delta\nu_{det}$ ) should be at least twice as large as the signal bandwidth,  $\Delta\nu_{signal}$  as

$$\Delta\nu_{det} \geq 2\Delta\nu_{signal} = 2N\alpha T_2^*. \quad (7.2)$$

This relation was used in ref. [234] for the determination of the quality factor required to achieve sufficient bandwidth to detect undistorted RS-EPR transients. For the EPRoC, the bandwidth of the PLL of approximately 10 MHz limits the maximum bandwidth of the FM signal to  $\sim 5$  MHz. With a conservative estimate of  $N$  and a  $T_2^*$  of 100 ns, a bandwidth of approximately 80 MHz of the PLL would be required to record an undistorted FM signal. Since the available bandwidth is significantly lower than the required signal bandwidth, the FM signal was not considered in these experiments.

### 7.2.3 Deconvolution of the AM RS-EPRoC transient

In the following, general considerations about sinusoidal MW frequency sweeps and the Fourier deconvolution of the AM signal are discussed before the digital post-processing steps of the AM RS-EPRoC transients are explained.

In resonator-based EPR, the RS-EPR signals are usually recorded in quadrature, by which both dispersion,  $\Re(s_{res})$ , and absorption signals,  $\Im(s_{res})$ , are detected, such that the complex RS signal may be described by

$$r_{res}(t) = \Re(s_{res}) + i\Im(s_{res}) \quad (7.3)$$

Here, one signal has a phase-shift of  $90^\circ$  with respect to the other, i.e., are orthogonal to each other. In practise, however, the phase-shift may deviate from  $90^\circ$  due to slightly different amplifications of both channels and imperfect phase shifters, which can be corrected in the post-processing [238].

Both FM and AM signal of the EPRoC exhibit different signal shapes as explained in Section 3.2.3 and Section 3.2.4 and thus the resulting rapid scan transients of FM and AM signal cannot simply be combined to form a complex signal of the kind of Equation 7.3. In addition, both

signals are demodulated with different demodulators (PLL for FM and intrinsic demodulator for AM). Not only do these demodulators exhibit different filter functions, they also lead to different measured signal voltages ( $V_x$  for AM and  $V_{\text{tune}}$  for FM). So, even if FM and AM signal would correspond to “clean” dispersion and absorption signals, the different recorded signal voltages would lead to a false complex RS-EPRoC transient.

Hence, only one of the signals may be used at a time to obtain an EPRoC spectrum from an RS-EPRoC transient. As the Fourier deconvolution (cf. [Section 2.5.4](#)) requires a complex transient signal of the form of [Equation 7.3](#), a complex RS-EPRoC transient has to be generated from the FM or AM transient, which is then used for the deconvolution algorithm. The utilised algorithm for deconvolution is the so-called *half-cycle* deconvolution for sinusoidal field/frequency sweeps [97]. The term *half cycle* refers to the fact that for sinusoidal MW frequency scans as discussed in [Section 2.5.3](#), resonance is achieved twice per period,  $T_{\text{rs}} = 1/f_{\text{rs}}$ , namely at  $t = T/4$  and  $t = 3T/4$ . Therefore, for each *full cycle* RS transient, i.e. for one period  $T_{\text{rs}}$ , the transient EPR signal is observed twice. Therefore, the two RS-EPRoC signals present in a full cycle are treated separately. To this end, the full-cycle transient is split into two half-cycle transients, one cycle where the MW frequency was swept from below to above resonance (up cycle) and one with a sweep in reverse direction (down cycle). The deconvolution is performed for both half-cycles separately. To obtain the complete deconvolved spectrum, i.e., from a full cycle, the resulting spectra are summed.

For general considerations, the AM RS-EPRoC signal was simulated with *blochsteady* of the *EasySpin* software package [70], which calculates the steady-state solution of Bloch’s equations with field/frequency modulation [96]. In the simulation, the AM signal is modelled as a mixture<sup>2</sup> of absorption,  $M_y$ , and dispersion,  $M_x$ ,

$$r_{\text{AM}}(t) = i [M_y(t) + Q_{\text{coil}}M_x(t)], \quad \text{with } Q_{\text{coil}} = 5, \quad (7.4)$$

where  $i$  is the imaginary unit.  $M_x(t)$  and  $M_y(t)$  were simulated with the following parameters:  $g = g_e$ ,  $T_1 = 110$  ns,  $T_2 = 100$  ns,  $B_1 = 10$   $\mu$ T,  $f_{\text{rs}} = 200$  kHz,  $\Delta f_{\text{rs}} = 128$  MHz. The simulated (purely imaginary) RS-EPRoC AM transient is shown in [Figure 7.2](#) (a), which corresponds to the AM signal recorded with the digitiser, i.e., without quadrature detection. The value of  $Q_{\text{coil}} = 5$  was chosen such that the asymmetry is easily observable in the figure. In the figure, the first column always shows the transients, while the second and third column show the output of the deconvolution function as implemented in Matlab based on the theory presented in [Section 2.5.4](#).

As seen in [Figure 7.2](#) (b) and (c), the deconvolution fails if only a purely real/imaginary input signal is used as the wiggles cannot be

<sup>2</sup> Please note that the absorption-like AM signal,  $r_{\text{AM}}$ , is purely imaginary to be consistent with common notations where the absorption is usually imaginary.



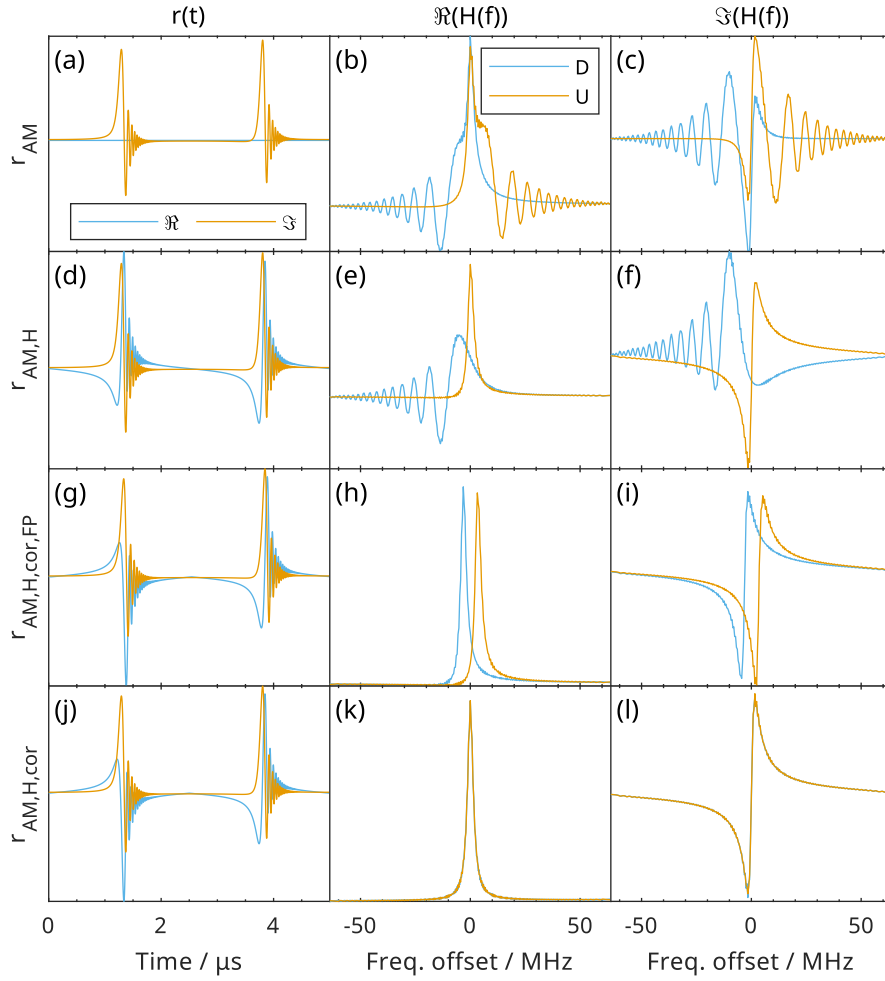


Figure 7.2: Simulated RS-EPRoC transients with corresponding deconvolutions. The first column ((a), (d), (g), (j)) displays the different RS-EPRoC transients, the real part,  $\Re$ , of the deconvolution of which is displayed in the second column ((b), (e), (h), (k)) and imaginary part,  $\Im$ , of the deconvolution of which is displayed in the third column ((c), (f), (i), (l)). For the deconvolutions, both half-cycle deconvolutions denoted with D and U are shown. **(a)** Purely imaginary AM transient as a mixture of  $M_x$  and  $M_y$  with  $r_{AM}(t) = i(M_y(t) + Q_{coil}M_x(t))$  with  $Q_{coil} = 5$ . **(b)** Real,  $\Re$ , and **(c)** imaginary,  $\Im$ , part of the deconvolution,  $H(f)$ , of the transient. **(d)** Complex AM transients obtained by  $r_{AM,H}(t) = \mathcal{H}(r_{AM}(t))$  with its deconvolutions in **(e)** and **(f)**. **(g)** Corrected complex AM transient,  $r_{AM,H,Cor,FP}(t)$ , with time-shift as described in the text with its deconvolutions in **(h)** and **(i)**. **(j)** Corrected complex AM transient,  $r_{AM,H,Cor}(t)$ , with its phase-corrected deconvolutions in **(k)** and **(l)**.

removed. Possibly, the complex driving function and the real-valued RS-EPR signal do not fit in this case. If the signal is unsaturated, however, the Kramers-Kronig relation (mathematically a Hilbert transform  $\mathcal{H}$ ) may be invoked to create a complex signal using the AM signal, i.e.,  $r_{AM,H}(t) = \mathcal{H}(r_{AM}(t))$ , as shown in [Figure 7.2 \(d\)](#).

Two RS-EPR signals per complete cycle are seen as the MW frequency hits the resonance field twice per cycle: from low frequency to high frequency and vice versa. Assuming a *Lorentzian* lineshape, only the absorption signal is symmetric with respect to the scan direction, i.e., the same signal appears twice per full cycle. The dispersion signal is asymmetric with respect to the scan direction. Therefore, the dispersion signal will be mirrored about the  $y$ -axis. When Hilbert transforming a full-cycle absorption signal to dispersion, the asymmetry due to the different scan direction is not reproduced as seen in [Figure 7.2 \(d\)](#) resulting in successful deconvolution of only one of the cycles as observed in [Figure 7.2 \(d\)](#) and (e). Hence, the Hilbert transform of up and down needs to be separated so that a proper complex RS signal is produced as

$$r_{AM,H,Cor}(t) = \text{sgn} \left( t - \frac{T_{rs}}{2} \right) \Re(r_{AM,H}(t)) + i\Im(r_{AM,H}(t)), \quad (7.5)$$

where  $T_{rs} = 1/f_{rs}$  is the period of a full cycle and

$$\text{sgn}(t) = \begin{cases} -1 & \text{if } t < 0 \\ +1 & \text{if } t \geq 0 \end{cases} \quad (7.6)$$

is a slightly adapted version of the *signum* function.

In addition, the transient,  $r_{AM,H,Cor}(t)$ , was deliberately time-shifted with respect to the excitation to investigate its influence on the deconvolved spectra since the so-called first point parameter needs to be manually adjusted in the deconvolution procedure. As  $r_{AM,H,Cor}(t)$  is a periodic function with a frequency,  $f_{rs}$ , the transient can be circularly shifted. A time shift of  $3^\circ$  (a shift by  $360^\circ$  would result in no shift) was applied to  $r_{AM,H,Cor}(t)$  and forms  $r_{AM,H,Cor,FP}(t)$  shown in [Figure 7.2 \(g\)](#). As seen in [Figure 7.2 \(h\)](#) and (i), the deconvolutions of both up and down sweep return reasonable spectra, which are, however, considerably shifted in frequency due to the mismatch of the excitation,  $d(t)$ , and the transient,  $r_{AM,H,Cor,FP}(t)$ . As both deconvolved spectra are summed, such misalignment may easily lead to false interpretation of the RS-EPRoC data, especially for samples with narrow linewidths.

[Figure 7.2 \(j\)](#) shows a properly time-aligned AM RS-EPRoC transient,  $r_{AM,H,Cor}(t)$ , with corrected Hilbert transformation. The resulting spectra in (k) and (l) are phase-corrected to remove admixture of the dispersion signal in the AM signal. The phase-correction procedure returns well-separated absorption and dispersion spectra, since complex signal in (j) generated from the AM signal and the corrected Hilbert



transform may be regarded as a signal with a certain constant phase shift  $\varphi$  as

$$r(t) = (M_x(t) + iM_y(t))e^{i\varphi}, \quad (7.7)$$

which can be phase-corrected by a multiplication of the complex-valued spectra by  $e^{-i\varphi}$  to recover the proper absorption and dispersion spectra.

#### *Deconvolution algorithm*

Usually, multiple full cycles of the transient signal are recorded. The as-recorded transient is cropped to an integer number of full cycles,  $N_{fc}$ , calculated from the experimental parameters which are then digitally averaged to obtain one full cycle transient. For the deconvolution, the so-called half-cycle deconvolution algorithm is used [97]. Therefore, both half-cycles (first half of the cycle and second half of the full cycle) were treated separately. Both half-cycle transients are zero-padded with a *Welch* apodisation window [249] prior to Fourier transformation. The same zero-padding and apodisation window is applied to each half-cycle excitation function,  $d(t)$ , which is calculated assuming a sinusoidal frequency scan and numerically integrated. The zero-padding improves the frequency resolution, while the apodisation window avoids spikes obtained from zero-padding. To obtain the half-cycle slow-scan spectrum, the Fourier transform of the signal is divided by that of the excitation for each half cycle. Both spectra are summed and subsequently phase-corrected so that a well-defined absorption spectrum, i.e., symmetric about the resonance frequency, is obtained.

#### 7.2.4 *Digital post-processing of CW- and RS-spectra and SNR*

Both CW- and RS-EPRoC spectra are digitally filtered using a moving-average, second-order *Savitzky-Golay* filter provided by *EasySpin*. The filter window is adjusted to ensure that the linewidth is broadened by less than 5%.

For the CW data, the effective acquisition time is calculated from the number of data points of the sweep,  $N_{\text{points}}$ , and the time constant of the LIA,  $\tau_{\text{LIA}}$ , and the number of averages,  $N_{\text{avg,cw}}$ , as

$$T_{\text{acq,cw}} = 3N_{\text{points}}N_{\text{avg,cw}} \cdot \tau_{\text{LIA}}. \quad (7.8)$$

The factor of 3 is introduced to take into account the rise time/settle time of the LIA required to avoid overshoot and achieve 99.9% of the maximum signal intensity.

For the RS data, the effective acquisition time is calculated using the number of averages,  $N_{\text{avg,rs}}$ , and both the number,  $N_{fc}$ , and the period,  $T_{fc}$ , of all RS cycles present in the signal acquisition, respectively, as

$$T_{\text{acq,rs}} = N_{\text{avg,rs}}N_{fc} \cdot T_{fc}. \quad (7.9)$$

For CW spectra, the signal amplitude is defined as the peak-to-peak amplitude of the AM signal, while the signal amplitude of the deconvolved RS-EPRoC spectrum is defined as the maximum value of the imaginary part of the deconvolved RS spectrum, i.e., the absorption. The root mean square (RMS) noise is determined from the baseline regions of the spectra taking approximately 61 % of the data points of the spectra into consideration. The SNR is calculated as the ratio of the signal amplitude to the RMS noise.

For the saturation analysis, the signal amplitude of the RS measurements is defined as the peak-to-peak amplitude of the transient RS signals since deconvolving the transients at the highest scan rate was impossible due to overlapping signals. To compare the signal amplitudes of CW and RS methods and scan rates, the relative signal amplitude is used.

### 7.2.5 *Sample*

A single grain of BDPA (1:1 with benzene from Sigma Aldrich) was placed in the AM1 coil of the EPRoC detector as shown in [Figure 7.1 \(b\)](#). BDPA gives an EPR signal at  $g = 2.003$  [150] with linewidths between 0.04 to 0.08 mT [157]. The sample volume was approximated using multiple photographs of the sample as shown in [Figure 7.1 \(b\)](#) while varying the light present to differentiate shadows from the sample material. To calculate the sample volume, a cuboid was assumed. The planar dimensions of the cuboid were determined from the shape of the sample in the photograph, while its height was determined using its shadow on the chip. In this way, the sample volume might be overestimated. Therefore, a relative error of 10 % for each direction is assumed. The sample volume was  $7(2) \times 10^{-4} \text{ mm}^3$  (0.7(2) nL). With the density of the BDPA-benzene complex of  $1.220 \text{ g cm}^{-3}$  [154] the mass of the sample was determined to be approximately 0.8(2)  $\mu\text{g}$ . In combination with the molecular weight of BDPA of  $495.63 \text{ g mol}^{-1}$ , an approximate number of spins in the sample of  $1.0(2) \times 10^{15}$  spins was calculated.

## 7.3 RESULTS AND DISCUSSION

In this section, the experimental results and discussion are presented. First, the CW- and deconvolved RS-EPRoC spectra are compared and analysed with respect to SNR. Second, the most important results will be shown, namely the saturation behaviour. And third, the theoretical limits of RS-EPR is discussed by means of simulations.

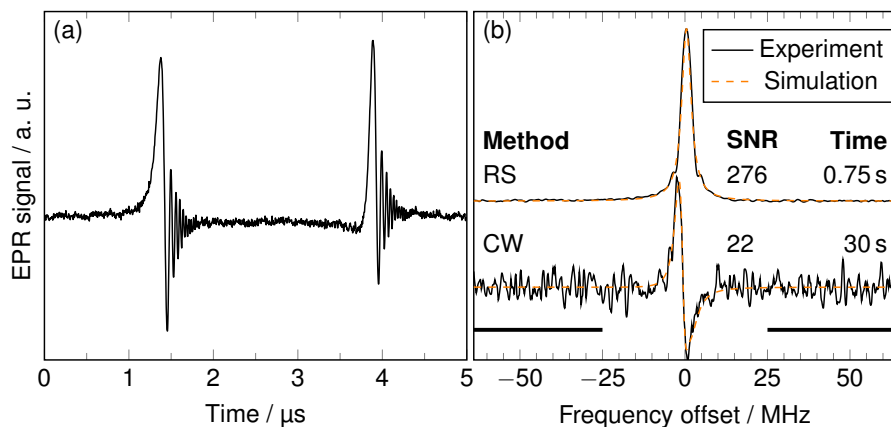


Figure 7.3: **(a)** Transient baseline-corrected full-cycle AM RS-EPRoC signal of BDPA recorded with a scan rate of  $80 \text{ THz s}^{-1}$  (corresponding to  $2.9 \text{ kT s}^{-1}$ ,  $f_{\text{RS}} = 200 \text{ kHz}$ ,  $\Delta f_{\text{RS}} = 64 \text{ MHz}$ ,  $I_{\text{bias}} = 7 \text{ mA} \approx 46 \text{ } \mu\text{T}$ ). **(b)** Top: Deconvolved spectrum of the transient seen in (a). Bottom: CW-EPRoC spectrum of the same sample ( $f_{\text{m}} = 100 \text{ kHz}$ ,  $\Delta f_{\text{m,pp}} = 768 \text{ kHz}$  (corresponding to  $0.028 \text{ mT}$ ),  $\tau = 10 \text{ ms}$ , roll-off:  $24 \text{ dB}$ ,  $I_{\text{bias}} = 5 \text{ mA} \approx 27 \text{ } \mu\text{T}$ ). The dashed orange lines depict the simulation of both spectra. Reprinted from [131] ©.

### 7.3.1 Comparison of CW- and RS-EPRoC spectra

Figure 7.3 shows an example of a full-cycle transient AM RS-EPRoC signal recorded with a bias current of  $7 \text{ mA}$  ( $B_1$  of approximately  $45.5 \text{ } \mu\text{T}$ ) and a scan rate of  $80 \text{ THz s}^{-1}$ . The signal exhibits characteristic “wiggles” resulting from the non-adiabatic rapid passage. As the resonance is passed twice in each full cycle, the signal is recorded twice during the experiment. As anticipated, the AM EPRoC signal displays an asymmetric line shape due to the mixture of absorption and dispersion, as described in Equation 3.20, dependent on the direction of the frequency sweep. In the case of a pure absorption signal, the two lines would be symmetric; in the case of a pure dispersion signal, they would appear as “mirrored” about the  $y$ -axis with respect to each other since the resonance is traversed once from low frequency to high frequency and again in the opposite direction. To recover the EPR spectrum, the transient RS-EPRoC signal is Fourier deconvolved to remove the effects of the sinusoidally modulated MW frequency used for excitation, as discussed in Section 7.2.3.

In Figure 7.3 (b), only the imaginary component of the deconvolved RS-EPRoC spectrum, corresponding to the imaginary component of magnetic susceptibility, i.e., the absorption, is displayed. For comparison, the CW-EPRoC spectrum of the same sample was recorded using a bias current of  $5 \text{ mA}$  ( $B_1 \approx 27 \text{ } \mu\text{T}$ ), which is also displayed. The purpose of the different bias currents in the two experiments was to ensure operation within the linear regime, thereby avoiding microwave saturation.

Table 7.1: SNR for the CW-EPRoC and RS-EPRoC methods.

Method	$I_{\text{bias}}$ mA	$B_1$ $\mu\text{T}$	$n_{\text{avg}}$ 1	$\alpha_{\text{rs}}$ $\text{THz s}^{-1}$	SNR 1	$t_{\text{acq}}$ s	$\text{SNR}_{\text{norm}}$ $\text{s}^{-0.5}$
CW	5	27.0	1	0.5	22	30.0	4.0
RS	7	45.5	$1.5 \times 10^5$	80.4	276	0.75	318.6

As anticipated from Equation 3.20, the CW-EPRoC signal displays an asymmetric line shape, similar to the AM RS-EPRoC transient displayed in Figure 7.3 (a). In contrast, there is no asymmetry in the RS-EPRoC spectrum because it can be phase-adjusted to selectively display only the absorption signal as explained in Equation 7.2.3. In CW-EPRoC measurements, quadrature detection is not possible with our setup, and *Kramers-Kronig* manipulation is unsuitable due to minor signal saturation. As the minimum bias current defining  $B_1$  has been used to record the AM CW-EPRoC spectrum, recording a spectrum with lower bias current was not possible.

Both spectra in Figure 7.3 are simulated using the *pepper* function from the *EasySpin* software package [70], assuming a spin-1/2 system with *Lorentzian* broadening. For the RS spectrum, the only free fit parameter is the *Lorentzian* peak-to-peak linewidth. The asymmetry in the line shape of the CW spectrum is incorporated into the simulation through a customised fitting function based on Equation 3.21b, which encompasses a combination of absorption and dispersion as  $Q_{\text{coil}}\chi'' - \chi'$ . The free fit parameters for the CW spectrum is the *Lorentzian* peak-to-peak linewidths and  $Q_{\text{coil}}$ . The peak-to-peak linewidth of the fit is 1.98 MHz (0.071 mT) for the RS-EPRoC spectrum. For the CW-EPRoC spectrum the linewidth is 2.58 MHz (0.094 mT) and  $Q_{\text{coil}} = 1.21$ . The linewidth of the RS-EPRoC spectrum is well within the range which is expected for BDPA as discussed in Section 5.3.1 assuming a relaxation-determined broadening. The linewidth of the CW-EPRoC spectrum, however, is larger than that of the RS-EPRoC spectrum and also too large for relaxation-determined broadening. In the fit,  $Q_{\text{coil}}$  was a fit parameter in addition to the broadening. As the lineshape and with that the linewidth strongly depends on the  $Q_{\text{coil}}$  both parameters may be correlated, potentially leading to false results. Possibly, the sample is slightly saturated in CW-EPRoC due to the relatively large  $B_1$  as discussed in Section 5.3.4.3 and Section 7.3.2 leading to a broadening of the spectrum. Such a broadening has been observed for the FM signal in Section 5.3.1, too. As mentioned above the minimum bias current to achieve stable oscillations of the VCO of the EPRoC has been used to record the AM CW-EPRoC spectrum. Therefore, a further lowering was not possible.

Table 7.1 summarises the SNR and other relevant parameters for both CW- and RS-EPRoC measurements. Only the imaginary component

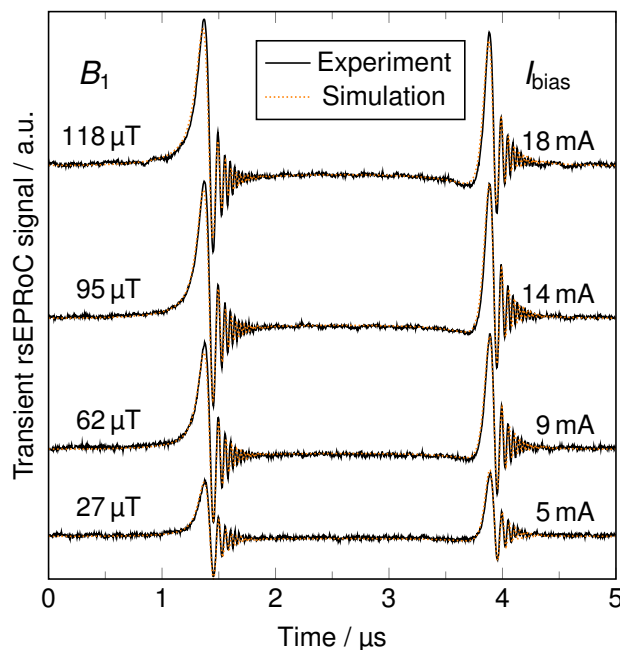


Figure 7.4: Transient AM RS-EPRoC signals with increasing bias currents (5, 9, 14 and 18 mA) corresponding to four different  $B_1$  magnitudes (27, 62, 95 and 118  $\mu\text{T}$ ) with simulation at a scan rate of 80  $\text{THz s}^{-1}$ . The resonance is passed twice for each period of modulation. Reprinted from [131] ©.

of the deconvolved spectrum is displayed in Figure 7.3, even though the deconvolution returns both real and imaginary component as discussed in Section 7.2.3. In case of quadrature detection, in which the noise of the real and imaginary component of RS transient are uncorrelated, it is in theory possible to further increase the SNR by a factor of  $\sqrt{2}$  by adding the real and imaginary components of the deconvolved RS-EPRoC spectrum [250] similar to doubling the number of averages. However, in the presented data, for which the Kramers-Kronig relation is utilised to obtain the complex transient RS-EPRoC signal for deconvolution, the SNR cannot be enhanced in this way as the noise is correlated. RS-EPRoC measurements provide an increased SNR per unit measurement time, resulting in an overall SNR improvement of nearly two orders of magnitude.

These findings align well with those reported for field-swept RS-EPR measurements across various sample classes, including nitroxyl radicals [234], irradiated fused quartz [233], and samples with long relaxation times, such as a-Si:H or  $\text{N@C}_{60}$  [5, 242].

### 7.3.2 Analysis of the transient RS-EPRoC signal and its saturation behaviour

To investigate the saturation behaviour of the EPRoC, 14 transient AM RS-EPRoC signals at increasing bias currents of 5 to 18 mA at a scan

rate of  $80 \text{ THz s}^{-1}$  were recorded, covering the complete range where AM signals were observed. For clarity, [Figure 7.4](#) shows only four AM RS-EPRoC transients at varying bias currents of 5, 9, 14 and 18 mA. As expected from [Equation 3.20](#), the transients exhibit a slight asymmetry of both signals due to the slight admixture of the dispersion to the AM signal. All transients were simulated and fitted globally by means of steady-state solutions of the *Bloch* equations with sinusoidal modulation [[70](#), [97](#)] using *EasySpin's* *blochsteady* function as an absorption signal with a slight admixture of dispersion similar to [Equation 7.4](#). These solutions assume a spin-1/2 system with a *Lorentzian* lineshape. For the simulation, a *g*-value of 2.003 and relaxation times of  $T_1 = 110 \text{ ns}$  and  $T_2 = 100 \text{ ns}$  were assumed based on previous reports for BDPA [[156](#), [157](#)]. As the  $B_1$  magnitude required for the simulation can neither be calculated analytically from the bias current and the parameters of the EPRoC nor directly be determined by measuring *Rabi* oscillations due to the limited bandwidth of the PLL, an empirical model was developed. The square-root model describes the relationship between the coil current  $I_{\text{coil}}$  and the bias current as

$$I_{\text{coil}} = a + b\sqrt{I_{\text{bias}}} \quad \text{and} \quad (7.10)$$

*Biot-Savart's* law for the magnetic field in the centre of a circular single-turn inductor as

$$B_1 = \frac{1}{2}\mu_0 \frac{I_{\text{coil}}}{2R} = \frac{1}{2}\mu_0 \frac{a + b\sqrt{I_{\text{bias}}}}{2R} \quad (7.11)$$

Here,  $\mu_0$  is the magnetic constant,  $R = 100 \mu\text{m}$  is the radius of the coil, and  $a$  and  $b$  are empirical parameters for the proposed square-root model. The square-root model was introduced to take the curvature of the coil current at low bias current into consideration as seen from [Equation \(8\)](#) in [[133](#)], where the gate transconductance  $G_{m0} = \sqrt{\beta I_{\text{bias}}/n}$  depends on the bias current. In the simulations, the quality factor  $Q$  accounting for the asymmetry of the transients as well as  $a$  and  $b$  were the only fit parameters. The empirical parameters for the model are given by

$$a = -23.6 \text{ mA} \quad \text{and} \quad b = 14.4 \sqrt{\text{mA}} \quad (7.12)$$

The conversion of the bias current to  $B_1$  is shown in [Figure 7.5](#). Please note, that for the square-root model, no  $B_1$  distribution was assumed as the  $B_1$  was only calculated for the centre of the circular single-turn inductor. Nevertheless, the simulations are in good agreement with the experimental data.

[Figure 7.6](#) shows the relative signal amplitudes of the CW signal and RS-EPRoC signal at varying scan rates of 80.4, 201.1 and 402.1  $\text{THz s}^{-1}$  as a function of  $B_1$  as calculated from  $I_{\text{bias}}$ , demonstrating the saturation behaviour of the sample. The signal amplitudes are normalised such that their linear regime is overlapping below  $40 \mu\text{T}$ . As expected, the

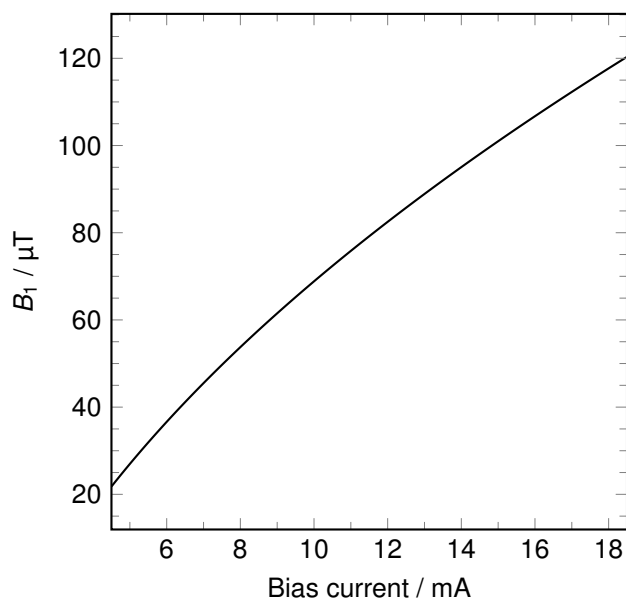


Figure 7.5:  $B_1$  magnitude obtained by the square-root model of the bias current used to calibrate the EPRoC. Reprinted from [131] © ⓘ.

signal amplitudes of both CW- and RS-EPRoC increase with increasing  $B_1$  and saturate at higher  $B_1$  depending on the scan mode and scan rate. In CW, the sample expectedly saturates at lower  $B_1$  values than in RS operation. In addition, with increasing scan rate,  $\alpha$ , the sample saturates at higher  $B_1$  as expected, allowing the use of larger  $B_1$  values for the experiment beyond the relaxation-determined limit in CW. Despite the relatively short relaxation times of BDPA of the order of 100 ns, it was chosen for these experiments allowing for experiments in the linear regime for both CW- and RS-EPRoC (c.f Equation 2.63 and Equation 2.64). For many slowly relaxing samples, the obtainable large minimum  $B_1$  of the EPRoC saturates the EPR signal, rendering the lineshape distorted and thereby inhibiting quantitative analysis. The RS technique is particularly suited for samples with long relaxation times such as single substitutional nitrogen centres in diamonds,  $\text{N@C}_{60}$ , or a-Si:H [5, 242] for which MW saturation is observed even at low MW powers when utilising CW methods.

### 7.3.3 Theoretical limits of rapid-scan EPR

In this section, the theoretical limits of the AM RS-EPRoC technique are explored similar to the discussions in [226]. Please note that these considerations are of general nature as they also apply for RS-EPR. To this end, signal amplitudes obtained from deconvolved RS-EPR transients as a function of both  $B_1$  and scan rate,  $\alpha$ , were simulated as shown in Figure 7.7. For each point in the figure, an RS-EPR transient was simulated assuming relaxation times of  $T_1 = 110$  ns and  $T_2 = 100$  ns as well a  $g$ -value of 2.003 of BDPA (cf. Section 7.3.2), which were



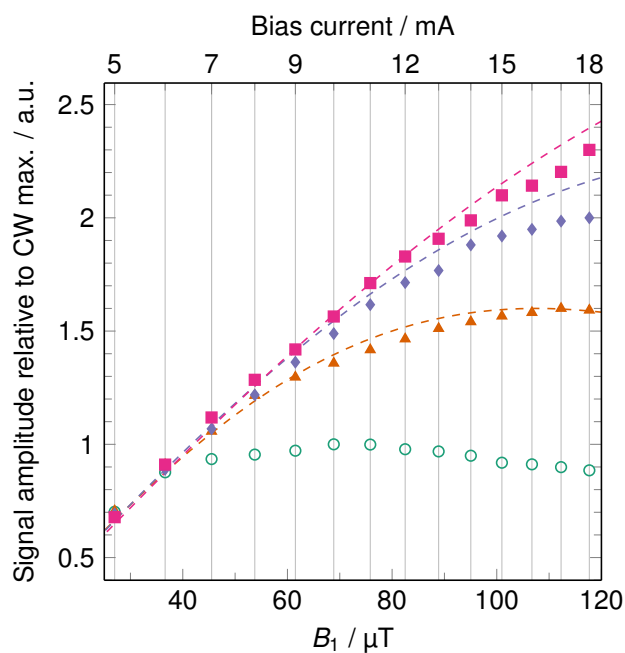


Figure 7.6: Signal amplitudes of the AM CW-EPRoC (green open circle) and of the transient AM RS-EPRoC signals (filled symbols) at three different scan rates (orange triangle:  $80.4 \text{ THz s}^{-1}$ ; purple diamond:  $201.1 \text{ THz s}^{-1}$ ; pink square:  $402.1 \text{ THz s}^{-1}$ ) as a function of the bias current ( $x$ -axis, top). The bottom  $B_1$ -axis is calculated from the square-root model shown in Figure 7.5. The dashed lines depict simulations for the saturation of the RS-EPRoC signals. Reprinted from [131] ©.

subsequently deconvolved. The signal amplitude was extracted at the maximum of the absorption component of the deconvolved spectrum. The signal amplitudes were normalised to their global maximum to probe the limits of the RS-EPRoC technique with respect to SNR. Since the scan rate is the product of scan width and repetition rate, either may be adjusted to change the scan rate. In the simulation, however, the scan rate was increased by increasing the sweep width while keeping the repetition rate constant (200 kHz) to ensure that the wiggles have completely decayed within a half cycle.

As seen by the dotted rectangle (Max. reported) in Figure 7.7, this analysis extends the RS-EPR technique far beyond what is possible with field-swept RS-EPR to encompass a regime that is only accessible via frequency-swept RS-EPR, which has now been implemented with RS-EPRoC.

The simulations show that an improvement of the signal amplitude of a factor of approximately 5 compared to the presented data may be achieved with larger  $B_1$  (0.8 mT) and faster scan rates (approximately  $10\,000 \text{ THz s}^{-1}$ ) for samples with relaxation times of approximately 100 ns.



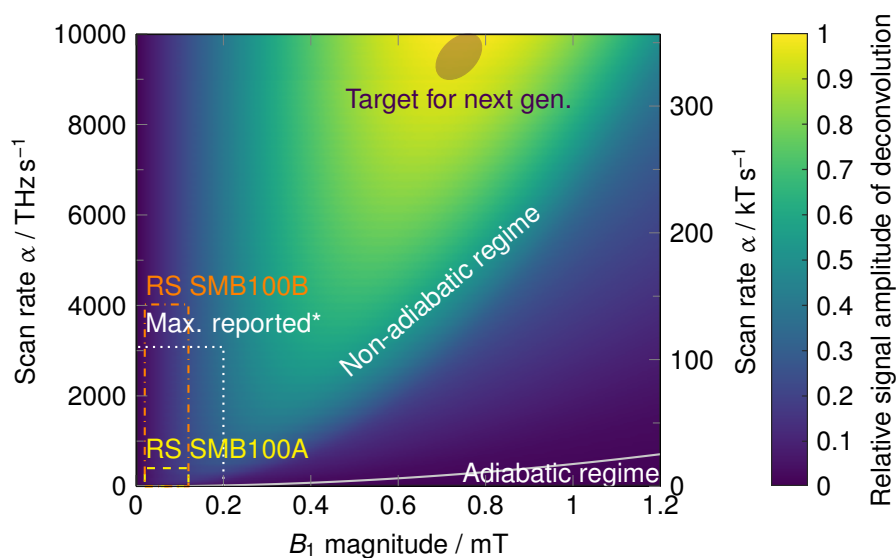


Figure 7.7: Relative signal amplitude of the deconvolution of simulated RS spectra as a function of both  $B_1$  and scan rate  $\alpha$ . The relaxation times were  $T_1 = 110$  ns and  $T_2^* = 100$  ns. The simulations were performed with a constant RS-EPR frequency of 200 kHz and increasing scan width. The solid white line defines the adiabatic and non-adiabatic regions. The yellow dashed rectangle shows the accessible  $B_1$  and scan rate combinations explored in this work with the R&S SMB<sub>100A</sub>, while the white dotted rectangle shows that of the field-swept RS-EPR experiment where the maximum scan rate was reported. The orange dashed-dotted rectangle shows the maximum scan rate achievable with the R&S SMB<sub>100B</sub> signal generator. (\*The fastest scan rate currently reported for a frequency-swept high-field/high-frequency RS-EPR experiment was 267 000 THz s<sup>-1</sup> [86], which is far beyond the limits of the plot.). Adapted from [131] © ⓘ.

Generally, a larger signal amplitude may be achieved if both  $B_1$  and  $\alpha$  are increased simultaneously. An optimal scan rate may be found for a constant  $B_1$  which maximises the relative signal amplitude without saturating the sample (along the  $y$ -axis). A further increase of the scan rate beyond the optimal value (non-saturating) does not further increase the signal amplitude. Likewise, for a constant scan rate (along the  $x$ -axis), an optimal  $B_1$  may be found maximising the relative signal amplitude without saturation. A further increase of  $B_1$  without an accompanying increase in scan rate leads to a loss of signal intensity due to saturation-induced line broadening. Hence, an increase of relative signal amplitude is only seen by increasing both  $B_1$  and  $\alpha$ . This principle provides the direction for the development of future RS-EPRoC designs.

In the presented experiments, the  $B_1$  of the EPRoC was limited by the passive cooling of the chip to about  $125 \mu\text{T}$ . Active cooling may improve this value by a factor of 2 to approximately  $250 \mu\text{T}$ . A further increase in  $B_1$  may be obtained by reducing the coil diameter. Here, halving the coil diameter to  $100 \mu\text{m}$  would provide another factor of 2 in  $B_1$  as seen by *Biot-Savart's* law (Equation 7.11). While the current RS-EPRoC design was produced using CMOS technology, other fabrication techniques such as bipolar CMOS (BiCMOS) and indium-gallium-arsenide (InGaAs) would allow for an increased total  $B_1$  of approximately  $1 \text{ mT}$  (factor of  $\sim 10$ ).

As mentioned before, the scan rate may be enhanced by either widening the sweep range, decreasing the time spent on resonance, or employing faster repetition rates,  $f_{\text{rs}}$ , increasing the number of sweeps per unit time. While there is no fundamental limitation for increasing the sweep range, the repetition rate, that is the number of sweeps per unit time, is limited by the effective transversal relaxation time  $T_2^*$  [251] as

$$\frac{1}{f_{\text{rs}}} > N \cdot T_2^*, \quad (7.13)$$

where  $N$  is a factor between 3 and 5, describing the amount of acceptable line broadening introduced by Fourier deconvolution. This relation means that the wiggles of the RS-EPR signal must have completely decayed before the next scan cycle. As these wiggles decay exponentially with  $T_2^*$ , a factor  $N = 3$  (5) means approximately 5% (0.7%) of the maximum signal is remaining before the next cycle is recorded.

In the current experiment, however, the scan rate is not limited by the EPRoC itself or the PLL, but by the signal generator used for generating the reference frequency (R&S SMB100A). Other commercial analogue signal generators such as the R&S SMB100B, the Keysight UXG N5193A, or the Anapico APSIN allow access to larger scan rates. With the R&S SMB100B, the scan width may be increased by a factor of 2.5 ( $\Delta f_{\text{rs,max}} = 160 \text{ MHz}$  (sweep width  $320 \text{ MHz}$  or  $11.4 \text{ mT}$ )) and the re-

petition rate by a factor of 10 ( $f_{rs,max} = 10$  MHz). When operating the R&S SMB100B outside its specifications, scan widths of up to 640 MHz may be achievable ( $\Delta f_{rs,max} = 10$  MHz) as depicted in Figure 7.7. The Keysight UXG N5193A signal generator provides an enormous maximum modulation amplitudes of up to 128 MHz at rates of up to 10 MHz at 420 MHz base frequency, which would lead to theoretical sweep widths of 8.2 GHz, which is even larger than the frequency sweep width of the EPRoC. The high sales price, however, did not permit experiments with this device so far. The Anapico APSIN26G offers scan widths of up to 1.4 GHz ( $\Delta f_{rs,max} = 21$  MHz). Additionally, according to the specifications, the single sideband phase noise of the Anapico APSIN26G is lower from 1 Hz to 100 kHz and slightly higher above approximately 100 kHz frequency offset than the R&S SMB100A. In practise, however, experiments utilising this device were inconclusive. The experiment was performed such that RS-EPRoC AM transient of a grain of BDPA was recorded with the setup described in Section 7.2.1, once with the R&S SMB100A and once with the Anapico device as RF generator. The experimental parameters were the same in these experiments, apart from the utilised RF generator. The recorded transients are shown in Figure 7.8. The RS transient recorded with the Anapico device decays approximately 20% faster than that of the R&S SMB100A, with a seemingly lower  $T_2^*$ . This may be attributed to higher noise characteristics of the Anapico device used as PLL reference noise is convolved with the RS transient, essentially quenching the observed  $T_2^*$ . Hence, this device seems to show worse noise characteristics compared to the Rohde & Schwarz devices. So, the single sideband phase noise does not seem to be a good metric to evaluate the best signal generator for RS.

As discussed above, the repetition rate, in general, is limited by the effective transversal relaxation time, limiting the use of such high repetition rates of the R&S SMB100B or similar devices. In addition, repetition rate,  $f_{rs}$ , is limited by the bandwidth of the PLL to about 5 MHz, so that improvements of the scan rate of a factor of 10 compared to the presented setup are realistic.

Recent experiments using a similar EPRoC instrument as discussed in this chapter utilising the FM RS-EPRoC signal of slowly relaxing trityl radicals were successfully performed. As the scan rates necessary to achieve the non-adiabatic RS regime are much lower than for the BDPA sample shown in these experiments, the PLL bandwidth poses no limitation due to the much smaller signal bandwidth of the FM RS transients. These experiments, however, will be discussed in a forthcoming publication. In the meantime, a next-generation single-coil EPRoC prototype with a base frequency of 30 GHz and a sweep width of 2.5 GHz has been developed [130] offering an on-chip PLL with a bandwidth larger than 200 MHz. This large PLL bandwidth allows the extraction of the FM signal for RS-EPRoC in addition to the

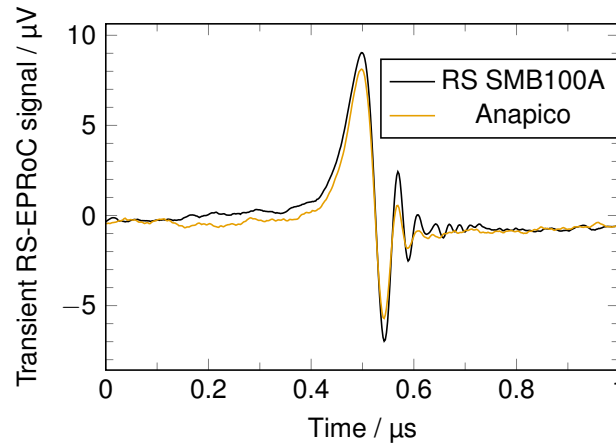


Figure 7.8: Comparison of half-cycle RS-EPRoC transients of a BDPA sample acquired using the Rohde & Schwarz SMB100A (R&S SMB100A) and the Anapico APSIN26G signal generator as frequency reference for the PLL at a scan rate of  $201 \text{ THz s}^{-1}$  ( $f_{\text{rs}} = 500 \text{ kHz}$ ,  $\Delta f_{\text{mod}} = 64 \text{ MHz}$ ) and a bias current of  $5 \text{ mA}$ .

AM signal even at fast scan rates so that the improved noise floor of the EPRoC array may be exploited, which improves the sensitivity by means of spatial averaging of multiple VCOs as discussed in [Section 3.4](#).

#### 7.4 CONCLUSIONS

In this chapter, we introduced the usage of the EPRoC for closed-loop non-adiabatic frequency-swept RS-EPRoC experiments. The embedding of the VCO in PLL in combination with the usage of the implicit AM demodulation capabilities allows acquiring RS transients with a much simpler experimental setup compared to field-swept RS-EPR. In these experiments, the SNR per unit time of the deconvolved RS-EPRoC spectrum could be improved by almost 2 orders of magnitude compared to the CW spectrum using the same EPRoC detector and the same BDPA sample. The improved SNR can be attributed to combination an increased signal amplitude because of a later onset of sample saturation (factor of approximately 2) and a lowered noise floor due to (temporal) averaging. Similar to field-swept RS-EPR, these results confirm that the RS-EPRoC signal is less prone to saturation. The RS-EPRoC signal remains in the linear regime up to  $90 \mu\text{T}$  for BDPA at the fastest investigated scan rate of  $402.1 \text{ THz s}^{-1}$ . This allows to acquire unsaturated EPR spectra for samples with relaxation times longer than that of BDPA of approximately  $100 \text{ ns}$ . With that, one substantial limitation for utilisation of the EPRoC for (quantitative) spectroscopy is alleviated.

From multiple AM RS-EPRoC transients recorded at varying bias current, the conversion of the bias current to  $B_1$  was experimentally determined by means of a square-root model for the first time for the EPRoC. Previously, this conversion could only be calculated from circuit

simulations of the EPRoC. This conversion is similar to the conversion factors of commercial resonators, from which  $B_1$  may be calculated from the applied MW power. In addition, it was shown that the AM RS-EPRoC transients can reliably be deconvolved to the corresponding CW spectrum. For spectroscopists, the deconvolution of AM RS-EPRoC transients and possible obstacles when using experimental RS-EPRoC data were discussed in great detail. This may serve as a framework for further AM RS-EPRoC experiments but is also valid for FM RS-EPRoC experiments.

In these experiments, the frequency was swept to acquire the CW- and RS-EPRoC data, while the magnetic field was kept constant, so that in principle a suitable permanent magnet could have been used. The large frequency sweep width capability of up to 2.4 GHz (corresponding to 86 mT) around a central frequency of about 14 GHz at RS frequencies of up to 5 MHz may set milestones in terms of sweep width ( $4 \times$  compared to commercial RS accessories) and scan rate given that a suitable means of generating a low noise frequency-modulated reference frequency is found. This would allow one to investigate TMI and other samples with broad spectra with RS-EPRoC. In combination with small permanent magnets, application-specific RS-EPRoC sensors for multi-line fingerprinting applications in chemistry, medicine, biology, material science, and physics may be developed.



## STATE OF CHARGE MONITORING OF A VANADIUM REDOX FLOW BATTERY WITH EPR-ON-A-CHIP

---

### 8.1 INTRODUCTION

So far, this thesis has dealt with the understanding of and method development for EPR-on-a-Chip (EPRoC) devices. In this chapter, we will combine the results of most of the previous chapters and apply the knowledge to an actual real-world problem. The climate crisis is the major challenge humanity currently faces. To reduce its impact, anthropogenic greenhouse gas emissions must become net neutral or even negative as quickly as possible. Therefore, a transition from a fossil fuel-based economy to one based on renewable energy sources such as wind power and photovoltaics is required. However, due to the intermittent nature of these renewable energy sources not only energy production but also storage solutions play an essential role in this transition. As the electrical grid is not able to store electricity, demand and “production” needs to be equal at all times. This requires short-, mid- and long-term electrical energy storage (EES) solutions with timescales from below seconds to hours/days and power values from a few kW to GW. While the long- and mid-term EES (minutes to hours) provide so-called energy management including load levelling and time shifting, short-term EES (seconds to minutes) are needed for grid stabilisation and frequency regulation [252].

For long-term EES pumped hydroelectric storage (PHES) and compressed air energy storage (CAES) are used with power values ranging from hundreds of MW to GW, where PHES is most widely used and accounted for approximately 94 % of the worldwide installed storage capacity in 2022 of up to 9 TWh with an estimated power of 158 GW [253]. Yet, the immense cost of construction, substantial environmental costs, and the special geographical requirements limit implementation of this technology on a (much) larger scale than today. While underground CAES is much less capital-intensive than PHES with a much lower impact on the environment, it has geographical requirements, too, as the air is usually stored in underground caves. Therefore, the globally installed power is only 0.45 GW [254], much smaller than that of PHES. Among others, super-capacitors as well as lithium-ion and lead-acid batteries are used for short term EES due to their very fast response time [252, 255]. For mid-term EES, varying types of bat-

---

A significant portion of this chapter is from S. Künstner, J. E. McPeak, A. Chu, M. Kern, K.-P. Dinse, B. Naydenov, P. Fischer, J. Anders, K. Lips, Monitoring the State of Charge of Vanadium Redox Flow Batteries with an EPR-on-a-Chip Dipstick Sensor. *Physical Chemistry Chemical Physics* 2024, 26 (25), 17785–17795. DOI: [10.1039/D4CP00373J](https://doi.org/10.1039/D4CP00373J).

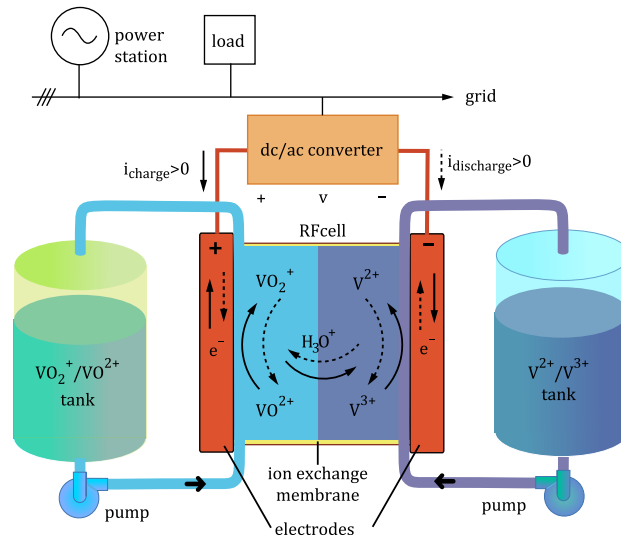


Figure 8.1: Schematic of a vanadium redox flow battery. The electrochemical cell, in which the vanadium reactions take place, is denoted with RFcell. The catholyte (positive electrolyte) is pumped from the tank on the left-hand side (denoted with  $\text{VO}_2^+/\text{VO}^{2+}$ ) to the half-cell with the cathode, while the anolyte is pumped from the tank on the right-hand side (denoted with  $\text{V}^{2+}/\text{V}^{3+}$ ) to the half-cell with the anode. The ion exchange membrane allows transfer of ions to ensure electrical neutrality. In case of a cation-exchange membrane, hydronium ions ( $\text{H}_3\text{O}^+$ ) are transferred. The connection of the battery to the electrical grid via a direct current/alternating current (DC/AC) converter is shown at the top. An electrical load and a power station connected to the grid is indicated. The solid arrows in the electrochemical cell indicate the conversion of vanadium species and the ones in the electrolyte the direction of the electron flow during charge, while the dashed arrows indicate the discharge. Reproduced with permission from Elsevier from ref. [252].

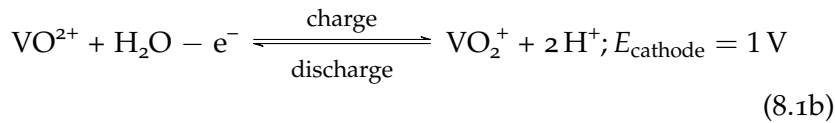
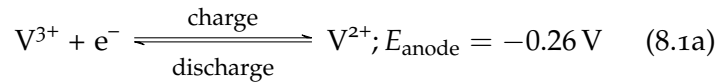
teries are commonly used such as lithium-ion, lead-acid, and redox flow batteries (RFBs) of varying chemistry. The latter are considered a promising technology as the power and capacity are independent of each other in contrast to other battery types. This makes RFBs well suited not only for mid-term EES but also short-term and possibly even long-term storage, while offering flexible and scalable solutions with fast response times and relatively low capital costs [255–257].

Redox flow batteries store energy by chemical reactions of different electro-active species, so-called redox couples, dissolved in electrolytes. Upon charging and discharging, the redox couples change from one oxidation state to another. A sketch of an RFB, more precisely of a vanadium redox flow battery (VRFB), is shown in Figure 8.1. In the RFB, an electrochemical cell (denoted with RFcell in the figure) consisting of anode and cathode half-cells filled with anolyte (negative electrolyte) and catholyte (positive electrode) is used for the energy



conversion, with the two half-cells being separated by an ion-exchange membrane [252, 258]. Typically, Nafion is used for the ion-exchange membrane, while the electrodes are typically composed of porous graphite-felt materials to increase their surface area [259]. The internal current collectors, so-called bipolar plates, are composed of graphite composite material, while the external current collectors are most often composed of copper [258].

The capacity of RFBs depends on the molar concentration of the redox couples used and the electrolyte volume in the tanks, in which the electrolytes are stored and from which they are pumped to the respective half-cells as indicated in Figure 8.1. The power of such a system, on the other hand, depends on the number of utilised electrochemical cells. Therefore, the capacity and power is independent of each other as mentioned above. Compared to others the VRFB utilises the same element, namely vanadium, which greatly minimises problems with cross-contamination and loss through the membrane [260]. More specific, the VRFB utilises the  $V^{2+} / V^{3+}$  and  $VO^{2+} / VO_2^+$  redox couples with the respective oxidation states V(II) / V(III) and V(IV) / V(V) to store electricity:



During charge, tetravalent ( $VO^{2+}$ ) ions are oxidised to pentavalent ( $VO_2^+$ ) ions at the cathode (Equation 8.1b), while trivalent ( $V^{3+}$ ) ions are reduced to bivalent ( $V^{2+}$ ) ions at the anode (Equation 8.1a). This process is reversed during discharge. To ensure electrical neutrality of both electrolytes, positively charged hydronium ions ( $H_3O^+$ ) move through the membrane, when using a cation-exchange membrane.<sup>1</sup>

Mid-concentrated sulphuric acid ( $\sim 2 \text{ mol L}^{-1}$ ) maximises the solubility of vanadium such that the total concentration of vanadium ranges from  $1.5$  to  $1.8 \text{ mol L}^{-1}$ . The high solubility of vanadium in the sulphuric acid is the main driver of the capacity with theoretical values of up to  $20$  to  $25 \text{ Wh L}^{-1}$  [255]. The conductivity of the electrolyte may up to a few hundred  $\text{mS cm}^{-1}$  [258].

In an optimal charging/discharging process, the quantity of oxidised and reduced species remains constant throughout successive battery cycles. Then, the electrolytes maintain balance, meaning the amounts of  $VO^{2+}$  and  $V^{3+}$ , as well as  $VO_2^+$  and  $V^{2+}$  in the electrolytes, are equal, respectively. The state of charge (SOC) of the VRFB is defined by both the ratios of  $VO_2^+$  and  $V^{2+}$  concentration to the

<sup>1</sup> Free protons ( $H^+$ ) are not stable in aqueous solutions and are always bound to water molecules forming so-called hydronium ions,  $H_3O^+$ .

total vanadium concentration. In reality, however, electrolyte imbalance is the main cause for performance degradation and capacity loss. Concentration imbalances may be caused by water crossover through the membrane [261], differential transfer of vanadium ions or volumetric transfer of electrolyte between half cells [262]. In the case of vanadium crossover, the  $V^{2+}$  and  $V^{3+}$  ions rapidly react with the  $VO_2^+$  ions forming  $VO^{2+}$  ions in the catholyte, while  $VO^{2+}$  and  $VO_2^+$  ions react with the  $V^{2+}$  forming  $V^{3+}$  ions. If the flux of  $V^{2+}$  and  $V^{3+}$  from the anolyte to the catholyte is equal to the flux of  $VO^{2+}$  and  $VO_2^+$ , the crossover is symmetric and only causes a self-discharge of the VRFB. The aforementioned processes may be corrected for by periodic electrolyte remixing, where both anolyte and catholyte are mixed producing a solution containing a 1:1 mixture of  $V^{3+}$  and  $VO^{2+}$ . From this condition, the VRFB can be re-initialised as this mixture is equivalent to the electrolyte used to build the battery. This is known as the pre-charge or preconditioning phase, where all  $V^{3+}$  ions in the catholyte are oxidised to  $VO^{2+}$  ions and all  $VO^{2+}$  ions in the anolyte are reduced to  $V^{3+}$ , which corresponds to an SOC of 0% [263, 264]. Imbalances may also arise from oxidation of  $V^{2+}$  ions in the negative half-cell caused by gassing due to impurities or hydrogen evolution [263, 265] as well as from reduction of  $VO_2^+$  ions caused by corrosion of battery material or precipitation of  $VO_2^+$  at elevated temperatures [266, 267]. As these processes involve oxidations and reductions of the vanadium ions, electrolyte remixing is not sufficient in this case and more rigorous approaches such as electrochemical rebalancing or utilisation of a regeneration cell are required to restore the balance of  $VO^{2+}$  and  $V^{3+}$  as well as  $VO_2^+$  and  $V^{2+}$  [257, 262].

Early detection may help to mitigate these problems and hence several methods have been developed to monitor the SOC. These include open cell potential [268–271], conductivity [258, 262, 272], ultraviolet–visible (UV-VIS) absorption [262, 273] as well as transmission [274] and infrared absorption [275], viscosity [276] and hydraulic pressure monitoring [277] or a combination thereof. It has been shown that *Beer's law* when applied to vanadium electrolyte systems was only valid up to a vanadium concentration of  $0.04 \text{ mol L}^{-1}$ . Hence, UV-VIS absorption techniques cannot be directly applied at the high vanadium concentrations present in the half cells of commercial VRFBs [258, 273]. The first independent SOC measurement system based on conductivity was patented by Skyllas-Kazacos et al., which allows monitoring of the SOC of each half-cell separately. This replaced the previously dominant open-circuit potential measurements [258, 268]. Additionally, other monitoring methods utilising conductivity, potential, and current measurements have been suggested. To estimate the SOC with these methods, considerable modelling due to indirect measurements of vanadium and electrolyte concentrations is required [269–272, 278]. Similarly, the SOC estimations based on the electrolyte viscosity re-

quired the use of complex computations and a neural network for optimisation [276]. Most of the previously mentioned methods are based on measurements of indirect variables (conductivity, density, viscosity), which may be problematic as they may significantly vary with different flux of the electrolyte in the cell [279]. Measurements using potentiometry with reference electrodes require periodic maintenance rendering prolonged measurements in a remote battery unreliable. Consequently, the need for direct quantification of the vanadium species in the electrolyte is high.

The utilisation of EPR has recently been proposed as a direct measurement of the vanadium ( $\text{VO}^{2+}$ ) concentration to monitor SOC as well as ion mobility and ion diffusion into the Nafion membrane [35, 36]. So far EPR was mainly used to monitor the V(IV) ( $S = 1/2$ ) / V(V) ( $S = 0$ ) cycle, i.e., the catholyte, which exhibits a typical 8-line spectrum of the vanadyl ion in solution caused by the nuclear spin of  $^{51}\text{V}$  of  $I = 7/2$  with widths larger than 100 mT mainly due to the relatively large  $A$ -tensor. One solution spectrum of  $\text{V}^{2+}$  was presented in literature [280] with a vanadium concentration of only  $0.1 \text{ mol L}^{-1}$ . The  $\text{V}^{2+}$  was assumed to be a high spin system with  $S = 3/2$  and showed a single possibly relaxation-broadened line. The latter was confirmed by concentration studies in which the linewidth was found to be unchanged. Well-resolved spectra of V(II) species have been shown in ref. [281].  $\text{V}^{3+}$ , on the other hand, is a non-*Kramers* system with a total spin of  $S = 1$  that may be investigated in perpendicular-mode EPR only at high microwave (MW) frequencies (larger than 95 GHz) and high magnetic fields due to large zero-field splitting [282]. Parallel-mode EPR at X-band, however, was used to investigate mixed valence systems of V(III) and V(IV) [283]. Here, the EPR signal of V(III) was found at a  $g$ -value of approximately 4, i.e., at half-field, compared to the V(IV), where the resonance was at  $g \approx 2$ . Furthermore, it was found that it is possible to differentiate between V(IV) and V(II) by utilising standard perpendicular-mode X-band EPR [284]. Lawton and co-workers investigated interactions of vanadium with the Nafion membrane and electrolyte solution in detail using standard X-band EPR [35, 36, 38, 280, 285–287]. In their *in situ* experiments, electrolyte solutions were guided through the centre of the resonator of a Magnettech MS5000 spectrometer by means of tubings. For instance, a decreased mobility in Nafion 117 after exposure to vanadium ions was demonstrated via EPR using a Tempone spin probe [280, 285]. Lawton later expanded these studies to concentration dependent investigations without the use of spin probes. Also, the effect of the sulphuric acid concentration viscosity of the electrolyte was investigated [35]. The *in situ* experiments showed that the concentration of the sulphuric acid in the electrolyte solution has a significant impact on the permeation rate of  $\text{VO}^{2+}$  through the Nafion membrane [38], which is lower for higher acid concentrations. To summarise, EPR alone can provide a wealth of

information of the paramagnetic species  $V^{2+}$ ,  $V^{3+}$ , and  $VO^{2+}$ , such as the concentrations – independent of the flux of water etc. –, mobility, and diffusion across the ion exchange membrane.

Therefore, EPR seems ideally suited for the SOC monitoring of VRFBs. To apply EPR as an online monitoring tool for the SOC, small, robust and affordable EPR sensors are required with a time resolution adequate to the time of charge/discharge cycles. For instance, the submersible EPRoC dipstick sensor discussed in [Section 5.3.3.2](#) is a promising candidate for this purpose. While it would generally be possible to utilise commercially available EPR spectrometers for this purpose, their sales prices between €50 000 for small benchtop devices and over €1 000 000 for fully equipped research spectrometers limits their use to dedicated laboratories. For this reason, a complete redesign of the EPR spectrometer is required to achieve the goal of a small, cost-effective EPR spectrometer. Several partly redesigned EPR spectrometers have been developed recently such as a hand-held EPR scanner for transcutaneous oximetry [50] and an EPR “dipstick” spectrometer [47]. Both spectrometers are based on miniaturised loop-gap resonators (LGRs) in the S-band ( $\sim 2$  GHz) in combination with miniaturised permanent magnets, requiring pulsed EPR (P-EPR) operation to acquire spectra limiting their application to species with relaxation times longer than the instrument dead time and with spectra narrower than the bandwidth of the resonator. Here, the bandwidth of the “dipstick” spectrometer submersed in water is a few hundred MHz. In addition, P-EPR necessitates (sophisticated) external MW circuitry for pulse generation and detection, i.e., a pulse MW bridge. The EPR mobile-universal-surface-explorer (EPR-MOUSE) [48], on the other hand, utilised a surface coil at a frequency of 355 MHz in combination with a small electromagnet with a sweep range between 0 to 40 mT allowing continuous wave EPR (CW-EPR), drastically reducing the complexity of the required MW bridge compared to the P-EPR approaches. Even simpler MW circuitry was used in a compact field-swept CW-EPR spectrometer for monitoring the degradation of car lubrication oil [206], which is also based on a  $\sim 2$  GHz LGR coupled to a marginal oscillator, a Colpitts circuit with a high electron mobility transistor. While this is somewhat similar to the EPRoC in ref. [186], the LGR is not part of the oscillator but merely coupled to it. Hence, the LGR determines the resonance frequency and bandwidth of the whole circuit, resulting in the necessity of a sweepable electromagnet for the acquisition of EPR spectra. This is accomplished with a small electromagnet with a sweep range of 10 mT around 73.3 mT.

Pulsed EPR is not suited for the investigation of the spectra due to the short relaxation times at room temperature (RT) caused by the high concentration of vanadium, and spectral widths larger than 100 mT ( $\sim 3.5$  GHz) caused by the hyperfine interaction. As the sweep range of the small electromagnets is limited to 40 mT for the EPR-MOUSE

and 10 mT for the marginal-oscillator based spectrometer, only small parts of the entire vanadium electrolyte spectrum may be recorded. Furthermore, the hand-held EPR scanner and EPR-MOUSE are optimised for surface experiments, while the EPRoC dipstick is optimised to be submersed in sample solutions due to its protective coating. The frequency-sweep width the EPRoC dipstick is limited to  $\sim 1.6$  GHz in  $\text{H}_2\text{O}$ , so it is expected that only approximately 50% of the entire spectrum may be acquired at a fixed field. As the EPRoC dipstick has a similar design as the 12-coil EPRoC array, it may be used for rapid-scan EPR (RS-EPR) operation discussed in [Chapter 7](#), too. Yet, an improved signal-to-noise ratio (SNR) is not expected due to the short relaxation times of the vanadium species in the electrolyte. This allows recording unsaturated EPRoC spectra even in CW operation. In addition, the even further limited frequency-sweep range in RS operation due to the signal generator would not allow acquiring spectra with a width of more than 640 MHz ( $\sim 22.8$  mT).

Proof-of-principle field-swept quantitative EPRoC dipstick experiments on vanadium catholyte solutions with varying SOC are presented in this chapter. These experiments demonstrate the possibility to utilise EPRoC as an online SOC monitoring sensor for VRFBs when using the entire EPRoC spectra as well as only parts of the spectra for quantification. In contrast to previous experiments with VRFB electrolyte samples, the samples in the presented experiments were prepared from commercial vanadium electrolyte used in industrial VRFBs. Furthermore, these experiments demonstrate that the coating effectively protects the EPRoC in a strongly acidic environment. In addition, these experiments show the potential for detecting EPRoC spectra of samples with a relatively high conductivity of up to 1 S. To demonstrate the feasibility of using a permanent magnet, a frequency-swept spectrum of the catholyte is shown exhibiting the same spectral shape as the field-sweep. A thorough comparison of the spectral shape of the EPRoC FM spectra with EPR absorption spectra of the sample is performed. The sensitivity of both EPRoC and resonator-based EPR for such catholyte samples is compared.

This chapter is structured as follows. First, the materials and methods are described. This includes the sample preparation of the electrolyte solutions, the experimental configuration, and the quantitation procedure. Second, the experimental results are presented and discussed. The EPRoC FM spectra are compared to EPR spectra obtained with a resonator-based X-band spectrometer. A simulation of both X-band and EPRoC spectra is shown. The EPRoC and X-band spectra are quantified and compared. Possible reductions in the acquisition time using the EPRoC are discussed before the chapter concludes with a summary.

## 8.2 MATERIALS AND METHODS

In this section, the preparation of the vanadium electrolyte solutions and the experimental configuration are discussed. The acquisition parameters of the EPRoC and X-band experiments and the digital post-processing of the spectra are described. In addition, the quantitation procedure and the error estimation is explained.

### 8.2.1 Preparation of the vanadium electrolyte solutions

The vanadium electrolyte samples were prepared by Tobias Gerber and provided by Peter Fischer from the Fraunhofer-Institut für Chemische Technologie. A commercial VRFB electrolyte (Gesellschaft für Elektrometallurgie mbH) with a total concentration of  $1.6 \text{ mol L}^{-1}$  was charged in a lab-built cell described in detail in ref. [288] to obtain samples with a well-defined SOC. The half cells in the test cell assembly were separated by an anion-exchange membrane (Fumasept FAP 450). The test cell has a geometric area of  $40 \text{ cm}^2$  and utilised graphite bipolar plates (FU-4369, Schunk Kohlenstofftechnik, Germany) and graphite felts (GFA 5, SGL Carbon, Germany, thermally activated at  $400 \text{ }^\circ\text{C}$  for 1 h) as electrodes.

The total concentration of the pristine commercial electrolyte determined by cerimetric titration was  $1.58 \text{ mol L}^{-1}$ , with a composition of 48.85 %  $\text{V}^{3+}$  and 50.15 %  $\text{VO}^{2+}$ , prior to charging. To obtain a starting solution with an equal amount of vanadium species in both half cells, 1600 mL anolyte and 1609.63 mL of catholyte were charged to an SOC of 0 % by galvanostatic charging, i.e., with a constant electrical current of 1 A, which corresponds to  $25 \text{ mA cm}^{-2}$ , reaching a calculated charge of 33.9787 A h. At an SOC of 0 %, only  $\text{V}^{3+}$  and  $\text{VO}^{2+}$  are present in the anolyte and catholyte, respectively. To obtain an equalised VRFB, the amount of anolyte and catholyte needs to be equal in both half cells; therefore, the same amount of electrolyte was used in both half cells for the further charging to the desired SOC. Again, galvanostatic charging with 1 A was used until the calculated charge was reached for every SOC step 20, 40, 60 and 80 %, respectively. I-V-charging with a voltage of 1.625 V was used to obtain an SOC of 100 %. The actual SOC of samples used in this chapter was calculated from the sample concentration determined by cerimetric titration.

Figure 8.2 shows the saturation analysis of the vanadium catholyte solutions recorded with the Magnettech MS5000 spectrometer.<sup>2</sup> The signal intensity obtained by double integration is plotted as a function of the  $B_1$  magnitude, which was calculated from the resonator conversion efficiency of  $0.12 \text{ mT W}^{-0.5}$ . Linear fits of the signal intensity at

<sup>2</sup> Please note that the saturation behaviour of the 79 % SOC sample was not recorded due to user error. However, the saturation behaviour of this sample is expected to lie in between the 97 % and the 60 % sample, which do not differ much.



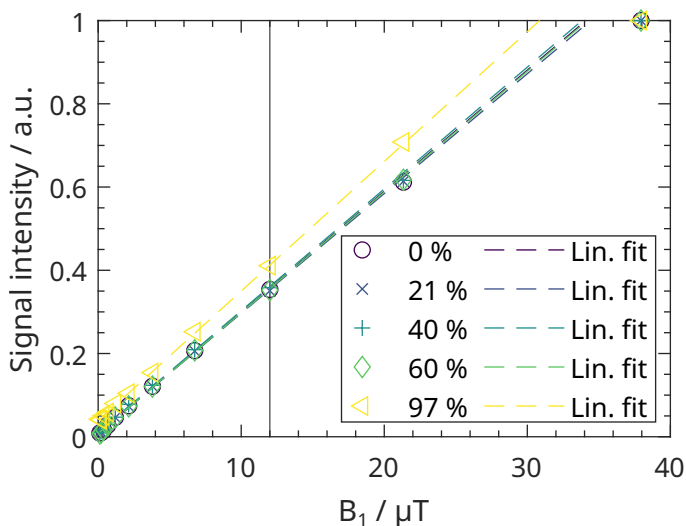


Figure 8.2: Saturation behaviour of the vanadium catholyte solutions recorded with the resonator-based MAgnettech MS5000 spectrometer. The signal intensity is obtained from the double integral (DI) of the absorption spectra. Linear fits of the experimental data below  $12 \mu\text{T}$  are shown as dashed lines. Slight saturation is observed above  $24 \mu\text{T}$ . The vertical line indicates the  $B_1$  value used to record the spectra for quantitation.

low  $B_1$  values are shown as solid lines. The linear regime is observed up to a  $B_1$  value of  $24 \mu\text{T}$ . Only at the largest available  $B_1$  of  $\sim 37 \mu\text{T}$  of the MAgnettech MS5000 spectrometer, a minor decrease of the signal intensity is observed.

### 8.2.2 EPRoC configuration and acquisition parameters

For the EPRoC measurements presented in this chapter, the single-coil EPRoC dipstick was used, which is discussed in detail in [Section 4.2.4.2](#). The samples were placed in a 10 mL glass beaker, into which the EPRoC was submersed. To avoid accidental spilling of the samples, the beaker was glued (Fixogum) to a holder inserted in the centre of the electromagnet of the ESP300 spectrometer (cf. [Section 4.2.1](#)). Consequently, the samples were placed in the beaker by means of a syringe. The glass beaker was rinsed with de-ionised water between the experiments. Because the catholyte samples are air-stable, the samples were handled without inert atmosphere.

The field-swept EPRoC spectra used for quantitation were recorded at RT with a fixed MW frequency of 14.34 GHz and at a bias current of 4 mA with frequency modulation ( $f_{\text{mod}} = 90 \text{ kHz}$ ,  $\Delta f_{\text{mod,pp}} = 25.6 \text{ MHz}$  (corresponding to  $0.91 \text{ mT}$ )). For phase-sensitive detection, the settings of the lock-in amplifier (LIA) were 100 ms for the time constant and  $24 \text{ dB oct}^{-1}$  for the roll-off. To improve the SNR, 9 spectra were averaged.

For spectral simulations, a sample with an SOC of 90 % was used. The acquisition parameters for the field sweep of this sample were the same as before, however, with a smaller modulation amplitude of 9.6 MHz (corresponding to 0.34 mT). The frequency-swept spectrum of the same sample was acquired with the same settings used for the field-swept spectrum and at a fixed static magnetic field of 480.6 mT. In total, 40 spectra were averaged to improve the SNR for both field- and frequency-swept spectra. To remove the baseline of the frequency-swept spectrum (cf. Section 4.2.2), an off-resonant spectrum at a fixed field of 200.6 mT was recorded.

All field-swept spectra were linearly baseline-corrected. All spectra were filtered with a 2<sup>nd</sup> order *Savitzky-Golay* moving average filter with a window chosen so small that the spectra were not broadened by the filtering procedure.

To reduce acquisition time, EPRoC spectra with only two field-points were obtained. For these so-called two-point experiment, the same acquisition settings ( $f_{mw} = 14.34$  GHz,  $I_{bias} = 4$  mA,  $f_{mod} = 90$  kHz,  $\Delta f_{mod,pp} = 25.6$  MHz (corresponding to 0.91 mT)) as for the spectra used for quantitation were used. 1000 acquisitions were averaged to improve SNR in the following procedure. The magnetic field was stepped between baseline (400.6 mT) and resonance (492.8 mT)  $100 \times$ . At each field point, the lock-in voltage was averaged ten times.

### 8.2.3 Resonator-based EPR

Due to the high polarity of the catholyte samples, they were placed in open-ended capillary tubes (1.02 mm inner diameter, Hirschmann ringcaps 50  $\mu$ L), of which both ends were sealed with capillary tube sealant (Critoseal) after the filling procedure. For reproducible sample placement in the resonator of the Magnetech MS5000 spectrometer, a capillary guidance tube (Magnetech F120/1.5 3.6 mm) was used. The filling height of the samples was larger than the height of the resonator. In combination with the capillary guidance tube, the same amount of sample was investigated for each sample, which allowed for quantitative results.

The X-band resonator-based EPR spectra were recorded at RT at a  $B_1$  of 12  $\mu$ T (10 mW with a resonator conversion efficiency of 0.12  $\text{mT W}^{-0.5}$ ), using field modulation with a frequency of 100 kHz and an amplitude of 0.4 mT. The spectrum of the 90 % SOC sample recorded at a temperature of 100 K was used to determine the  $g$ - and  $A$ -tensor. It was recorded with the same spectrometer settings. A powder sample of nitrogen-atom-endohedral  $C_{60}$  ( $N@C_{60}$ ) was used to calibrate the magnetic field of the Magnetech MS5000 spectrometer. Similar to the EPRoC spectra, the X-band EPR spectra were linearly baseline-corrected prior to filtering with a 2<sup>nd</sup> order *Savitzky-Golay* filter with a window



chosen so small that the spectra were not broadened by the filtering procedure.

#### 8.2.4 Spectral simulations

The software package *EasySpin* [70] (version 6.0.0-dev.53) was used to perform the spectral simulations of the 90% SOC sample. The vanadyl ion,  $\text{VO}^{2+}$ , has a total spin of  $S = 1/2$ , while the nuclear spin for the naturally abundant vanadium (0.25%  $^{50}\text{V}$  and 99.75%  $^{51}\text{V}$  [289]) is 6 and  $7/2$ , respectively, which were considered for the simulation. Due to the minuscule natural abundance of  $^{50}\text{V}$ , only the 8-line spectrum of the nuclear spin of  $^{51}\text{V}$   $I = 7/2$  is visible. The X-band EPR absorption spectrum at 100K was simulated with the function *pepper* for solid state powder samples to determine the axial  $g$ - and  $A$ -tensor. The initial parameters of the  $g$ - and  $A$ -tensors for the least-square fit of the simulation were taken from ref. [35]. A convolutional *Gaussian* broadening was an additional parameter to improve the fitting procedure.

The simulations of RT X-band absorption and EPRoC FM spectra were performed using the  $g$ - and  $A$ -tensors that were obtained from the previous simulation. As the spectra were recorded at RT, the function *garlic* for samples in the isotropic, fast-motion regime was utilised instead of the function *pepper*. In these simulations, the rotational correlation time,  $\tau_R$ , was the only free fit parameter.

*EasySpin* simulations usually return EPR absorption spectra as they are typically recorded with commercial EPR spectrometers. However, dispersion spectra or a mixture of absorption/dispersion may be returned by explicitly defining the MW phase in the simulation. While an MW phase of zero corresponds to an absorption spectrum, an MW phase of  $\pi/2$  corresponds to a dispersion spectrum. Any value in between returns a mixture of the two. As the EPRoC FM signal is dispersion-like, the MW phase was accordingly set to  $\pi/2$ .

#### 8.2.5 Quantitation procedure and error estimation

##### 8.2.5.1 X-band EPR

For the X-band data, the signal intensity was calculated by a numerical double integration of the spectrum with baseline corrections of 1<sup>st</sup> and 5<sup>th</sup> order for the as-recorded and singly integrated spectra, respectively.

To obtain an estimation of the quantitation error of the resonator-based X-band data, the quantitation procedure including baseline corrections described previously was applied to 100 individual spectra of the catholyte solutions. The resulting signal intensities defined as

the value of the DI at the highest field point were averaged, and the standard error was calculated for each SOC as

$$\Delta I = \frac{\sigma}{\sqrt{N_{\text{avg}}}}. \quad (8.2)$$

#### 8.2.5.2 EPR-on-a-Chip

Because EPRoC FM spectra are dispersion-like, using the “standard” double integration procedure described above would result in no meaningful results (as discussed in [Section 8.3.3](#)). Therefore, the EPRoC FM spectra were transformed to absorption-like spectra by means of the *Kramers-Kronig* relation assuming unsaturated samples, prior to the DI procedure described before. As discussed in [Chapter 7](#), this relation is only valid for non-saturated samples. Similarly, the synthetic absorption-like spectrum and the singly integrated spectrum were baseline-corrected with a 3<sup>rd</sup> and 5<sup>th</sup> order polynomial, respectively. The EPRoC FM signal intensity values were obtained as the value at the highest field position from the doubly-integrated synthetic absorption-like spectra.

Due to the rather long measurement time, the statistical error of the EPRoC measurements was determined with a 10 mmol L<sup>-1</sup> tempol/H<sub>2</sub>O solution. The spectra were recorded with the experimental parameters as for the catholyte sample. Similar to the error estimation of the resonator-based X-band data, the same quantitation procedures with the same baseline corrections were applied to 100 individual spectra (cf. [Figure 8.3](#) (a), (b), (c) and (d)). From the mean and the standard deviation (STD) of the value of the DI at the highest field, the standard error was calculated. The relative standard error of the quantitation of the EPRoC FM spectra is calculated by

$$\delta I_{\text{FM}} = \frac{\Delta I_{\text{FM}}}{I_{\text{FM}}} = 0.0121.$$

The lower number of transitions in the tempol spectrum (3) compared to the catholyte spectra (8) was not explicitly taken into consideration for the error calculation. However, the DI procedure ensures that the whole EPR spectrum is taken into consideration for quantitation for both samples.

In the analysis of the two-point measurement data extracted from the complete EPRoC FM spectra, the mean signal amplitude observed below 435.6 mT (off-resonance) was subtracted from the signal amplitude at 492.8 mT, slightly to the right of the second transition in the spectrum as indicated in [Figure 8.4](#) (a). The error associated with this measurement was estimated from the standard deviation of the same off-resonance region.

For the experimental two-point truncation measurement, the following analysis was used: For each SOC, the signal amplitude was calculated as the difference between the averages of the signal amplitude of

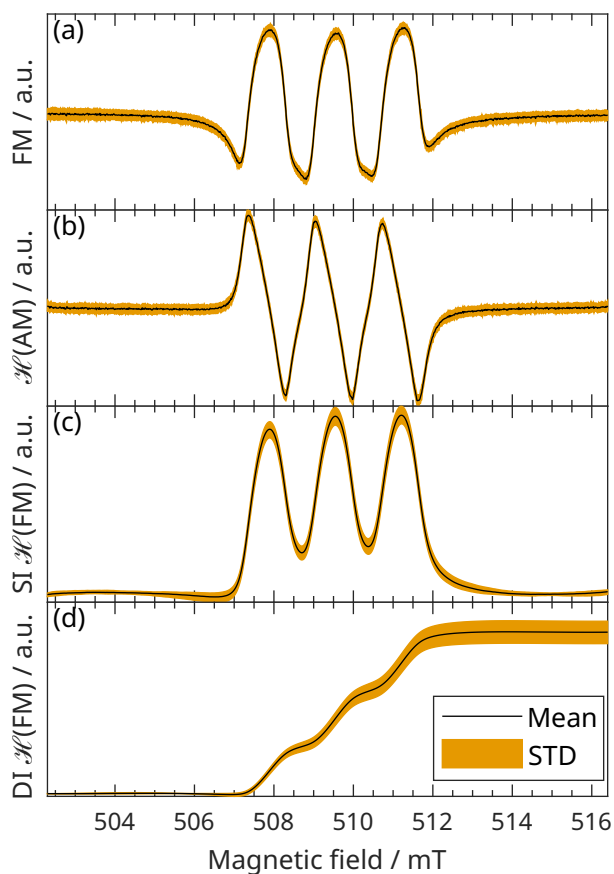


Figure 8.3: Quantitation of the FM spectrum of a  $10 \text{ mmol L}^{-1}$  tempol/ $\text{H}_2\text{O}$  solution for the estimation of its statistical error. **(a)** Mean and standard deviation (STD) of 100 EPRoC FM spectra, **(b)** of 100 EPRoC absorption-like spectra obtained from the *Hilbert* transform of the FM spectra, **(c)** of the single integral (SI), **(d)** of the double integral (DI). The signal intensity was obtained from the value at the highest field point.

the on- (492.8 mT) and off-resonance (400.6 mT) signal amplitude. The standard error for each SOC was calculated by means of propagation of uncertainty from the standard error of the off- and on-resonance signal amplitude. In the error analyses, only the statistical error was taken into consideration, and the systematic error introduced by potential variations in different baseline corrections was ignored [12, Section 4.10]. The approach is justified by fact that the systematic error would be consistently present across all analyses and can therefore be reasonably disregarded.

### 8.3 RESULTS AND DISCUSSION

In the following, a spectral analysis of the EPRoC FM data will be shown, followed by their quantitation, which is completed by a comparison with data of the same samples obtained with a resonator-based EPR spectrometer.

#### 8.3.1 Catholyte spectra obtained with the EPR-on-a-Chip

Figure 8.4 shows the EPRoC FM (a) and AM (b) spectra obtained using a magnetic field sweep of the vanadium catholyte solutions with an SOC of 0, 21, 40, 60, 79 and 97 %. The spectra between 0 to 79 % SOC show 8 lines with different amplitudes as expected for differently concentrated  $\text{VO}^{2+}$  in solution [38]. The spectrum at 97 % SOC, on the other hand, does not show an EPR signal. A small EPR signal is expected from this sample due to the  $0.04 \text{ mol L}^{-1}$  of  $\text{VO}^{2+}$ . Assuming a linear decrease of the signal amplitude with the concentration, an 8.25 times smaller signal amplitude is expected compared to the 79 % SOC sample. This would result in an SNR of 6, which should be barely distinguishable from noise. The spectra up to 60 % SOC show a strongly exchange-broadened behaviour because the linewidth of each line is so wide that they overlap due to the high  $\text{VO}^{2+}$  concentration of up to  $1.58 \text{ mol L}^{-1}$ . The spectrum at 79 % SOC shows only slight exchange broadening due to the lower  $\text{VO}^{2+}$  concentration of  $0.33 \text{ mol L}^{-1}$ .

The modulation amplitude was chosen such that the spectra are over-modulated, i.e., larger than  $1/3$  of the linewidth, improving the SNR, but not affecting the quantification [12]. In total 9 scans were averaged to improve SNR, which took  $11\,707 \text{ s}$  (3.25 h) per spectrum. This value of the acquisition time is not useful for the comparison with data obtained from other spectrometers as it contains all non-perfect parts of the experiment. As in Section 7.3.1, the effective measurement time defined as

$$t_{\text{meas,eff}} = 3 \cdot N_{\text{points}} N_{\text{avg}} \tau_{\text{LIA}} \quad (8.3)$$

is a more useful quantity, which is here  $4593 \text{ s}$  (1.28 h), i.e., the duty cycle of the experiment was about 40 %. The low duty cycle can mainly

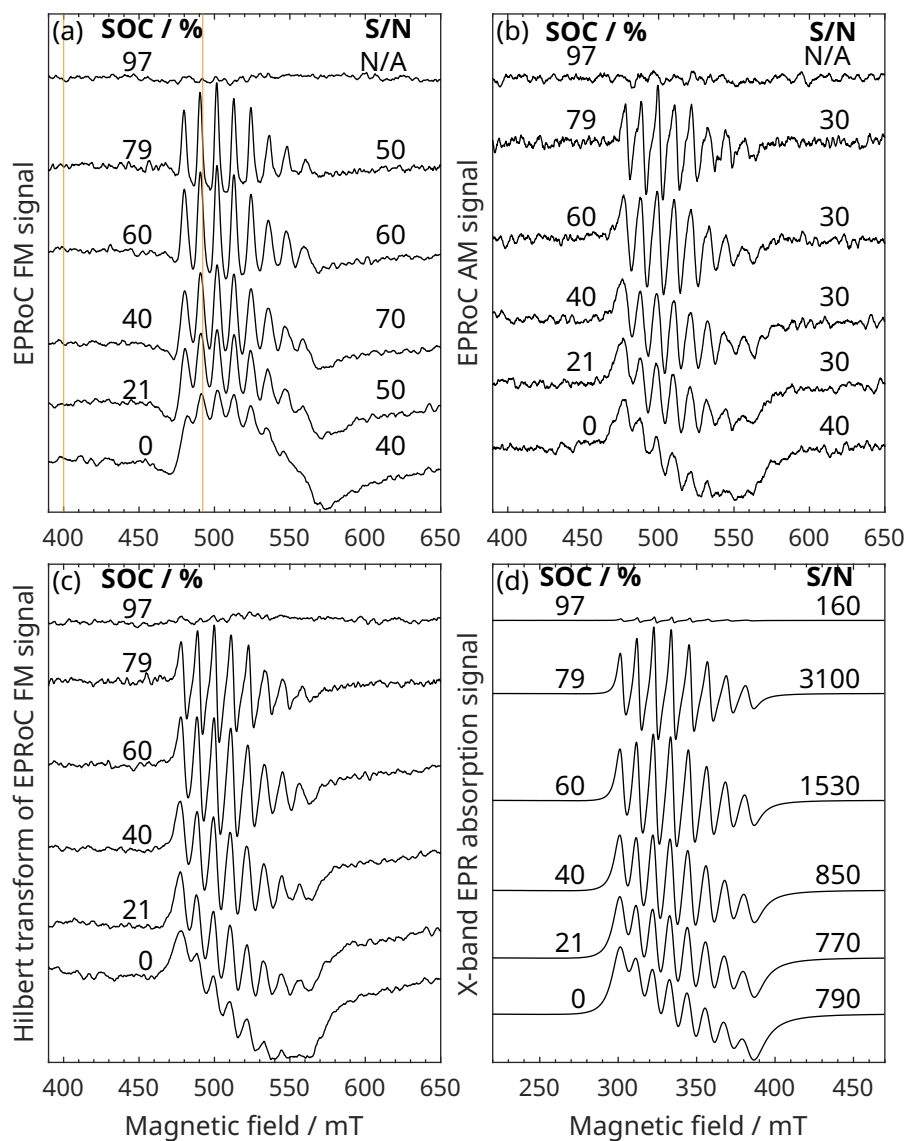


Figure 8.4: Field-swept EPRoC spectra of the vanadium catholyte solution with SOC of 0, 21, 40, 60, 79 and 97% obtained with an MW frequency of 14.34 GHz. **(a)** FM signal. The two vertical lines show the field positions of the two-point truncation experiment. **(b)** AM signal. **(c)** Hilbert transformation of FM signal. **(d)** Resonator-based X-band EPR obtained at an MW frequency of 9.47 GHz. All spectra are shifted vertically such that they do not overlap.

be attributed to the time required for the settling of the magnetic field for the electromagnet and power supply.

### 8.3.2 Comparison to resonator-based EPR

For a direct spectral comparison with resonator-based EPR, the AM spectra may be used. However, as the SNR FM spectra would benefit from the EPRoC array as discussed in Section 3.4, we will focus in the following on the FM signal, which may be transformed to a synthetic absorption-like spectrum using the *Kramers-Kronig* relation for a direct comparison with the resonator-based absorption EPR spectra. Mathematically, this is a special case of a *Hilbert* transform. The *Kramers-Kronig* relation may only be used if the sample is unsaturated [178], which is the case for the vanadium catholyte solutions due to their high vanadium concentration. In Section 8.2.1, the saturation of the samples in X-band was determined, which showed only minor saturation at the highest available MW power of 100 mW (c.f Section 8.2.1), therefore it is expected that the transformation does not introduce large errors. To confirm the reliability of the transformation, the synthetic absorption-like spectra shown in Figure 8.6 (c) may be compared to the AM signal (absorption-like) in Figure 8.4 (b). Both, the *Hilbert* transformed FM spectra and the directly-recorded AM spectra exhibit similar spectra for the same SOC with similar ratios of the peaks. Hence, the *Hilbert* transformation seems to be applicable.

In Figure 8.4 (d), the spectra obtained with the resonator-based EPR spectrometer are displayed. Although the MW frequencies differ by about 5 GHz, the main features and most of the amplitude ratios of the hyperfine components at the same SOC are reproduced. Compared to the spectrum of the 97% SOC sample measured with the EPRoC, there is a small signal visible in the resonator-based EPR spectrum.

#### 8.3.2.1 Simulation

A more rigorous comparison may be performed with simulations of the vanadium catholyte spectra both acquired with the resonator-based EPR spectrometer and with the EPRoC. As the  $\text{VO}^{2+}$  is dissolved in the electrolyte and at RT, the recorded spectrum is in the isotropic and fast-motional regime, which can be simulated with the function *garlic* of the *EasySpin* software package [70]. For the simulation, a catholyte sample with an SOC of 90% and therefore a lower concentration of  $0.16 \text{ mol L}^{-1}$  was used. The samples between 0 to 80% SOC exhibit exchange broadened lineshapes, which renders them difficult to simulate. Here, errors may easily be introduced.

To recover the native lineshape of the sample, the modulation amplitude was decreased substantially compared to the spectra earlier shown, such to avoid broadening of the spectra due to an excessive modulation amplitude. The *g*- and *A*-tensor of the sample were de-

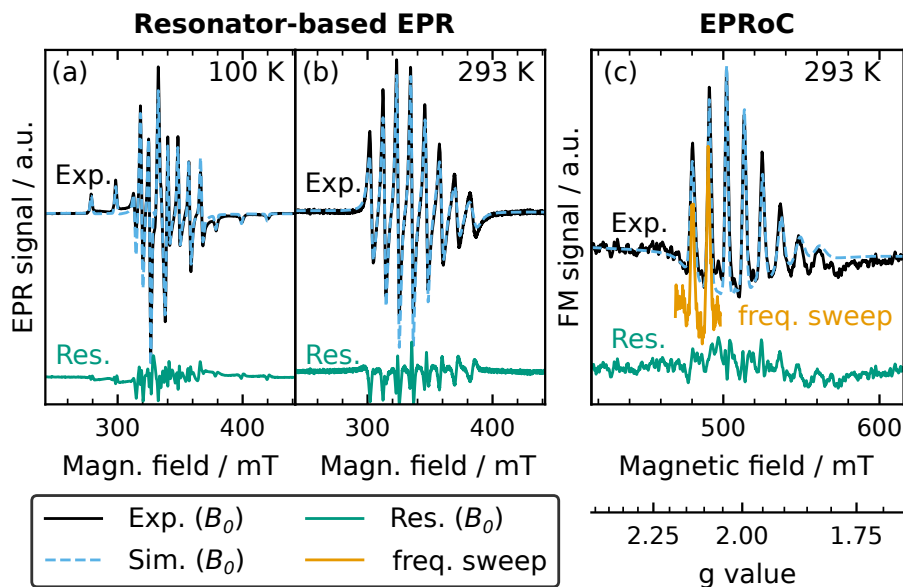


Figure 8.5: Experimental EPR and EPRoC spectra (Exp.) of a 90 % SOC ( $0.16 \text{ mol L}^{-1}$ ) vanadium catholyte solution with spectral simulations (Sim.) and the residual (Res.). (a) Field-swept EPR absorption spectrum at 100 K. (b) Field-swept EPR absorption at RT. (c) Field-swept EPRoC FM spectrum at a centre MW frequency of 13.44 GHz and frequency-swept (freq. sweep) EPRoC FM spectrum at a centre field of 500 mT at RT. The  $g$ -axis is calculated from the frequency axis and the centre field.

terminated with a spectrum recorded at 100 K in X-band as shown in Figure 8.5 (a), for which the sample is in the rigid limit and their values may directly be read-off the spectrum. For higher precision, this spectrum was simulated using the function *pepper* of the *EasySpin* software package [70]. For the simulation, an axial symmetry of the  $g$ - and  $A$ -tensors with convolutional *Gaussian* broadening was assumed. Both  $g$ - and  $A$ -tensors are similar to literature values [35] and are listed in Table 8.1.

The spectra at RT of the same sample in X-band and EPRoC together with the respective simulations are shown in Figure 8.5 (b) and (c). For these simulations,  $g$  and  $A$  parameters obtained previously were used, and the only free parameter for the fit was the rotational correlation time. No additional convolutional broadening was applied. Both values for the rotational correlation time are similar and in good agreement. Comparable literature values for such highly concentrated samples do not exist as the concentration of previously investigated vanadium catholyte samples ( $0.01 \text{ mol L}^{-1}$ , [35]) was much lower than that of the commercial vanadium catholyte sample investigated here ( $0.16 \text{ mol L}^{-1}$ ). Both simulations show a good agreement with the experimental data as seen from the residuals of the simulation shown below the spectra in Figure 8.5.



Table 8.1: Parameters of the spin system of the V electrolyte SOC 90%. The convolutional *Gaussian* broadening was applied to the resonator-based X-band spectrum at 100 K only.

Quantity	Value	Standard deviation
$g_{\perp}$	1.9798	0.0001
$g_{\parallel}$	1.9349	0.0001
$A_{\perp}$ / MHz	206.9	0.1
$A_{\parallel}$ / MHz	544.6	0.3
$\tau_{R,EPRoC}$ / ns	0.15	0.01
$\tau_{R,X}$ / ns	0.13	0.01
$\Delta B_G$ / mT	1.76	0.01

Additionally, a frequency-swept EPRoC FM spectrum of the same sample, recorded under the same experimental settings as the field-swept EPRoC FM spectrum, is presented. The frequency sweep covered approximately 1 GHz around the central MW frequency of  $f = 14.34$  GHz, while the magnetic field was fixed at  $B_0 = 480.6$  mT. This frequency-swept spectrum is depicted in [Figure 8.5](#). To facilitate the comparison of field- and frequency-swept spectra, both are plotted on a  $g$ -axis shown below the magnetic field axis. The  $g$ -axis is calculated using the EPR resonance condition of [Equation 2.8](#) (cf. [Section 2.1](#)). Given the limited frequency sweep width of the EPRoC, only two of the eight transitions can be recorded in a single scan. Despite this limitation, the signal shape remains the same for both spectra, demonstrating the equivalence of the two approaches. The noise level in the frequency-swept spectrum, however, is slightly higher than that in the field-swept spectrum as observed previously in [Section 5.3.2](#). The duty cycle of the frequency sweep exceeds 90%, effectively improving the overall duty cycle by more than a factor of 2 compared to the field-swept spectrum.

### 8.3.2.2 Sensitivity

The values of the SNR of the EPRoC FM spectra (50 to 70) are much lower than that of the resonator-based EPR spectra (160 to 3100) (cf. [Figure 8.4](#) and [Figure 8.5](#)). Considering the different acquisition times to record a spectrum using the two different instruments (resonator-based EPR: 60 s, EPRoC: 4593 s) it becomes clear that the SNR per second is much higher for the resonator-based EPR spectra (20 to 400) than for the EPRoC spectra ( $\sim 1$ ). The sample volume, however, probed in the resonator-based EPR spectrometer measurements is about 50  $\mu\text{L}$ , which is about  $5 \cdot 10^4$  larger than the active volume of the EPRoC ( $\sim 1$  nL) [[220](#)]. Hence, the SNR per second and per volume is much



Table 8.2: Comparison of the SNR and sample volumes of the EPRoC FM and the resonator-based X-band EPR spectra. The  $\text{VO}^{2+}$  concentration was calculated from the total vanadium concentration and the SOC assuming that at 0% SOC, all vanadium is in the form  $\text{VO}^{2+}$ .

SOC %	$\text{VO}^{2+}$ conc. $\text{mol L}^{-1}$	$\text{SNR}_{\text{EPRoC}}$ $\text{s}^{-0.5} \mu\text{L}^{-1}$	$\text{SNR}_X$ $\text{s}^{-0.5} \mu\text{L}^{-1}$	$\text{SNR}_{\text{EPRoC}}/\text{SNR}_X$ 1
-0.19	1.58	660	2.0	320
20.53	1.26	720	2.0	360
40.09	0.95	1040	2.2	470
60.01	0.63	810	3.9	210
79.03	0.33	790	8.0	100
97.28	0.04	N/A	0.4	N/A

higher for the EPRoC compared to resonator-based EPR (cf. Table 8.2), which corresponds to the absolute sensitivity of the EPRoC. Therefore, the EPRoC shows about 100 to 470  $\times$  better absolute spin sensitivity than the resonator-based EPR.

For the resonator-based EPR measurement we used the acquisition time instead of the effective measurement time as the Magnettech MS5000 spectrometer has a large duty cycle approaching 100%. Therefore, the acquisition time and the effective measurement time are very similar.

The theoretical spin sensitivity of the EPRoC dipstick may be calculated using Equation 3.29b as described in Section 3.3. Using the parameters for this EPRoC chip,  $B_0 = 500 \text{ mT}$ ,  $T = 300 \text{ K}$ ,  $R_{\text{coil}} = 6.8 \Omega$  and  $d_{\text{coil}} = 200 \mu\text{m}$ , we obtain a spin sensitivity of approximately  $2 \times 10^8 \text{ spins G}^{-1}$  spins. This is about a factor of 500 smaller, i.e., better, than the estimate of the theoretical spin sensitivity of a resonator-based EPR spectrometer operating at X-band of approximately  $1 \times 10^{11} \text{ spins G}^{-1}$  presented in ref. [69]. Hence, our experimental findings agree very well with the theoretical estimates of the ratio of the absolute spin sensitivities.

### 8.3.3 Estimation of the state of charge from the entire spectrum

In resonator-based EPR where the absorption signal is detected, the standard way for quantification is the so-called double integration method. Here, the lock-in detected, i.e., first-derivative, spectrum is integrated twice to obtain the signal intensity (area under the curve). The EPRoC FM spectra, however, are dispersion-like. Therefore, it is not possible to use the same technique for these data as the double integration yields 0 intensity because the dispersion is an odd function with point symmetry about the  $\Omega = 0$  (the resonance offset, i.e., on

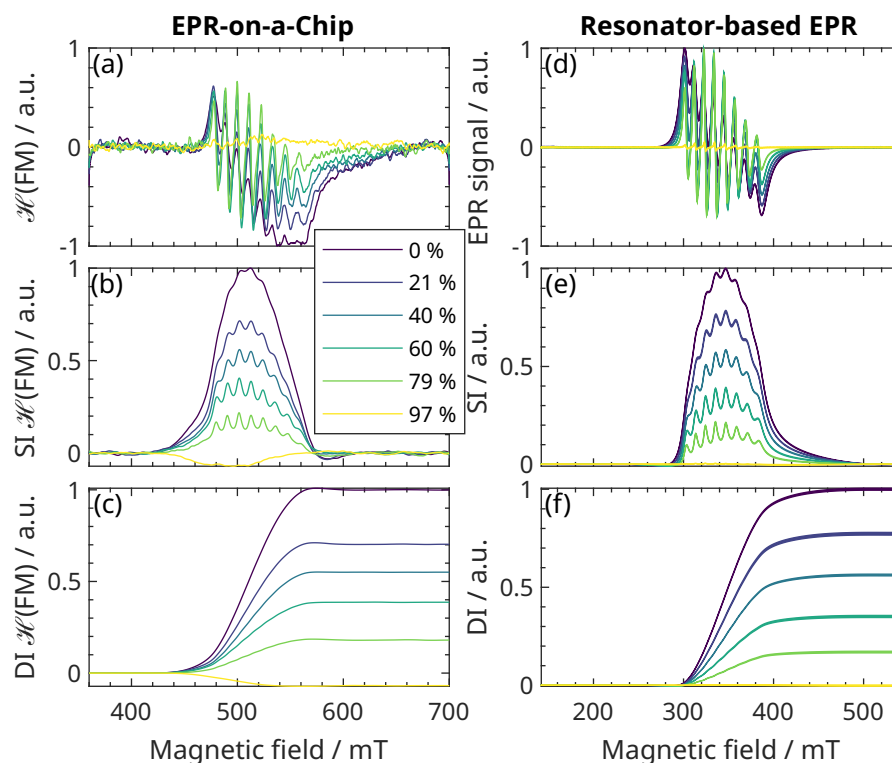


Figure 8.6: Quantitation procedure of the vanadium catholyte samples with varying SOC using the DI procedure. **EPR-on-a-Chip:** (a) Baseline-corrected synthetic absorption-like signal obtained by a *Hilbert* transformation of the FM signal. (b) Baseline-corrected single integral (SI) obtained by numerical integration of (a). (c) Double integral (DI) obtained by numerical integration of (b). The intensity values were extracted at largest  $B_0$  field. **Resonator based X-band EPR:** (d) X-band absorption spectra used for quantitation. (e) Baseline-corrected single integral (SI) obtained by numerical integration of (d). (f) Double integral (DI) obtained by numerical integration of (e). The intensity values were extracted at the largest  $B_0$  field. All X-band spectra were calculated from the mean of 100 averages. The thickness of the line depicts the standard deviation, from which the standard error is calculated.

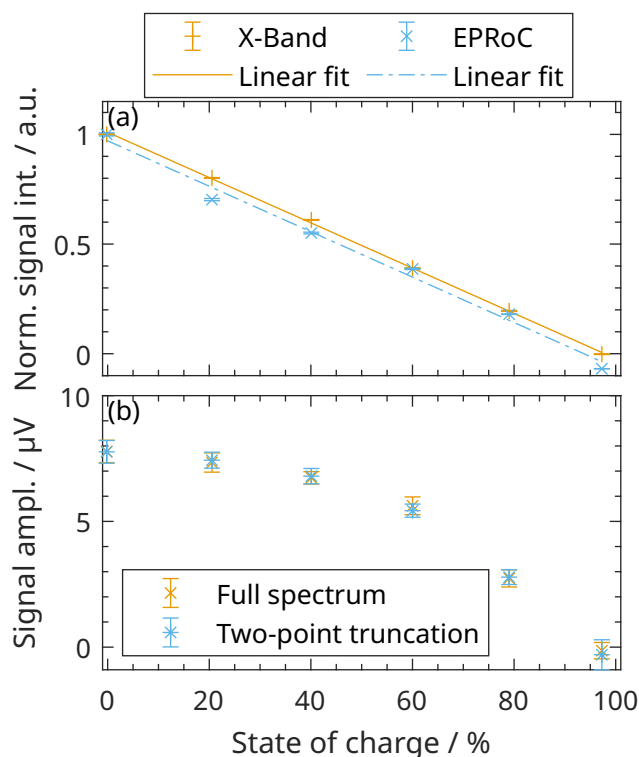


Figure 8.7: Quantitation of the EPR and EPRoC spectra. **(a)** Signal intensity as obtained from double integration of the EPR absorption spectra and of the *Hilbert* transformed EPRoC FM spectra, respectively. **(b)** Signal amplitude as obtained from the two-point experiment and from the full FM spectra. Reproduced from [290] ©

resonance) assuming a *Lorentzian* lineshape, of which the integral is always 0. To circumvent this problem, the dispersion-like FM spectra were *Hilbert* transformed using *Kramers-Kronig* relation to absorption-like spectra as before, which were subsequently doubly integrated (EPRoC DI) as the resonator-based X-band EPR spectra.

Figure 8.6 (a), (b) and (c) shows the spectra of the double integration procedure as described in Section 8.2.5.2. The EPRoC FM spectra in Figure 8.4 (a) are *Hilbert* transformed to a synthetic absorption-like EPRoC signal (a), the result of which is doubly integrated (cf. (c) and (e)). The DI spectra exhibit a sigmoid shape, as expected. As EPR spectra are usually recorded with extensive baseline on both sides of the actual spectrum, the baselines of the low- and high-field region should not return a signal value and the double integration should stay constant. Depending on the spectrum and the amount of transitions, the double integration result in a stepwise increase of the signal intensity as a function of the field as seen in Figure 8.3 (d) for the tempol/ $\text{H}_2\text{O}$  solution, or just increase as seen in Figure 8.6 (e) for the vanadium catholyte samples.

For the resonator-based X-band EPR data, the signal intensity was calculated as the DI of the first-derivative absorption spectrum as

described in Section 8.2.5.1 The absorption spectra, SI and DI are shown in Figure 8.6 (b), (d) and (f).

The signal intensity of each spectrum is defined as the DI value at the largest field position as marked in Figure 8.6 (e) and (f). To compare the signal intensities obtained from the resonator-based X-band data and the EPRoC, all intensities were normalised to the maximum values obtained within each dataset. As seen in Figure 8.7, the signal intensity of both datasets decreases with increasing SOC (decreasing  $\text{VO}^{2+}$  concentration). Linear fits of all datasets reveal that their slopes are the same within the margin of error for the resonator-based X-band EPR ( $-0.0103 \pm 0.0001$ ) and EPRoC DI ( $-0.0104 \pm 0.0004$ ).

These results show the potential of EPR in general and EPRoC in particular to be utilised as an SOC sensor in a VRFB. The most critical parameter for this is the measurement time required to achieve the necessary time resolution for SOC monitoring. The required time resolution is dependent on the charge/discharge time, which is determined by the capacity and power rating of the battery as well as the load. In the case of a high-power battery, a higher time resolution is needed in comparison to a low-power battery with the same capacity, as the charge/discharge time for the former is shorter. For large commercial VRFB, typical charge/discharge times ( $t_c$ ) range between 1 to 10 h [291]. To ensure an SOC accuracy of less than 1 %, the maximum acquisition time per SOC under full load should be approximately between 30 s (for  $t_c = 1$  h) and 300 s (for  $t_c = 10$  h).

While the time resolution of the Magnostech MS5000 spectrometer to obtain spectra with sufficient SNR for quantitation is in the order of tens of seconds, their high cost (exceeding €50 000) limits widespread implementation of VRFB. In contrast, the acquisition of the EPRoC spectra took more than 3 hours and 15 minutes. However, these experiments were primarily conducted to define the spectra at the investigated SOC levels and required a duty cycle of around 40 %. This duty cycle was mainly determined by the time needed for the magnetic field to settle in the electromagnet and power supply used in the experiments.

EPRoC spectra with lower SNR, combined with suitable post-processing techniques, may be adequate for accurately predicting the SOC, leading to a reduction in acquisition time. Additionally, the duty cycle of EPRoC may be increased to around 90 % with frequency sweeps at a constant magnetic field, effectively doubling the time resolution while maintaining the spectral shape as discussed in Section 8.3.2. This allows for a significant simplification of the EPRoC sensor if a suitable permanent magnet were to be used, the development and evaluation of which are discussed in reference [130].

#### 8.3.4 Estimation of the state of charge using a two-point truncation experiment

Significant reduction in acquisition time can be achieved by narrowing the spectral width for quantitation. The largest reduction would be achieved by reducing the spectral width to a single point, that is a measurement of the signal voltage at a fixed field and MW frequency. This, however, would require an extremely stable experiment and environment as a slight temperature drift affecting the oscillation frequency of the voltage-controlled oscillator (VCO) would lead to false SOC measurements as the baseline of the EPRoC is temperature-dependent. Temperature drifts originating from the EPRoC could be reduced with a temperature control loop using a for instance a *Peltier* element that could in principle be integrated into an EPRoC sensor device. For these proof-of-principle experiments, however, such temperature control was not available. To take the temperature-dependent baseline drift into consideration, the quantitation of the SOC was performed with a narrow spectrum with only two field positions: one on resonance at 492.8 mT (slightly right of the 2<sup>nd</sup> transition) and one off resonance at 400.6 mT. Both field positions are indicated in [Figure 8.4](#) (a) as orange vertical lines. This approach effectively reduces the acquisition time by a factor  $\sim 180$  compared to acquisition of the entire spectrum to approximately 10 minutes, already approaching the required time resolution for SOC monitoring in practical applications. For a quantitation of the SOC in a VRFB, a calibration curve mapping the SOC to each signal amplitude calculated as the difference of signal voltages of both field positions is required, which is shown in [Figure 8.7](#) (b). This calibration curve shows a strictly monotonically decreasing behaviour and is therefore suited for the determination of the SOC. The observed monotonic decrease in the calibration curve is not linear, which can be attributed to the spin-dependent broadening due to large  $\text{VO}^{2+}$  concentrations at low SOC. In general, for samples with such a low concentration of paramagnetic species that no concentration broadening takes place, the calibration curve is expected to be linear as observed in ref. [38]. In their study, electrolyte solutions with a significantly lower concentration of  $\text{VO}^{2+}$  (approximately 100 times less) were investigated. At large, many field points satisfy the requirement of being strictly monotonically decreasing with increasing SOC. The specific choice of the on-resonance field position of 492.8 mT for this proof-of-principle experiment was arbitrary and served merely as a demonstration of the concept. The overall trend of a monotonic decrease with increasing SOC remains a characteristic feature for each calibration curve.

While a single-point measurement (or a two-point measurement with baseline correction) corresponds to the minimal spectral width possible, the acquisition of the entire spectrum with extended baseline

on both sides of the actual signal for quantitation as in [Section 8.3.3](#) is the maximum. For improved accuracy, any spectral width in between these extrema may be used as long as suitable post-processing and calibration procedures are developed. This includes acquisition or integration of only parts of the entire spectrum such as one or two of the eight lines (fractional acquisition or integration). This includes frequency sweeps as discussed in [Section 8.3.2.1](#).

In summary, we have discussed two procedures to quantitate EPRoC data to obtain an estimation of the SOC of an electrolyte solution of a VRFB. The acquisition time to acquire complete EPRoC FM spectra of the vanadium electrolyte samples took approximately 3.25 h, which can mainly be attributed to a low duty cycle of the electromagnet and power supply of  $\sim 40\%$ . A frequency sweep with the same experimental parameters showed a much higher duty cycle of  $90\%$ , effectively reducing the acquisition time by a factor of  $\sim 2$ . However, a much larger reduction of the acquisition time to approximately 10 minutes was obtained by truncating the spectrum to only two field points.

A further reduction of the acquisition time may be achieved by improved sensitivity of the SOC sensor. One straightforward solution involves averaging the signals from multiple individual EPRoC sensors placed at different locations within the battery. This spatial averaging increases the effective sensitive volume of the EPRoC sensor. Beyond the improved SNR achieved through spatial averaging, this approach provides an average SOC measurement across the entire electrolyte tank. Additionally, to enhance the sensitivity of each individual EPRoC sensor, multiple EPRoC VCOs can be injection-locked to form an EPRoC array sensor as discussed in [Section 3.4](#). The injection-locking process reduces the phase noise of the FM signal by  $n^{1/2}$ , where  $n$  is the number of EPRoC VCOs in the array. This reduction in phase noise translates directly to a shorter measurement time. For the samples discussed in this chapter, for instance, the measurement time may be reduced by a factor of  $14^{1/2} \sim 3.7$  with the 14-VCO EPRoC array presented in ref. [128]. This improvement would suffice to approach the necessary time resolution for charge/discharge times  $t_c$  of 10 h by reducing the acquisition time to approximately 3 minutes. Further enhancements may be achieved by increasing the sensitive volume of individual VCO tank inductors by utilising larger coils, which is made possible by employing the segmented coil approach presented in reference [132].

As discussed in [Chapter 7](#), RS-EPR may improve the sensitivity especially for samples with long relaxation times due to a later onset of saturation. For these samples exhibiting short relaxation times due to the high concentration of  $\text{VO}^{2+}$ , RS is not expected to improve the sensitivity. However, RS operation has not been tested with these samples.

## 8.4 CONCLUSIONS

In conclusion, quantitative RT EPRoC experiments conducted on paramagnetic vanadium electrolyte solutions were presented. These experiments serve as proof-of-principle for a submersible EPRoC dipstick sensor designed to operate effectively in harsh, corrosive, and strongly acidic environments. The same linear dependence of the EPRoC FM and resonator-based X-band EPR signal intensity as a function for the SOC of the vanadium electrolyte solutions was found. This finding in combination with the submersibility suggests the potential utility of EPRoC as an SOC sensor for VRFB. Moreover, experiments utilising the signal amplitude calculated from only two data points demonstrate a strictly monotonically decreasing behaviour with increasing SOC. This approach enables SOC monitoring with the EPRoC on a significantly reduced measurement timescale. Additionally, the equivalence of field and frequency sweeps of the EPRoC for the vanadium electrolyte solutions was shown, paving the way for the utilisation of permanent magnets instead of electromagnets. This advancement in experimental methodology contributes to simplifying the overall experimental configuration.

While the proof-of-principle experiment focused on monitoring the SOC of VRFB electrolyte solutions in a challenging environment, the submersible EPRoC dipstick may be applied in other battery types such as tempol redox flow batteries, and generally, for the detection of radicals in solution in diverse fields such as chemistry, biology, or the life sciences. Here, a paradigm shift for quantitation of radicals in solution may be possible by using a submersible, battery-operated hand-held frequency-swept EPRoC-based device in combination with a permanent magnet.





## SUMMARY AND CONCLUSIONS

---

In this thesis, the advancement of the electron paramagnetic resonance on a chip (EPRoC) technology for performing quantitative EPR spectroscopy in harsh aqueous environments was presented. This resulted in the development of a submersible EPRoC device that can be used for quantitative measurements of paramagnetic species in solution. To arrive at this point, the technology was first characterised in detail, and practical considerations for its operation were explored. Then, the influence of the inhomogeneous microwave (MW) field distribution of the EPRoC on the measured signal and the injection locking of the EPRoC array were investigated. Rapid scan EPR (RS-EPR) capabilities were implemented and tested to improve the sensitivity of the EPRoC. Finally, the EPRoC was used to perform quantitative proof-of-concept experiments on positive electrolyte solution samples of a vanadium redox flow battery (VRFB) to demonstrate the potential of the technology for future applications in harsh aqueous environments. In the following, the results from [Chapter 5](#) to [Chapter 8](#) are summarised and conclusions are drawn.

In [Chapter 5](#), practical considerations for the operation of the EPRoC were discussed. This chapter laid the foundation for apprehending the subsequent chapters. Important features of the EPRoC were introduced that are especially relevant to understanding from a spectroscopic point of view. The equivalence between field and frequency sweeps was established. This allows the use of permanent magnets instead of the usual electromagnets, the implications of which will be discussed below. Additionally, sample handling of powder, thin film, and samples in solution was discussed. For powder and thin film samples, the absolute spin sensitivity, which is in the range of  $10^{10}$  to  $10^{13}$  spins  $G^{-1} Hz^{-0.5}$  could be correlated with the sample size used. For the investigation of samples in solution, the use of a dipstick device was introduced, which allowed the EPRoC to be submerged in the sample. The concentration sensitivity of the EPRoC dipstick was determined as approximately  $3 \mu\text{mol L}^{-1} G^{-1} Hz^{-0.5}$ . This value was verified by recording the spectrum of a nitroxide radical dissolved in water with a concentration of  $10 \mu\text{mol L}^{-1}$ . The absolute spin sensitivity calculated from the concentration sensitivity determined with a nitroxide radical dissolved in water and the sensitive volume was found to be of the same order of magnitude as the (best) absolute spin sensitivity determined from a powder sample of a stable free radical. This indicates that the EPRoC is not sensitive to the dielectric constant of the sample, which is a significant advantage compared

to resonator-based EPR. This hypothesis is supported by experiments with a nitroxide radical dissolved in water and ethanol, which indicated that the dielectric constant of the sample did not influence the measured signal intensity.

The mapping of the three-dimensional distribution of  $B_1$  of an EPRoC array device was shown in [Chapter 6](#), which is crucial for quantitative EPR experiments. The mapping of the effective  $B_1$  was performed with a point-like grain of  $\alpha,\gamma$ -bisdiphenylene- $\beta$ -phenylallyl (BDPA) and a thin-film sample of a-Si. The sensitive volume of a single coil of the EPRoC is approximately cylindrical with an elliptical ground plane with a total volume of  $\sim 1.6$  nL. Its major axis is aligned with the external magnetic field  $B_0$ . Simulations of the signal amplitude maps obtained from the steady-state solutions of *Bloch's* equations, in combination with finite-element simulations of the  $B_1$  distribution, were in good agreement with the experimental results. These simulations indicate the elliptical shape may originate from the inherently inhomogeneous  $B_1$  by considering both  $B_1$  components perpendicular to  $B_0$ . Because of the good agreement of the experiment and simulation, it may be sufficient to rely on finite-element calculations of the  $B_1$  distribution alone instead of repeating these tedious experiments for different coil geometries in the future. For reasons of symmetry, considerable  $B_1$  parallel to  $B_0$  is present, which could be viable for non-Kramers' systems to induce forbidden transitions. In addition, the effect of partially covering the injection-locked EPRoC array was studied. A linear dependence of the signal amplitude on the number of utilised coils was observed, which is in agreement with simulations performed on a transistor level. This consequently indicates that quantitative EPR may still be achievable, even if only a fraction of the EPRoC array is covered by the sample.

In [Chapter 7](#), closed-loop frequency-swept non-adiabatic rapid-scan EPR (RS-EPR) experiments were presented as a proof of concept. Embedding the EPRoC in a high-bandwidth phase-locked loop in conjunction with its implicit AM demodulation capabilities allowed the acquisition of RS transients with a much simpler experimental configuration compared to commonly performed field-swept RS experiments. In addition, owing to the phase locking of the EPRoC to an external reference frequency, the RS transients can reliably be *Fourier* deconvolved to obtain the slow-scan EPR spectra. The resulting RS spectra of a sample of BDPA showed an improved signal-to-noise ratio per unit time by almost two orders of magnitude compared with continuous wave EPR (CW-EPR) experiments of the same sample. This improvement may be attributed to a later onset of saturation effects in the RS experiments compared to the CW-EPR experiments as well as a lower noise floor due to averaging. The later onset of saturation shows the potential of the RS method, which is particularly useful for samples with long relaxation times, such as a-Si:H or oximetry spin probes. The saturation

of the RS transients acquired at varying scan rates showed that the onset of saturation occurred at higher bias currents at faster scan rates. In this work, only the AM signal of the EPRoC was utilised for the RS experiments. However, the FM signal may also be used in the future for a further gain in sensitivity by utilising the EPRoC array concept.

At last, in [Chapter 8](#) the knowledge gathered from most of the previous chapters was applied to investigate the potential for state of charge (SOC) monitoring of a vanadium redox flow battery (VRFB). To this end, quantitative field-swept EPR experiments on positive electrolyte samples with varying SOC were performed with the EPRoC dipstick device, that were compared to those obtained with a commercial EPR spectrometer. The results showed that the EPRoC device could detect the SOC of the electrolyte samples, similar to the commercial EPR spectrometer. The EPR signal intensity was found to be linearly correlated with the SOC of the electrolyte samples. By utilising the signal amplitude calculated from only two measurement points, the acquisition time could considerably be reduced, approaching the required timescale of commercial VRFBs. In addition, the field- and frequency-swept spectra of the electrolyte solution samples showed the same spectral shape, indicating that the EPRoC may be used with a permanent magnet for SOC monitoring of VRFBs. The electrolyte solution has a relatively high conductivity, of up to 1 S for VRFBs, indicating that the EPRoC dipstick is relatively insensitive to the conductivity of the sample. This is a significant advantage of the EPRoC compared to resonator-based EPR devices.

The EPRoC dipstick may be applied to a variety of other applications, in which paramagnetic species are dissolved in aqueous solutions. For instance, existing experimental configurations for *in situ* spectroelectrochemical EPR may radically be simplified eliminating most of the issues imposed by resonator-based EPR. This includes the mass transport, high conductivity, and high dielectric constant of the sample. Similarly, other *in situ* experiments may be simplified, which require the reactant to flow through the resonator, such as for the investigation of homogeneous catalytic gas-phase reactions. For chemical laboratories, for instance, a small and cost-effective benchtop spectrometer based on the EPRoC dipstick may be developed that allows for the rapid quality control of chemical syntheses.

In this work, an electromagnet was used for the experiments for practical reasons; the use of small permanent magnets via frequency-swept CW-EPR and RS-EPRoC over a wide frequency range of several gigahertz offers significant advantages in terms of flexibility for EPRoC applications up to field strengths of approximately 1.5 T. The compact size of these magnets, in combination with the low power consumption of the EPRoC, renders them attractive for portable hand-held battery-operated EPRoC sensor devices. In the future, quantitative EPRoC sensors that are tailored to the specific requirements of the application outside

dedicated laboratories may be developed. Possible fields of application include food quality monitoring, environmental monitoring, and point-of-care medical diagnostics. Conceivable applications in the food industry include monitoring the shelf life of beer and determining the stability of edible oils. In environmental science, the content and type of certain transition metal ions in water as well as crude oil contamination from sand and soil may be determined. In addition to reactive oxygen species detection in the blood via spin traps, the EPRoC could also be integrated into an endoscope in combination with an oximetry spin probe to measure the partial oxygen pressure level in carcinogenic tissue for improved radiation therapy.

Generally, this development described here is a paradigm shift in the field of EPR spectroscopy because it reverses the usual approach of inserting the sample into the spectrometer. Instead, the spectrometer is brought to the sample. This allows the application of EPR spectroscopy in ways that were previously not even conceivable.

## BIBLIOGRAPHY

---

- [1] Frederick A. Villamena. 'Chapter 5 - EPR Spin Trapping'. In: *Reactive Species Detection in Biology*. Ed. by Frederick A. Villamena. Boston, US: Elsevier, 2017, pp. 163–202. ISBN: 978-0-12-420017-3. DOI: [10.1016/B978-0-12-420017-3.00004-9](https://doi.org/10.1016/B978-0-12-420017-3.00004-9).
- [2] Robin G. Hicks. *Stable Radicals: Fundamentals and Applied Aspects of Odd-Electron Compounds*. Chichester, West Sussex: Wiley, 2010. ISBN: 978-0-470-66697-5.
- [3] M. Fehr et al. 'Influence of Deep Defects on Device Performance of Thin-Film Polycrystalline Silicon Solar Cells'. In: *Applied Physics Letters* 101.12 (2012), p. 123904. DOI: [10.1063/1.4754609](https://doi.org/10.1063/1.4754609).
- [4] M. Fehr et al. 'Dangling Bonds in Amorphous Silicon Investigated by Multifrequency EPR'. In: *Journal of Non-Crystalline Solids*. Proceedings of the 24th International Conference on Amorphous and Nanocrystalline Semiconductors (ICANS 24) Nara, Japan August 21-26, 2011 358.17 (2012), pp. 2067–2070. DOI: [10.1016/j.jnoncrysol.2011.12.105](https://doi.org/10.1016/j.jnoncrysol.2011.12.105).
- [5] J. Möser et al. 'Using Rapid-Scan EPR to Improve the Detection Limit of Quantitative EPR by More than One Order of Magnitude'. In: *Journal of Magnetic Resonance* 281 (2017), pp. 17–25. DOI: [10.1016/j.jmr.2017.04.003](https://doi.org/10.1016/j.jmr.2017.04.003).
- [6] B. M. George et al. 'Atomic Structure of Interface States in Silicon Heterojunction Solar Cells'. In: *Physical Review Letters* 110.13 (2013), p. 136803. DOI: [10.1103/PhysRevLett.110.136803](https://doi.org/10.1103/PhysRevLett.110.136803).
- [7] Alexander Schnegg et al. 'Pulsed Electrically Detected Magnetic Resonance for Thin Film Silicon and Organic Solar Cells'. In: *Physical Chemistry Chemical Physics* 14.42 (2012), p. 14418. DOI: [10.1039/c2cp41258f](https://doi.org/10.1039/c2cp41258f).
- [8] Jannik Möser. 'Charge Transport in Amorphous Silicon: A Study by Electrically Detected Magnetic Resonance'. Berlin: Freie Universität Berlin, 2019. URL: <https://refubium.fu-berlin.de/handle/fub188/24658>.
- [9] Sabine Van Doorslaer and Evi Vinck. 'The Strength of EPR and ENDOR Techniques in Revealing Structure–Function Relationships in Metalloproteins'. In: *Physical Chemistry Chemical Physics* 9.33 (2007), pp. 4620–4638. DOI: [10.1039/B701568B](https://doi.org/10.1039/B701568B).
- [10] Gareth R Eaton, Sandra S Eaton and Kev M Salikhov. *Foundations of Modern EPR*. WORLD SCIENTIFIC, 1998. ISBN: 978-981-02-3295-5 978-981-281-676-4. DOI: [10.1142/3624](https://doi.org/10.1142/3624).

- [11] Frank Neese. 'Quantum Chemistry and EPR Parameters'. In: *eMagRes*. Ed. by Robin K. Harris and Roderick L. Wasylishen. Chichester, UK: John Wiley & Sons, Ltd, 2017, pp. 1–22. ISBN: 978-0-470-03459-0 978-0-470-05821-3. DOI: [10.1002/9780470034590.emrstm1505](https://doi.org/10.1002/9780470034590.emrstm1505).
- [12] Gareth R. Eaton et al. *Quantitative EPR*. Vienna, Austria: Springer Vienna, 2010. ISBN: 978-3-211-92947-6 978-3-211-92948-3. DOI: [10.1007/978-3-211-92948-3](https://doi.org/10.1007/978-3-211-92948-3).
- [13] D. F. Regulla and U. Deffner. 'Dosimetry by ESR Spectroscopy of Alanine'. In: *The International Journal of Applied Radiation and Isotopes* 33.11 (1982), pp. 1101–1114. DOI: [10.1016/0020-708X\(82\)90238-1](https://doi.org/10.1016/0020-708X(82)90238-1).
- [14] F. Trompier et al. 'State of the Art in Nail Dosimetry: Free Radicals Identification and Reaction Mechanisms'. In: *Radiation and Environmental Biophysics* 53.2 (2014), pp. 291–303. DOI: [10.1007/s00411-014-0512-2](https://doi.org/10.1007/s00411-014-0512-2).
- [15] Paola Fattibene and Freddy Callens. 'EPR Dosimetry with Tooth Enamel: A Review'. In: *Applied Radiation and Isotopes* 68.11 (2010), pp. 2033–2116. DOI: [10.1016/j.apradiso.2010.05.016](https://doi.org/10.1016/j.apradiso.2010.05.016).
- [16] D. A. Schauer et al. 'Radiation Dosimetry of an Accidental Overexposure Using EPR Spectrometry and Imaging of Human Bone'. In: *Applied Radiation and Isotopes*. ESR Dosimetry and Applications: Proceedings of the 4th International Symposium 47.11 (1996), pp. 1345–1350. DOI: [10.1016/S0969-8043\(96\)00203-5](https://doi.org/10.1016/S0969-8043(96)00203-5).
- [17] Motoji Ikeya. 'Dating a Stalactite by Electron Paramagnetic Resonance'. In: *Nature* 255.5503 (5503 1975), pp. 48–50. DOI: [10.1038/255048a0](https://doi.org/10.1038/255048a0).
- [18] W. J. Rink. 'Electron Spin Resonance (ESR) Dating and ESR Applications in Quaternary Science and Archaeometry'. In: *Radiation Measurements* 27.5 (1997), pp. 975–1025. DOI: [10.1016/S1350-4487\(97\)00219-9](https://doi.org/10.1016/S1350-4487(97)00219-9).
- [19] Anne R. Skinner. 'Current Topics in ESR Dating'. In: *Radiation Measurements*. EPRBioDose 2010 International Conference 46.9 (2011), pp. 749–753. DOI: [10.1016/j.radmeas.2011.01.003](https://doi.org/10.1016/j.radmeas.2011.01.003).
- [20] Jo-Anna P. Boshard, D. E. Holmes and L. H. Piette. 'An Inherent Dosimeter for Irradiated Foods: Papayas'. In: *The International Journal of Applied Radiation and Isotopes* 22.5 (1971), pp. 316–318. DOI: [10.1016/0020-708X\(71\)90008-1](https://doi.org/10.1016/0020-708X(71)90008-1).
- [21] Marc F. Desrosiers. 'Current Status of the EPR Method to Detect Irradiated Food'. In: *Applied Radiation and Isotopes*. ESR Dosimetry and Applications: Proceedings of the 4th International Symposium 47.11 (1996), pp. 1621–1628. DOI: [10.1016/S0969-8043\(96\)00255-2](https://doi.org/10.1016/S0969-8043(96)00255-2).

- [22] Glenn Hanson, Andre Szabo and N. Dennis Chasteen. 'Determination of Molybdenum in Seawater by Electron Paramagnetic Resonance Spectrometry'. In: *Analytical Chemistry* 49.3 (1977), pp. 461–463. DOI: [10.1021/ac50011a033](https://doi.org/10.1021/ac50011a033).
- [23] Adam Jezierski, Ewa Bylinska and Mark R.D. Seaward. 'Electron Paramagnetic Resonance (EPR) Investigations of Lichens – 1: Effects of Air Pollution'. In: *Atmospheric Environment* 33.28 (1999), pp. 4629–4635. DOI: [10.1016/S1352-2310\(99\)00258-7](https://doi.org/10.1016/S1352-2310(99)00258-7).
- [24] Bulat Gizatullin et al. 'Quantifying Crude Oil Contamination in Sand and Soil by EPR Spectroscopy'. In: *Applied Magnetic Resonance* 52.5 (2021), pp. 633–648. DOI: [10.1007/s00723-021-01331-4](https://doi.org/10.1007/s00723-021-01331-4).
- [25] M. Stutzmann. 'The Defect Density in Amorphous Silicon'. In: *Philosophical Magazine B* 60.4 (1989), pp. 531–546. DOI: [10.1080/13642818908205926](https://doi.org/10.1080/13642818908205926).
- [26] Tobias Sontheimer et al. 'Identification of Intra-Grain and Grain Boundary Defects in Polycrystalline Si Thin Films by Electron Paramagnetic Resonance'. In: *physica status solidi (RRL) – Rapid Research Letters* 7.11 (2013), pp. 959–962. DOI: [10.1002/pssr.201308061](https://doi.org/10.1002/pssr.201308061).
- [27] S. Steffens et al. 'Impact of Dislocations and Dangling Bond Defects on the Electrical Performance of Crystalline Silicon Thin Films'. In: *Applied Physics Letters* 105.2 (2014), p. 022108. DOI: [10.1063/1.4890625](https://doi.org/10.1063/1.4890625).
- [28] Andreas Sperlich, Michael Auth and Vladimir Dyakonov. 'Charge Transfer in Ternary Solar Cells Employing Two Fullerene Derivatives: Where Do Electrons Go?' In: *Israel Journal of Chemistry* 61 (2021), pp. 1–9. DOI: [10.1002/ijch.202100064](https://doi.org/10.1002/ijch.202100064).
- [29] Bin Wang, Alistair J. Fielding and Robert A.W. Dryfe. 'Electron Paramagnetic Resonance as a Structural Tool to Study Graphene Oxide: Potential Dependence of the EPR Response'. In: *The Journal of Physical Chemistry C* 123.36 (2019), pp. 22556–22563. DOI: [10.1021/acs.jpcc.9b04292](https://doi.org/10.1021/acs.jpcc.9b04292).
- [30] Pengfei Xia et al. 'Localized  $\pi$ -Conjugated Structure and EPR Investigation of g-C<sub>3</sub>N<sub>4</sub> Photocatalyst'. In: *Applied Surface Science* 487 (2019), pp. 335–342. DOI: [10.1016/j.apsusc.2019.05.064](https://doi.org/10.1016/j.apsusc.2019.05.064).
- [31] Natalia Cortés et al. 'Development and Correlation between the Organic Radical Concentration in Different Malt Types and Oxidative Beer Stability'. In: *Journal of the American Society of Brewing Chemists* 68.2 (2010), pp. 107–113. DOI: [10.1094/ASBCJ-2010-0412-01](https://doi.org/10.1094/ASBCJ-2010-0412-01).



- [32] M. Francesca Ottaviani et al. 'Electron Paramagnetic Resonance Investigations of Free Radicals in Extra Virgin Olive Oils'. In: *Journal of Agricultural and Food Chemistry* 49.8 (2001), pp. 3691–3696. DOI: [10.1021/jf001203+](https://doi.org/10.1021/jf001203+).
- [33] Richard L. Blakley et al. 'Quantitative Electron Paramagnetic Resonance: The Importance of Matching the Q-Factor of Standards and Samples'. In: *Applied Spectroscopy* 55.10 (2001), pp. 1375–1381. DOI: [10.1366/0003702011953504](https://doi.org/10.1366/0003702011953504).
- [34] Kahina Abbas, Nikola Babić and Fabienne Peyrot. 'Use of Spin Traps to Detect Superoxide Production in Living Cells by Electron Paramagnetic Resonance (EPR) Spectroscopy'. In: *Methods. Current Methods to Unravel Reactive Oxygen Species (ROS) Biology* 109 (2016), pp. 31–43. DOI: [10.1016/j.ymeth.2016.05.001](https://doi.org/10.1016/j.ymeth.2016.05.001).
- [35] Jamie S. Lawton et al. 'The Effect of Sulfuric Acid Concentration on the Physical and Electrochemical Properties of Vanadyl Solutions'. In: *Batteries* 4.3 (3 2018), p. 40. DOI: [10.3390/batteries4030040](https://doi.org/10.3390/batteries4030040).
- [36] Wyndom S. Chace et al. 'Effects of State of Charge on the Physical Characteristics of v(IV)/V(V) Electrolytes and Membrane for the All Vanadium Flow Battery'. In: *Batteries* 6.4 (2020), p. 49. DOI: [10.3390/batteries6040049](https://doi.org/10.3390/batteries6040049).
- [37] Evan Wenbo Zhao et al. 'Coupled In Situ NMR and EPR Studies Reveal the Electron Transfer Rate and Electrolyte Decomposition in Redox Flow Batteries'. In: *Journal of the American Chemical Society* 143.4 (2021), pp. 1885–1895. DOI: [10.1021/jacs.0c10650](https://doi.org/10.1021/jacs.0c10650).
- [38] Jamie S. Lawton, Amanda Jones and Thomas Zawodzinski. 'Concentration Dependence of VO<sup>2+</sup> Crossover of Nafion for Vanadium Redox Flow Batteries'. In: *Journal of The Electrochemical Society* 160.4 (2013), A697–A702. DOI: [10.1149/2.004306jes](https://doi.org/10.1149/2.004306jes).
- [39] Jabor Rabeah et al. 'Multivariate Analysis of Coupled Operando EPR/XANES/EXAFS/UV-Vis/ATR-IR Spectroscopy: A New Dimension for Mechanistic Studies of Catalytic Gas-Liquid Phase Reactions'. In: *Chemistry – A European Journal* 26.33 (2020), pp. 7395–7404. DOI: [10.1002/chem.202000436](https://doi.org/10.1002/chem.202000436).
- [40] Shannon A. Bonke et al. 'In Situ Electron Paramagnetic Resonance Spectroscopy for Catalysis'. In: *Nature Reviews Methods Primers* 1.1 (1 2021), pp. 1–20. DOI: [10.1038/s43586-021-00031-4](https://doi.org/10.1038/s43586-021-00031-4).
- [41] Kaltum Abdiaziz et al. 'Protein Film Electrochemical EPR Spectroscopy as a Technique to Investigate Redox Reactions in Biomolecules'. In: *Chemical Communications* 55.60 (2019), pp. 8840–8843. DOI: [10.1039/C9CC03212F](https://doi.org/10.1039/C9CC03212F).



- [42] Satoshi Yamasaki et al. 'In Situ Electron-Spin-Resonance Measurements of Film Growth of Hydrogenated Amorphous Silicon'. In: *Applied Physics Letters* 70.9 (1997), pp. 1137–1139. DOI: [10.1063/1.119073](https://doi.org/10.1063/1.119073).
- [43] Satoshi Yamasaki, Ujjwal K. Das and Kenji Ishikawa. 'Direct Observation of Surface Dangling Bonds during Plasma Process: Chemical Reactions during H<sub>2</sub> and Ar Plasma Treatments'. In: *Thin Solid Films* 407.1-2 (2002), pp. 139–143. DOI: [10.1016/s0040-6090\(02\)00028-7](https://doi.org/10.1016/s0040-6090(02)00028-7).
- [44] Wataru Futako et al. 'In Situ Electron Spin Resonance Observation of Si(111) 7×7 Surface during Hydrogenation Process'. In: *Journal of Vacuum Science & Technology B: Microelectronics and Nanometer Structures* 19.5 (2001), p. 1898. DOI: [10.1116/1.1403439](https://doi.org/10.1116/1.1403439).
- [45] W Futako et al. 'In Situ ESR Observation of Interface Dangling Bond Formation Processes during Amorphous SiO<sub>2</sub> Growth on Si'. In: *Journal of Non-Crystalline Solids* 299–302 (2002), pp. 575–578. DOI: [10.1016/s0022-3093\(01\)00964-4](https://doi.org/10.1016/s0022-3093(01)00964-4).
- [46] Cuyler K. Borrowman et al. 'Formation of Environmentally Persistent Free Radicals from the Heterogeneous Reaction of Ozone and Polycyclic Aromatic Compounds'. In: *Physical Chemistry Chemical Physics* 18.1 (2016), pp. 205–212. DOI: [10.1039/c5cp05606c](https://doi.org/10.1039/c5cp05606c).
- [47] Oleg Zgadzai et al. 'Electron-Spin-Resonance Dipstick'. In: *Analytical Chemistry* 90.13 (2018), pp. 7830–7836. DOI: [10.1021/acs.analchem.8b00917](https://doi.org/10.1021/acs.analchem.8b00917).
- [48] Lauren E. Switala et al. 'An Electron Paramagnetic Resonance Mobile Universal Surface Explorer'. In: *Journal of Magnetic Resonance* 285 (2017), pp. 18–25. DOI: [10.1016/j.jmr.2017.10.004](https://doi.org/10.1016/j.jmr.2017.10.004).
- [49] Jason P. Campbell et al. 'Electron Spin Resonance Scanning Probe Spectroscopy for Ultrasensitive Biochemical Studies'. In: *Analytical Chemistry* 87.9 (2015), pp. 4910–4916. DOI: [10.1021/acs.analchem.5b00487](https://doi.org/10.1021/acs.analchem.5b00487).
- [50] Helen Wolfson et al. 'A Hand-Held EPR Scanner for Transcutaneous Oximetry'. In: *Medical Imaging 2015: Biomedical Applications in Molecular, Structural, and Functional Imaging*. Ed. by Barjor Gimi and Robert C. Molthen. Orlando, Florida, United States: International Society for Optics and Photonics, 2015, p. 941706. DOI: [10.1117/12.2083864](https://doi.org/10.1117/12.2083864).
- [51] Tolga Yalçın and Giovanni Boero. 'Single-Chip Detector for Electron Spin Resonance Spectroscopy'. In: *Review of Scientific Instruments* 79.9 (2008), p. 094105. DOI: [10.1063/1.2969657](https://doi.org/10.1063/1.2969657).

- [52] Jens Anders, Alexander Angerhofer and Giovanni Boero. 'K-Band Single-Chip Electron Spin Resonance Detector'. In: *Journal of Magnetic Resonance* 217 (2012), pp. 19–26. DOI: [10.1016/j.jmr.2012.02.003](https://doi.org/10.1016/j.jmr.2012.02.003).
- [53] Xuebei Yang and Aydin Babakhani. 'A Single-Chip Electron Paramagnetic Resonance Transceiver in 0.13- $\mu\text{m}$  SiGe BiCMOS'. In: *IEEE Transactions on Microwave Theory and Techniques* 63.11 (2015), pp. 3727–3735. DOI: [10.1109/tmtt.2015.2481895](https://doi.org/10.1109/tmtt.2015.2481895).
- [54] Luya Zhang and Ali M. Niknejad. 'An Ultrasensitive 14-GHz 1.12-mW EPR Spectrometer in 28-Nm CMOS'. In: *IEEE Microwave and Wireless Components Letters* (2021), pp. 1–1. DOI: [10.1109/LMWC.2021.3060730](https://doi.org/10.1109/LMWC.2021.3060730).
- [55] Jonas Handwerker et al. 'A 14GHz Battery-Operated Point-of-Care ESR Spectrometer Based on a 0.13 $\mu\text{m}$  CMOS ASIC'. In: *2016 IEEE International Solid-State Circuits Conference (ISSCC)*. San Francisco, CA, USA: IEEE, 2016, pp. 476–477. DOI: [10.1109/ISSCC.2016.7418114](https://doi.org/10.1109/ISSCC.2016.7418114).
- [56] R. V. Pound and W. D. Knight. 'A Radiofrequency Spectrograph and Simple Magnetic-Field Meter'. In: *Review of Scientific Instruments* 21.3 (1950), pp. 219–225. DOI: [10.1063/1.1745537](https://doi.org/10.1063/1.1745537).
- [57] James S. Hyde et al. 'W-Band Frequency-Swept EPR'. In: *Journal of Magnetic Resonance* 205.1 (2010), pp. 93–101. DOI: [10.1016/j.jmr.2010.04.005](https://doi.org/10.1016/j.jmr.2010.04.005).
- [58] B. Schlecker et al. 'VCO-based ESR-on-a-chip as a Tool for Low-Cost, High-Sensitivity Point-of-Care Diagnostics'. In: *2017 IEEE SENSORS*. Glasgow: IEEE, 2017, pp. 1–3. DOI: [10.1109/ICSENS.2017.8233896](https://doi.org/10.1109/ICSENS.2017.8233896).
- [59] B. Schlecker et al. 'Live Demonstration: A VCO-based Point-of-Care ESR Spectrometer'. In: *2017 IEEE SENSORS*. Glasgow: IEEE, 2017, pp. 1–1. DOI: [10.1109/ICSENS.2017.8234031](https://doi.org/10.1109/ICSENS.2017.8234031).
- [60] J. Anders and K. Lips. 'MR to Go'. In: *Journal of Magnetic Resonance* 306 (2019), pp. 118–123. DOI: [10.1016/j.jmr.2019.07.007](https://doi.org/10.1016/j.jmr.2019.07.007).
- [61] Anh Chu et al. 'An 8-Channel 13GHz ESR-on-a-Chip Injection-Locked VCO-array Achieving 200 $\mu\text{M}$ -concentration Sensitivity'. In: *2018 IEEE International Solid - State Circuits Conference - (ISSCC)*. San Francisco, CA, USA: IEEE, 2018, pp. 354–356. DOI: [10.1109/ISSCC.2018.8310330](https://doi.org/10.1109/ISSCC.2018.8310330).
- [62] Gareth R. Eaton and Sandra S. Eaton. 'Rapid-Scan Electron Paramagnetic Resonance'. In: *eMagRes*. Ed. by Robin K. Harris and Roderick Wasylshen. Chichester, UK: John Wiley & Sons, Ltd, 2016, pp. 1529–1542. ISBN: 978-0-470-03459-0 978-0-470-05821-3. DOI: [10.1002/9780470034590.emrstm1522](https://doi.org/10.1002/9780470034590.emrstm1522).

- [63] Anatole Abragam, Maurice Henry Lecorney Pryce and Franz Eugen Simon. 'Theory of the Nuclear Hyperfine Structure of Paramagnetic Resonance Spectra in Crystals'. In: *Proceedings of the Royal Society of London. Series A. Mathematical and Physical Sciences* 205.1080 (1950), pp. 135–153. DOI: [10.1098/rspa.1951.0022](https://doi.org/10.1098/rspa.1951.0022).
- [64] Joshua Telser. 'EPR Interactions – Zero-Field Splittings'. In: *eMagRes*. Ed. by Roderick Wasylshen. John Wiley & Sons, Ltd, 2017, pp. 207–233. ISBN: 978-0-470-03459-0. DOI: [10.1002/9780470034590.emrstm1501](https://doi.org/10.1002/9780470034590.emrstm1501).
- [65] N. M. Atherton. *Principles of Electron Spin Resonance*. Ellis Horwood PTR Prentice Hall Physical Chemistry Series. New York: Ellis Horwood PTR Prentice Hall, 1993. ISBN: 978-0-13-721762-5.
- [66] Arthur Schweiger and Gunnar Jeschke. *Principles of Pulse Electron Paramagnetic Resonance*. Oxford, UK New York: Oxford University Press, 2001. ISBN: 978-0-19-850634-8.
- [67] Marina Bennati. 'EPR Interactions – Hyperfine Couplings'. In: *eMagRes*. Ed. by Roderick Wasylshen. John Wiley & Sons, Ltd, 2017, pp. 271–281. ISBN: 978-0-470-03459-0. DOI: [10.1002/9780470034590.emrstm1503](https://doi.org/10.1002/9780470034590.emrstm1503).
- [68] Peter Gast and Edgar J.J. Groenen. 'EPR Interactions – g-Anisotropy'. In: *eMagRes*. Ed. by Roderick Wasylshen. John Wiley & Sons, Ltd, 2016, pp. 1435–1444. ISBN: 978-0-470-03459-0. DOI: [10.1002/9780470034590.emrstm1500](https://doi.org/10.1002/9780470034590.emrstm1500).
- [69] John A. Weil and James R. Bolton. *Electron Paramagnetic Resonance: Elementary Theory and Practical Applications, Second Edition*. John Wiley & Sons, Inc., 2007. 688 pp. ISBN: 978-0-471-75496-1. DOI: [10.1002/0470084987](https://doi.org/10.1002/0470084987).
- [70] Stefan Stoll and Arthur Schweiger. 'EasySpin, a Comprehensive Software Package for Spectral Simulation and Analysis in EPR'. In: *Journal of Magnetic Resonance* 178.1 (2006), pp. 42–55. DOI: [10.1016/j.jmr.2005.08.013](https://doi.org/10.1016/j.jmr.2005.08.013).
- [71] Jeffrey R. Harmer. 'Hyperfine Spectroscopy – ENDOR'. In: *eMagRes*. Ed. by Roderick Wasylshen. John Wiley & Sons, Ltd, 2016, pp. 1493–1514. ISBN: 978-0-470-03459-0. DOI: [10.1002/9780470034590.emrstm1515](https://doi.org/10.1002/9780470034590.emrstm1515).
- [72] Daniella Goldfarb. 'ELDOR-Detected NMR'. In: *eMagRes*. Ed. by Roderick Wasylshen. John Wiley & Sons, Ltd, 2017, pp. 101–114. ISBN: 978-0-470-03459-0. DOI: [10.1002/9780470034590.emrstm1516](https://doi.org/10.1002/9780470034590.emrstm1516).
- [73] Sabine Van Doorslaer. 'Hyperfine Spectroscopy: ESEEM'. In: *eMagRes*. Ed. by Roderick Wasylshen. John Wiley & Sons, Ltd, 2017, pp. 51–69. ISBN: 978-0-470-03459-0. DOI: [10.1002/9780470034590.emrstm1517](https://doi.org/10.1002/9780470034590.emrstm1517).

- [74] C. P. Slichter. *Principles of Magnetic Resonance*. Springer Series in Solid-State Sciences. Springer Berlin Heidelberg, 1996. ISBN: 978-3-540-50157-2. URL: <https://books.google.de/books?id=zgnrRkaIhFoC>.
- [75] Daniella Goldfarb and Stefan Stoll, eds. *EPR Spectroscopy: Fundamentals and Methods*. Hoboken, N.J: Wiley/Blackwell, 2018. 1 p. ISBN: 978-1-119-16297-1 978-1-119-16298-8.
- [76] F. Bloch. 'Nuclear Induction'. In: *Physical Review* 70.7-8 (1946), pp. 460–474. DOI: [10.1103/PhysRev.70.460](https://doi.org/10.1103/PhysRev.70.460).
- [77] Sandra S. Eaton and Gareth R. Eaton. 'Relaxation Mechanisms'. In: *eMagRes*. Ed. by Roderick Wasylshen. John Wiley & Sons, Ltd, 2016, pp. 1543–1556. ISBN: 978-0-470-03459-0. DOI: [10.1002/9780470034590.emrstm1507](https://doi.org/10.1002/9780470034590.emrstm1507).
- [78] C. P. Poole. *Electron Spin Resonance: A Comprehensive Treatise on Experimental Techniques*. Dover Books on Physics. Dover Publications, 1996. ISBN: 978-0-486-69444-3.
- [79] R. de L. Kronig. 'On the Theory of Dispersion of X-Rays'. In: *JOSA* 12.6 (1926), pp. 547–557. DOI: [10.1364/JOSA.12.000547](https://doi.org/10.1364/JOSA.12.000547).
- [80] J. P. Lloyd and G. E. Pake. 'Spin Relaxation in Free Radical Solutions Exhibiting Hyperfine Structure'. In: *Physical Review* 94.3 (1954), pp. 579–591. DOI: [10.1103/PhysRev.94.579](https://doi.org/10.1103/PhysRev.94.579).
- [81] G. E. Pake and T. R. Tuttle. 'Anomalous Loss of Resolution of Paramagnetic Resonance Hyperfine Structure in Liquids'. In: *Physical Review Letters* 3.9 (1959), pp. 423–425. DOI: [10.1103/PhysRevLett.3.423](https://doi.org/10.1103/PhysRevLett.3.423).
- [82] Edward Reijerse and Anton Savitsky. 'Electron Paramagnetic Resonance Instrumentation'. In: *eMagRes*. Ed. by Roderick Wasylshen. John Wiley & Sons, Ltd, 2017, pp. 187–205. ISBN: 978-0-470-03459-0. DOI: [10.1002/9780470034590.emrstm1511](https://doi.org/10.1002/9780470034590.emrstm1511).
- [83] G. Feher. 'Sensitivity Considerations in Microwave Paramagnetic Resonance Absorption Techniques'. In: *Bell System Technical Journal* 36.2 (1957), pp. 449–484. DOI: [10.1002/j.1538-7305.1957.tb02406.x](https://doi.org/10.1002/j.1538-7305.1957.tb02406.x).
- [84] Fritz Schneider and Martin Plato. *Elektronenspin-Resonanz: experimentelle Technik*. K. Thiemig, 1971. 246 pp. ISBN: 978-3-521-06057-9.
- [85] G. Boero et al. 'Electron-Spin Resonance Probe Based on a 100 Mm Planar Microcoil'. In: *Review of Scientific Instruments* 74.11 (2003), pp. 4794–4798. DOI: [10.1063/1.1621064](https://doi.org/10.1063/1.1621064).
- [86] O. Laguta et al. 'Multi-Frequency Rapid-Scan HFEPN'. In: *Journal of Magnetic Resonance* 296 (2018), pp. 138–142. DOI: [10.1016/j.jmr.2018.09.005](https://doi.org/10.1016/j.jmr.2018.09.005).

- [87] O. Laguta et al. 'Rapid Scan ESR: A Versatile Tool for the Spin Relaxation Studies at (Sub)THz Frequencies'. In: *Applied Physics Letters* 120.12 (2022), p. 120502. DOI: [10.1063/5.0083010](https://doi.org/10.1063/5.0083010).
- [88] Mark Tseitlin et al. 'Rapid Frequency Scan EPR'. In: *Journal of Magnetic Resonance* 211.2 (2011), pp. 156–161. DOI: [10.1016/j.jmr.2011.05.006](https://doi.org/10.1016/j.jmr.2011.05.006).
- [89] Jannik Möser. 'Rapid Scan Electron Paramagnetic Resonance on Silicon Thin-Film Solar Cell Materials'. MA thesis. Berlin: Freie Universität Berlin, 2015.
- [90] Boris A. Jacobsohn and Roald K. Wangsness. 'Shapes of Nuclear Induction Signals'. In: *Physical Review* 73.9 (1948), pp. 942–946. DOI: [10.1103/physrev.73.942](https://doi.org/10.1103/physrev.73.942).
- [91] Philipp E. Spindler et al. 'Shaped Pulses in EPR'. In: *eMagRes*. Ed. by Roderick Wasylshen. John Wiley & Sons, Ltd, 2016, pp. 1477–1491. ISBN: 978-0-470-03459-0. DOI: [10.1002/9780470034590.emrstm1520](https://doi.org/10.1002/9780470034590.emrstm1520).
- [92] M. Weger. 'Passage Effects in Paramagnetic Resonance Experiments'. In: *The Bell System Technical Journal* 39.4 (1960), pp. 1013–1112. DOI: [10.1002/j.1538-7305.1960.tb03951.x](https://doi.org/10.1002/j.1538-7305.1960.tb03951.x).
- [93] J. G. Powles. 'The Adiabatic Fast Passage Experiment in Magnetic Resonance'. In: *Proceedings of the Physical Society* 71.3 (1958), pp. 497–500. DOI: [10.1088/0370-1328/71/3/424](https://doi.org/10.1088/0370-1328/71/3/424).
- [94] I. I. Rabi, N. F. Ramsey and J. Schwinger. 'Use of Rotating Coordinates in Magnetic Resonance Problems'. In: *Reviews of Modern Physics* 26.2 (1954), pp. 167–171. DOI: [10.1103/RevModPhys.26.167](https://doi.org/10.1103/RevModPhys.26.167).
- [95] Aaron W. Kittell et al. 'Detection of Undistorted Continuous Wave (CW) Electron Paramagnetic Resonance (EPR) Spectra with Non-Adiabatic Rapid Sweep (NARS) of the Magnetic Field'. In: *Journal of Magnetic Resonance* 211.2 (2011), pp. 228–233. DOI: [10.1016/j.jmr.2011.06.004](https://doi.org/10.1016/j.jmr.2011.06.004).
- [96] Mark Tseitlin, Gareth R. Eaton and Sandra S. Eaton. 'Computationally Efficient Steady-State Solution of the Bloch Equations for Rapid Sinusoidal Scans Based on Fourier Expansion in Harmonics of the Scan Frequency'. In: *Applied Magnetic Resonance* 44.12 (2013), pp. 1373–1379. DOI: [10.1007/s00723-013-0494-2](https://doi.org/10.1007/s00723-013-0494-2).
- [97] Mark Tseitlin et al. 'Deconvolution of Sinusoidal Rapid EPR Scans'. In: *Journal of Magnetic Resonance* 208.2 (2011), pp. 279–283. DOI: [10.1016/j.jmr.2010.11.015](https://doi.org/10.1016/j.jmr.2010.11.015).
- [98] I. N. Geifman et al. 'Raising the Sensitivity of the Electron-Paramagnetic-Resonance Spectrometer Using a Ferroelectric Resonator'. In: *Technical Physics* 45.2 (2000), pp. 263–266. DOI: [10.1134/1.1259610](https://doi.org/10.1134/1.1259610).

- [99] Yuri E. Nesmelov, Jack T. Surek and David D. Thomas. 'Enhanced EPR Sensitivity from a Ferroelectric Cavity Insert'. In: *Journal of Magnetic Resonance* 153.1 (2001), pp. 7–14. DOI: [10.1006/jmre.2001.2415](https://doi.org/10.1006/jmre.2001.2415).
- [100] Victoria N. Syryamina et al. 'Improving B<sub>1</sub> Field Homogeneity in Dielectric Tube Resonators for EPR Spectroscopy via Controlled Shaping of the Dielectric Insert'. In: *Journal of Magnetic Resonance* 311 (2020), p. 106685. DOI: [10.1016/j.jmr.2020.106685](https://doi.org/10.1016/j.jmr.2020.106685).
- [101] R. Narkowicz, D. Suter and R. Stonies. 'Planar Microresonators for EPR Experiments'. In: *Journal of Magnetic Resonance* 175.2 (2005), pp. 275–284. DOI: [10.1016/j.jmr.2005.04.014](https://doi.org/10.1016/j.jmr.2005.04.014).
- [102] Fred J. Rosenbaum. 'Dielectric Cavity Resonator for ESR Experiments'. In: *Review of Scientific Instruments* 35.11 (1964), pp. 1550–1554. DOI: [10.1063/1.1719205](https://doi.org/10.1063/1.1719205).
- [103] Iryna Golovina, Ilia Geifman and Anatolii Belous. 'New Ceramic EPR Resonators with High Dielectric Permittivity'. In: *Journal of Magnetic Resonance* 195.1 (2008), pp. 52–59. DOI: [10.1016/j.jmr.2008.08.015](https://doi.org/10.1016/j.jmr.2008.08.015).
- [104] Lazar Shtirberg et al. 'High-Sensitivity Q-band Electron Spin Resonance Imaging System with Submicron Resolution'. In: *Review of Scientific Instruments* 82.4 (2011), p. 043708. DOI: [10.1063/1.3581226](https://doi.org/10.1063/1.3581226).
- [105] Jens Anders and Klaus Lips. 'Vorrichtung und Verfahren zur Erzeugung und Detektion einer transienten Magnetisierung einer Probe'. German pat. 102015120644B3. 2017.
- [106] R A Wind. 'The Sensitivities of Five Transistorized Nuclear Magnetic Resonance Spectrometers'. In: *Journal of Physics E: Scientific Instruments* 3.1 (1970), p. 31. DOI: [10.1088/0022-3735/3/1/307](https://doi.org/10.1088/0022-3735/3/1/307).
- [107] R. Narkowicz, D. Suter and I. Niemeyer. 'Scaling of Sensitivity and Efficiency in Planar Microresonators for Electron Spin Resonance'. In: *Review of Scientific Instruments* 79.8 (2008), p. 084702. DOI: [10.1063/1.2964926](https://doi.org/10.1063/1.2964926).
- [108] D.I. Hoult. 'The NMR Receiver: A Description and Analysis of Design'. In: *Progress in Nuclear Magnetic Resonance Spectroscopy* 12.1 (1978), pp. 41–77. DOI: [10.1016/0079-6565\(78\)80002-8](https://doi.org/10.1016/0079-6565(78)80002-8).
- [109] D.I. Hoult and R.E. Richards. 'The Signal-to-Noise Ratio of the Nuclear Magnetic Resonance Experiment'. In: *Journal of Magnetic Resonance* (1969) 24.1 (1976), pp. 71–85. DOI: [10.1016/0022-2364\(76\)90233-X](https://doi.org/10.1016/0022-2364(76)90233-X).
- [110] H. Mahdjour, W. G. Clark and K. Baberschke. 'High-sensitivity Broadband Microwave Spectroscopy with Small Nonresonant Coils'. In: *Review of Scientific Instruments* 57.6 (1986), pp. 1100–1106. DOI: [10.1063/1.1138664](https://doi.org/10.1063/1.1138664).



- [111] Keiichi Ohno and Takeshi Murakami. 'Microscopic ESR Imaging Using a Microcoil System'. In: *Journal of Magnetic Resonance (1969)* 79.2 (1988), pp. 343–347. DOI: [10.1016/0022-2364\(88\)90228-4](https://doi.org/10.1016/0022-2364(88)90228-4).
- [112] Y. Morita and K. Ohno. 'EPR of Submicroliter Aqueous Samples Using a Microcoil'. In: *Journal of Magnetic Resonance, Series A* 102.3 (1993), pp. 344–347. DOI: [10.1006/jmra.1993.1113](https://doi.org/10.1006/jmra.1993.1113).
- [113] Andrew G. Webb. 'Radiofrequency Microcoils in Magnetic Resonance'. In: *Progress in Nuclear Magnetic Resonance Spectroscopy* 31.1 (1997), pp. 1–42. DOI: [10.1016/S0079-6565\(97\)00004-6](https://doi.org/10.1016/S0079-6565(97)00004-6).
- [114] Nir Dayan et al. 'Advanced Surface Resonators for Electron Spin Resonance of Single Microcrystals'. In: *Review of Scientific Instruments* 89.12 (2018), p. 124707. DOI: [10.1063/1.5063367](https://doi.org/10.1063/1.5063367).
- [115] Nandita Abhyankar et al. 'Scalable Microresonators for Room-Temperature Detection of Electron Spin Resonance from Dilute, Sub-Nanoliter Volume Solids'. In: *Science Advances* 6.44 (2020), eabbo620. DOI: [10.1126/sciadv.abb0620](https://doi.org/10.1126/sciadv.abb0620).
- [116] W Froncisz and James S Hyde. 'The Loop-Gap Resonator: A New Microwave Lumped Circuit ESR Sample Structure'. In: *Journal of Magnetic Resonance (1969)* 47.3 (1982), pp. 515–521. DOI: [10.1016/0022-2364\(82\)90221-9](https://doi.org/10.1016/0022-2364(82)90221-9).
- [117] W. Froncisz, T. Oles and James S. Hyde. 'Murine L-band ESR Loop-Gap Resonator'. In: *Journal of Magnetic Resonance (1969)* 82.1 (1989), pp. 109–114. DOI: [10.1016/0022-2364\(89\)90169-8](https://doi.org/10.1016/0022-2364(89)90169-8).
- [118] Jason W. Sidabras et al. 'Extending Electron Paramagnetic Resonance to Nanoliter Volume Protein Single Crystals Using a Self-Resonant Microhelix'. In: *Science advances* 5.10 (2019), eaay1394. DOI: [10.1126/sciadv.aay1394](https://doi.org/10.1126/sciadv.aay1394).
- [119] A. C. Torrezan, T. P. Mayer Alegre and G. Medeiros-Ribeiro. 'Microstrip Resonators for Electron Paramagnetic Resonance Experiments'. In: *Review of Scientific Instruments* 80.7 (2009), p. 075111. DOI: [10.1063/1.3186054](https://doi.org/10.1063/1.3186054).
- [120] W. J. Wallace and R. H. Silsbee. 'Microstrip Resonators for Electron-spin Resonance'. In: *Review of Scientific Instruments* 62.7 (1991), pp. 1754–1766. DOI: [10.1063/1.1142418](https://doi.org/10.1063/1.1142418).
- [121] Tolga Yalçın. 'Microwave Integrated Electronics for ESR Spectroscopy'. PhD thesis. Lausanne, EPFL, 2006. DOI: [10.5075/EPFL-THESIS-3687](https://doi.org/10.5075/EPFL-THESIS-3687).
- [122] F. N. H. Robinson. 'Nuclear Resonance Absorption Circuit'. In: *Journal of Scientific Instruments* 36.12 (1959), pp. 481–487. DOI: [10.1088/0950-7671/36/12/301](https://doi.org/10.1088/0950-7671/36/12/301).

- [123] W. M. Walsh and L. W. Rupp. 'A Microwave Frequency Marginal Oscillator for Electron Spin Resonance'. In: *Review of Scientific Instruments* 41.9 (1970), pp. 1316–1318. DOI: [10.1063/1.1684804](https://doi.org/10.1063/1.1684804).
- [124] W. M. Walsh and L. W. Rupp. 'A Self-Detecting Microwave Marginal Oscillator'. In: *Review of Scientific Instruments* 42.4 (1971), pp. 468–470. DOI: [10.1063/1.1685132](https://doi.org/10.1063/1.1685132).
- [125] W. M. Walsh Jr. and L. W. Rupp Jr. 'Self-detecting Microwave Spectrometer Based on the BARITT Diode'. In: *Review of Scientific Instruments* 52.7 (1981), pp. 1029–1031. DOI: [10.1063/1.1136729](https://doi.org/10.1063/1.1136729).
- [126] Jens Anders. 'Fully-Integrated CMOS Probes for Magnetic Resonance Applications'. Lausanne: École polytechnique fédérale de Lausanne, 2011. DOI: [10.5075/EPFL-THESIS-5154](https://doi.org/10.5075/EPFL-THESIS-5154).
- [127] Jens Anders. 'Nonlinear Modeling of Continuous-Wave Spin Detection Using Oscillator-Based ESR-on-a-Chip Sensors'. In: *Studies in Systems, Decision and Control*. Springer International Publishing, 2017, pp. 57–87. DOI: [10.1007/978-3-319-58996-1\\_4](https://doi.org/10.1007/978-3-319-58996-1_4).
- [128] Mohamed Atef Hassan et al. 'A 14-Channel 7 GHz VCO-based EPR-on-a-chip Sensor with Rapid Scan Capabilities'. In: *2021 IEEE Sensors*. 2021, pp. 1–4. DOI: [10.1109/SENSORS47087.2021.9639513](https://doi.org/10.1109/SENSORS47087.2021.9639513).
- [129] Khubaib Khan et al. 'A 12.2 to 14.9 GHz Injection-Locked VCO Array with an on-Chip 50 MHz BW Semi-Digital PLL for Transient Spin Manipulation and Detection'. In: *2022 IEEE 65th International Midwest Symposium on Circuits and Systems (MWSCAS)*. 2022, pp. 1–4. DOI: [10.1109/MWSCAS54063.2022.9859288](https://doi.org/10.1109/MWSCAS54063.2022.9859288).
- [130] Mohamed Atef Hassan et al. 'Towards Single-Cell Pulsed EPR Using VCO-based EPR-on-a-chip Detectors'. In: *Frequenz* 76.11-12 (2022), pp. 699–717. DOI: [10.1515/freq-2022-0096](https://doi.org/10.1515/freq-2022-0096).
- [131] Silvio Künstner et al. 'Rapid-Scan Electron Paramagnetic Resonance Using an EPR-on-a-Chip Sensor'. In: *Magnetic Resonance* 2.2 (2021), pp. 673–687. DOI: [10.5194/mr-2-673-2021](https://doi.org/10.5194/mr-2-673-2021).
- [132] Anh Chu et al. 'A 263GHz 32-Channel EPR-on-a-Chip Injection-Locked VCO-Array'. In: *2023 IEEE International Solid-State Circuits Conference (ISSCC)*. 2023, pp. 20–22. DOI: [10.1109/ISSCC42615.2023.10067623](https://doi.org/10.1109/ISSCC42615.2023.10067623).
- [133] Anh Chu et al. 'On the Modeling of Amplitude-Sensitive Electron Spin Resonance (ESR) Detection Using Voltage-Controlled Oscillator (VCO)-Based ESR-on-a-chip Detectors'. In: *Magnetic Resonance* 2.2 (2021), pp. 699–713. DOI: [10.5194/mr-2-699-2021](https://doi.org/10.5194/mr-2-699-2021).



- [134] J. Anders, M. Ortmanns and G. Boero. 'Noise in Frequency-Sensitive ESR Detectors'. In: *IFAC Proceedings Volumes* 45.2 (2012), pp. 451–456. DOI: [10.3182/20120215-3-AT-3016.00079](https://doi.org/10.3182/20120215-3-AT-3016.00079).
- [135] Dominic William Jordan and Peter Smith. *Nonlinear Ordinary Differential Equations: An Introduction for Scientists and Engineers*. 4th ed. Oxford: Oxford university press, 2007. ISBN: 978-0-19-920825-8.
- [136] Anh Chu et al. 'VCO-based ESR-on-a-chip as a Tool for Low-Cost, High-Sensitivity Food Quality Control'. In: *2017 IEEE Biomedical Circuits and Systems Conference (BioCAS)*. Torino, Italy: IEEE, 2017, pp. 1–4. DOI: [10.1109/BIOCAS.2017.8325172](https://doi.org/10.1109/BIOCAS.2017.8325172).
- [137] Jens Anders, Maurits Ortmanns and Giovanni Boero. 'Frequency Noise in Current-Starved CMOS LC Tank Oscillators'. In: *NDES 2012; Nonlinear Dynamics of Electronic Systems*. VDE, 2012, pp. 1–4.
- [138] Hiroshi Hirata et al. '1.1-GHz Continuous-Wave EPR Spectroscopy with a Frequency Modulation Method'. In: *Journal of Magnetic Resonance* 155.1 (2002), pp. 140–144. DOI: [10.1006/jmre.2002.2507](https://doi.org/10.1006/jmre.2002.2507).
- [139] Hiroshi Hirata et al. 'Detection of Electron Paramagnetic Resonance Absorption Using Frequency Modulation'. In: *Journal of Magnetic Resonance* 164.2 (2003), pp. 233–241. DOI: [10.1016/S1090-7807\(03\)00236-2](https://doi.org/10.1016/S1090-7807(03)00236-2).
- [140] Hiroshi Hirata et al. 'Nonequivalent Spectra of Unpaired Electrons in Field and Frequency Modulation'. In: *Journal of Magnetic Resonance* 168.2 (2004), pp. 252–258. DOI: [10.1016/j.jmr.2004.03.014](https://doi.org/10.1016/j.jmr.2004.03.014).
- [141] Albert Neuberger and Laurens L. M. van Deenen. *Modern Physical Methods in Biochemistry. Part A*. Amsterdam, New York: Elsevier ; Sole distributors for the USA and Canada, Elsevier Science Pub. Co., 1985. ISBN: 978-0-444-80649-9.
- [142] Moritz Kälin, Igor Gromov and Arthur Schweiger. 'The Continuous Wave Electron Paramagnetic Resonance Experiment Revisited'. In: *Journal of Magnetic Resonance* 160.2 (2003), pp. 166–182. DOI: [10.1016/S1090-7807\(02\)00186-6](https://doi.org/10.1016/S1090-7807(02)00186-6).
- [143] James S. Hyde et al. 'Microwave Frequency Modulation in CW EPR at W-band Using a Loop-Gap Resonator'. In: *Journal of Magnetic Resonance* 185.2 (2007), pp. 259–263. DOI: [10.1016/j.jmr.2007.01.002](https://doi.org/10.1016/j.jmr.2007.01.002).
- [144] Daniel Abou-Ras, Thomas Kirchartz and Uwe Rau, eds. *Advanced Characterization Techniques for Thin Film Solar Cells*. Wiley-VCH Verlag GmbH & Co. KGaA, 2011. DOI: [10.1002/9783527636280](https://doi.org/10.1002/9783527636280).

- [145] Benedikt Schleckner et al. 'Towards Low-Cost, High-Sensitivity Point-of-Care Diagnostics Using VCO-based ESR-on-a-chip Detectors'. In: *IEEE Sensors Journal* (2018), pp. 1–1. DOI: [10.1109/jsen.2018.2875767](https://doi.org/10.1109/jsen.2018.2875767).
- [146] Floyd M Gardner. *Phase-lock Techniques*. John Wiley & Sons, 2005.
- [147] P. Kinget. 'Amplitude Detection inside CMOS LC Oscillators'. In: *2006 IEEE International Symposium on Circuits and Systems*. IEEE, 2006. DOI: [10.1109/ISCAS.2006.1693791](https://doi.org/10.1109/ISCAS.2006.1693791).
- [148] A. Chu, B. Schleckner and J. Anders. 'Transistor-Level Simulation of LC-tank VCO Electron Spin Resonance Detectors'. In: *ANALOG 2018; 16th GMM/ITG-Symposium*. 2018, pp. 1–2.
- [149] C. F. Koelsch. 'Syntheses with Triarylvinylmagnesium Bromides.  $\alpha,\gamma$ -Bisdiphenylene- $\beta$ -phenylallyl, a Stable Free Radical'. In: *Journal of the American Chemical Society* 79.16 (1957), pp. 4439–4441. DOI: [10.1021/ja01573a053](https://doi.org/10.1021/ja01573a053).
- [150] Virginia Meyer, Sandra S. Eaton and Gareth R. Eaton. 'X-Band Electron Spin Relaxation Times for Four Aromatic Radicals in Fluid Solution and Comparison with Other Organic Radicals'. In: *Applied Magnetic Resonance* 45.10 (2014), pp. 993–1007. DOI: [10.1007/s00723-014-0579-6](https://doi.org/10.1007/s00723-014-0579-6).
- [151] M. Bennati et al. 'Pulsed Electron-Nuclear Double Resonance (ENDOR) at 140 GHz'. In: *Journal of Magnetic Resonance* 138.2 (1999), pp. 232–243. DOI: [10.1006/jmre.1999.1727](https://doi.org/10.1006/jmre.1999.1727).
- [152] C. Durkan and M. E. Welland. 'Electronic Spin Detection in Molecules Using Scanning-Tunneling- Microscopy-Assisted Electron-Spin Resonance'. In: *Applied Physics Letters* 80.3 (2002), pp. 458–460. DOI: [10.1063/1.1434301](https://doi.org/10.1063/1.1434301).
- [153] Daniella Goldfarb et al. 'HYSCORE and DEER with an Upgraded 95GHz Pulse EPR Spectrometer'. In: *Journal of Magnetic Resonance* 194.1 (2008), pp. 8–15. DOI: [10.1016/j.jmr.2008.05.019](https://doi.org/10.1016/j.jmr.2008.05.019).
- [154] Nagao Azuma, Takehiro Ozawa and Jun Yamauchi. 'Molecular and Crystal Structures of Complexes of Stable Free Radical BDPA with Benzene and Acetone'. In: *Bulletin of the Chemical Society of Japan* 67.1 (1994), pp. 31–38. DOI: [10.1246/bcsj.67.31](https://doi.org/10.1246/bcsj.67.31).
- [155] *BDPA Complex with Benzene(1:1), Free Radical* 35585-94-5. URL: <https://www.sigmaaldrich.com/DE/de/product/aldrich/152560> (visited on 07/11/2023).
- [156] J. P. Goldsborough, M. Mandel and G. E. Pake. 'Influence of Exchange Interaction on Paramagnetic Relaxation Times'. In: *Physical Review Letters* 4.1 (1960), pp. 13–15. DOI: [10.1103/PhysRevLett.4.13](https://doi.org/10.1103/PhysRevLett.4.13).

- [157] Deborah G. Mitchell et al. 'Electron Spin Relaxation and Heterogeneity of the 1:1  $\alpha,\gamma$ -Bisdiphenylene- $\beta$ -phenylallyl (BDPA) / Benzene Complex'. In: *The Journal of Physical Chemistry B* 115.24 (2011), pp. 7986–7990. DOI: [10.1021/jp201978w](https://doi.org/10.1021/jp201978w).
- [158] J. Krzystek et al. 'DPPH as a Standard for High-Field EPR'. In: *Journal of Magnetic Resonance* 125.1 (1997), pp. 207–211. DOI: [10.1006/jmre.1996.1098](https://doi.org/10.1006/jmre.1996.1098).
- [159] N. D. Yordanov. 'Is Our Knowledge about the Chemical and Physical Properties of DPPH Enough to Consider It as a Primary Standard for Quantitative EPR Spectrometry'. In: *Applied Magnetic Resonance* 10.1 (1996), pp. 339–350. DOI: [10.1007/BF03163117](https://doi.org/10.1007/BF03163117).
- [160] C. T. Kiers et al. 'The Crystal Structure of a 2,2-Diphenyl-1-Picrylhydrazyl (DPPH) Modification'. In: *Acta Crystallographica Section B: Structural Crystallography and Crystal Chemistry* 32.8 (8 1976), pp. 2297–2305. DOI: [10.1107/S0567740876007632](https://doi.org/10.1107/S0567740876007632).
- [161] Donald Elmer. Williams. 'Crystal Structure of 2,2-Diphenyl-1-Picrylhydrazyl Free Radical'. In: *Journal of the American Chemical Society* 89.17 (1967), pp. 4280–4287. DOI: [10.1021/ja00993a005](https://doi.org/10.1021/ja00993a005).
- [162] Hong Wang et al. 'Crystal and Molecular Structures of Two Polymorphs of 2,2-Di(p-Nitrophenyl)-1-Picrylhydrazine Dichloromethane,  $C_{18}H_{11}N_7O_{10} \cdot CH_2Cl_2$ '. In: *Canadian Journal of Chemistry* 69.8 (1991), pp. 1306–1314. DOI: [10.1139/v91-194](https://doi.org/10.1139/v91-194).
- [163] Hong Wang et al. 'Structural Studies of 2,2-Diphenyl-1-picrylhydrazine: A Clathrate Forming Compound'. In: *Journal of inclusion phenomena and molecular recognition in chemistry* 10.2 (1991), pp. 203–217. DOI: [10.1007/BF01066204](https://doi.org/10.1007/BF01066204).
- [164] *2,2-Diphenyl-1-picrylhydrazyl 1898-66-4*. URL: <https://www.sigmaaldrich.com/DE/en/product/aldrich/d9132> (visited on 07/11/2023).
- [165] Walther Fuhs. 'Hydrogenated Amorphous Silicon - Material Properties and Device Applications'. In: *Charge Transport in Disordered Solids with Applications in Electronics*. Ed. by S. Baranovski. Chichester: John Wiley & Sons, Ltd, 2006. ISBN: 0-470-09505-9.
- [166] M. H. Brodsky and R. S. Title. 'Electron Spin Resonance in Amorphous Silicon, Germanium, and Silicon Carbide'. In: *Physical Review Letters* 23.11 (1969), pp. 581–585. DOI: [10.1103/PhysRevLett.23.581](https://doi.org/10.1103/PhysRevLett.23.581).
- [167] Martin Stutzmann and David K. Biegelsen. 'Microscopic Nature of Coordination Defects in Amorphous Silicon'. In: *Physical Review B* 40.14 (1989), pp. 9834–9840. DOI: [10.1103/PhysRevB.40.9834](https://doi.org/10.1103/PhysRevB.40.9834).

- [168] D. Amkreutz et al. 'Electron-Beam Crystallized Large Grained Silicon Solar Cell on Glass Substrate'. In: *Progress in Photovoltaics: Research and Applications* 19.8 (2011), pp. 937–945. DOI: [10.1002/pip.1098](https://doi.org/10.1002/pip.1098).
- [169] Anders Lund et al. 'Relaxation-Time Determination from Continuous-Microwave Saturation of EPR Spectra'. In: *Radiation Research* 172.6 (2009), pp. 753–760. DOI: [10.1667/rr1890.1](https://doi.org/10.1667/rr1890.1).
- [170] Bruker. *EPR Resonators*. manual. Bruker Biospin GmbH.
- [171] Enrica Bordignon. 'EPR Spectroscopy of Nitroxide Spin Probes'. In: *eMagRes*. Ed. by Roderick Wasylshen. John Wiley & Sons, Ltd, 2017, pp. 235–253. ISBN: 978-0-470-03459-0. DOI: [10.1002/9780470034590.emrstm1513](https://doi.org/10.1002/9780470034590.emrstm1513).
- [172] M. Francesca Ottaviani, Giacomo Martini and Laura Nuti. 'Nitrogen Hyperfine Splitting of Nitroxide Solutions: Differently Structured and Charged Nitroxides as Probes of Environmental Properties'. In: *Magnetic resonance in chemistry* 25.10 (1987), pp. 897–904. DOI: [10.1002/mrc.1260251014](https://doi.org/10.1002/mrc.1260251014).
- [173] Ashley Clark et al. 'Dependence of Electron Paramagnetic Resonance Spectral Lineshapes on Molecular Tumbling: Nitroxide Radical in Water:Glycerol Mixtures'. In: *Concepts in Magnetic Resonance Part A* 45A.5 (2016), e21423. DOI: [10.1002/cmr.a.21423](https://doi.org/10.1002/cmr.a.21423).
- [174] L. G. Stoodley. 'The Sensitivity of Microwave Electron Spin Resonance Spectrometers for Use with Aqueous Solutions†'. In: *Journal of Electronics and Control* 14.5 (1963), pp. 531–546. DOI: [10.1080/00207216308937527](https://doi.org/10.1080/00207216308937527).
- [175] Daksha P Dalal, Sandra S Eaton and Gareth R Eaton. 'The Effects of Lossy Solvents on Quantitative EPR Studies'. In: *Journal of Magnetic Resonance (1969)* 44.3 (1981), pp. 415–428. DOI: [10.1016/0022-2364\(81\)90276-6](https://doi.org/10.1016/0022-2364(81)90276-6).
- [176] Minoru Sueki et al. 'Impact of High-Dielectric-Loss Materials on the Microwave Field in EPR Experiments'. In: *Journal of Magnetic Resonance, Series A* 118.2 (1996), pp. 173–188. DOI: [10.1006/jmra.1996.0025](https://doi.org/10.1006/jmra.1996.0025).
- [177] Richard R. Mett and James S. Hyde. 'Aqueous Flat Cells Perpendicular to the Electric Field for Use in Electron Paramagnetic Resonance Spectroscopy'. In: *Journal of Magnetic Resonance* 165.1 (2003), pp. 137–152. DOI: [10.1016/S1090-7807\(03\)00275-1](https://doi.org/10.1016/S1090-7807(03)00275-1).
- [178] A. M. Portis. 'Electronic Structure of F Centers: Saturation of the Electron Spin Resonance'. In: *Physical Review* 91.5 (1953), pp. 1071–1078. DOI: [10.1103/PhysRev.91.1071](https://doi.org/10.1103/PhysRev.91.1071).
- [179] Kazuhisa Tomita. 'A General Theory of Magnetic Resonance Saturation'. In: *Progress of Theoretical Physics* 19.5 (1958), pp. 541–580. DOI: [10.1143/PTP.19.541](https://doi.org/10.1143/PTP.19.541).

- [180] James S. Hyde. 'Saturation of the Magnetic Resonance Absorption in Dilute Inhomogeneously Broadened Systems'. In: *Physical Review* 119.5 (1960), pp. 1492–1495. DOI: [10.1103/PhysRev.119.1492](https://doi.org/10.1103/PhysRev.119.1492).
- [181] P. Höfer et al. *The SuperQ-FT Accessory*. 152/153. Rheinstetten, Germany: EPR Division, Bruker Biospin GmbH, 2003, pp. 37–43.
- [182] G. Breit and I. I. Rabi. 'Measurement of Nuclear Spin'. In: *Physical Review* 38.11 (1931), pp. 2082–2083. DOI: [10.1103/PhysRev.38.2082.2](https://doi.org/10.1103/PhysRev.38.2082.2).
- [183] F. Marin, A. Rohatgi and S. Charlot. *WebPlotDigitizer, a Polyvalent and Free Software to Extract Spectra from Old Astronomical Publications: Application to Ultraviolet Spectropolarimetry*. 2017. DOI: [10.48550/arXiv.1708.02025](https://doi.org/10.48550/arXiv.1708.02025). Pre-published.
- [184] Gabriele Gualco et al. 'Cryogenic Single-Chip Electron Spin Resonance Detector'. In: *Journal of Magnetic Resonance* 247 (2014), pp. 96–103. DOI: [10.1016/j.jmr.2014.08.013](https://doi.org/10.1016/j.jmr.2014.08.013).
- [185] Alessandro V. Matheoud et al. 'Single-Chip Electron Spin Resonance Detectors Operating at 50 GHz, 92 GHz, and 146 GHz'. In: *Journal of Magnetic Resonance* 278 (2017), pp. 113–121. DOI: [10.1016/j.jmr.2017.03.013](https://doi.org/10.1016/j.jmr.2017.03.013).
- [186] Alessandro V. Matheoud, Nergiz Sahin and Giovanni Boero. 'A Single Chip Electron Spin Resonance Detector Based on a Single High Electron Mobility Transistor'. In: *Journal of Magnetic Resonance* 294 (2018), pp. 59–70. DOI: [10.1016/j.jmr.2018.07.002](https://doi.org/10.1016/j.jmr.2018.07.002).
- [187] Piotr Fajer and Derek Marsh. 'Microwave and Modulation Field Inhomogeneities and the Effect of Cavity Q in Saturation Transfer ESR Spectra. Dependence on Sample Size'. In: *Journal of Magnetic Resonance (1969)* 49.2 (1982), pp. 212–224. DOI: [10.1016/0022-2364\(82\)90185-8](https://doi.org/10.1016/0022-2364(82)90185-8).
- [188] A. J. Hoff. *Advanced EPR: Applications in Biology and Biochemistry*. Elsevier, 1989. 946 pp. ISBN: 978-0-444-88050-5.
- [189] Felipe Chen, Carlos F. O. Graeff and Oswaldo Baffa. 'K-Band EPR Dosimetry: Small-Field Beam Profile Determination with Miniature Alanine Dosimeter'. In: *Applied Radiation and Isotopes*. Proceedings of the 6th International Symposium on ESR Dosimetry and Applications 62.2 (2005), pp. 267–271. DOI: [10.1016/j.apradiso.2004.08.036](https://doi.org/10.1016/j.apradiso.2004.08.036).
- [190] Silvio Künstner. 'Characterisation of Field- and Frequency-Swept EPR-on-a-Chip'. MA thesis. Berlin: Freie Universität Berlin, 2017.

- [191] Ke Jing et al. 'Broadband Electron Paramagnetic Resonance Spectrometer from 1 to 15 GHz Using Metallic Coplanar Waveguide'. In: *Review of Scientific Instruments* 90.12 (2019), p. 125109. DOI: [10.1063/1.5119333](https://doi.org/10.1063/1.5119333).
- [192] Dijana Žilić et al. 'Single Crystals of DPPH Grown from Diethyl Ether and Carbon Disulfide Solutions – Crystal Structures, IR, EPR and Magnetization Studies'. In: *Journal of Magnetic Resonance* 207.1 (2010), pp. 34–41. DOI: [10.1016/j.jmr.2010.08.005](https://doi.org/10.1016/j.jmr.2010.08.005).
- [193] G. Boero et al. 'Room Temperature Strong Coupling between a Microwave Oscillator and an Ensemble of Electron Spins'. In: *Journal of Magnetic Resonance* 231 (2013), pp. 133–140. DOI: [10.1016/j.jmr.2013.04.004](https://doi.org/10.1016/j.jmr.2013.04.004).
- [194] P. Neugebauer et al. 'Ultra-Broadband EPR Spectroscopy in Field and Frequency Domains'. In: *Physical Chemistry Chemical Physics* 20.22 (2018), pp. 15528–15534. DOI: [10.1039/C7CP07443C](https://doi.org/10.1039/C7CP07443C).
- [195] Alexander Schnegg et al. 'Frequency Domain Fourier Transform THz-EPR on Single Molecule Magnets Using Coherent Synchrotron Radiation'. In: *Physical Chemistry Chemical Physics* 11.31 (2009), pp. 6820–6825. DOI: [10.1039/B905745E](https://doi.org/10.1039/B905745E).
- [196] Alexander Schnegg. 'Very-High-Frequency EPR'. In: *eMagRes*. Ed. by Roderick Wasylshen. John Wiley & Sons, Ltd, 2017, pp. 115–131. ISBN: 978-0-470-03459-0. DOI: [10.1002/9780470034590.emrstm1526](https://doi.org/10.1002/9780470034590.emrstm1526).
- [197] Jeffrey B. Fortin and Toh-Ming Lu. *Chemical Vapor Deposition Polymerization: The Growth and Properties of Parylene Thin Films*. Springer Science & Business Media, 2003. 128 pp. ISBN: 978-1-4020-7688-6.
- [198] *Magnettech ESR5000*. URL: <https://www.bruker.com/de/products-and-solutions/mr/epr-instruments/magnettechesr5000.html> (visited on 20/03/2024).
- [199] George A. Rinard et al. 'Frequency Dependence of EPR Sensitivity'. In: *EPR: Instrumental Methods*. Ed. by Lawrence J. Berliner and Christopher J. Bender. Biological Magnetic Resonance. Boston, MA: Springer US, 2004, pp. 115–154. ISBN: 978-1-4419-8951-2. DOI: [10.1007/978-1-4419-8951-2\\_3](https://doi.org/10.1007/978-1-4419-8951-2_3).
- [200] Yusuke Makino et al. 'Simplifying Quantitative Measurement of Free Radical Species Using an X-band EPR Spectrometer'. In: *Journal of Clinical Biochemistry and Nutrition* 70.3 (2022), pp. 213–221. DOI: [10.3164/jcbn.21-83](https://doi.org/10.3164/jcbn.21-83).



- [201] Muhammad Kamran et al. 'Semi-Automated EPR System for Direct Monitoring the Photocatalytic Activity of TiO<sub>2</sub> Suspension Using TEMPOL Model Compound'. In: *Photochemical & Photobiological Sciences* 21.12 (2022), pp. 2071–2083. DOI: [10.1007/s43630-022-00279-z](https://doi.org/10.1007/s43630-022-00279-z).
- [202] Kent R. Thurber, Wai-Ming Yau and Robert Tycko. 'Low-Temperature Dynamic Nuclear Polarization at 9.4T with a 30mW Microwave Source'. In: *Journal of Magnetic Resonance* 204.2 (2010), pp. 303–313. DOI: [10.1016/j.jmr.2010.03.016](https://doi.org/10.1016/j.jmr.2010.03.016).
- [203] J. Barthel et al. 'Dielectric Spectra of Some Common Solvents in the Microwave Region. Water and Lower Alcohols'. In: *Chemical Physics Letters* 165.4 (1990), pp. 369–373. DOI: [10.1016/0009-2614\(90\)87204-5](https://doi.org/10.1016/0009-2614(90)87204-5).
- [204] George A. Rinard et al. 'Dispersion and Superheterodyne EPR Using a Bimodal Resonator'. In: *Journal of Magnetic Resonance, Series A* 122.1 (1996), pp. 58–63. DOI: [10.1006/jmra.1996.0174](https://doi.org/10.1006/jmra.1996.0174).
- [205] Fan Cheng et al. *Development of an Oil Degradation Sensor Based on Detection of Free Radicals*. SAE Technical Paper 2019-01-2299. Warrendale, PA: SAE International, 2019. DOI: [10.4271/2019-01-2299](https://doi.org/10.4271/2019-01-2299).
- [206] Fan Cheng et al. 'A 2.0-GHz Compact ESR Spectrometer for Monitoring Automobile Lubrication Oil Degradation'. In: *Journal of Magnetic Resonance* 332 (2021), p. 107081. DOI: [10.1016/j.jmr.2021.107081](https://doi.org/10.1016/j.jmr.2021.107081).
- [207] Harold M. Swartz et al. 'Clinical Applications of EPR: Overview and Perspectives'. In: *NMR in Biomedicine* 17.5 (2004), pp. 335–351. DOI: [10.1002/nbm.911](https://doi.org/10.1002/nbm.911).
- [208] Philip E. Schaner et al. 'OxyChip Implantation and Subsequent Electron Paramagnetic Resonance Oximetry in Human Tumors Is Safe and Feasible: First Experience in 24 Patients'. In: *Frontiers in Oncology* 10 (2020). DOI: [10.3389/fonc.2020.572060](https://doi.org/10.3389/fonc.2020.572060).
- [209] Simona Mrakic-Sposta et al. 'A Quantitative Method to Monitor Reactive Oxygen Species Production by Electron Paramagnetic Resonance in Physiological and Pathological Conditions'. In: *Oxidative Medicine and Cellular Longevity* 2014 (2014), e306179. DOI: [10.1155/2014/306179](https://doi.org/10.1155/2014/306179).
- [210] Wilfred R. Hagen. 'EPR Spectroscopy of Complex Biological Iron–Sulfur Systems'. In: *JBIC Journal of Biological Inorganic Chemistry* 23.4 (2018), pp. 623–634. DOI: [10.1007/s00775-018-1543-y](https://doi.org/10.1007/s00775-018-1543-y).
- [211] Malin Persson et al. 'Comparison of Electron Paramagnetic Resonance Methods to Determine Distances between Spin Labels on Human Carbonic Anhydrase II'. In: *Biophysical Journal* 80.6 (2001), pp. 2886–2897. DOI: [10.1016/S0006-3495\(01\)76254-6](https://doi.org/10.1016/S0006-3495(01)76254-6).



- [212] Kathy A. Rages, Robert E. Sawyer and Edward B. Hale. 'Properties of Microwave Cavities Containing Magnetic Resonant Samples'. In: *Review of Scientific Instruments* 44.7 (2003), pp. 830–834. DOI: [10.1063/1.1686258](https://doi.org/10.1063/1.1686258).
- [213] James S. Hyde, Jason W. Sidabras and Richard R. Mett. 'Uniform Field Resonators for EPR Spectroscopy: A Review'. In: *Cell biochemistry and biophysics* 77.1 (2019), pp. 3–14. DOI: [10.1007/s12013-018-0845-6](https://doi.org/10.1007/s12013-018-0845-6).
- [214] Nicola D. Yordanov, Borjana Mladenova and Pavel Petkov. 'Studies on the Uncertainties in Quantitative EPR Estimations Due to the Construction of the Cavities Used'. In: *Analytica chimica acta* 453.1 (2002), pp. 155–162. DOI: [10.1016/S0003-2670\(01\)01487-8](https://doi.org/10.1016/S0003-2670(01)01487-8).
- [215] W. Froncisz, T. Oles and James S. Hyde. 'Q-Band Loop-Gap Resonator'. In: *Review of scientific instruments* 57.6 (1986), pp. 1095–1099. DOI: [10.1063/1.1138663](https://doi.org/10.1063/1.1138663).
- [216] Jason W. Sidabras et al. 'Multipurpose EPR Loop-Gap Resonator and Cylindrical TE<sub>011</sub> Cavity for Aqueous Samples at 94 GHz'. In: *Review of scientific instruments* 78.3 (2007), p. 034701. DOI: [10.1063/1.2709746](https://doi.org/10.1063/1.2709746).
- [217] Andrin Doll et al. 'Adiabatic and Fast Passage Ultra-Wideband Inversion in Pulsed EPR'. In: *Journal of Magnetic Resonance* 230 (2013), pp. 27–39. DOI: [10.1016/j.jmr.2013.01.002](https://doi.org/10.1016/j.jmr.2013.01.002).
- [218] Philipp E. Spindler et al. 'Perspectives of Shaped Pulses for EPR Spectroscopy'. In: *Journal of Magnetic Resonance* 280 (2017), pp. 30–45. DOI: [10.1016/j.jmr.2017.02.023](https://doi.org/10.1016/j.jmr.2017.02.023).
- [219] Nandita Abhyankar et al. 'Recent Advances in Microresonators and Supporting Instrumentation for Electron Paramagnetic Resonance Spectroscopy'. In: *Review of Scientific Instruments* 93.10 (2022), p. 101101. DOI: [10.1063/5.0097853](https://doi.org/10.1063/5.0097853).
- [220] Silvio Künstner et al. 'Microwave Field Mapping for EPR-on-a-chip Experiments'. In: *Science Advances* 10.33 (2024), ead05467. DOI: [10.1126/sciadv.ado5467](https://doi.org/10.1126/sciadv.ado5467).
- [221] Giovanni Boero. 'Integrated NMR Probe for Magnetometry'. École polytechnique fédérale de Lausanne, 2000. DOI: [10.5075/epfl-thesis-2211](https://doi.org/10.5075/epfl-thesis-2211).
- [222] Milan Mazur et al. 'Analysis of the Radial and Longitudinal Effects of a Planar Sample in a Single TE<sub>102</sub> Rectangular Electron Paramagnetic Resonance (EPR) Cavity'. In: *Analytica Chimica Acta* 526.2 (2004), pp. 163–176. DOI: [10.1016/j.aca.2004.09.062](https://doi.org/10.1016/j.aca.2004.09.062).

- [223] Alessandro V. Matheoud, Nergiz Sahin Solmaz and Giovanni Boero. 'A Low-Power Microwave HEMT LC Oscillator Operating down to 1.4 K'. In: *IEEE Transactions on Microwave Theory and Techniques* 67.7 (2019), pp. 2782–2792. DOI: [10.1109/tmtt.2019.2916552](https://doi.org/10.1109/tmtt.2019.2916552).
- [224] N. Bloembergen, E. M. Purcell and R. V. Pound. 'Relaxation Effects in Nuclear Magnetic Resonance Absorption'. In: *Physical Review* 73.7 (1948), pp. 679–712. DOI: [10.1103/PhysRev.73.679](https://doi.org/10.1103/PhysRev.73.679).
- [225] E. E. Salpeter. 'Nuclear Induction Signals for Long Relaxation Times'. In: *Proceedings of the Physical Society. Section A* 63.4 (1950), pp. 337–349. DOI: [10.1088/0370-1298/63/4/303](https://doi.org/10.1088/0370-1298/63/4/303).
- [226] R. R. Ernst and W. A. Anderson. 'Sensitivity Enhancement in Magnetic Resonance. II. Investigation of Intermediate Passage Conditions'. In: *Review of Scientific Instruments* 36.12 (1965), pp. 1696–1706. DOI: [10.1063/1.1719444](https://doi.org/10.1063/1.1719444).
- [227] Richard R. Ernst. 'Sensitivity Enhancement in Magnetic Resonance'. In: *Advances in Magnetic and Optical Resonance*. Ed. by John S. Waugh. Vol. 2. Academic Press, 1966, pp. 1–135. DOI: [10.1016/B978-1-4832-3115-0.50008-9](https://doi.org/10.1016/B978-1-4832-3115-0.50008-9).
- [228] Raj K Gupta, James A Ferretti and Edwin D Becker. 'Rapid Scan Fourier Transform NMR Spectroscopy'. In: *Journal of Magnetic Resonance* (1969) 13.3 (1974), pp. 275–290. DOI: [10.1016/0022-2364\(74\)90022-5](https://doi.org/10.1016/0022-2364(74)90022-5).
- [229] A. M. Portis. 'Rapid Passage Effects in Electron Spin Resonance'. In: *Physical Review* 100.4 (1955), pp. 1219–1221. DOI: [10.1103/PhysRev.100.1219](https://doi.org/10.1103/PhysRev.100.1219).
- [230] R. Beeler et al. 'Rapid-Passage Effects in Electron Spin Resonance'. In: *Physical Review* 102.1 (1956), pp. 295–295. DOI: [10.1103/PhysRev.102.295](https://doi.org/10.1103/PhysRev.102.295).
- [231] James R. Harbridge et al. 'Enhanced Signal Intensities Obtained by Out-of-Phase Rapid-Passage EPR for Samples with Long Electron Spin Relaxation Times'. In: *Journal of Magnetic Resonance* 156.1 (2002), pp. 41–51. DOI: [10.1006/jmre.2002.2526](https://doi.org/10.1006/jmre.2002.2526).
- [232] James W. Stoner et al. 'Direct-Detected Rapid-Scan EPR at 250 MHz'. In: *Journal of Magnetic Resonance* 170.1 (2004), pp. 127–135. DOI: [10.1016/j.jmr.2004.06.008](https://doi.org/10.1016/j.jmr.2004.06.008).
- [233] Deborah G. Mitchell et al. 'Comparison of Continuous Wave, Spin Echo, and Rapid Scan EPR of Irradiated Fused Quartz'. In: *Radiation Measurements* 46.9 (2011), pp. 993–996. DOI: [10.1016/j.radmeas.2011.03.035](https://doi.org/10.1016/j.radmeas.2011.03.035).
- [234] Deborah G. Mitchell et al. 'X-Band Rapid-Scan EPR of Nitroxyl Radicals'. In: *Journal of Magnetic Resonance* 214 (2012), pp. 221–226. DOI: [10.1016/j.jmr.2011.11.007](https://doi.org/10.1016/j.jmr.2011.11.007).

- [235] Richard W. Quine, Tomasz Czechowski and Gareth R. Eaton. 'A Linear Magnetic Field Scan Driver'. In: *Concepts in Magnetic Resonance Part B: Magnetic Resonance Engineering* 35B.1 (2009), pp. 44–58. DOI: [10.1002/cmrb.20128](https://doi.org/10.1002/cmrb.20128).
- [236] Richard W. Quine et al. 'A Resonated Coil Driver for Rapid Scan EPR'. In: *Concepts in Magnetic Resonance Part B: Magnetic Resonance Engineering* 41B.4 (2012), pp. 95–110. DOI: [10.1002/cmrb.21222](https://doi.org/10.1002/cmrb.21222).
- [237] Janhavi P. Joshi et al. 'Rapid-Scan EPR with Triangular Scans and Fourier Deconvolution to Recover the Slow-Scan Spectrum'. In: *Journal of Magnetic Resonance* 175.1 (2005), pp. 44–51. DOI: [10.1016/j.jmr.2005.03.013](https://doi.org/10.1016/j.jmr.2005.03.013).
- [238] Mark Tseitlin et al. 'Corrections for Sinusoidal Background and Non-Orthogonality of Signal Channels in Sinusoidal Rapid Magnetic Field Scans'. In: *Journal of Magnetic Resonance* 223 (2012), pp. 80–84. DOI: [10.1016/j.jmr.2012.07.023](https://doi.org/10.1016/j.jmr.2012.07.023).
- [239] Mark Tseitlin et al. 'Background Removal Procedure for Rapid Scan EPR'. In: *Journal of Magnetic Resonance* 196.1 (2009), pp. 48–53. DOI: [10.1016/j.jmr.2008.10.012](https://doi.org/10.1016/j.jmr.2008.10.012).
- [240] Deborah G. Mitchell et al. 'Use of Rapid-Scan EPR to Improve Detection Sensitivity for Spin-Trapped Radicals'. In: *Biophysical Journal* 105.2 (2013), pp. 338–342. DOI: [10.1016/j.bpj.2013.06.005](https://doi.org/10.1016/j.bpj.2013.06.005).
- [241] Yilin Shi et al. 'Rapid Scan Electron Paramagnetic Resonance at 1.0 GHz of Defect Centers in  $\gamma$ -Irradiated Organic Solids'. In: *Radiation Measurements* 85 (2016), pp. 57–63. DOI: [10.1016/j.radmeas.2015.12.011](https://doi.org/10.1016/j.radmeas.2015.12.011).
- [242] Deborah G. Mitchell et al. 'X-Band Rapid-Scan EPR of Samples with Long Electron Spin Relaxation Times: A Comparison of Continuous Wave, Pulse and Rapid-Scan EPR'. In: *Molecular Physics* 111.18-19 (2013), pp. 2664–2673. DOI: [10.1080/00268976.2013.792959](https://doi.org/10.1080/00268976.2013.792959).
- [243] J. P. Joshi, G. R. Eaton and S. S. Eaton. 'Impact of Resonator on Direct-Detected Rapid-Scan EPR at 9.8 GHz'. In: *Applied Magnetic Resonance* 28.3 (2005), pp. 239–249. DOI: [10.1007/BF03166759](https://doi.org/10.1007/BF03166759).
- [244] Zhelin Yu et al. 'Field-Stepped Direct Detection Electron Paramagnetic Resonance'. In: *Journal of Magnetic Resonance* 258 (2015), pp. 58–64. DOI: [10.1016/j.jmr.2015.06.011](https://doi.org/10.1016/j.jmr.2015.06.011).
- [245] James S. Hyde et al. 'Moving Difference (MDIFF) Non-Adiabatic Rapid Sweep (NARS) EPR of Copper(II)'. In: *Journal of Magnetic Resonance* 236 (2013), pp. 15–25. DOI: [10.1016/j.jmr.2013.08.004](https://doi.org/10.1016/j.jmr.2013.08.004).

- [246] Joseph McPeak et al. 'Electron Spin Relaxation of Tb<sup>3+</sup> and Tm<sup>3+</sup> Ions'. In: *Applied Magnetic Resonance* 51.9 (2020), pp. 961–976. DOI: [10.1007/s00723-020-01262-6](https://doi.org/10.1007/s00723-020-01262-6).
- [247] Michele Segantini et al. 'Compact Electron Paramagnetic Resonance on a Chip Spectrometer Using a Single Sided Permanent Magnet'. In: *ACS Sensors* (2024). DOI: [10.1021/acssensors.4c00788](https://doi.org/10.1021/acssensors.4c00788).
- [248] SS Eaton et al. 'Multifrequency Electron Paramagnetic Resonance'. In: ed. by Sushil K. Misra. Wiley-VCH Verlag GmbH & Co. KGaA, 2014, pp. 3–64. DOI: [10.1002/9783527672431](https://doi.org/10.1002/9783527672431).
- [249] P. Welch. 'The Use of Fast Fourier Transform for the Estimation of Power Spectra: A Method Based on Time Averaging over Short, Modified Periodograms'. In: *IEEE Transactions on Audio and Electroacoustics* 15.2 (1967), pp. 70–73. DOI: [10.1109/TAU.1967.1161901](https://doi.org/10.1109/TAU.1967.1161901).
- [250] Mark Tseitlin et al. 'Combining Absorption and Dispersion Signals to Improve Signal-to-Noise for Rapid-Scan EPR Imaging'. In: *Journal of Magnetic Resonance* 203.2 (2010), pp. 305–310. DOI: [10.1016/j.jmr.2010.01.013](https://doi.org/10.1016/j.jmr.2010.01.013).
- [251] Mark Tseytlin. 'Full Cycle Rapid Scan EPR Deconvolution Algorithm'. In: *Journal of Magnetic Resonance* 281 (2017), pp. 272–278. DOI: [10.1016/j.jmr.2017.06.008](https://doi.org/10.1016/j.jmr.2017.06.008).
- [252] Piergiorgio Alotto, Massimo Guarnieri and Federico Moro. 'Redox Flow Batteries for the Storage of Renewable Energy: A Review'. In: *Renewable and Sustainable Energy Reviews* 29 (2014), pp. 325–335. DOI: [10.1016/j.rser.2013.08.001](https://doi.org/10.1016/j.rser.2013.08.001).
- [253] Catalina Spataru et al. '31 - Energy Storage Worldwide'. In: *Storing Energy (Second Edition)*. Ed. by Trevor M. Letcher. Elsevier, 2022, pp. 753–767. ISBN: 978-0-12-824510-1. DOI: [10.1016/B978-0-12-824510-1.00029-5](https://doi.org/10.1016/B978-0-12-824510-1.00029-5).
- [254] Catarina R. Matos, Patrícia P. Silva and Júlio F. Carneiro. 'Overview of Compressed Air Energy Storage Projects and Regulatory Framework for Energy Storage'. In: *Journal of Energy Storage* 55 (2022), p. 105862. DOI: [10.1016/j.est.2022.105862](https://doi.org/10.1016/j.est.2022.105862).
- [255] Kyle Lourenssen et al. 'Vanadium Redox Flow Batteries: A Comprehensive Review'. In: *Journal of Energy Storage* 25 (2019), p. 100844. DOI: [10.1016/j.est.2019.100844](https://doi.org/10.1016/j.est.2019.100844).
- [256] Xiao-Zi Yuan et al. 'A Review of All-Vanadium Redox Flow Battery Durability: Degradation Mechanisms and Mitigation Strategies'. In: *International Journal of Energy Research* 43.13 (2019), pp. 6599–6638. DOI: [10.1002/er.4607](https://doi.org/10.1002/er.4607).
- [257] Nicola Poli et al. 'Novel Electrolyte Rebalancing Method for Vanadium Redox Flow Batteries'. In: *Chemical Engineering Journal* 405 (2021), p. 126583. DOI: [10.1016/j.cej.2020.126583](https://doi.org/10.1016/j.cej.2020.126583).

- [258] Maria Skyllas-Kazacos et al. 'Vanadium Electrolyte Studies for the Vanadium Redox Battery—A Review'. In: *ChemSusChem* 9.13 (2016), pp. 1521–1543. DOI: [10.1002/cssc.201600102](https://doi.org/10.1002/cssc.201600102).
- [259] Yu Shi et al. 'Recent Development of Membrane for Vanadium Redox Flow Battery Applications: A Review'. In: *Applied Energy* 238 (2019), pp. 202–224. DOI: [10.1016/j.apenergy.2018.12.087](https://doi.org/10.1016/j.apenergy.2018.12.087).
- [260] D. Schulte et al. 'Nafion Hybrid Membranes for Use in Redox Flow Batteries'. In: *Journal of The Electrochemical Society* 157.9 (2010), A989. DOI: [10.1149/1.3456625](https://doi.org/10.1149/1.3456625).
- [261] Kyeongmin Oh et al. 'Water Crossover Phenomena in All-Vanadium Redox Flow Batteries'. In: *Electrochimica Acta* 297 (2019), pp. 101–111. DOI: [10.1016/j.electacta.2018.11.151](https://doi.org/10.1016/j.electacta.2018.11.151).
- [262] Maria Skyllas-Kazacos and Michael Kazacos. 'State of Charge Monitoring Methods for Vanadium Redox Flow Battery Control'. In: *Journal of Power Sources* 196.20 (2011), pp. 8822–8827. DOI: [10.1016/j.jpowsour.2011.06.080](https://doi.org/10.1016/j.jpowsour.2011.06.080).
- [263] Thomas Puleston, Maria Serra and Ramon Costa-Castelló. 'Vanadium Redox Flow Battery Capacity Loss Mitigation Strategy Based on a Comprehensive Analysis of Electrolyte Imbalance Effects'. In: *Applied Energy* 355 (2024), p. 122271. DOI: [10.1016/j.apenergy.2023.122271](https://doi.org/10.1016/j.apenergy.2023.122271).
- [264] Beatriz Oraá-Poblete et al. 'Preconditioning Operation of Membraneless Vanadium Micro Redox Flow Batteries'. In: *Batteries & Supercaps* (2023), e202300367. DOI: [10.1002/batt.202300367](https://doi.org/10.1002/batt.202300367).
- [265] Che-Nan Sun et al. 'Hydrogen Evolution at the Negative Electrode of the All-Vanadium Redox Flow Batteries'. In: *Journal of Power Sources* 248 (2014), pp. 560–564. DOI: [10.1016/j.jpowsour.2013.09.125](https://doi.org/10.1016/j.jpowsour.2013.09.125).
- [266] M. Kazacos, M. Cheng and M. Skyllas-Kazacos. 'Vanadium Redox Cell Electrolyte Optimization Studies'. In: *Journal of Applied Electrochemistry* 20.3 (1990), pp. 463–467. DOI: [10.1007/BF01076057](https://doi.org/10.1007/BF01076057).
- [267] Nadeem Kausar, Asem Mousa and Maria Skyllas-Kazacos. 'The Effect of Additives on the High-Temperature Stability of the Vanadium Redox Flow Battery Positive Electrolytes'. In: *ChemElectroChem* 3.2 (2016), pp. 276–282. DOI: [10.1002/celec.201500453](https://doi.org/10.1002/celec.201500453).
- [268] Maria Skyllas-Kazacos et al. 'State of Charge of Redox Cell'. Pat. WO1990003666A1 (WO). Unisearch Limited. 1990.
- [269] Binyu Xiong et al. 'Extended Kalman Filter Method for State of Charge Estimation of Vanadium Redox Flow Battery Using Thermal-Dependent Electrical Model'. In: *Journal of Power Sources* 262 (2014), pp. 50–61. DOI: [10.1016/j.jpowsour.2014.03.110](https://doi.org/10.1016/j.jpowsour.2014.03.110).

- [270] Zhongbao Wei et al. 'Online State of Charge and Model Parameter Co-Estimation Based on a Novel Multi-Timescale Estimator for Vanadium Redox Flow Battery'. In: *Applied Energy* 172 (2016), pp. 169–179. DOI: [10.1016/j.apenergy.2016.03.103](https://doi.org/10.1016/j.apenergy.2016.03.103).
- [271] M. R. Mohamed, H. Ahmad and M. N. Abu Seman. 'Estimating the State-of-Charge of All-Vanadium Redox Flow Battery Using a Divided, Open-circuit Potentiometric Cell'. In: *Elektronika ir Elektrotechnika* 19.3 (3 2013), pp. 37–42. DOI: [10.5755/j01.eee.19.3.1623](https://doi.org/10.5755/j01.eee.19.3.1623).
- [272] Sara Corcuera and Maria Skyllas-Kazacos. 'State-of-Charge Monitoring and Electrolyte Rebalancing Methods for the Vanadium Redox Flow Battery'. In: *European Chemical Bulletin* 1.12 (2012), pp. 511–519. DOI: [10.17628/ECB.2012.1.5112012.26/02/2023](https://doi.org/10.17628/ECB.2012.1.5112012.26/02/2023).
- [273] F. Grossmith et al. 'Evaluation of Membranes for All-Vanadium Redox Cell'. In: *Stationary Energy Storage: Load Leveling and Remote Applications*. Landgrebe, A. R., Van Voorhees, S. L., Rand, D. J., Sen, R. K., Eds., 1988.
- [274] Dilong Liu et al. 'Improved Cycling Performance of 5 V Spinel  $\text{LiMn}_{1.5}\text{Ni}_{0.5}\text{O}_4$  by Amorphous  $\text{FePO}_4$  Coating'. In: *Journal of Power Sources* 219 (2012), pp. 333–338. DOI: [10.1016/j.jpowsour.2012.07.058](https://doi.org/10.1016/j.jpowsour.2012.07.058).
- [275] S. Rudolph et al. 'High Resolution State of Charge Monitoring of Vanadium Electrolytes with IR Optical Sensor'. In: *Journal of Electroanalytical Chemistry* 694 (2013), pp. 17–22. DOI: [10.1016/j.jelechem.2013.01.042](https://doi.org/10.1016/j.jelechem.2013.01.042).
- [276] Xiangrong Li et al. 'Investigation of the Use of Electrolyte Viscosity for Online State-of-Charge Monitoring Design in Vanadium Redox Flow Battery'. In: *Applied Energy* 211 (2018), pp. 1050–1059. DOI: [10.1016/j.apenergy.2017.12.009](https://doi.org/10.1016/j.apenergy.2017.12.009).
- [277] Bin Li et al. 'Capacity Decay Mechanism of Microporous Separator-Based All-Vanadium Redox Flow Batteries and Its Recovery'. In: *ChemSusChem* 7.2 (2014), pp. 577–584. DOI: [10.1002/cssc.201300706](https://doi.org/10.1002/cssc.201300706).
- [278] Zhongbao Wei et al. 'Adaptive Estimation of State of Charge and Capacity with Online Identified Battery Model for Vanadium Redox Flow Battery'. In: *Journal of Power Sources* 332 (2016), pp. 389–398. DOI: [10.1016/j.jpowsour.2016.09.123](https://doi.org/10.1016/j.jpowsour.2016.09.123).
- [279] Alejandro Clemente and Ramon Costa-Castelló. 'Redox Flow Batteries: A Literature Review Oriented to Automatic Control'. In: *Energies* 13.17 (17 2020), p. 4514. DOI: [10.3390/en13174514](https://doi.org/10.3390/en13174514).



- [280] Jamie S. Lawton et al. 'Qualitative Behavior of Vanadium Ions in Nafion Membranes Using Electron Spin Resonance'. In: *Journal of Membrane Science* 428 (2013), pp. 38–45. DOI: [10.1016/j.memsci.2012.11.003](https://doi.org/10.1016/j.memsci.2012.11.003).
- [281] Timothy A. Jackson et al. 'Vanadocene *de Novo*: Spectroscopic and Computational Analysis of Bis( $\eta^5$ -Cyclopentadienyl)Vanadium(II)'. In: *Organometallics* 31.23 (2012), pp. 8265–8274. DOI: [10.1021/om300892y](https://doi.org/10.1021/om300892y).
- [282] J. Krzystek et al. 'High-Frequency and -Field Electron Paramagnetic Resonance of Vanadium(IV, III, and II) Complexes'. In: *Coordination Chemistry Reviews*. The Ninth International Symposium on the Chemistry and Biological Chemistry of Vanadium 301–302 (2015), pp. 123–133. DOI: [10.1016/j.ccr.2014.10.014](https://doi.org/10.1016/j.ccr.2014.10.014).
- [283] Chao Li et al. 'Unraveling the Redox Couples of VIII/VIV Mixed-Valent  $\text{Na}_3\text{V}_2(\text{PO}_4)_2\text{O}_{1.6}\text{F}_{1.4}$  Cathode by Parallel-Mode EPR and In Situ/Ex Situ NMR'. In: *The Journal of Physical Chemistry C* 122.48 (2018), pp. 27224–27232. DOI: [10.1021/acs.jpcc.8b09151](https://doi.org/10.1021/acs.jpcc.8b09151).
- [284] Igor E. Soshnikov et al. 'An EPR Study of the Vanadium Species Formed upon Interaction of Vanadyl N and C-capped Tris(Phenolate) Complexes with  $\text{AlEt}_3$  and  $\text{AlEt}_2\text{Cl}$ '. In: *Journal of Molecular Catalysis A: Chemical* 303.1 (2009), pp. 23–29. DOI: [10.1016/j.molcata.2008.12.013](https://doi.org/10.1016/j.molcata.2008.12.013).
- [285] Jamie S. Lawton et al. 'Electron Spin Resonance Investigation of the Effects of Vanadium Ions in Ion Exchange Membranes for Uses in Vanadium Redox Flow Batteries'. In: *ECS Transactions* 41.23 (2012), p. 53. DOI: [10.1149/1.3697454](https://doi.org/10.1149/1.3697454).
- [286] Jamie S. Lawton et al. 'Ion Effects on Vanadium Transport in Nafion Membranes for Vanadium Redox Flow Batteries'. In: *Journal of The Electrochemical Society* 164.13 (2017), A2987. DOI: [10.1149/2.1791712jes](https://doi.org/10.1149/2.1791712jes).
- [287] Ramez A. Elgammal et al. 'Species Uptake and Mass Transport in Membranes for Vanadium Redox Flow Batteries'. In: *Electrochimica Acta* 237 (2017), pp. 1–11. DOI: [10.1016/j.electacta.2017.03.131](https://doi.org/10.1016/j.electacta.2017.03.131).
- [288] Jens Noack and Jens Tübke. 'A Comparison of Materials and Treatment of Materials for Vanadium Redox Flow Battery'. In: *ECS Transactions* 25.35 (2010), p. 235. DOI: [10.1149/1.3414022](https://doi.org/10.1149/1.3414022).
- [289] National Nuclear Data Center, Information Extracted from the NuDat Database. 2023. URL: <https://www.nndc.bnl.gov/nudat/>.



- [290] Silvio Künstner et al. 'Monitoring the State of Charge of Vanadium Redox Flow Batteries with an EPR-on-a-Chip Dipstick Sensor'. In: *Physical Chemistry Chemical Physics* 26.25 (2024), pp. 17785–17795. DOI: [10.1039/D4CP00373J](https://doi.org/10.1039/D4CP00373J).
- [291] *DOE Global Energy Storage Database*. DOE Global Energy Storage Database. 2023. URL: <https://gesdb.sandia.gov/> (visited on 09/11/2023).



## DANKSAGUNG

---

Eine solche Arbeit entsteht nicht im luftleeren Raum, sondern ist nur mit der Hilfe vieler Menschen möglich.

Meinen größten Dank möchte ich *Klaus Lips* aussprechen, der es mir ermöglichte, an diesem tollen Projekt zu arbeiten, für die Freiheit bei der Wahl der Schwerpunkte meiner Arbeit, für die langjährige und kontinuierliche Förderung sowie für seine unendliche Geduld.

Ohne meinen Zweitgutachter, *Jens Anders*, von der Universität Stuttgart gäbe es *EPR-on-a-Chip* in dieser Form nicht. Ich danke ihm herzlich für seine Unterstützung und für die vielen Stunden, die er in die Entwicklung gesteckt hat.

Ein großes Dankeschön an *Boris Naydenov* für seine ausgezeichnete Betreuung. Auf ihn konnte ich immer zählen, auch wenn er alle Hände voll zu tun hatte. Er schenkte mir immer ein offenes Ohr für meine Probleme und hat mir stets Lösungswege gezeigt.

Auch bedanke ich mich herzlich bei *Alexander Schnegg* für die inspirierenden Diskussionen und Gespräche, für seine Ratschläge sowie dafür, dass er es mir ermöglichte, zeitweise in seiner sympathischen Forschungsgruppe am Max-Planck-Institut für chemische Energiekonversion (MPI-CEC) zu arbeiten.

I am deeply grateful to *Joseph McPeak* for his continuous help, guidance not only in the lab, proofreading my scribbles, explaining chemistry to a physicist and our countless hours of discussions.

*Klaus-Peter Dinse* stand mir immer zur Verfügung, hat mir unzählige hilfreiche Kommentare sowie Impulse für meine Arbeit gegeben sowie pünktlich und zuverlässig Rückmeldung gegeben. Dafür danke ich ihm von ganzem Herzen.

I am especially thankful to *Anh Chu* for the great collaboration over the past years, the preparation and repair of the *EPRoC* (PCBs) and for answering my many questions about electrical engineering.

Special thanks to the fabulous *EPR* crew of *HZB*, *Joseph McPeak*, *Ekaterina Shabratova*, *Michele Segatini*, *Gianluca Marcozzi* and *Elizaveta Kobleva*, for bearing my 60 slides in our meetings, for our endless discussions of data, for sharing data and their emotional support.

*Jannik Möser* danke ich für die unkomplizierte Zusammenarbeit, sowie insbesondere für die Einführung in die *EPR* und speziell in die *RS-EPR*. Bei *Peter Fischer* vom Fraunhofer-Institut für Chemische Technologie bedanke ich mich für die gute Zusammenarbeit im *VRFB*-Projekt und für unser unverhofftes Frühstück in Brüssel.

I thank *Takuma Sato* of MPI-CEC for the pleasant cooperation and for performing suggested experiments immediately. He recorded the data on the influence of the dielectric constant.

Ein herzliches Dankeschön an *Jan Behrends* und *Thomas Lohmiller* für die Diskussionen über EPR sowie über Gott und die Welt.

Some data were not collected by me, but by others. For this, I thank *Daria Dymnikova* and *Jan Behrends* for the S-band and for the quantitative X-band data of the a-Si sample, respectively. I thank *Gianluca Marcozzi* and *Joseph McPeak* for recording the X- and Q-band data of BDPA, respectively. *Markus Wick* performed the initial FEM simulations of the electric and magnetic field of the 12-coil array board, which were continued and refined by *Michal Kern*, which is greatly appreciated. I thank *Elizaveta Kobeleva* for providing the field calibration data.

I thank *Martin Muske* for the preparation and *Michele Segantini* for spending 2 days with me to understand the dicing saw used to cut the sample in small pieces. The catholyte samples were prepared by *Tobias Gerber*, which is gratefully acknowledged.

Außerdem möchte ich allen bisher nicht genannten Mitarbeitenden der Abteilung Spins in der Energieumwandlung und Quanteninformatik bzw. des Instituts für Nanospektroskopie am HZB für die angenehme Arbeitsatmosphäre danken. Insbesondere sind hier *Natalia Scherbina*, *Jutta Proszak* und *Oshrat Galili* zu nennen, ohne deren Hilfe in bürokratischen Fragen nichts gelaufen wäre.

Auch danke ich allen Mitarbeitenden der EPR-Forschungsgruppe am MPI-CEC für die unkomplizierte hauptsächlich fernmündliche, -bildliche und -schriftliche Zusammenarbeit.

Des Weiteren möchte ich mich bei *Andreas von Kozirowski* und *Thomas Lußky* sowie *Marion Krusche* vom Institut für Silizium-Photovoltaik am HZB für den großartigen technischen bzw. bürokratischen Support bedanken.

Weiterhin bedanke ich mich bei den Menschen, die mir in den letzten Monaten geholfen haben, die langen Schreibtage zu überleben. Dazu gehören auch die AGs *Behrends* und *Bittl* am Fachbereich Physik der FU, denen ich für ihre Gastfreundschaft danke.

Nicht zu vergessen sind natürlich die großartigen Menschen außerhalb meines beruflichen Kontextes, die mir immer wieder gezeigt haben, dass es noch andere Dinge außer der Promotion gibt. Bei diesen bedanke ich mich besonders dafür, dass sie meine immer gleichen Geschichten angehört und mir Mut zugesprochen haben, wenn ich gezweifelt habe.

Abschließend danke ich meiner Familie für ihre kontinuierliche Unterstützung und Zuspruch während meines Studiums und meiner Promotion. Ich danke meiner Mama, *Sigrid*, dass sie immer für mich da ist und mir bei den schwierigsten Kapiteln geholfen hat. Meinem Papa, *Franz*, möchte ich dafür danken, dass er die komplette Arbeit Korrektur gelesen hat und mich dazu inspiriert hat, den Dingen auf den Grund gehen zu wollen. Ganz besonders danke ich *Julia*, dass sie mich immer daran erinnert, auch mal Pause zu machen, für unsere gemeinsame Zeit und den emotionalen Rückhalt.

## SELBSTSTÄNDIGKEITSERKLÄRUNG

---

Name: Künstler

Vorname: Silvio Dominik Lorenzo

Ich erkläre gegenüber der Freien Universität Berlin, dass ich die vorliegende Dissertation selbstständig und ohne Benutzung anderer als der angegebenen Quellen und Hilfsmittel angefertigt habe. Die vorliegende Arbeit ist frei von Plagiaten. Alle Ausführungen, die wörtlich oder inhaltlich aus anderen Schriften entnommen sind, habe ich als solche kenntlich gemacht. Diese Dissertation wurde in gleicher oder ähnlicher Form noch in keinem früheren Promotionsverfahren eingereicht.

Mit einer Prüfung meiner Arbeit durch ein Plagiatsprüfungsprogramm erkläre ich mich einverstanden.

*Berlin, 23.05.2024*

---

Silvio Dominik Lorenzo Künstler



#### COLOPHON

The image on the rear of the title page was created using the *Bing AI Image Creator* with the prompt “A green caterpillar with 12 eyes made of printed circuit boards in van Gogh style”.

*Final Version* as of 11th October 2024 (version 1.4).